The recovery of critical metals from low metal concentrations using impact electrochemistry

by

Abiola Victoria Oladeji

A thesis submitted to the University of Birmingham for the degree of

DOCTOR OF PHILOSOPHY

Centre for Fuel Cells and Their Fuels

School of Chemical Engineering

University of Birmingham

December 2023

Abstract

According to the definition provided by the European Commission, critical metals are materials that are commercially significant and have a high risk of supply disruption. The recapture of these critical metals from waste streams are essential for their sustainable use as they are often scarce and expensive. Traditional extraction techniques such as ion exchange, chemical precipitation, and adsorption/biosorption have often proven economically impractical for low concentrations of critical metals. These methods are limited by the environmental impact associated with the need for large volumes of reagent, and additional preconcentration and separation steps resulting in secondary waste generation. Electrochemical methods, including impact electrochemistry, would appear to be well-suited for the recovery metals, contingent upon the use of a suitable solvent and reduction potential. The key advantage of this technique is the high mass transport, operational feasibility, and potential for in-situ catalyst fabrication.

This thesis aims to investigate impact electrochemistry as a method to recover critical metals such as copper, palladium, and platinum from low concentration (0.5 mM) solutions. The study commences with the recovery of copper from 0.5 mM copper (II) sulphate, 1 mM sulphuric acid and 19 mM potassium sulphate to ensure a supported solution while minimising nanoparticle aggregation. Recovery would first be tested using metallic (silver and gold) nanoparticles where reductive transient peaks were observed indicating the deposition of copper onto the nanoparticles. After demonstrating this technique, the investigation was extended to study impact deposition onto fly-ash cenosphere particles which are generally considered as a waste material. The copper modified particles were characterised via scanning electron microscopy/energy-dispersive X-ray spectroscopy (SEM-EDX) and inductively coupled plasma mass spectrometry (ICP-MS) methods.

Next, the recovery of palladium and platinum from 0.5 mM palladium (II) chloride and hexachloroplatinic acid solution respectively was investigated as they are highly valued platinum group metals. Impact electrochemistry was conducted with 50 nm carbon black nanoparticles as they offer

an inexpensive core material with advantageous properties, such as good electrical conductivity and a high hydrogen overpotential. The fabricated Pd/CB NPs and the Pt/CB NPs where characterised via SEM-EDX, inductively coupled plasma optical emission spectrometry (ICP-OES), X-ray photoelectron spectroscopy (XPS), transmission electron microscopy (TEM), and thermogravimetric analysis of the modified particles. Additionally, the catalytic performance of the synthesised Pd/CB NPs and Pt/CB NPs was tested without any further modification in the Suzuki coupling reaction (Pd), hydrogen evolution reaction (Pd, Pt) and oxygen reduction reaction (Pt). Long term impact electrochemistry tests were also conducted to measure the extraction of palladium and platinum over time resulting in recoveries of 85% and 70% respectively in 26 h. It was noted that the use of nanoparticles optimised the recovery of both metals as the recovery rate increased by a factor of approximately 2 under the chosen experimental conditions.

Dedication

I want to start by thanking God for giving me the opportunity, resilience, and strength to complete this work (Philippians 4:13).

This endeavour would not have been possible without the indispensable support of numerous individuals, for whom I am profoundly thankful.

Firstly, I would like to acknowledge and dedicate this thesis to my wonderful fiancé Andrew Adelakun, for his unwavering support and encouragement through this time. I would also like to express gratitude to my parents Prof. Olayinka and Mrs Oyenike Oladeji, thank you for believing in me and always having words of comfort. And to my sisters, Abimbola Obembe and Boluwatife Oladeji, thank you for always being there and celebrating every small and big achievement with great enthusiasm. I want to extend a heartfelt thanks to my incredible friends Natasha Kandengwa, Nikita Rana, Ifeoluwa Asefon, Molly Keal, Fardowsa Mohamed, and Michelle Rigava. Thank you all so much for your encouragement and constant motivation. Finally, I would like to thank my supervisors Dr. Neil V. Rees and Dr. James M. Courtney for their vital contributions, guidance, and advice. Thank you both for always being so ready to help and for providing invaluable feedback which has enhanced the quality of this research. Your supervision and kindness have positively shaped my experience as a PhD candidate.

Acknowledgements

I would like to thank the Leverhulme Trust (RPG-2019-146) for funding this work, and the University of Birmingham EPSRC CDT for fuel cells and their fuels for the studentship. I would also like to acknowledge Dr Emma Schofield and Dr Barbara Breeze at Johnson Matthey plc for collaborative discussions. Prof. N.A. Rowson for supplying the waste cenosphere materials, Dr. R. Sommerville for hXRF spectroscopy, Mr. Y. Yan for support with the TGA, Dr. C. Stark for assistance with ICP-MS/ICP-OES, Dr. L. Jiang, and Dr. M. Fay (University of Nottingham) for discussions on XPS and TEM.

Abbreviations

E-waste	Electronic Waste
PCB	Printed Circuit Boards
CRMs	Critical Raw Materials
SRMs	Strategic Critical Metals
EC	European Commission
PGMs	Platinum Group Metals
PBDD/Fs	Polybrominated Dibenzofurans
Eh	Oxidation-Reduction Potential
OHP	Outer Helmholtz Plane
IHL	Outer Helmholtz Plane
LUMO	Lowest Unoccupied Molecular Orbital
HOMO	Highest Occupied Molecular Orbital
CV	Cyclic Voltammetry
LSV	Linear Sweep Voltammetry
RDE	Rotating Macro Electrode Disc Electrode
PEMFC	Proton Exchange Membrane Fuel Cells
MEA	Membrane Electrode Assembly
ORR	Oxygen Reduction Reaction
HOR	Hydrogen Oxidation Reaction
HER	Hydrogen Evolution Reaction
ECSA	Electrochemically Active Surface Area
GC	Glassy Carbon
CF	Carbon Fibre
MSE	Mercury Sulphate Electrode
SCE	Saturated Standard Calomel Electrode
RHE	Reversible Hydrogen Electrode
SHE	Standard Hydrogen Electrode
hXRF	Handheld X-Ray Fluorescence Spectrometer
SEM	Scanning Electron Microscopy
EDX	Energy Dispersive X-Ray
TEM	Transmission Electron Microscopy
ICP-MS	Inductively Coupled Plasma Mass Spectrometry
ICP-OES	Inductively Coupled Optical Emission Spectrometry
XPS	X-Ray Photoelectron Spectroscopy
TGA	Thermogravimetric Analysis
CFA	Coal Fly Ash
FACs	Fly-Ash Cenospheres
UPD	Underpotential Deposition
CB	Carbon Black
NP	Nanoparticles
ISAC	Interface And Surface Analysis Centre (ISAC)
RPM	Rotation Per Min

Table of Contents

List of figures

Publications

- **Chapter 3:** Oladeji AV, Courtney JM, Rees NV. Copper Deposition on Metallic and Non-Metallic Single Particles Via Impact Electrochemistry. Electrochim Acta. 2022;405:139838.

- **Chapter 4:** Oladeji AV, Courtney JM, Fernandez-Villamarin M, Rees NV. Electrochemical Metal Recycling: Recovery of Palladium from Solution and In Situ Fabrication of Palladium-Carbon Catalysts via Impact Electrochemistry. J Am Chem Soc. 2022:144(40):18562-74.

- **Chapter 5:** Submitted to ACS Sustainable Chemistry & Engineering

1. Introduction

1.1 Primary mining, environmental impact, and prospects of electronic waste recycling

1.1.1 Environmental challenges of finite primary metal sources

Metals underpin modern technology and infrastructures, thus are considered a core aspect of the economy and are essential raw materials integral to several industries ranging from manufacturing and construction to energy production. This is due to their physical and chemical properties such as ductility, corrosion resistance, reactivity, thermal and electrical conductivity. As metals are naturally occurring commodities obtained via mining and extraction methods, they are finite resources with varying abundancy and accessibility. For instance, aluminium (Al), although usually found as bauxite and cryolite, accounts for 8% of the lithosphere thus is relatively abundant with applications in industries such as aerospace and architecture.

Metals categorised as platinum group metals (PGM) including platinum (Pt), palladium (Pd), iridium (Ir), osmium (Os), rhodium (Rh) and ruthenium (Ru) are considered far scarcer with annual productions lower than that of gold and silver.[1-3] These metals are identified by their chemical resistance, high melting points and unique catalytic properties leading to a broad spectrum of applications in consumer and commercial products. Platinum and palladium are in relatively higher demand than other PGMs, with major applications in electronic devices, industrial chemical production and as catalyst within the automotive industry. The significance and versatility of these critical metals has resulted in a sustained increase in demand on these resources.[4]

These metals are typically obtained via mining activities from conventional reserves such as ores where the extraction is a multistep process which varies depending on whether the host minerology is sulphate or silicate in nature. Ores deposits are found in specific geographic locations with South Africa (Bushveld region) and Russia (Norilsk and Talnakh) serving as notable hubs for PGMs consequently exerting a dominate influence over the extraction of these metals.[5]

The mining of ores from South African reserves begins by using physical separation methods such as froth floatation to produce a mineral concentrate. This method relies on the differences in surface properties and the hydrophobic nature of some minerals to enable selective separation. Depending on the extent of the oxidation, this process yields 60% to 90% of the sulphide content with PGMs varying from 100 to 1000 g/tonne. Once dried, pyrometallurgical methods are utilised at a temperature of 1450^{o}C- 1500^{o}C resulting in the formation of Cu-Ni-Fe-S matte. Hydrometallurgical separation methods are then implemented using sulfuric acid under high pressure and temperature in the presence of excess oxygen. This process leaches the base metals (copper, nickel and iron) resulting in a precious metal concentrate that is further refined using selective extraction methods such as ion exchange, electrolytic and solvent processes.[6,7]

The extraction of metals via mining activities are considered energy intensive and associated with significant environmental impacts resulting from the generation of mining waste leading to the pollution of ground and surface water.[8,9] Metal extraction from primary sources is also associated with extensive land utilisation, waste generation and the emission of gases such as sulphur and carbon dioxides. Additionally, as these primary resources become depleted due to increasing demand, mining production costs will increase because of the challenges associated with accessing more remote and impractical deposits.[10] Due to the limited nature of raw metal reserves, alternative and more sustainable secondary sources of metals such as electronic wastes (e-wastes) are being explored. The term sustainability varies depending on the context however it is widely accepted as the definition provided in the Brundtland report stating that sustainable development is considered as meeting present needs without compromising the ability of future generations to meet their own needs .[11] Sustainability, specifically 'eco-efficiency' emphasises the reduction of resource consumption through more efficient use of raw materials, recyclability, and an overall reduction of environmental footprint.[10]

1.1.2 Exploration of secondary metal sources

Electronic wastes (E-wastes) refer to discarded electronic devices and can be categorised into 6 groups namely large equipment, small equipment, small information exchange equipment, monitors, temperature exchange equipment, and lamps.[12,13] The accelerated progress in technological development and increased affordability has resulted in a shorter lifespan for electronic equipment making them dispensable consequently resulting in the rapid generation of e-waste.[14-16] Approximately 53.6 million tonnes of electronic waste were produced in 2019, with an additional 38% increase forecasted by the year 2030 resulting in 74 million tonnes of electronic waste. As only a limited proportion of this waste is recycled (17.4 %), this has resulted in major environmental concerns thus making waste management a key topic of interest, specifically using sustainable methods of recovery.[17] The inadequate management of e-waste is associated with both adverse environmental impacts and health issues owing to the presence of toxic and heavy metal mixtures such as lead, mercury, chromium, and cadmium.[9,18-20] The presence of these heavy metals has been documented to disrupt ground cover, hinder plant growth, and have adverse effects on soil microorganisms. Additional challenges arise as heavy metals cannot be chemically degraded thus require physical removal or conversion to non-toxic substances.[19,21-23]

E-wastes are often referred to as urban mines and are a rapidly expanding sector of the modern economy as they are a major source of commercially valuable metals.[14,24] In addition to environmental considerations, there are also compelling economic incentives for extracting these metals. For instance, the raw materials within e-waste generated in 2019 had an approximate value of $57 billion. This is driven by key factors such as urbanisation, industrialisation, and increased consumer demand. Components such as printed circuit boards account for a significant portion of electronic waste and are important given their rich content of critical metals.[9,17,25] According to the definition provided by the European Commission, critical metals are classified using two key parameters. The first refers to the economic importance of the raw material in terms of the end-use applications and the value

added. The second parameter focuses on the risk associated with supply, considering factors such as domestic production, global supply and import dependence. Using these criteria, the European Commission compiled a catalogue of 34 critical raw materials (CRMs) of which 17 materials were noted as strategic critical metals (SRMs) where palladium, and platinum were highlighted. Strategic raw materials are defined as materials important in technologies that support the twin green, digital transition, defence, and aerospace applications. Copper and nickel (indicated by asterisks in Table 1) are listed on the EC CRM list, however, it is noted that they do not meet the CRM threshold requirements but are included solely as SRMs.[26]

Table 1 2023 list of critical raw materials including strategic raw materials in italics.

Aluminium/Bauxite	Coking coal	***Lithium***	***Copper****	Vanadium
Antimony	Feldspar	***LREE***	Phosphorus	***Nickel****
Arsenic	Fluorspar	Magnesium	Scandium	
Baryte	***Gallium***	***Manganese***	***Silicon metal***	
Beryllium	***Germanium***	***Natural graphite***	Strontium	
Bismuth	Hafnium	Niobium	Tantalum	
Boron/Borate	Helium	***PGM***	***Titanium metal***	
Cobalt	***HREE***	Phosphate rock	***Tungsten***	

Copper is considered an essential industrial commodity due to characteristics such as having a high melting point, corrosion resistance and high conductivity thus having various applications in electrical and construction sectors to highlight a few. Although present in lower concentrations than copper, e-waste is also a source of PGM and often contains higher concentrations than that obtained from traditional ores. For instance, 13% of the global mining output of palladium is utilised in the manufacturing of mobile phones and personal computers therefore contributing to the increased

value of e-waste.[21] The recovery of these metals from waste is essential to their long-term sustainable application, especially metals that have high commercial value and are considered scarce.

Metal extraction from both primary and secondary sources result in the generation of waste solutions containing low concentrations of critical metals. The inefficiencies at various stages of the recovery process result in the loss of commercially valuable resources to waste rock, tailings, slag, and leached ore. These independent streams encounter the wastewater during the production stage, producing wastewater charged with dissolved metals which then contributes to the spread of environmental contamination.[27,28] This is a challenge as the recovery from low concentration using current metal recovery methods is deemed in efficient due to added preconcentration processing steps which often result in more waste generation. For this reason, there is major interest in the removal of metals from low concentration waste and subsequently creating value-added products.

1.2 Current methods of metal recovery

1.2.1 Pyrometallurgy methods

Traditional methods of metal recovery from electronic wastes primarily utilises chemical, mechanical, and biological extraction processes with hydrometallurgy and pyrometallurgy serving as primary methods. In general, metallurgy encompasses various techniques for the production and manipulation of metals to produce specific materials and alloys that meet industrial specifications. Pyrometallurgy is considered one of the earliest techniques of metal separation and uses high temperatures to extract metals from both ores and secondary sources, for instance e-waste. This method is employed at an industrial scale with plants located across Europe.[20,24,29,] As pyrometallurgy occurs at high temperatures above 1000 ^{o}C, it is typically achieved in a specialised incinerator where the metal undergoes processes such as smelting, combustion, and pyrolysis.[30] Smelting is a well-established method frequently utilised for the recovery of non-ferrous metals.[31] This is broadly categorised into two smelting process flows where the metal is processed for the recovery of lead or copper. For the

lead smelting route, both concentrated sulphide ores and electronic wastes are treated for the extraction of lead and precious metals via sintering, reduction using coke, and further refining in a reverberatory furnace. During the final stages of this process, the precious metals are isolated from the lead using zinc from insoluble intermetallic compounds with gold and silver. The copper smelting route is employed for the extraction of precious metals to a larger extent than the lead route as it is considered more environmentally friendly in comparison as fewer toxic fumes are generated. For copper smelting using secondary sources of copper, crude copper-containing impurities such as iron and zinc are produced during reduction. This is further refined by oxidation in a converter where impurities are separated into a vapour phase.[31,32]

While the pyrometallurgy method is an efficient recovery technique with a high yield, it is associated with notable environmental drawbacks rendering it unsustainable. Processes such as smelting, conflagrating, and sintering result in the formation of slag which contains toxic elements posing a health risk to operators. Additionally, studies have shown that pyrometallurgy is associated with significant air pollution due to the release of harmful particulates and gases such as sulphur dioxide, carbon dioxide and polybrominated dibenzofurans (PBDD/Fs), which are detrimental to the environment.[21,29,30] Although, some of the SO_2 is captured and converted to sulphuric acid, or reacted with lime to form gypsum, quantities released remain high. Additionally, the organic PBDD/Fs pollutants generated have been documented to also exhibit comparable or greater levels of toxicity to dioxins.[33,34] A further limitation of this process is that a substantial amount of energy is required to reach the operational parameters thus contributing to higher operational costs.

1.2.2 Hydrometallurgy methods

Hydrometallurgy is the process of extracting metals using chemical separation methods and is conducted at lower temperatures typically under 200 ^{o}C.[35,] This process was introduced after the development of two critical techniques: the cyanidation method for silver and gold extraction and the Bayer process used for the treatment of bauxite to obtain aluminium. Broadly, hydrometallurgy

comprises of two fundamental stages, with the first step requiring the dissolution of the metal using the appropriate acid or alkaline leaching agents. Once leached, metals are subsequently extracted from the solution via a precipitation.

There are four common hydrometallurgical techniques used in industry namely, cyanide leaching, halide leaching, thiosulfate leaching and thiourea leaching. Cyanide leaching is considered an effective method of extracting gold and silver. This technique is prevalent in the gold mining industry as it is relatively cost efficient and operates in an alkaline environment.

During this process a lixiviant, typically a cyanide solution is introduced to e-wastes such as PCBs in an oxygen rich environment where it dissolves the surface metal present by forming cyanide complexes such as gold cyanide $[Au(CN)_2]^-$ and silver $[Ag(CN)_2]^-$.[36] Following this, the gold present in the solution is then extracted via adsorption onto activated carbon or ion exchange resins.[37] Although cyanide leaching has the added advantage of having a low energy consumption and does not require the use of a catalyst, there are important environmental and health concerns associated with the technique. A major drawback of this method is the long production cycle due to the slow leaching rate and the generation of large amounts of wastewater contaminated with cyanide, which pose a health risk to both operators and those in the surrounding environment.[21,36,37] Mild cases of cyanide poisoning occur at cyanide concentrations of 0.5-1.0 µg mL^{-1} and result in symptoms such as headaches, nausea, and vertigo. Cyanide concentrations of 2.5 µg mL^{-1} or higher result in severe symptoms including hypotension, arrhythmia and can even be lethal at higher exposures of 250 mg KCN.[38-40] The use of cyanide as a chemical reagent is also associated with environmental challenges for instance, the contamination of rivers and streams which have resulted in the death of aquatic biota.[41,42]

Due to the disadvantages associated with the use of cyanide, different leaching methods such as thiosulphate, halide and thiourea leaching have been investigated as metal extraction techniques of which thiosulfate leaching is the most notable as an alternative industrial process.[36] The thiosulphate leaching process is less understood than the traditional cyanide leaching process and is considered

complicated given the simultaneous presence of complexing ligands ammonia and thiosulphate.[37,43,44] Although this is a non-toxic extraction process with a high recovery rate, this technique is slower than cyanide leaching and results in the consumption of large volumes of thiosulfate as decomposition occurs in the presence of copper increasing operational costs.[45]

Halide leaching has a higher leaching rate and is achieved with either bromide, iodide or chloride chemical reagents forming both Au^{+} and Au^{3+} complexes. The stability of these complexes decrease as the electronegativity of the donor ligand increases; thus, iodine produces the most stable complexes. Additionally, the stability of the gold-halide complex depends on factors such as the Eh (oxidation-reduction potential), pH, concentration of the halide and processing material. Currently, industrial applications primarily employ chlorine leaching, requiring the use of stainless steel and rubber lined equipment to protect against the highly corrosive environment. There is growing interest in the use of iodine for metal extraction due to its stability, metal selectivity, and quick leaching rate. However, operational challenges remain such as the high cost of iodine and the consumption of large amounts of reagents.[37]

There has also been interest in the use of thiourea, as an organic reducing agent to form soluble cationic complexes with gold under acidic conditions with the addition of an oxidant.[29,46] This process is considered less detrimental to the environment as it is a non-cyanide lixiviant and exhibits rapid reaction kinetics. Similar to thiosulfate, thiourea is prone to rapid decomposition: consequently, there are limited industrial applications of this technique as it is not yet economically viable. Unless replenished, the concentration of thiourea decreases therefore reducing the number of active species available for leaching. Additionally, the use of this process as a method of gold recovery is inhibited by the presence of copper and other base metals as they form stable complexes with thiourea thus making it less selective.[47] There are also operational challenges attributed to the precise process conditions required including pH, temperature, and oxygen level.

Hydrometallurgical methods are less energy intensive than pyrometallurgy processes as they can operate at significantly lower temperatures. Additionally, hydrometallurgical metal extraction can achieve a high degree of selectivity via the pre-treatment of e-waste, identifying the appropriate leaching agent and conditions. Furthermore, although emerging hydrometallurgy processes emphasise the use of non-cyanide lixiviant, these processes continue to have a negative environmental impact due to the use of large quantities of chemical reagents generating large volumes of toxic waste that pose disposal challenges.[48,49]

1.2.3 Bio-hydrometallurgy methods

Bio-hydrometallurgical metal recovery is a cheaper and greener alternative to more widely used pyrometallurgy and hydrometallurgy as this process does not involve the use of complex machinery and is operated at mild conditions leading to reduced process costs.[50,51] Bio-hydrometallurgy, specifically bioleaching, relies on the use of microorganisms to extract metals by solubilising them to ensure they are accessible for recovery. This method of metal recovery is heavily affected by operating conditions namely, microbe selection, temperature, pH, nutrients, and aeration.

Bioleaching occurs via both direct and indirect bioleaching where the direct method refers to the conversion of solid metals to aqueous metals via the actions of the microorganism utilised.[52] The mechanism begins with the attachment of the bacteria i.e, *Acidithiobacillus,* to the metal sulphide where ferric ions (Fe^{3+}) in the bacteria are reduced to ferrous ions (Fe^{2+}) in the presence of oxygen by directly oxidising the metal.[21,53-57]

Alternatively, indirect bioleaching refers to the oxidation of sulphate minerals via the generation of intermediate oxidising agents produced by the microorganisms. In this case, ferrous ions are oxidised by the bacteria forming ferric ions which are then used to oxidise the metal sulphide. Industrially, mesophilic bacteria such as *Acidithiobacillus ferrooxidans and Acidithiobacillus thiooxidans* are commonly used as they depend on inorganic reagents for energy, and optimal growth can be achieved at temperatures between 28 ^{o}C and 37 ^{o}C.[21] The use of fungi (*Aspergillus* and *Penicillium*) for

bioleaching of metal has also been documented within literature.[53,58] Although bioleaching is more environmentally friendly than traditional methods, this process is notably slower resulting in longer processing times and is associated with the excessive use of water. Furthermore, there are also efficiency and operational challenges associated with the scale-up of this technique.

1.2.4 Electrodeposition methods

Metal electrodeposition from aqueous solution is a well-established industrial method used for metal recovery via electroplating, electrowinning, and electro-refining processes. This method offers many advantages as a technique for metal recovery such as selectivity, energy efficiency, reduced chemical usage and low operating costs as high temperature and pressure is not required.[59] Due to the versatility and ability to control the deposition rate, morphology and thickness, this technique is extensively used commercially. For example, applications include: the fabrication of energy storage technology, and surface modification techniques to enhance decorative and functional characteristics such as corrosion resistance.[60]

The electrodeposition system consists of a power supply (i.e rectifier) connected to a positively charged anodic electrode, and a negatively charged cathodic electrode to drive the reaction. Both electrodes are immersed into an electrolytic bath to maintain contact between them. Several reactor designs are used commercially for the process of electrodeposition with the most simplistic being the tank reactor where vertically held cathodes and anodes are suspended in the plating bath. This design is easily scaled and considered economical and allows the easy extraction of the electrodes to obtain the deposited metal foil. The primary limitation of this design is mass transport thereby making it only suitable for electrolyte solutions with high metal concentrations. To address this, the mass transport characteristics can be improved via the use of agitation employing gas sparging or pumping the electrolyte through the cell. Alternatively, rotating electrode reactors can be used to enhance mass transfer of the metallic ions from the bulk solution to the electrode-electrolyte interface.

During the electrochemical reaction, metal is recovered on the cathodic substrate as the metallic ions are reduced while oxidation processes occur at the anode. The aqueous electrolyte solution consists of both negative and positive metal ions prepared by dissolving metal salts or impure metals. When an external potential is applied, electrical current flows between the conductive electrodes as the charged ions species move via migration and diffusion.[61] In a mixed metal electrolyte solution, the recovery of the metals is influenced by the position of the metals in the electrochemical series and the chemistry of the solution itself.[60]

The operating parameters for industrial deposition are designed to optimise the process and adhere to commercial guidelines. For instance, metal plating requires the deposit formed to be of uniform thickness, sufficiently corrosion resistant and have a good adhesion to the surface. To achieve this, additives are commonly added to the electroplating bath to improve the adhesive material properties of the deposited metal. Organic species such as levelling agents are also added to the solution to accelerate deposition at surface defects (i.e trenches) by adsorbing to their surface ensuring the deposit produced is smooth and bright.[62,63]

1.3 Electrodeposition Principles

1.3.1 Electrodeposition Mechanism

Upon the dissolution of critical metals into aqueous solution, they can subsequently be recovered via electrochemical methods such as electrodeposition. In general, the electrodeposition process involves the application of an external electrical current to the system driving the reduction of the metal ions onto the cathode surface resulting in the formation of a metallic deposit as illustrated by Equation 1:

$$[M^{z+}\ (X^{y-})_m]\ (solution) + ze^- \leftrightarrows M\ (lattice) + mX^{y-} \qquad \text{Equation 1}$$

where M refers to the deposited metal, X is a neutral dipole or anion (y = 0, 1, 2, 3…) that can solvate or form complexes with the metal ions (M^{z+}) and e^- indicates an electron.[64-68]

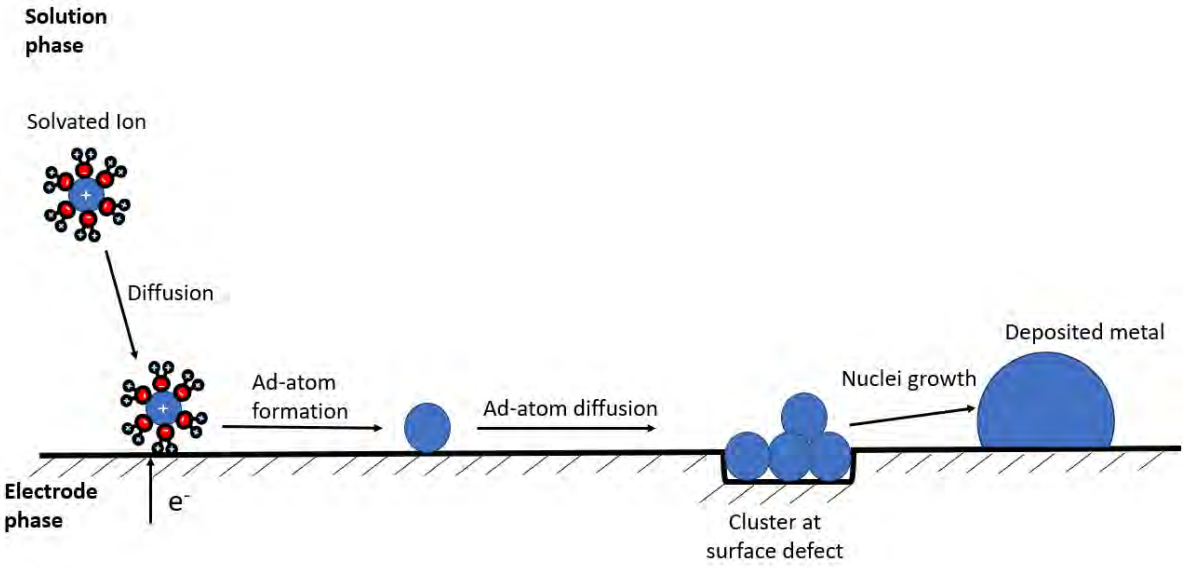

Figure 1 General schematic depicting the mechanism for formation of metal nuclei on surface of an electrode, adapted from literature.[61]

The deposition process encompasses distinct stages as shown in Figure 1, each contributing to the recovery of critical metals at the surface of the cathode. As this is a surface reaction, the process commences with the transport of the hydrated metal ion or complexes from the bulk solution to the surface of the cathodic electrode via diffusion, migration and convection if stirred. As the hydrated metal ions approach the electrode, the water molecules orientate in the diffusion layer where upon reaching the Helmholtz double layer, the process necessitates the partial removal of the hydration sheath from the metal ions at the electrode-solution interface where it retains some charge and solvation.[60] Specifically, within the electric double layer, once within tunnelling distance (10-20 Å),[65] electrons are transferred to the ions leading to the formation of adsorbed atoms (ad-atoms) onto the cathodic material. In the case of complex electrolytes, analogous to the removal of the surrounding hydration present on simple salts, the removal of ligand occurs before the discharge of metal ions. However, electrodeposition from complex electrolytes require higher overpotentials in comparison to simple salt solutions. Nucleation then occurs due to the mobile state of the ad-atoms which rapidly

move across the surface of the cathode via lateral diffusion controlled-migration forming thermodynamically stable crystalline nuclei. The growth phase then occurs upon the nuclei reaching a critical size subsequently merging to form a coherent metallic layer.[60]

1.3.2 Fundamentals of metal deposition

As the recovery of metals from waste solution is a faradaic process involving the reduction of metal ions it adheres to Faraday's law which establishes the theoretical concepts for the process of electrodeposition. For instance, the quantity of metal deposited is proportional to the number of moles of electrons transferred thus can be expressed as:

$$m = \frac{Q}{nF} \qquad \text{Equation 2}$$

where m is the mass of metal deposit, Q is the electric charge transfer (in coulombs) and n the number of electrons transferred. Given that t refers to time, at a constant current (I) the charge can be expressed as:

$$Q = \int I.dt = I\,t \qquad \text{Equation 3}$$

1.3.3 Electrochemical nucleation and growth

Nucleation refers to the initial formation of metal nuclei and is an essential step in the electrodeposition process as it determines the structure and properties of the larger deposit. Nucleation requires an overpotential to drive the electron transfer needed for the formation of nuclei centres on punctual or extended surface defects.[61,69] Initial nucleation on foreign substrates poses a challenge as the nucleus must reach a critical size threshold before growth can proceed as smaller nuclei have a propensity to dissolve in the electrolyte environment. Surface vacancies or kinks present on the electrode surface act as active centres by reducing the activation energy barrier for the formation of nuclei greater than critical size.[64,69]Once formed, the metal clusters develop and grow

rapidly where they frequently exhibit distinct hemispherical or cone shapes thus increasing the electroactive surface area of the substrate.[70]

Polycrystalline deposits are generally characterised by their size, shape, distribution, and orientation of crystallites. Zero-dimensional nuclei refers to individual ad-atoms on the cathode active sites which has the lowest energy requirement. Next, one-dimensional (point) nucleation described as a series of ad-atoms congregating along the edge of a mono-atomic step requires an overpotential of 0-10 mV. This growth occurs slowly resulting in the formation of dendritic or acicular (smooth flanks) which are typically avoided as they do not have useful technical properties. At overpotentials of 10-100 mV, two-dimensional nucleation, deposits form an initial monolayer before an additional layer can occur. As a result, crystallites in the deposit layer emulate the crystal structure of the substrate forming a coarse and compact structure. At even higher overpotentials of 100- 150 mV, three-dimensional nucleation occurs resulting in a thicker deposit that can be formed without an initial monolayer via hemispherical and cone shaped nuclei. At higher rates of electro-crystallisation, (where overpotential is greater than 200 mV), small crystal structures form resulting in randomly orientated crystallites with no visible orientation. This produces industrially relevant properties for technical applications.[64,71] Electrochemical techniques such as chronoamperometry can be used to study nucleation and growth for instance, for two- and three-dimensional nucleation processes by analysing the current profile. Furthermore, the chronoamperometry scan can also be used to deduce whether the nucleation kinetics are instantaneous or progressive. Instantaneous nucleation is characterised by the immediate formation of nuclei at all accessible sites once a sufficient overpotential is applied, whereas for progressive nucleation this happens in a more gradual manner.[72] The current density varies with $t^{1/2}$ and $t^{3/2}$ during instantaneous (Equation 4) and progressive (Equation 5) nucleation as shown:[73]

$$j_{inst} = zF\pi(2DC)^{3/2}M^{1/2}Nt^{1/2}\rho^{-1/2} \qquad \text{Equation 4}$$

$$j_{prog} = \left(\frac{2}{3}\right)zF\pi(2DC)^{3/2}M^{1/2}AN_{\infty}t^{3/2}\rho^{-1/2} \qquad \text{Equation 5}$$

Here, j_{inst} and j_{prog} refers to the current density for instantaneous and progressive nucleation respectively. The term zF is the molar charge deposited during deposition, D is the diffusion coefficient, C is the molar concentration of the electrolyte, M is the molecular weight, ρ metal density, N is the total number of nuclei, A is the nucleation rate and N_{∞} is the number density of active sites. The nucleation process is influenced by factors such as the crystal structure and substrate material where projections, edges, holes, and other defects act as centres of orientation of crystal growth.[64] Additional influencing parameters include: the crystalline structure of deposited metal, the electrolyte composition, pH and operating conditions such as applied current density and temperature. In general, conditions that increase the availability of metal ions at the surface of the electrode such as increased agitation and a higher temperature result in increased crystal size.[71]

1.4 Deposition of critical metals

1.4.1 Electrodeposition of copper from copper sulphate

The electrodeposition of copper is a well-established industrial process where the electroplating bath is predominantly an aqueous solution of copper (II) sulphate and sulphuric acid with trace amounts of impurities such as copper and organic addition agent.[74] Copper deposition from different electrolyte solutions have been extensively studied in the literature.[75-77]

Copper (II) sulphate salt ($CuSO_4.5H_2O$) exothermically dissolves in water resulting in the formation of octahedral aquo complexes $[Cu(H_2O)_6]^{2+}$.[78,79] When an overpotential is applied to the electrochemical cell, copper deposition occurs on the surface of the negatively polarised electrode via the 2-electron transfer reduction equation shown by Equation 6:

$$Cu^{2+}{}_{(aq)} + 2e^- \rightarrow Cu_{(s)} \qquad E^0 = +0.34\ V \qquad \text{Equation 6}$$

Whereas the oxidative water hydrolysis reaction shown by Equation 7 occurs at the anode:

$$2H_2O_{(l)} \rightarrow O_{2(g)} + 4H^+ + 4e^- \qquad E^0 = -1.23\ V \qquad \text{Equation 7}$$

The deposition of copper occurs via two consecutive one-electron reduction reactions and involves mass transport, electron transfer, adatom diffusion, and crystallisation.[80] This process can be described as CECE[81] and is elucidated in following reaction steps (Equation 8-Equation 13):[77,82]

$$Cu(H_2O)_6^{2+} \rightleftharpoons Cu(H_2O)_{6-x}^{2+} + xH_2O \quad \text{Equation 8}$$

$$Cu(H_2O)_{6-x}^{2+} + e^- \rightleftharpoons Cu(H_2O)_{6-x}^{+} \quad \text{Equation 9}$$

$$Cu^+(H_2O)_{6-x} \rightleftharpoons Cu(H_2O)_{6-x-y}^{+} + yH_2O \quad \text{Equation 10}$$

$$Cu(H_2O)_{6-x}^{+} \rightleftharpoons Cu(H_2O)_{5-x-y}(OH) + yH_2O + H^+ \quad \text{Equation 11}$$

$$Cu(H_2O)^{+}{}_{6-x-y} + e^- \rightleftharpoons Cu + yH_2O \quad \text{Equation 12}$$

$$Cu(H_2O)^{+}{}_{5-x-y}(OH)^- + e^- \rightleftharpoons Cu + yH_2O + OH^- \quad \text{Equation 13}$$

The initial chemical reaction is the removal of the water molecules surrounding the Cu^{2+} ions, followed by the reduction of the Cu^{2+} ions to Cu^{+} ions during the first electron transfer step. Next, a secondary chemical reaction occurs involving the dehydration of Cu^{+} ions which is then further reduced to copper metal. Within the mechanism, the first electron transfer is considered as the rate limiting step. The mechanism of copper deposition has been studied within literature where parameters such as pH, copper concentration, temperature, and electrolyte composition has been identified as influential on the nuclei size. For instance, an increase in pH or copper concentration results in larger nuclei formation but a reduced nuclei population density.[76,82-84]

1.4.2 Electrodeposition of palladium form palladium chloride solution

Pd is a platinum group metal, thus is a valuable resource utilised in several commercial applications. Due to the scarcity of this metal, effective recovery is necessary for their continued sustainable use. Deposition of palladium from an aqueous electrolyte solution has been explored in literature to further understand the complexity of the mechanism .[85-89] The deposition of palladium is traditionally conducted in basic or acidic solutions with palladium chloride aqueous solution predominantly used.

In chloride media, palladium exists primarily as $PdCl_2$, where the deposition mechanism for palladium occurs via a 2-electron transfer as Pd^{2+} is reduced to Pd. In solutions with low chloride concentrations, a reversible adsorption onto the metal electrode (M) first occurs (Equation 14), followed by a slower electrochemical reaction shown by (Equation 15):[90]

$$M + PdCl_4^{2-} \rightleftarrows M - PdCl_2 + 2Cl^- \quad \text{Equation 14}$$

$$M - PdCl_2 + 2e^- \longrightarrow M - Pd^0 + 2Cl^- \quad \text{Equation 15}$$

Alternatively, at high chloride concentrations, chloride ions adsorb on the metal and are displaced by a palladium chloride ion as shown by the following Equation 16 and Equation 17:

$$M - Cl^- + PdCl_4^{2-} \rightleftarrows M - PdCl_3^- + 2Cl^- \quad \text{Equation 16}$$

$$M - PdCl_3^- + 2e^- \longrightarrow M - Pd^0 + 3Cl^- \quad \text{Equation 17}$$

1.4.3 Electrodeposition of platinum from hexachloroplatinic acid solution

Similar to Pd, Pt is a PGM with valuable applications in automotive and electronic industries. For this reason, there has been great interest in recapturing spent Pt metal from both Pt (II) and Pt (IV) electroplating baths. The deposition of Pt from hexachloroplatinic acid ($PtCl_6^{2-}$) involves a 4-electron transfer reduction reaction, however there are two proposed mechanisms for this. A number of authors suggest that this occurs via an initial 2-electron reduction reaction of Pt^{4+} to Pt^{2+}, followed by further reduction to Pt as shown by Equation 18 and Equation 19:[91]

$$PtCl_6^{2-} + 2e^- \longrightarrow PtCl_4^{2-} + 2Cl^- \qquad E^0 = +0.73V \quad \text{Equation 18}$$

$$PtCl_4^{2-} + 2e^- \longrightarrow Pt + 2Cl^- \qquad E^0 = +0.76\,V \quad \text{Equation 19}$$

Alternatively, within literature it has also been suggested that the reaction proceeds directly from Pt^{4+} to Pt without the Pt^{2+} intermediate as shown by Equation 20:[91]

$$PtCl_6^{2-} + 4e^- \longrightarrow Pt + 6Cl^- \qquad E^0 = +0.74\,V \quad \text{Equation 20}$$

1.5 Electrochemistry principles

1.5.1 Structure of the electrical double layer

At the interface between the solid electrode and the electrolyte solution, an electrically charged double layer is present due to the difference in the phase boundary. This is a non-Faradaic phenomenon that occurs when the metal electrode is immersed in an electrolyte solution containing corresponding metal ions (M^{z+}) resulting in the charging and discharge of the double layer.[65] A reaction described by Equation 21 occurs at the surface where either the forward or reverse reaction is thermodynamically more favourable.

$$M^{z+}{}_{(aq)} + ze^- \rightleftarrows M_{(s)} \qquad \text{Equation 21}$$

When the forward reaction is favoured, the electrode becomes positively charged due to the loss of electrons (e-) where the charge remains at the surface due to the high conductivity within the metal. The positive charge attracts anions towards the electrode resulting in different potential at the electrode and in the solution. The forces that govern the behaviour of the electrolyte in the bulk solution is disrupted by the discontinuity at the interface and the electrode charge can be controlled via the potential applied. The structure at the electrical double layer greatly influences the kinetics of the metal deposition process.[64] Various models have been proposed to establish the nature of the process that occurs at the electrode-electrolyte interface with the primary models including: the Helmholtz-Perrin model, the Gouy-Chapman model, and the Stern-Graham model.[65,68,92,93]

Helmholtz-Perrin model

The Helmholtz-Perrin model describes the double layer structure as a rigid array of charged species at the electrode-electrolyte interface where ions are considered as point charges. This structure assumes that the electrons located at the surface of the cathodic electrode exist in a compact and structured

order and the positively charged metal ions within the electrolyte solution exist in a more distributed arrangement with a single layer at the surface of the electrode with the outer Helmholtz plane (OHP) passing through the solvated ions as shown in Figure 2.

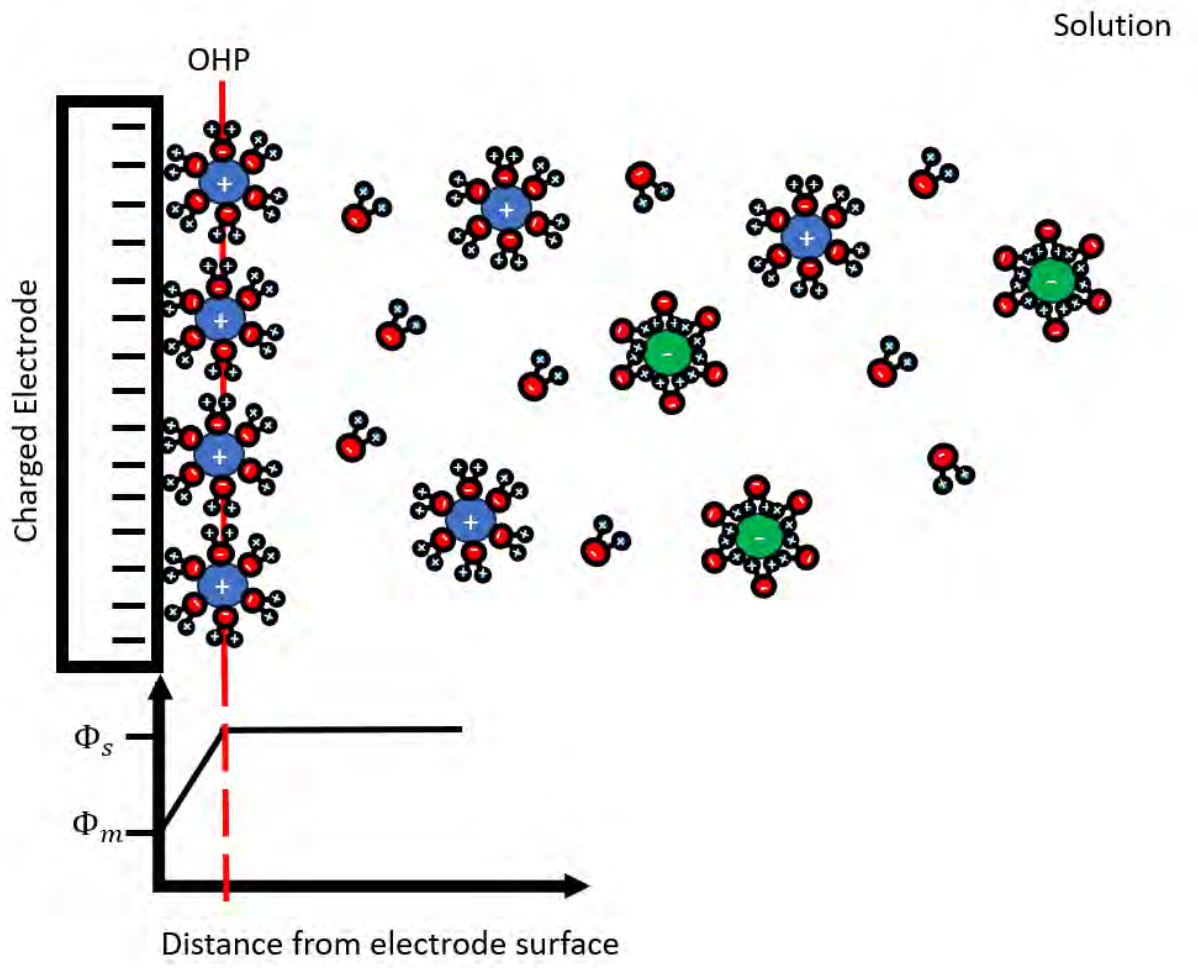

Figure 2 schematic depicts the Helmholtz-Perrin model showing the interaction at the solid- liquid interface where the negative charge is present on the surface of the electrode and positive ions arrange to form the outer Helmholtz plane (OHP).

The nature of charge at the cathode and in the electrolyte, solution is of equal and opposite magnitude thus maintaining electric neutrality as shown by Equation 22:

$$-Q_m = Q_s \qquad \text{Equation 22}$$

where Q_m refers to the charge at the cathodic surface and Q_s refers to the charge in the electrolyte solution. This charge separation results in an interfacial potential difference across the electrode-electrolyte boundary (δV) given by Equation 23:

$$\delta V = \frac{4\pi d}{\varepsilon\, \delta Q} \qquad \text{Equation 23}$$

where d is the distance between the two layers, ε is the dielectric constant of the medium and δQ is the charge density of each area. Additionally, it is assumed that the property of the electrical double layer is similar to that of a parallel plate capacitor with a separation distance of order one ionic radius and a constant capacitance value. This model does not consider the effect of the electrostatic attraction of the positive metal ions to the negative cathodic electrode, or the movement caused by thermal motion resulting to their statistical spatial distribution. Therefore, it is considered as a simplistic model that can be applied to solutions with high electrolyte concentrations but not dilute solutions.[64]

Gouy-Chapman model

Similar to the Helmholtz-Perrin model, the electrons remain on the surface of the negatively charge electrode, however the key difference is that the ions are not exclusively situated at the OHP as shown by Figure 3. Instead, these ions also exist across a diffuse layer as a three-dimensional arrangement where the concentration of ions decrease exponentially with distance from the cathode. The ions are considered as point charges where the charge density in the solution is contained within the diffuse layer. In this model, ions in the diffuse layer are required in addition to ions present at the OHP to balance the charge and are governed by the electrostatic force of attraction attracting or repelling ions from the electrode.[65-68]

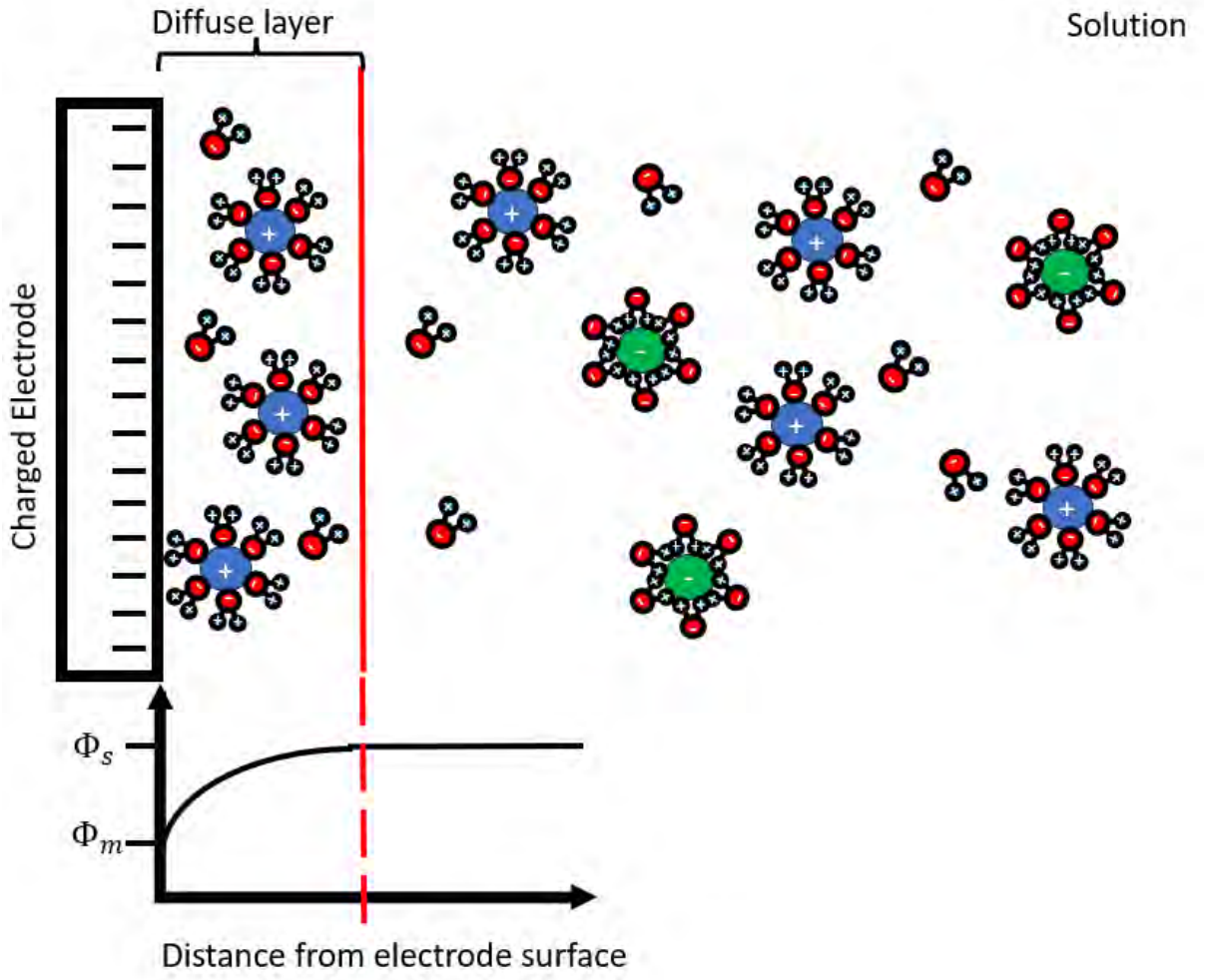

Figure 3 schematic of the Gouy-Chapman model describing the electric double layer where the positive ions exist across the diffuse layer as a three-dimensional arrangement and the concentration of ions decrease exponentially with distance from the cathode.

These ions are also influenced by Brownian motion which acts as a competing force driving the dispersion of the excess ions. For the Gouy-Chapman model, the net charge density in the diffuse layer indicates an exponential change in potential with distance away from the surface boundary where the potential drop across this layer is heavily concentrated in the region closest to the electrode surface. The change in potential across the diffuse layer can be given by Equation 24:

$$\delta V_{diff} = \sqrt{\frac{2RT}{\varepsilon} \sum_{i=1}^{s} c_1 \left[\exp\left(-\frac{z_i F \varphi}{RT}\right) - 1\right]} \qquad \text{Equation 24}$$

where R is the gas constant, T the absolute temperature, ε the dielectric constant, c_i the metal ion concentration in the bulk solution, z_i the metallic ion charge, φ is the total potential difference across the solution side of the double layer and F is the Faraday constant. For the Gouy-Chapman model, the spatial charge density is calculated via a summation of all the charge. The strength of this model is that it accounts for the change in capacitance as the double layer varies with potential and is not constant as the Helmholtz-Perrin model implies. Additionally, this model is relevant to electrolytes with a low concentration where they are unable to form a compact ion layer. Although this model is aligned with experimental results of differential capacity for dilute solutions and at potential of zero charge (E_{pze}), the limitation of this model occurs at higher concentration away from the potential of zero charge.[65-68]

Stern-Grahame model

The Stern-Grahame model was proposed to address the challenges identified with the Gouy-Chapman model as it is unable to accurately represent the condition at the electrode- electrolyte interface. In 1924, Stern combines the key principles proposed by both the Helmholtz-Perrin model and the Gouy-Chapman model as this offered a more accurate alignment with experimental results. The model proposed incorporated the concept of the diffuse layer and the outer Helmholtz plane where ions have a minimum distance from the cathode resulting from their size. In 1947, Grahame furthered this model by suggesting that although the region closest to the cathodic surface is predominantly occupied by solvent molecules, it is feasible that some ionic and uncharged species can penetrate the OHP. This occurs when the ions have no solvation shells or alternatively the solvation shell was lost as the ions approached the electrode. The absence of the solvation shells allows the ions to specifically adsorb to the electrode irrespective of the charge on the ion forming the inner Helmholtz layer (IHL) along with adsorbed layer of water molecules electrostatically attracted to the cathode.[65-68]

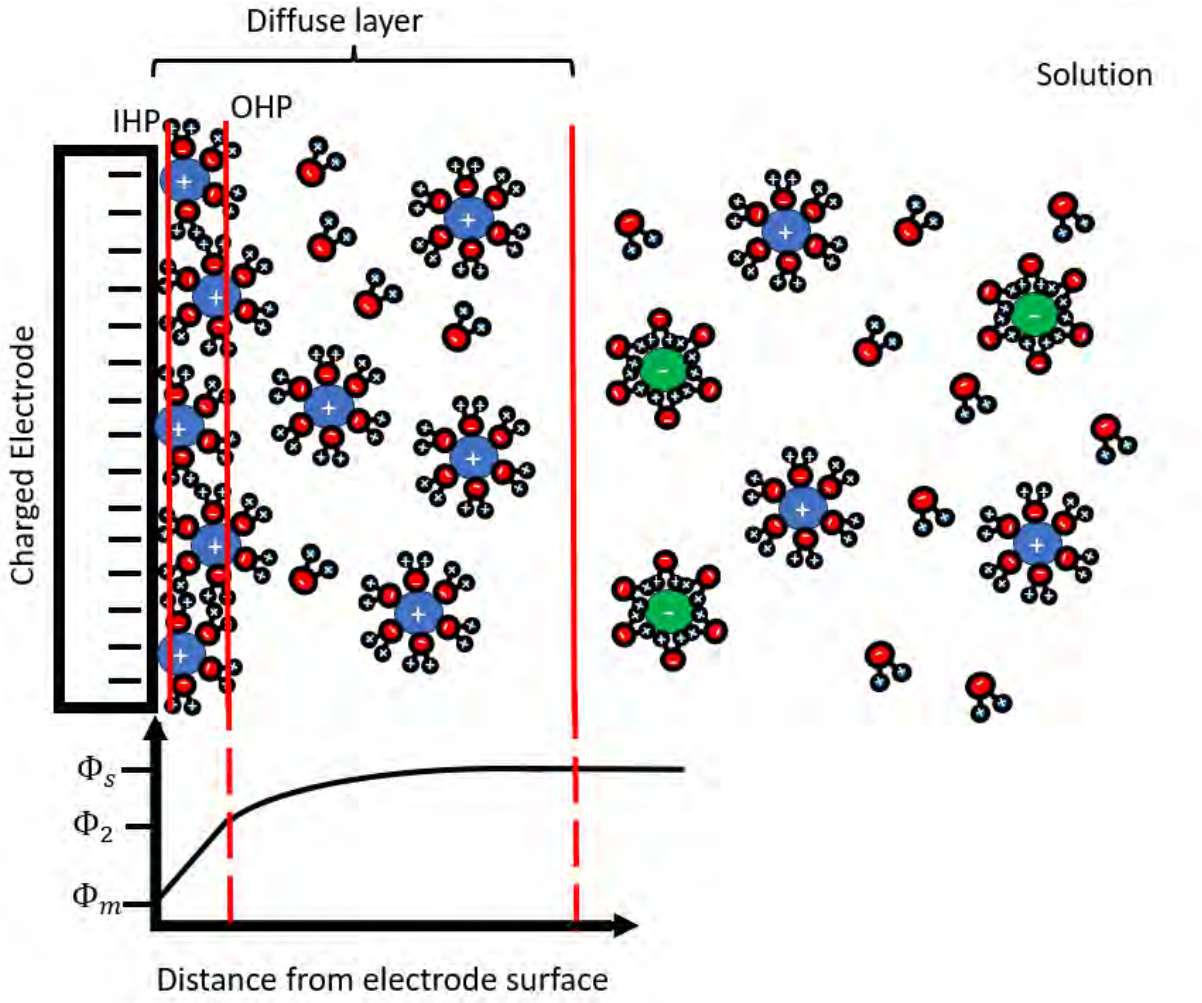

Figure 4 schematic of the Stern-Grahame model describing the electric double layer at the interface between two charged surfaces. This model is refining the Gouy-chapman model by introducing the inner Helmholtz layer produced by the specific adsorption of ions and molecules.

The IHL is identified by an axis through the specific adsorbed ions and molecules. Anions have a smaller closest approach distance than the cations as they are less strongly hydrated. The Stern-Graham model identifies four regions including the inner Helmholtz layer located closest to the electrode surface, followed by the outer Helmholtz layer, diffuse layer, and bulk solution, as shown in Figure 4. The Stern-Grahame model identifies two potential regions, the first is between the cathode and the OHP where the potential change increases steeply in a linear manner, followed by the diffuse layer indicating an exponential change in potential as described by the Gouy-Chapman model.[65-68]

1.5.2 Faradaic and non-Faradaic processes

Current flowing across the working electrode can be categorised as either non-Faradaic or Faradaic processes. Non-Faradaic processes are considered capacitive as charged particles do not transfer across the solid-liquid interface rather the charge is progressively stored for example during adsorption. For a simple capacitor like that described for the Helmholtz-Perrin model, the capacitance is assumed to be constant independent of potential as the charge separation is fixed. However, as later models suggest, the double layer is dependent on the applied potential and concentration. At potentials further from the potential of zero charge (E_{pzc}), the thickness of the double layer is reduced due to the attraction or repulsion of the electrolyte ions.[68,94] The differential capacitance (C_d) for the electrochemical cells is given by:

$$C_d = \frac{I\,\partial t}{\partial E} \qquad \text{Equation 25}$$

where I refer to the current, ∂t is change in time and ∂E is change in potential. On the other hand, Faradaic processes describe the method where electrons are transferred across the electrode-electrolyte interface during electrochemical reactions resulting in the continuous flow of electrons as seen in electrodeposition, fuel cells and corrosion.

1.5.3 Mass transport

To initiate the electrochemical deposition process, an overpotential is applied to the system which shifts the potential from equilibrium and results in the flow of electrons. Electrochemical processes are influenced by three fundamental principles: the mass transport of the reactants to the electrode, the transfer of charge at the electrode surface and the mass transport of products away from the electrode where the overall rate is governed by the slowest step (this is referred to as the rate determining step).

Diffusion

When the applied overpotential increases and the reaction kinetics are rapid, the system becomes mass transport controlled as the reaction is limited by the movement of ions from the bulk solution to the electrode surface. Mass transport can be achieved via three mechanisms, namely: diffusion, migration, and convection. Diffusion is driven by the presence of a concentration gradient thus occurs primarily in the diffusion layer near the electrode surface as species (i.e metal ions) are consumed upon undergoing redox reactions. In contrast, the concentration in the bulk solution remains relatively higher as this region is not depleted of ionic species. Diffusion can be described mathematically by Fick's first and second Laws as shown by Equation 26 and Equation 27 where the former refers to linear diffusion to a planar surface and the latter refers to the change in the concentration of electroactive species in a region with respect to time.[65,67]

$$j_B = -D_B \frac{\partial [B]}{\partial x} \qquad \text{Equation 26}$$

$$\frac{\partial [B]}{\partial t} = D_B \left(\frac{\partial^2 [B]}{\partial x^2} \right) \qquad \text{Equation 27}$$

Where j is the diffusional flux of species B, D_B is the diffusion coefficient, $[B]$ refers to the concentration of species B, ∂x is the change in distance from the electrode and ∂t is change in time. The morphological properties of the electrode surface influence the electrodeposition occurring under a diffusion control regime. The asperities on the electrode surface result in a reduction of the diffusion layer thickness thus intensifying the concentration gradient. This results in a localised increase in current and deposition rate.[61]

Migration

As it is assumed that there is no significant concentration gradient within the bulk solution, mass transport is governed by migration and occurs to move the ions from the bulk solution to the vicinity of the double layer. This mechanism involves the movement of charged species under the influence

of an applied electrical field across a potential gradient, where the migratory flux (J_m) is proportional to the concentration of species B, the electric field and ionic mobility. This electrostatic force (F) is given by Equation 28:[65]

$$F = \frac{zF}{N_A}\frac{\partial \phi}{\partial x} \qquad \text{Equation 28}$$

where z is the charge of the species, N_A is the Avogadro constant and ϕ is the potential.

Convection

Convection is the movement of molecules due to mechanical forces and can be categorised as natural or forced convection. Natural convection is driven by the presence of a thermal gradient or density gradient where the first results from exothermic or endothermic reactions and the second is associated with the disparity in density between the products generated at the electrode surface and the reactants in the bulk solution. Alternatively, forced convection is induced by agitation methods such as gas bubbling, pumping, or stirring where the change in concentration as a result of velocity in the x direction (v_x) is given by Equation 29:[60,65]

$$\frac{\partial [B]}{\partial t} = -v_x \frac{\partial [B]}{\partial x} \qquad \text{Equation 29}$$

The diffusion, migration and convection effect can be expressed mathematically by the Nernst-Planck equation as shown by Equation 30:

$$j_B = -D_B \frac{\partial [B]}{\partial x} - \frac{z_B F}{RT} D_B [B] \frac{\partial \phi}{\partial x} + [B]v \qquad \text{Equation 30}$$

where j_B is the flux of species B to the electrode, v is velocity of the volume moving across the axis. Typically, electrochemical studies are conducted under conditions to mitigate the effects of migration by using supporting electrolyte solution. The presence of excess ions provided by the supporting electrolyte enables the solution to maintain near electrical neutrality except in the region immediately adjacent to the electrode surface thus the migration effect is considered negligible. Furthermore, the

use of supporting electrolyte offers additional benefits such as increasing the solution conductivity thus the reaction solution has less resistance to current flow. The excess electrolyte also ensures the ionic strength of the solution remains effectively constant during the reaction as reactants are consumed and products are formed, therefore, the activity coefficient remain constant as they are influenced by ionic strength. Additionally, the presence of excess electrolyte solution compresses the electric double layer to a small region of 10-20 Å in line with the electron tunnelling distance.[65-68]

1.5.4 Two and three electrode system

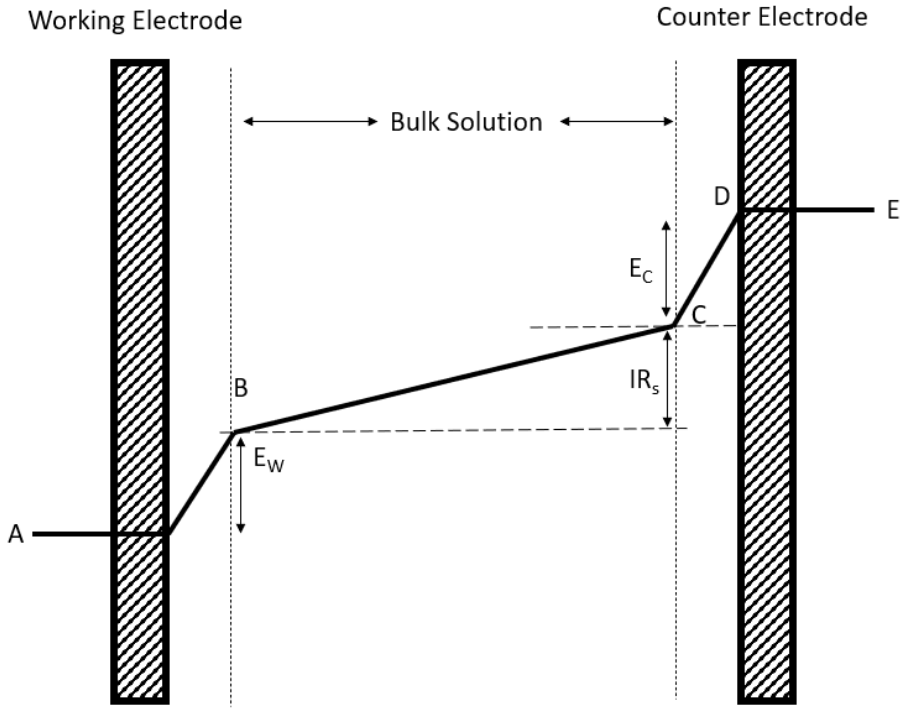

Figure 5 schematic of two electrode setup where E_w is the working electrode potential, E_c is the counter electrode potential and IR_s refer to the potential drop across the bulk solution. A-D indicates different potential between the two electrodes.

Electrochemical studies were conducted inside an earthed Faraday cage to prevent the interference of electromagnetic fields. In general, the simplest electrode configuration facilitating electrochemical measurements requires a minimum of two electrodes consisting of a working and counter electrode where the potential drop across the whole cell is measured (point A and E in Figure 5). For this project

all electrochemical studies were conducted using a traditional three-electrode system involving the working electrode, reference electrode, and counter electrode immersed in an electrolyte solution as shown in Figure 6. The use of three electrodes enables the isolated measurement at point A and B in Figure 5, thus the potential changes at the working electrode can be measured independently of the counter electrode reactions.

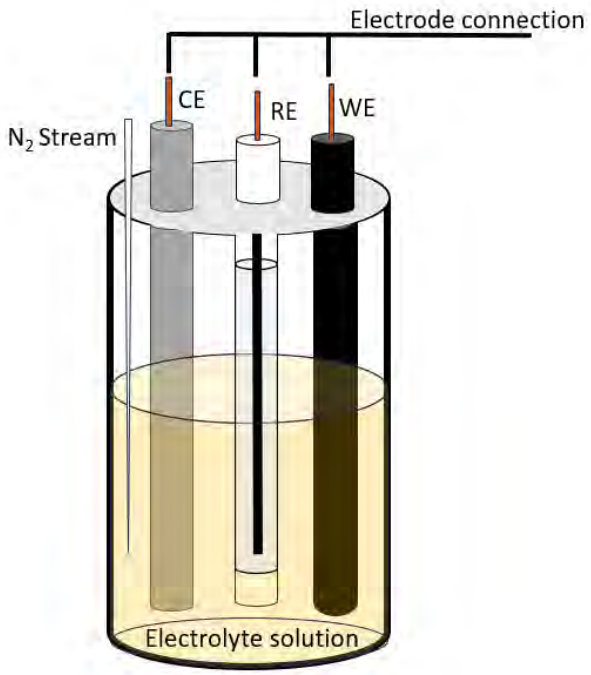

Figure 6 Schematic representation of a typical three electrode set

Additionally, the use of a reference electrode enables better control of the potential by maintaining a constant and well-defined interfacial potential as shown by Equation 31. Alternatively, for the two-electrode configuration, the counter electrode simultaneously acts as the reference therefore as current is drawn through the reference this induces chemical changes altering $(\phi_M - \phi_S)_{RE}$ according to the Nernst equation. Furthermore, a voltage drop (IR) occurs as a result of the electrical resistance of the bulk solution between the working and reference electrode (Equation 32). Changes to the potential E, would result in unknown changes to *IR,* and $(\phi_M - \phi_S)_{RE}$ thus the reference potential is no longer constant.[67]

$$E = (\phi_M - \phi_S)_{WE} - (\phi_M - \phi_S)_{RE}$$ Equation 31

$$E = (\phi_M - \phi_S)_{WE} + IR - (\phi_M - \phi_S)_{RE}$$ Equation 32

For the three-electrode system, when a potential is applied, electrons are transferred from the electrode to the metal ion during a reduction reaction; the ions in the supporting electrolyte move in solution to balance the charge and close the electrical circuit. During the electrochemical experiment, the potentiostat allows current flow between the working and counter electrode while current between the working electrode and reference electrode is negligible. This is because the potentiostat is modified with a high input resistor between working and reference electrode resulting in an infinite impedance of the reference electrode.

1.5.5 Nernst equation

Typically, an electrochemical set up will have a minimum of two electrodes to enable measurements provided an equilibrium is reached. However, an example of a simple Faradaic process is the submersion of a metal wire into an aqueous solution containing metal ions (M^{z+}) as seen in Equation 21. Once immersed, the wire acts as an electron sink or source facilitating the oxidation and reduction of the metal ions. When the equilibrium favours the oxidative reaction, the Pt electrode will carry a net negative charge due to the loss of electrons from the metal ions, while the solution will exhibit a net positive charge. However, in the case where the reductive reaction is favoured, the electrode become positive as the metal ions gain electrons resulting in a net negative charge in the solution. The redox reaction will persist until the electrochemical cell has reached thermodynamic equilibrium. This process is achieved by aligning the Fermi level of the metal with the highest occupied molecular orbital (HOMO) and lowest unoccupied molecular orbital (LUMO) of the charged metal species. Under this condition, the rate of the forward and backward reaction is equal, resulting in a consistent concentration of both reactant and product.[65,67]

Equation 34 represent a simple electron transfer reaction where A and B represents species in the solution that are reduced and oxidised at a rate given by k_{red} and k_{ox} respectively.

$$A_{(aq)} + e^- \underset{k_{ox}}{\overset{k_{red}}{\rightleftarrows}} B_{(aq)} \qquad \text{Equation 33}$$

At equilibrium there is no current flow through the electrochemical cell hence the cell potential of the working electrode can be determined via the Nernst equation. The Nernst equation can be derived from Gibbs energy under standard conditions. When at equilibrium, under conditions of constant temperature and pressure the minimisation is mathematically given by Equation 34 and Equation 35:

$$\Delta G^0 = 0 \qquad \text{Equation 34}$$

$$\Delta G^0 = -RT\ In\ K_{eq} \qquad \text{Equation 35}$$

where R is the ideal gas constant, T the absolute temperature and K_{eq} the equilibrium constant. The Gibbs energy under standard (ΔG^o) and non-standard (ΔG) conditions are given by Equation 36-Equation 38:

$$\Delta G^o = -nFE^o \qquad \text{Equation 36}$$

$$\Delta G = -nFE \qquad \text{Equation 37}$$

$$\Delta G = \Delta G^o + RT\ InQ \qquad \text{Equation 38}$$

Where E^o is the standard potential, E is the cell potential, Q refers to the reaction quotient, which is a measure of the relative chemical activities of products and reactants in a reaction mixture. The activity (a) is defined as shown in Equation 39 where γ is the activity coefficient and $[\mathrm{B}]$ is the concentration of species, B in this case. By substituting Equation 36 and Equation 37 into Equation 38, the equation can be rearranged to obtain the following Nernst equation (Equation 40) where Q is equal to the K_{eq} at equilibrium:

$$a = \gamma[B] \qquad \text{Equation 39}$$

$$E = E^o - \frac{RT}{nF}\, In\, Q$$ Equation 40

Overpotential

The term overpotential can be expressed as the difference between the applied voltage (E) and the standard reduction potential (E^0) and is given by Equation 41:[95]

$$\eta = E - E^0$$ Equation 41

However, under non-standard conditions the standard reduction potential can be replaced by the formal potential $E_f{}^0$ .An overpotential is required to shift the potential away from equilibrium thus driving the rate of metal deposition assuming, no mass transport limitations.[64]

1.5.6 Electrochemical techniques

Electrochemical methods offer a rapid, simple, reproducible, and reliable analysis method. Thus, electrochemical techniques are a powerful tool extensively employed for electroanalysis to probe reactions involving the transfer of electrons and used for material electrosynthesis applications.

Cyclic Voltammetry

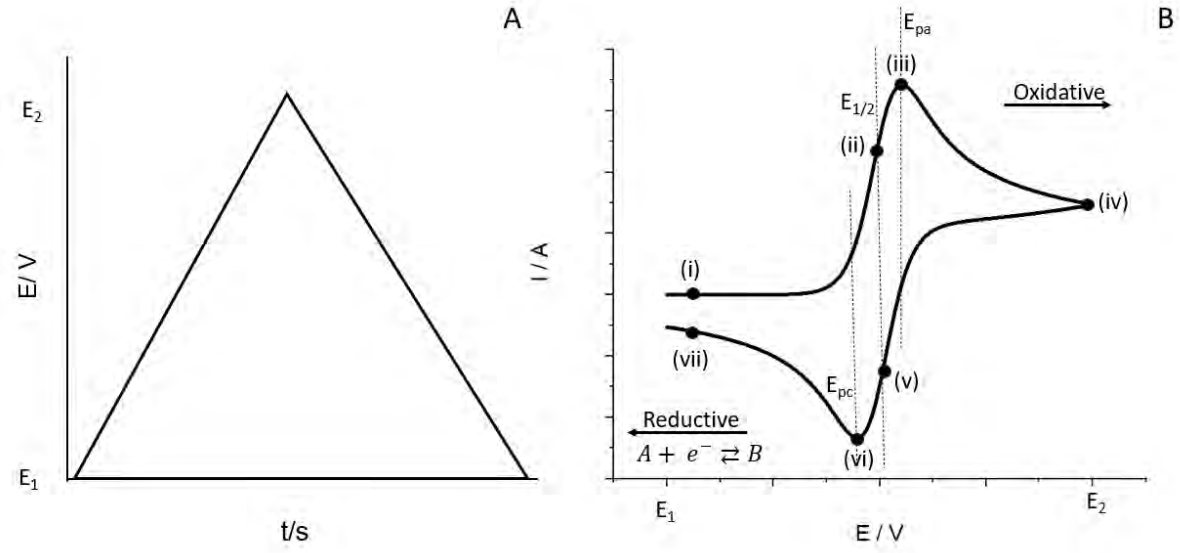

Figure 7A shows a potential-time profile for a cyclic voltammetry scan between E_1 to E_2 initially in the oxidative direction then reversing to scan from E_2 to E_1 in the reductive direction. Figure 7B shows a simulated cyclic voltammetry scan between the potential window E_1 to E_2. The anodic peak potential E_{pa}, cathodic peak potential E_{pc} and $E_{1/2}$ halfway potential has been shown.

Cyclic Voltammetry (CV) commences with a potential sweep from E_1 to E_2 where upon reaching E_2 the sweep is reversed and the potential returns to E_1 as shown by Figure 7A. Figure 7B illustrates a reversible CV where seven notable locations on the voltammetric wave indicated by (i)-(vii) have been highlighted. Point (i) to (ii) indicates the oxidation of the electroactive species resulting in the steady depletion of reactant (species B) at the electrode surface and formation of product (species A). Peak (iii) highlights the maximum oxidative current corresponding to a greater depletion of reactants and generation of product resulting in a thicker diffusion layer compared to point (ii). At point (iii)-(iv), the concentration of reactants available at the electrode is low thus a drop in current is observed. Upon scanning in the cathodic potential direction (iv-vii), the reduction of the product occurs resulting in a negative current (iv-v) subsequently reaching a maximum peak (vi) indicating mass transport limitations thereafter (vi-vii).

Reversible and irreversible electrode couples

Electrochemical reversibility refers to the rate of the electrode kinetics (k_0) in comparison to the rate of mass transport of the electroactive species (m_T) to the surface. For reversible processes, the electrode kinetics are fast as shown by Equation 42. Alternatively, irreversible behaviour is characterised by 'slow' electrode kinetics as indicated by Equation 43.[67]

$$k_0 \gg m_T \qquad \text{Equation 42}$$

$$k_0 \ll m_T \qquad \text{Equation 43}$$

In the case of an irreversible electrode couple, a larger overpotential is required to facilitate the oxidation of species B to species A and the reduction of species A to B thus the peak separation on voltammogram appears further apart. Evaluating the peak-to-peak separation and the peak current can be used to determine the reversibility of the electrode couple.

For a reversible system:

$$\left|E_p - E_{p_{\frac{1}{2}}}\right| = 2.22\frac{RT}{nF} = 59\ mV \qquad \text{Equation 44}$$

For an irreversible reductive system:

$$\left|E_p - E_{p_{\frac{1}{2}}}\right| = 1.86\frac{RT}{\alpha nF} \qquad \text{Equation 45}$$

For an irreversible oxidative system:

$$\left|E_p - E_{p_{\frac{1}{2}}}\right| = 1.86\frac{RT}{n\beta F} \qquad \text{Equation 46}$$

Where E_p is the potential at peak current, $E_{p1/2}$ is the potential at half the peak current, R is the gas constant, T is temperature, β is the symmetry factor, α is the transfer coefficient and F is the Faraday constant. For the reversible case with a one electron transfer (n=1), the peak potential thus the peak-to-peak separation is constant (59 mV at 298 K) and independent of the scan rate applied (Equation 44). However, for the irreversible reduction (Equation 45) and oxidation (Equation 46), the peak potential shifts more negatively or positively as the scan rate increases. For the same scan rate, reversible electrode couples exhibit a larger peak current than irreversible cases. However, regardless of the reversibility, the absolute magnitude is influenced by the voltage scan rate as shown by the Randles- Ševčík equations (Equation 47 and Equation 48). For both cases, an increase in current is observed at higher scan rates as a thinner diffusion layer is formed. This increase in the peak current is linear and proportional to the square root of the scan rate for reversible cases.

$$I_{p(rev)} = 2.69 \times 10^5 AD^{\frac{1}{2}}Cv^{\frac{1}{2}} \qquad \text{Equation 47}$$

$$I_{p(irrev)} = 2.99 \times 10^5 \sqrt{\alpha}AD^{\frac{1}{2}}Cv^{\frac{1}{2}} \qquad \text{Equation 48}$$

$I_{p(rev)}$ and $I_{p(irrev)}$ are the reversible and irreversible peak current, A is the electrode area, D is the diffusion coefficient, C is the concentration of the electroactive species, υ is the voltage scan rate and α is the transfer coefficient.

Linear sweep voltammetry

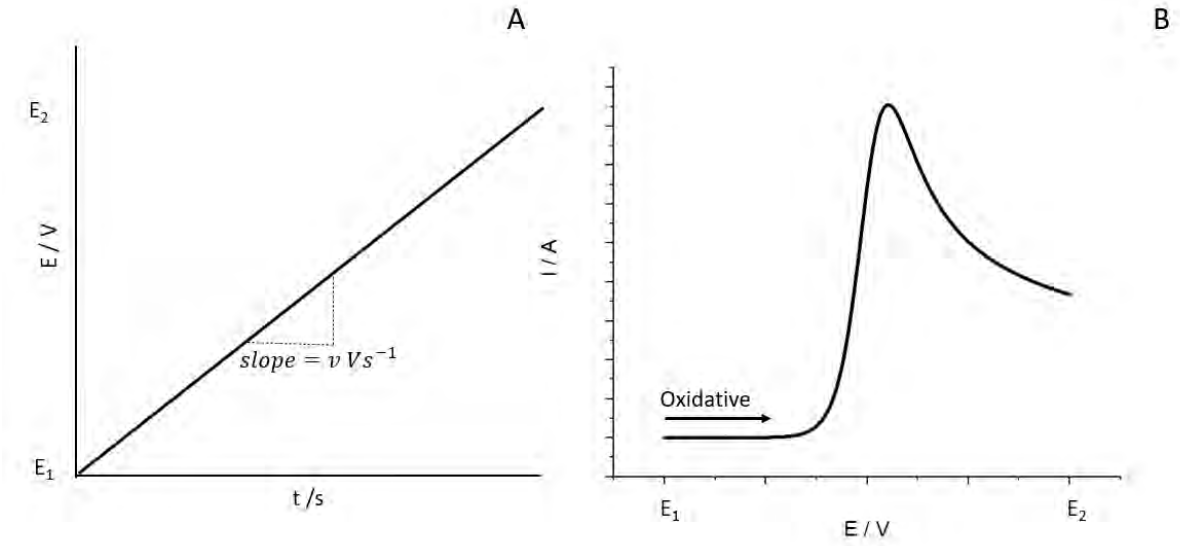

Figure 8A Potential-time profile and Figure 8B shows a simulated current-potential for linear voltammetry sweeping between E_1 to E_2 in the oxidative direction.

Linear sweep voltammetry (LSV) is a simple electrochemical scan where a potentiostat is used to apply a progressively increasing voltage to the working electrode. This results in a voltammogram showing the current response plotted as a function of voltage where the integrated area can be used to determine the charge transferred. Figure 8B shows a voltammetry where the potential is swept oxidatively from E_1 (where the reaction is unable to occur) to E_2 where the kinetics are rapid. Typically, the scan commences at a potential where the electroactive species under investigation does not undergo reduction or oxidation as a sufficient overpotential has not been applied thus negligible current flow is expected (E_1). As the sweep continues, current flow increases until a maximum is reached signifying that the system is mass transport controlled subsequently leading to a decrease in current. Once the peak current is reached, although the heterogeneous rate constant increases, the reaction is limited by the movement of reactant to the surface of the electrode. The LSV is influenced by voltage scan rate, rate of electron transfer and chemical reactivity of the electroactive species.

Chronoamperometry

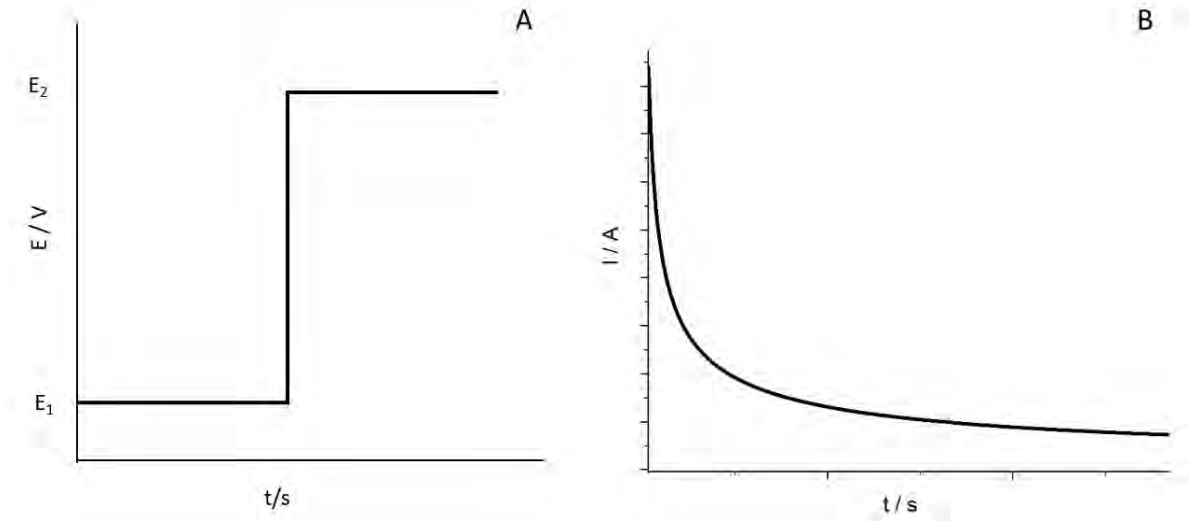

Figure 9A shows a potential-time profile where the voltage has been applied as a potential step and Figure 9B shows a simulated current-time profile for a chronoamperometry scan between E_1 to E_2.

Chronoamperometry is an electroanalytical method where the potential is instantaneously stepped from E_1 to E_2 (Figure 9A). Initially a large current is measured resulting from the high concentration of reactant at the electrode surface. The current then progressively decreases with time as shown by Figure 9B, this is because the reactants are consumed, and the reaction becomes mass transport controlled. The Cottrell equation is used to describe the decay of the current response as a function of time (Equation 49) at a planar macroelectrode:[67]

$$|I| = \frac{nFAD^{1/2}C_b}{\pi^{1/2}t^{1/2}} \qquad \text{Equation 49}$$

where C_b refers to the bulk concentration of the analyte, D is the diffusion coefficient of the analyte, n is the number of electrons transferred during redox reaction, t is time, F is the Faraday constant, and A is the electrode area.

Macro and micro electrodes

Both macro and micro electrodes were employed for electrochemical investigations with macro electrodes used for initial deposition studies to determine the onset potential in the various metal systems. Macro electrodes are characterised by their large surface area and perpendicular mass

transport. The use of macro electrodes enabled surface modification using the drop cast method for material testing as discussed in chapter 2.1. Large macro electrodes were also utilised in the scaled-up impact studies as the large size made it ideal the generation of metal modified carbon black nanoparticles during in-situ catalyst synthesis.

A rotating macro electrode disc electrode (RDE) was used for electrocatalyst studies of the synthesised Pt/CB via the oxygen reduction reaction. The use of hydrodynamic electrodes mitigates mass transport limitations by introducing forced convection thus increasing the rate at which reactants are introduced to the surface and products are removed resulting in a steady supply of electro actives species. The relationship between the limiting current and the diffusion layer is given by Equation 50 and Equation 51:[67]

$$I_L = 0.62nFAD^{\frac{2}{3}}\omega^{\frac{1}{2}}\upsilon^{-\frac{1}{6}}C \qquad \text{Equation 50}$$

$$\delta = 1.61D^{\frac{1}{3}}\omega^{-\frac{1}{2}}\upsilon^{\frac{1}{6}} \qquad \text{Equation 51}$$

where A is the electrode area, D is the diffusion coefficient, ω is the angular rotation rate and v is the kinematic viscosity. These equations can be used to quantify the number of electrons transferred, the diffusion coefficient, analyte concentration and theoretical limiting current.

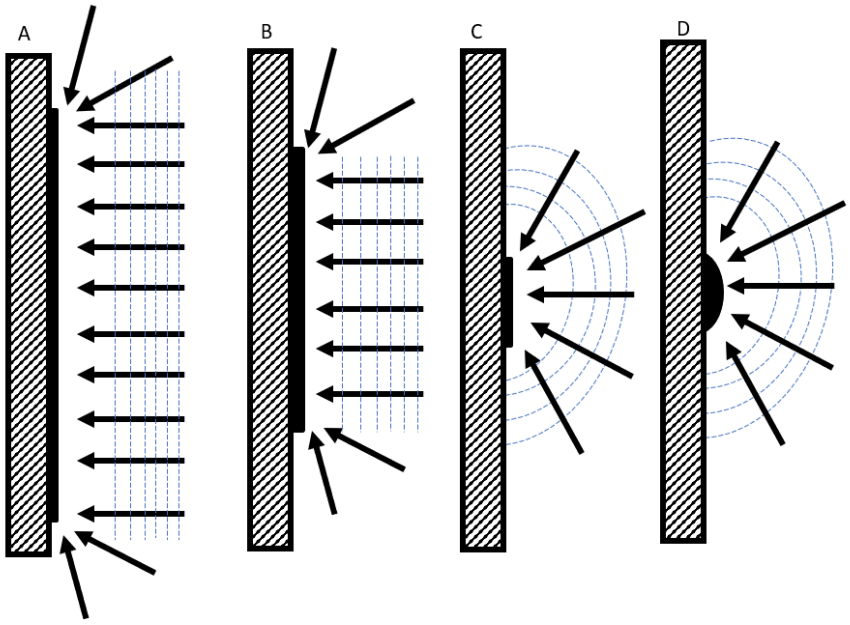

Figure 10 schematic of planar and spherical diffusion of species to the electrode surface where the arrow shows the movement of material, and the dotted lines (- - -) indicate the diffusion regime. At larger electrode surfaces (A) planar diffusion dominates, as the electrode size becomes progressively smaller as seen in (B) becoming a microelectrode (C) and also in the case of a spherical electrode (D) the diffusion is no longer planar.

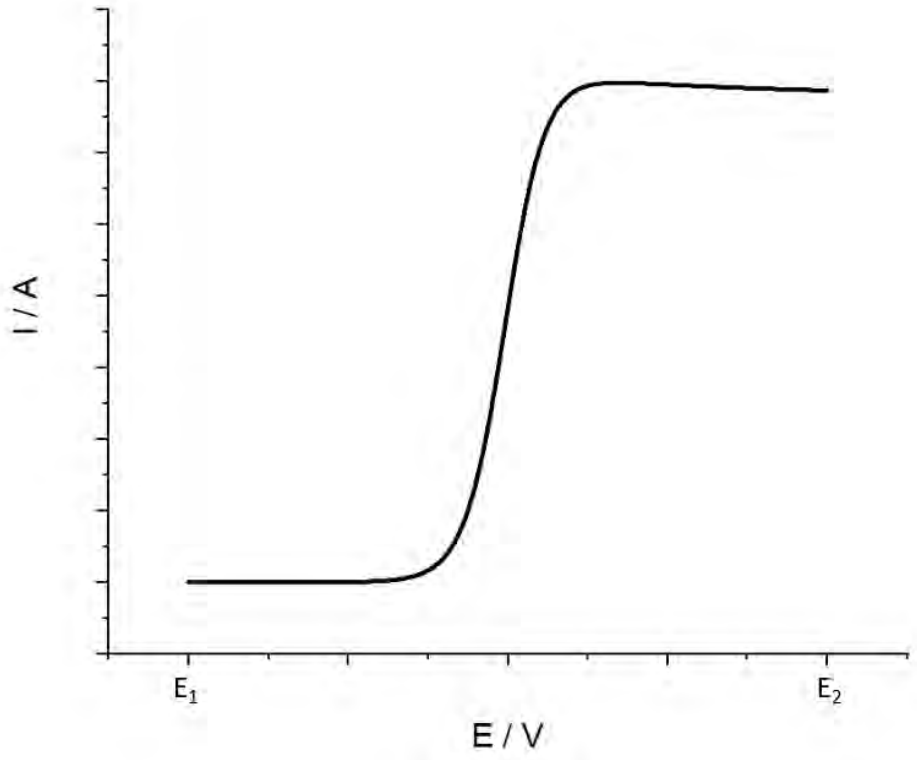

Figure 11 shows simulated microelectrode linear sweep voltammogram indicating steady state has been reached.

Micro electrodes are characterised by their small scale. Due to the nature of the electrode size, the diffusion layer at the electrode surface is considerably smaller than that of a macroelectrode resulting in a higher concentration gradient. Mass transport of the reactants to the electrode surface is rapid as it occurs via a three-dimensional diffusion thus the steady state mass transport regime is established quickly (Figure 10). As a result, the voltammogram response of microelectrode differs from that of a macroelectrode as steady state is reached therefore no peaks indicating mass transport limitations are present (Figure 11). To investigate the occurrence of steady state, microelectrodes are considered as points with the diffusion layer being spherical or hemispherical in shape and so Ficks second law can be modified to express the following:[96]

$$\frac{\partial[B]}{\partial t} = D_B \left(\frac{\partial^2[B]}{\partial r^2} + \frac{2}{r}\frac{\partial[B]}{\partial r}\right) \qquad \text{Equation 52}$$

$$\frac{\partial[B]}{\partial t} = D_B \left(\frac{\partial^2[B]}{\partial r^2} + \frac{1}{r}\frac{\partial[B]}{\partial r}\right) \qquad \text{Equation 53}$$

where r is the radius of the hemisphere. The mass transfer of the electroactive species is governed by the volume enclosed by the expanding hemisphere or sphere (Equation 52) rather than the linear plane projecting into the solution as seen for a disc electrode (Equation 53). At short time limits or larger radii when the diffusion layer is significantly smaller than the electrode radius (Equation 54), the mass transport exhibits an almost linear diffusion and can be predicted by the Cottrell equation (Equation 49). At long time limits or smaller electrode radii where the diffusion layer is larger (Equation 55), the flux of electroactive species to the electrode surface is more rapid. As the reaction continues, the diffusion layer thickens due to spherical expansion thus has more access to the electroactive species with time thus maintaining a constant diffusion gradient resulting in steady state current given by Equation 56:[67,72]

$$\sqrt{D\pi t} \ll r \qquad \text{Equation 54}$$

$$\sqrt{D\pi t} \gg r \qquad \text{Equation 55}$$

$$I_{ss} = 4nFDC_b r \qquad \text{Equation 56}$$

Here, I_{ss} refers to the limiting current, n the number of electrons transferred, D the diffusion coefficient, r the electrode radius, F is Faraday constant and C_b the bulk concentration. Microelectrodes can be used to study the fast kinetics and mechanisms of the metal nucleation and growth. Another advantage of a smaller electrode area is the reduced background current associated with the changes to ionic distribution of electrolyte as the applied electrode potential changes.[67,69,97] This is of great importance for particle impact electrochemistry as the presence of excessive background noise can make it difficult to identify transient current peaks as discussed later in chapter 2.2.

Microelectrode arrays

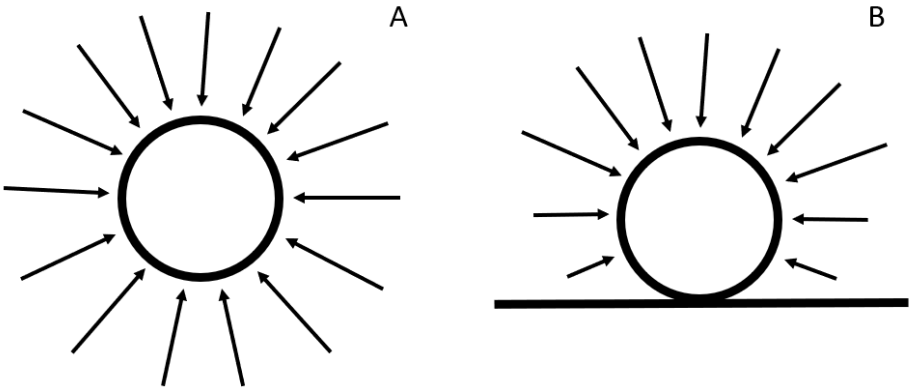

Figure 12A schematic of spherical electrode isolated in solution and Figure 12B shows a sphere on a plane. The arrow indicates the diffusion of electroactive species to the particle surface.

The use of nanoparticle modified electrodes, achieved via methods such as drop casting has become increasingly popular (see chapter 2.1). For an isolated spherical electrode which is not in contact with a plane as shown in Figure 12A, the steady state current is given by:[67]

$$I_{ss} = 4\pi rFDC_b \qquad \text{Equation 57}$$

When the spherical electrode is in contact with a surface as shown by Figure 12B, for example a nanoparticle impacting on an electrode surface, a correction factor is applied to Equation 57 giving:

$$I_{ss} = 4\pi \ \ln(2)\, rDC_b \qquad \text{Equation 58}$$

Microelectrode arrays are often employed for analytical measurements and consists of multiple (tens to thousands) of microelectrodes in an array. For an electrode array with microelectrodes separated using non-conductive material, individual diffusion layers are present and continue to grow through the duration of the experiment. The diffusion of electroactive species to the surface of the microelectrode array is dependent on a number of factors for example, the size of the individual diffusion layer in comparison to the size of the microelectrode, and the size of the diffusion layer in comparison to centre-to-centre separation of the microelectrodes. These characteristics are used to group microelectrodes arrays into four distinct categories as shown in Figure 13A-D. [98,99,100]

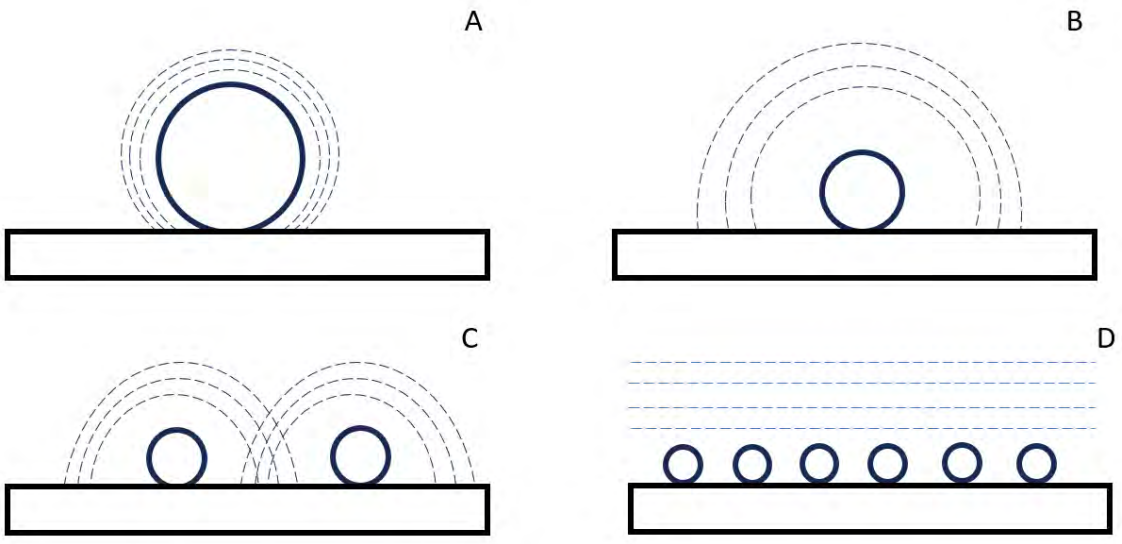

Figure 13 shows the categorisation of diffusional behaviour for spherical particles on the surface of a plane in a microelectrode array arrangement. Figure 13A illustrates category 1, B shows category 2, C shows category 3 and D represents category 4.

For category 1 where the diffusion layer is smaller than the radius of the spherical electrode and isolated to individual nanoparticles, the mass transport is one-dimensional therefore resulting in current peaks observed in the cyclic voltammetry similar to that of a macro electrode. For category 2,

the diffusion layer is larger than the radius of the spherical electrode with diffusion isolated to individual nanoparticles resulting in a steady state behaviour. In the case of category 3, the spherical particles are closer together therefore the diffusion layers are larger than the particle radius and they partially overlap as the diffusion zone is larger than the centre-to-centre separation distance. This behaviour results in a voltammetry response described as a combination of category 2 and 4. For the final case, category 4, the diffusion layer is larger than the particle radius similar to category 3, however due to the closer centre-to-centre separation distance there is significant overlap of diffusion zones. In this scenario the mass transport to the microelectrode array is linear and one-dimensional across the entire electrode surface resulting is a peak shaped cyclic voltammetry response.[67]

1.5.7 Kinetics

Electron transfer

As the potential deviates from the equilibrium (lower overpotential), the reaction is under charge transfer control thus the reaction kinetics are occurring at a slower rate than the transfer of reactants and products to and from the electrode. During the electrochemical reaction, the transfer of electrons can occur in either the forward (reductive) and reverse (oxidative) direction as shown by Equation 33. The cathodic current (I_c), anodic current (I_a) and net current are given by Equation 59-Equation 62:[67]

$$I_c = -nFAk_{red}[A]_0^{n=1} \quad \text{Equation 59}$$

$$I_a = nFAk_{ox}[B]_0^{n=1} \quad \text{Equation 60}$$

$$I = I_c + I_a = nFA(k_{ox}[B]_0^{n=1} - k_{red}[A]_0^{n=1}) \quad \text{Equation 61}$$

$$I = nFAj \quad \text{Equation 62}$$

Where I is the magnitude of the current, n is the number of electrons transferred, F refers to Faraday constant, A is the electrode area and j the flux describing the rate of the reaction at the electrode surface thus can be evaluated using heterogeneous rate laws for a first order reaction denoted by

$Rate = k_n[reactant]_0^{n=1}$ where 0 is the concentration at the electrode surface rather than the bulk solution.

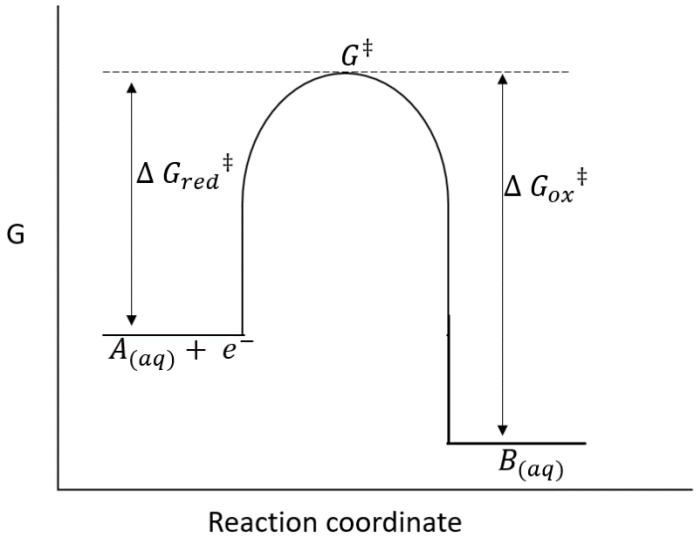

Figure 14 schematic of Gibbs energy plot for a single electron transfer as species A is reduced.

The transition state theory depicted by Figure 14, indicates that the reduction reaction ($A_{(aq)} + e^-$) must overcome an energy barrier to produce product $B_{(aq)}$. The Arrhenius equation can be used to relate the Gibbs energy of activation with both the reductive and oxidative rate constant as shown by Equation 63 and Equation 64, where $\Delta G_{red}^{\ddagger}$ the free energy of activation, A is a frequency factor that account for the rate of collision of electroactive molecules with the electrode surface.[65,67]

$$k_{red} = A_{red} \exp\left(\frac{-\Delta G_{red}^{\ddagger}}{RT}\right) \qquad \text{Equation 63}$$

$$k_{ox} = A_{ox} \exp\left(\frac{-\Delta G_{ox}^{\ddagger}}{RT}\right) \qquad \text{Equation 64}$$

As electrochemical reactions are influenced by the interfacial potential difference, the effect of overpotential on the rate of electron transfer must be considered and is indicated by Equation 65 and Equation 66 w here $k_{red}^0 = k_{ox}^0$ and are independent of the overpotential. The transfer coefficient represented by α and β is the symmetry factor which ranges from 0 to 1 providing an indication of the

sensitivity of the transition state to favour the more cathodic reaction at β > 0.5 and an anodic reaction β < 0.5. The transfer coefficient and symmetry factor can be expressed by Equation 67.

$$k_{red} = k_{red}^{0} \exp\left(\frac{-\alpha\, nF\eta}{RT}\right) \quad \text{Equation 65}$$

$$k_{ox} = k_{ox}^{0} \exp\left(\frac{\beta nF\eta}{RT}\right) \quad \text{Equation 66}$$

$$\beta = 1 - \alpha \quad \text{Equation 67}$$

By substituting Equation 65 and Equation 66 into Equation 61 this gives the Butler-Volmer equation (Equation 68) which describes the relationship between the overpotential (η) and current density (j) at the electrode surface. As the applied overpotential increases, the current density thus the rate of deposition also increases according to Faraday's law.

$$j = j_a + j_c = j_o \left[\exp\left(\frac{\beta nF\eta}{RT}\right) - exp\left(\frac{-\alpha nF\eta}{RT}\right)\right] \quad \text{Equation 68}$$

J_a is the anodic current density, J_c cathodic current density and J_o is the exchange current density where a higher magnitude results in a larger net current density at a given overpotential and is dependent on the electrode surface.

Tafel equation

At larger oxidative or reductive overpotentials, assuming there is no mass transport limitation, the Butler- Volmer equation can be used to derive the Tafel equation used to study electrode properties and reaction mechanisms. The Tafel equation relates the rate of reaction measured by electrical current to the overpotential via the linear relationship between η and log (j). At significantly high negative potentials, the oxidative current contribution is considered negligible thus the Butler Volmer equation can be expressed as Equation 69. Alternatively, when overpotential drives the oxidative reaction, the cathodic current is insignificant thus is represented by Equation 70.[65,101]

$$\log(j) = \log(j_o) - \frac{\alpha nF\eta}{RT}$$ Equation 69

$$log(j) = log(j_o) + \frac{\beta nF\eta}{RT}$$ Equation 70

1.6 Fuel cells and catalyst

In the following section, the application of platinum as an electrocatalyst is discussed in reference to fuel cell technology. Hydrogen economy, initially discussed in the 1960's,[102] refers to the widespread use of hydrogen gas (H_2) as a versatile and sustainable energy carrier across various industries.[103] A key application of hydrogen gas is as a fuel to produce electricity using fuel cells technology. Fuel cells are electrochemical devices that convert the chemical energy of hydrogen and an oxidising agent (oxygen) to electrical energy with water, and heat as a by-product.[104,105] When hydrogen is generated from renewable energy sources, this is considered an environmentally sustainable and efficient method of energy generation.

Fuel cells are predominantly classified by the electrolyte used as this influences the chemical reaction, catalyst selection, operating conditions, and fuel type. The focus within this section will be on the hydrogen electrification through proton exchange membrane fuel cells (PEMFC). PEMFCs utilise a solid polymer membrane electrolyte and are considered low temperature fuel cells with operation conditions of 40°C to 90°C resulting in a rapid start up time. Due to these properties, PEM fuel cells are considered a viable option for automotive applications specifically within the transportation industry for instance fleets of taxis, buses, and logistics vehicles.[105]

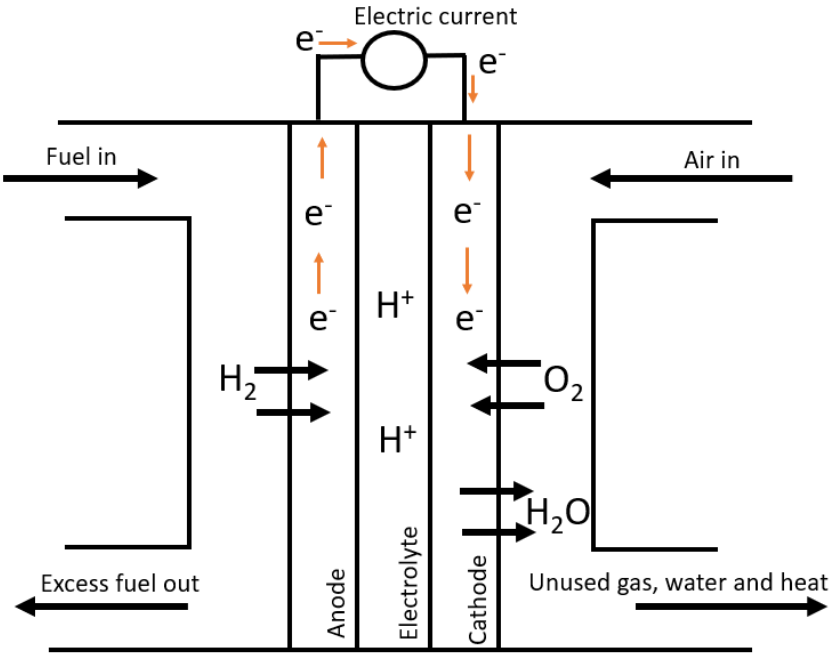

Figure 15 Schematic of PEM fuel cell where hydrogen oxidation reaction occurs at the anode and oxygen reduction reaction at the cathode.

A typical PEM fuel cell stack consists of the end plates, insulating plates, current collector, bipolar plate, and the membrane electrode assembly (MEA). The MEA is a crucial component with three identifiable layers namely the membrane, gas diffusion layer and the catalyst layer. The membrane is designed to conduct the protons but prevent the flow of electrons and gas, while the function of the diffusion layer is to facilitate mass transport by providing a channel for the gas and electron movement. The electrochemical reaction occurs at the catalyst layer, specifically at the cathodic and anodic (Figure 15). At the anode, the hydrogen undergoes an oxidative reaction resulting in the generation of protons and electrons. The hydrogen oxidation reaction (HOR) is a well-studied electrochemical system and is shown via the Tafel, Volmer and Heyrovsky reaction mechanism where S^* is the catalytic active site:[106,107]

Tafel step:

$$H_{2(aq)} + 2S^* \rightleftarrows 2H_{ads} \qquad \text{Equation 71}$$

Heyrovsky step:

$$H_{2(aq)} + S^* \rightleftarrows H_{ads} + H^+{}_{(aq)} + e^- \quad \text{Equation 72}$$

Volmer step:

$$H_{ads} \rightleftarrows H^+{}_{(aq)} + S^* + e^- \quad \text{Equation 73}$$

Overall reaction:

$$H_2 \rightleftarrows H^+{}_{(aq)} + 2e^- \qquad E^o = 0.00\,V \quad \text{Equation 74}$$

The ions move from the anodic electrode to the cathodic electrode via the electrolyte while the electrons flow through the external circuit producing electricity. At the cathode, the oxygen reacts with the protons via the oxygen reduction reaction (ORR) producing water. Similar to the HOR, the ORR is also a well-studied system where different mechanisms have been suggested. The reaction can occur via an efficient and direct 4 electron transfer as shown:[108]

$$O_2 + 2S^* \longrightarrow 2O^* \quad \text{Equation 75}$$

Overall reaction:

$$O_2 + 4H^+ + 4e^- \longrightarrow 2H_2O \qquad E^0 = 1.23\,V \quad \text{Equation 76}$$

Alternatively, the reaction can indirectly occur via a sluggish two-electron pathway as shown:

$$O_2 + S^* \longrightarrow O_2{}^* \quad \text{Equation 77}$$

$$O_2{}^* + H^+ + e^- \longrightarrow HOO^* \quad \text{Equation 78}$$

$$HOO^* + H^+ + e^- \longrightarrow O^* + H_2O \quad \text{Equation 79}$$

$$O^* + H^+ + e^- \longrightarrow HO^* \quad \text{Equation 80}$$

$$HO^* H^+ + e^- \longrightarrow H_2O \quad \text{Equation 81}$$

Overall reaction:

$$O_2 + 2H^+ + 2e^- \longrightarrow 2H_2O_2 \qquad E^0 = 0.70\,V \qquad \text{Equation 82}$$

$$H_2O_2 + 2H^+ + 2e^- \longrightarrow H_2O_2 \qquad E^0 = 1.78\,V \qquad \text{Equation 83}$$

Heterogeneous catalysis refers to the use of a catalyst in a different phase to the reactant or product; thus, an interface is present where a sequence of adsorption reaction desorption occurs at the active sites.[109] These catalysts are crucial as they facilitate many significant industrial reactions, for instance, the synthesis of organic and inorganic chemicals, energy production and are considered a promising solution for water treatment.[110,111] In comparison to homogenous catalyst, heterogeneous catalysts enable easier retrieval and reuse thus making them desirable for a vast range of applications.[112,113]

Due to the sluggish nature of the ORR, highly effective and stable Pt based electrocatalyst are traditionally required to enhance their performance. Although, Pt catalyst is present at both the cathode and anode electrode, the HOR is comparatively more rapid than the ORR therefore requires a lower Pt loading. The requirement of this low abundance and expensive resource contributes to the high manufacturing costs associated with PEM fuel cells.[114] To overcome this challenge, the use of platinum free catalyst has been investigated extensively in literature with catalyst such as Fe/N/C and Co/N/C based composites cited as possible alternatives.[104,114-116] Despite the progress made in these studies, Pt based catalysts are regarded as the most effective catalyst for the ORR and HOR. According to the Sabatier principle used to generate the volcano plots showing ORR activity as a function of binding energy to O or OH, Pt exhibits the ideal balance between the adsorption strength and turn over frequency. As a result, Pt catalysts can bind strongly enough with the reactant to facilitate the reaction but also weakly enough to desorb from the product. [116-119]

An alternative approach is to reduce the platinum loading required to generate the same current which reduces associated costs. However, due to the particle size effect, a direct reduction in size of the

catalyst can result in reduced activity. To prevent this, Pt catalyst is dispersed onto the surface of a support material to enhance the catalytic performance. Within low temperature PEM fuel cell applications, the Pt catalyst is supported on the surface of carbon black nanoparticles to promote catalyst stability and increase surface area. Carbon nanoparticles are commercially viable core materials due to their low cost, high conductivity and diverse morphology making them suitable to a wide range of electrochemical applications. The interaction between the Pt and the carbon black support material can also influence the electro-catalytic properties of the active sites in two ways. The first pertains to an electronic modification that results in changes to reaction characteristics of the active sites while the second modification is to the geometry of the catalyst particles.[120,121]

The controlled integration of complementary material functions for the purpose of optimised compositions and morphologies via the synthesis of core-shell structures is of major interest. Fundamentally, core shell structures are composite nanomaterial consisting of an inner core material surrounded by a shell material identified by their structural or compositional features with dimensions at a nano scale. This can be categorised as inorganic, organic and inorganic-organic materials where the former has been widely investigated. For inorganic compositions, examples include the use of metals, metal oxides, metal sulphides and recently silica cores combined with a metal or metal oxide shell. Alternatively for organic compositions, polymers consisting of three-dimensional networks and carbon-based materials are typically used.[122]

Due to growing interest, this definition has been broadened to encompass structures with a distinct boundary between two or more constituent materials where the outer material partially or completely encapsulates the inner material. Core-shell structures capitalise on the desirable physical and chemical properties of different materials to produce particles with improved catalytic activity, adsorption capacity, conductivity and stability, thus making them valuable to several applications in catalysis, optoelectronics and semiconductors.[122]

The nanoscale structure of Pt/CB catalysts also contribute significantly to their effectiveness as nanoparticles exhibit different properties from their bulk counterparts because of the quantum size effect. At the nano-range, the Pt/CB particles have a significantly higher surface-to-volume ratio thus providing a large number of active sites per unit area and enhancing its catalytic properties. The size of the particles also contributes to a higher zeta potential thus reducing the aggregation of nanoclusters in solution. The fabrication of Pt/CB can be achieved using several methods for instance via the chemical impregnation-reduction technique. However, Pt/CB synthesis via electrochemical reduction method is advantageous as it does not lead to the generation of additional waste as is seen with chemical methods. Furthermore, electrochemical methods are economical, efficient and offers a greater level of selectivity in the placement of Pt onto the surface of the substrate electrode. However, limitations still exist, for instance controlling the particle size as deposition continues to grow after nuclei are formed.[123,124]

1.7 Impact electrochemistry

1.7.1 Introduction to impact electrochemistry

The electrochemistry of redox active species is a long-established field of study; however, the exploration of individual nanoparticles remains relatively recent. Impact electrochemistry is used to study single entity electrochemistry but has advanced to encompass electrodeposition applications within literature. This method of electrochemically analysing particles in suspensions was introduced by Micka as early as 1957 through observations of cathodic peaks during the study of insoluble HgS, PbS, CuS and Ag_2O particles using a mercury electrode.[125] Similar observations were made by Jones and Kaye when studying a system of activated charcoal in 0.1 M KCl solution in 1969.[126] The first practical application of these observations was implemented by Moller in 1971 and developed by Holland and Feinerman. This was a turntable designed to reduce silver bromide particles upon contact with a platinum needle electrode and was used in the photographic industry.

These concepts were further explored by Heyrovsky in 1995 through his research of stable colloidal solution of polydisperse nanoparticles. Although individual nanoparticle impacts were not studied specifically, insight from his research indicated that the electrochemical responses of the impacting colloids represented an accumulation of individual reduction events.[127] These observations from the voltammogram (current vs. voltage) was used to deduce the presence of distinct particle sizes. Additional studies were conducted using metal oxide semiconducting nanoparticles such as TiO_2, SnO_2 or Fe_2O_3 where the impact signals associated with the electrocatalytic proton reduction was observed.[128-131] Furthermore, investigations into the electrochemical response of metal nanoparticles (Al, Fe, Ni, Cu, Mo and W) with a hydroxide layer were studied with peaks attributed where impacting the surface of the mercury electrode was observed.[132] The study of impact electrochemistry was further established by the work of Xiao, Bard, Scholz and Compton's group where both Faradaic and non-Faradaic systems have been studied.[133-139]

1.7.2 Direct and Indirect electrochemistry

During impact voltammetry, particles are introduced to a solution where under uncontrolled conditions they move under Brownian motion until collision with a substrate electrode held at a potential. Upon collision, the particles can either undergo oxidation or reduction ('direct impacts')[131,140-148] or provide a surface for solution species to be oxidised or reduced ('indirect impacts'),[135,149-155] provided a suitable potential is applied to the substrate electrode. Due to their commercial relevance, nanoparticles are ubiquitous leading to environmental contamination during use and disposal. Direct impact electrochemistry can be used to determine the composition and proportions of metal, metal oxide and polymer nanoparticles thus can be used in application such as environmental monitoring.[137,156,157] The early Compton group studies investigated the detection and characterisation of colliding Ag NPs on the surface of a glassy carbon (GC) electrode resulting in individual oxidative peaks which was used to determine the number of atoms thus particle size. Further work demonstrated this technique in both aqueous and non-aqueous solution.[156-158]

Indirect impact, also referred to as electrocatalytic amplification was first demonstrated by Xiao and Bard through their investigation of single impacting platinum nanoparticles on the surface of ultramicroelectrode. The current generated by the electrocatalysis of proton reduction was observed via reductive peaks.[159] These transient signals were studied to determine the concentration of nanoparticles via impact frequency, while the peak amplitude was used to determine the concentration of the redox active species. This technique was used to investigate other systems including Pt, Au and IrO_x nanoparticles by exploiting the oxidation of water and hydrazine.[151,160] For indirect impact electrochemistry, while the substrate electrode may not be catalytic towards the redox reaction, upon contact with the electrode the nanoparticles are able to catalyse the reaction on the surface on the nanoparticle. Both direct and indirect impact techniques result in transient peaks that can be used to determine electrical current, and charge transferred per impact. This can be analysed to examine the system under study elucidating information such as particle size, concentrations, and kinetics.[131,133] Recently, the application of particle impact electrochemistry for bulk electrodeposition and underpotential deposition (upd) has been demonstrated in a few examples using both metallic and non-metallic nanoparticles. These instances include the deposition of cadmium onto impacting silver nanoparticles, the upd on silver nanoparticles, the deposition of zinc onto zinc nanoparticles and reduction of manganese onto the surface of carbon black nanoparticles.[137,161-163]

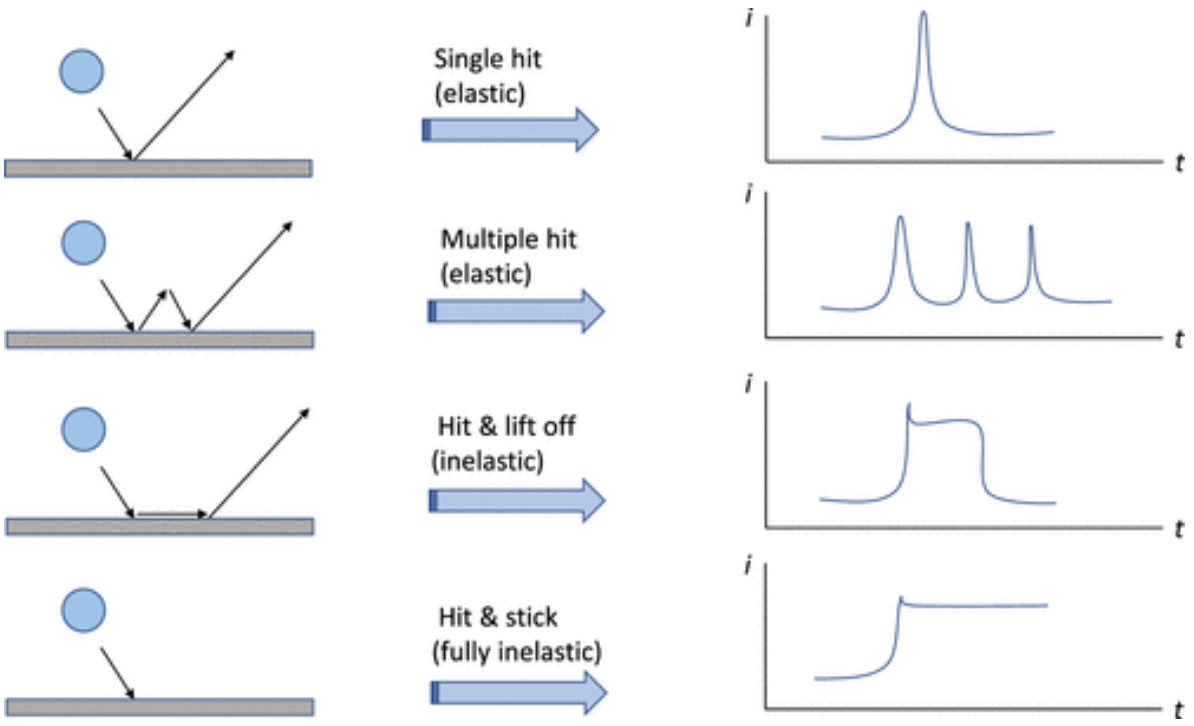

Figure 16 Schematic showing some possible impact scenarios and simplified transient signals.

Experimental observation indicate that impacts are more prominent within the initial period of the measurement evidenced by the higher frequency of collision. The transient peaks observed reflects the interaction between the nanoparticle and the substrate surface where the width of the peak reflects the impact duration.[131] The nature of the impact also affects peaks shapes where two distinct signal types have been identified as spikes/blips and stepwise/staircase responses as shown in Figure 16.[164] This is influenced by the electrochemical reaction mechanism, electrolyte solution, characteristics of the nanoparticles and electrode material. The spike response is observed during elastic collisions resulting in an initial increase in current upon contact followed by a rapid decrease back to background level as the NP is deactivated as it leaves the vicinity of the electrode. This response is well documented, for example observations made by the Stevenson group during Pt nanoparticle impacts.[138,165] On the other hand, stepwise current signals are associated with the sticking of nanoparticles on the substrate electrode upon collision resulting in an increase current response. Examples of stepwise impacts have been documented for the single Pt impact on Au

ultramicroelectrodes and iridium oxide nanoparticle collisions with Pt ultramicroelectrodes.[134,135,149,159] The sticking coefficient defined as the rate at which nanoparticles stick to the surface in comparison to the overall impacting frequency. This has been studied for Au, Ni and Ag impacts onto a carbon electrode in aqueous solution and determined to be 0.19 $\pm$0.03, <0.01 and 0.12 $\pm$0.02 respectively.[133,166]

1.8 Aim and objective of thesis

Metals are a fundamental resource that play a vital role in the economy across various industries. However, as highlighted in the introduction, the adequate management of electronic waste is a major challenge that contributes to negative environmental and health hazards. Moreover, these metals are a finite resource thus the recovery of commercially valuable metals for example copper, palladium, and platinum is essential for their continued use. Current methods of metal recycling such as pyrometallurgy, hydrometallurgy bio-metallurgy are associated with adverse environmental effects due to energy requirements or production of large volumes of waste solution. Additionally, wastewater discharged from manufacturing processes often contain low concentrations of metals which are deemed too toxic to aquatic life thus must be treated for appropriate disposal. The current recovery methods highlighted is not economically feasible for the recovery of metals from low concentrations as they would require additional preconcentration and separation processes. This results in an increased operational cost and the generation of secondary pollutants.[167-170]

The aim of this project is to investigate electrodeposition specifically using impact electrochemistry as a method of metal recovery from low concentrations of metal solution. The impact investigations will be conducted using inexpensive core materials, where the modified particles will be characterised and tested as catalysts. Although traditional electrochemical techniques such as electrowinning offers high selectivity and is considered as a more environmentally acceptable method making it suitable for industrial recovery processes. An operational requirement is to maintain a high concentration of metal

ions which is not viable when recovering metals from effluent streams. Metal deposition via particle impact electrochemistry has distinct advantages compared to other electrochemical techniques. For example, the use of nanoparticles in some cases can reduce the extent of electrode fouling in comparison to the use of a single electrode and facilitates rapid mass transport of the metal ions to the surface because of radial diffusion.[171]

2. General methodology

2.1 Electrochemical configuration and preparation

In this chapter, an overview of the electrochemical systems employed to study the deposition of copper, palladium and platinum through the impact electrochemistry method is provided. The theory of the electrochemical instruments has been introduced in chapter 1. This section presents a summary of the techniques utilised to perform the surface modifications and characterisation methods applied to study the modified nanoparticles. Further details of each electrochemical cell, including chemical reagents, specific configuration and characteristics have been presented in the corresponding experimental sections of this thesis.

2.1.1 Working electrode

Macro and micro electrochemical studies were conducted using carbon-based electrodes as the working electrode. In general, the working electrode is where the redox reaction of interest occurs thus it is essential that the electrode material is inert in the potential range of interest and in the electrolyte solution used.

Surface preparation

As the reduction process occurs at the working electrode, surface preparation is crucial to eliminate any contamination or fouling thus ensuring a clean and well-defined surface area. Before use, all working electrodes were polished using alumina suspensions of 1 µm, 0.3 µm and 0.05 µm sequentially, on a micro-cloth pad (all from Buehler Inc, USA). In cases where additional electrode preparation methods were required, this has been specified in the relevant experimental chapters.

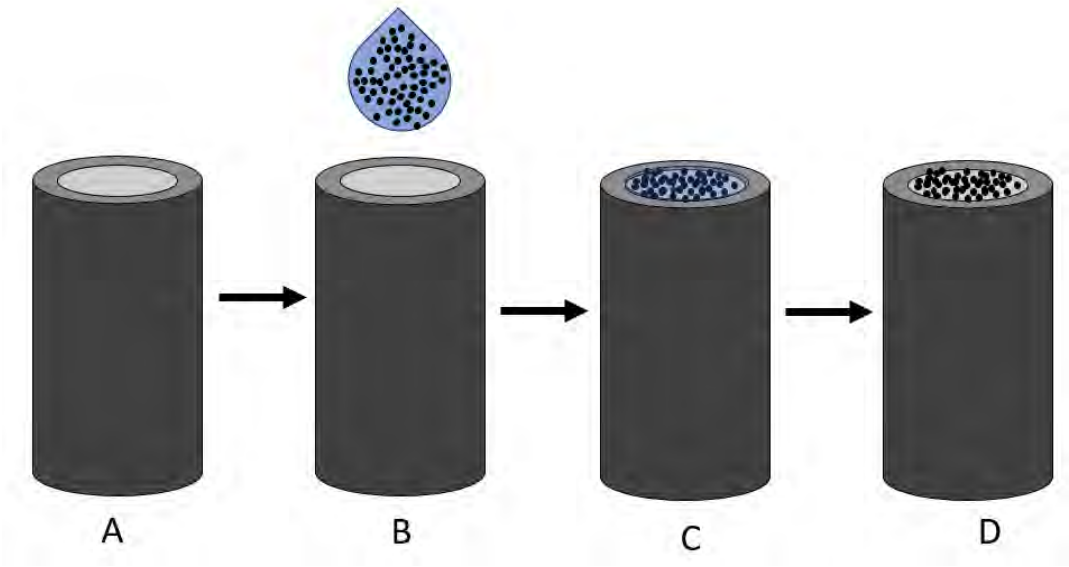

Figure 17 Schematic showing the process of drop casting nanoparticles onto the surface of a working electrode where A represents a polished bare GC electrode, B the process of drop casting nanoparticles on to the GC surface. C shows the process of drying the solution resulting in D which illustrates a modified GC electrode.[172]

Surface modification

To examine the electrochemical deposition of Cu, Pd and Pt on non-glassy carbon surfaces and to investigate the catalytic properties of the modified nano particle, drop cast and spin coating methods were employed. Drop casting is a popular surface modification method conducted using a solution containing the desired test material. This is cast onto the surface of the electrode followed by the evaporation of the solvent as depicted in Figure 17. During preparation the drying of the solvent was accelerated using a lamp as a heat source. Drop casting is a widely used process as it offers a simple and rapid method of surface modification however it can be limited by the occurrence of non-uniform distribution of nanoparticles resulting in the coffee-ring effect.[172] For electrocatalytic studies, the spin coating method was used to minimise this effect,[173] and further detail is provided in the Pt deposition experimental in section 5.3.3 Catalytic studies.

2.1.2 Reference electrode

The reference electrode is designed to provide a well-defined and stable equilibrium potential that can be used to determine the applied potential. The reference electrodes used for each investigation was selected based on the electrolyte solution to reduce junction potentials.

For the copper sulphate study, a mercury sulphate electrode (MSE, IJ Cambria Ltd) was used as the reference electrode to prevent the addition of chloride ions from possible cross contamination as this may alter the mechanism. At low chloride concentrations, an accelerated chloride mediated reduction pathway occurs as shown[80]

$$Cu^{2+} + {Cl^-}_{ads} + e^- \rightleftarrows CuCl_{ads} \qquad E^0 = +0.58\,V \qquad \text{Equation 84}$$

$$CuCl_{ads} + e^- \rightleftarrows Cu + Cl^- \qquad E^0 = +0.18\,V \qquad \text{Equation 85}$$

This occurs in parallel to the two-stage Cu^{2+} reduction pathway shown in Equation 6 thus resulting in an overall accelerated kinetics. However, at higher chloride concentration, the copper deposition mechanism is inhibited by the chloride ions thus a larger overpotential is required. The MSE is based on the reaction between mercury metal and mercurous sulphate in a saturated potassium sulphate solution as shown:

$$Hg_2SO_4 + 2e^- \rightleftarrows 2Hg + {SO_4}^{2-} \qquad E^0 = +0.64\,V \qquad \text{Equation 86}$$

As both the palladium and platinum impact electrochemistry studies were conducted in chloride solutions a saturated standard calomel electrode (SCE, ALS Inc) was used. This is based on the reaction between mercury metal and mercury (I) chloride in saturated potassium chloride electrolyte:

$$Hg_2Cl_2 + 2e^- \rightleftarrows 2Hg + 2Cl^- \qquad E^0 = +0.24\,V \qquad \text{Equation 87}$$

For the electrocatalytic studies via of the Pt/CB generated, a reversible hydrogen electrode (RHE, BioLogic) limiting the presence of additional chloride ions to the perchloric acid. This reference electrode is based on the reduction of hydrogen ions (Equation 88).[174]

$$H^+ + e^- \rightleftarrows \frac{1}{2}H_2$$ Equation 88

$$E = E^0 - \frac{RT}{F} \ln\left(\frac{\sqrt{f(H_2)/p^0}}{a(H^+)}\right)$$ Equation 89

The potential for the RHE deviates from the standard hydrogen electrode (SHE) according to Equation 89. Here, E is the potential of the redox couple given by Nernst equation, E^0 is the standard potential, $f(H_2)$ is the fugacity of H_2, p^0 is the standard pressure (1.00 bar), $a(H^+)$ is the activity of $H^+_{(aq)}$, R is the gas constant, T is the temperature and F is Faraday constant. At conditions of $f(H_2)$ =1.00 bar and T =298.15 K, the potential decreases by 0.059 V per pH unit, therefore for the electrochemical active surface area (ECSA) and oxygen reduction reaction (ORR) studies (see chapter 5) where the RHE is used in a solution of 0.1 M perchloric acid (pH=1), the potential is 0.00 vs. RHE= -0.059 V SHE.

2.1.3 Counter electrode

For all electrochemical investigations a graphite rod (3 mm diameter, Goodfellow Cambridge Ltd) served as a counter electrode. The purpose of the counter electrode in a three-electrode configuration is to complete the electrical circuit where a large surface area is provided to ensure fast kinetics. While Pt wire is conventionally employed as a counter electrode, a graphite rod was selected to avoid the possibility of introducing Pt ions to the solution as a result of dissolution.

2.1.4 Electrolyte solution

For each results chapter, details have been provided regarding the composition and preparation of the electrolyte solution. In general, to ensure the metal would remain in a solution phase prior to electrodeposition, a Pourbaix diagram was used to determine pH 2 was appropriate for the copper, palladium, and platinum investigations.[175-177]

2.2 Low-noise potentiostat

Impact chronoamperometric scans were measured using a bespoke low-noise potentiostat, fitted with a high-speed variable-gain low-noise current amplifier (DHPCA-100, femto.de) with a bandwidth of 220 kHz and rise time of 1.6 µs at the operating gain of 10^8, and a data acquisition card (NI-6003, National Instruments, bandwidth 300 kHz) which combined enabled a sampling rate of 100 kS s^{-1}.[178,179]

2.2.1 Effects of filtration on signals

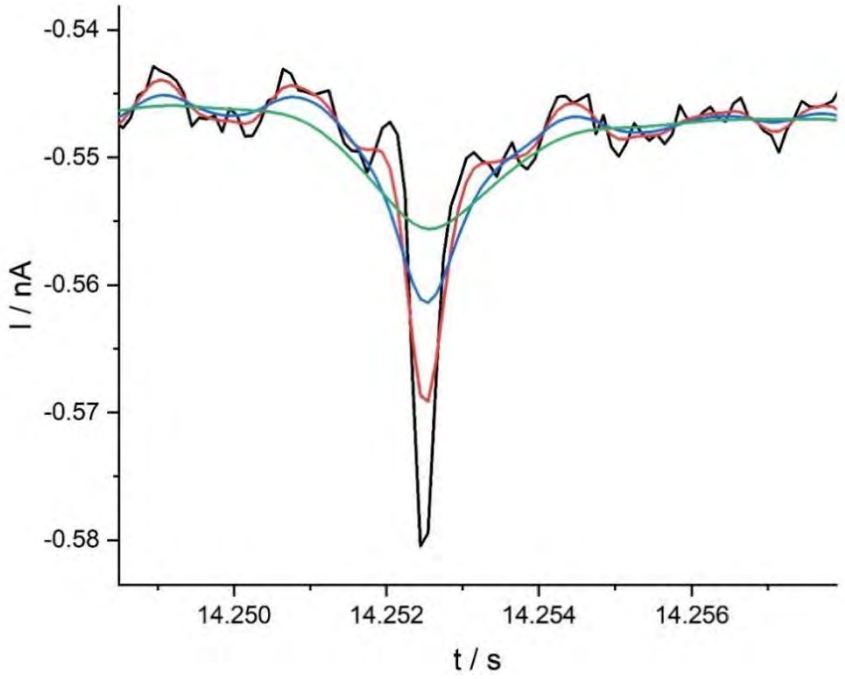

Figure 18 Effects on a reductive impact signal of at 5 kHz (—), 1 kHz (—), 0.5 kHz (—) and 0.25 kHz (—) digital filters.

This section provides an illustration of the effect of varying the applied digital filter on an isolated reductive peak. Digital filters are required in general to improve the signal-to-noise ratio enabling peaks to be more clearly identified and analysed. Although the charge is conserved, the peak height and duration values become distorted.[180] Therefore, the use of peak height or duration measurements for quantitative analysis must be treated with particular caution, since even in the absence of applied (low pass) filtering, the data is subjected to sampling rates (typically 10^5 s^{-1}) that are probably

insufficient to accurately capture the current signals. Figure 18 displays an isolated reductive peak obtained from a chronoamperometric scan conducted at -0.8 V (vs. MSE) in a solution of 0.5 mM $CuSO_4$, 1 mM H_2SO_4 and 19 mM K_2SO_4 in the presence of 60 nm AgNPs. This figure demonstrates the effect of digitally filtering a reductive peak at 5 kHz (—), 1 kHz (—), 0.5 kHz (—) and 0.25 kHz (—). Although the peak height changes, the peak charge remains conserved.

2.3 Characterisation techniques

The following section introduces the methods used to characterise core materials such as cenosphere particles discussed in chapter three and the synthesised nanoparticles modified during impact investigations.

2.3.1 Handheld X-ray fluorescence spectrometer (hXRF)

The handheld X-ray fluorescence spectrometer (hXRF) was used to characterise the cenosphere particles before use. The composition of cenospheres primarily comprise of aluminosilicate with trace amounts of Ca, Fe, K and Mg however the this varies depending on the formation conditions. As cenospheres are consider waste materials, it was necessary to first characterise them before use. XRF is a non-destructive and rapid characterisation method thus making it suitable as no additional sample preparation is required. This operates by subjecting the cenosphere samples to high-energy x-rays, which impact with sufficient energy to displace the inner-shell electron subsequently causing a release of energy in the form of secondary x-rays that can be characterised for element identification.[181]

2.3.2 Imaging characterisation techniques

Scanning electron microscopy (SEM) with energy dispersive X-ray (EDX) analysis

Scanning electron microscopy (Hitachi TM3030 and Philips XL30 FEG ESEM) were used to provide qualitative analysis of the nanoparticles before and after modification as a visual confirmation of deposition. This was conducted alongside EDX to provide quantitative analysis on the extent of the

material modification. This instrument operates by directing an electron beam through a magnetic field where a lens focuses the beam at the sample held in a vacuum.[182]

Transmission electron microscopy (TEM)

Transmission electron microscopy (JEM-2100F Field Emission Electron Microscope) was used to characterise both the palladium and platinum modified nanoparticles. TEM analysis has a higher resolution than SEM and was used to confirm the modification of the impacting nanoparticles during impact events by capturing the distribution of the deposited metals on the carbon nanoparticle surface.[183]

2.3.3 Inductively coupled plasma spectrometry (ICP)

Both Inductively coupled plasma mass spectrometry (Nexion 300X ICP-MS, Perkin Elmer) and optical emission spectrometry (Optima 8000 ICP-OES, Perkin Elmer) were used to characterise modified nanoparticles and electroplating solution as metal concentrations depleted. ICP-MS and ICP-OES operates by converting the sample into ions then measuring the sample via a mass spectrometer and optical spectrometer respectively. ICP-MS was used for samples requiring a lower detection limit. Details on specific sample preparation and detection limits for the element of interest is provided in the corresponding chapters.[184]

2.3.4 X-ray photoelectron spectroscopy (XPS)

X-ray photoelectron spectroscopy is a quantitative analysis technique used to identify elements on the sample surface. During XPS electrons are emitted from atoms in response to impinging electromagnetic radiation. This method was used to identify the chemical state of the platinum and palladium detected in the sample to confirm deposition had occurred.[185] XPS analysis was conducted using Kratos Liquid Phase Photoelectron Spectroscopy (LiPPS) with a mono-chromated Al kα X-ray source.

2.3.5 Thermogravimetric analysis (TGA)

Thermogravimetric analysis (NETZSCH TG 209 F1) was used to characterise the palladium modified carbon nanoparticles and platinum modified nanoparticles. TGA operates based on the change in mass of the material as temperature changes. When sufficient heat is applied in a nitrogen atmosphere the carbon black nanoparticles decompose leaving the metal behind.[186]

3. Copper deposition on metallic and non-metallic single particles

3.1 Abstract

To begin, this chapter demonstrates the possibility of depositing metals onto low-metal content particles via impact electrochemistry, a technique used to measure transient current signals (electrochemical impacts) produced from the collision between particles moving under Brownian motion and a potentiostatted interface. The deposition of copper onto the surface of fly-ash cenospheres via electrochemical impacts is reported, along with its deposition onto silver and gold nanoparticles. A comparison with linear sweep voltammetry confirmed that impact signals correlated with deposition potentials (bulk and underpotential deposition). Reductive impact events were observed at potentials negative of −0.3 V (for Ag) and −0.1 V (for Au) (vs. MSE), with evidence for a change in coverage of deposition from ca. 103% at −0.1 V to 261% at −0.8 V vs. MSE for Au. Cenospheres were shown to be sufficiently electrochemically active to facilitate copper deposition, either on modified electrodes or showing transient impact spikes indicating copper deposition, which was confirmed via SEM/EDX and ICP-MS analysis.

3.2 Introduction

The recovery of critical and commercially significant metals from waste streams is an essential aspect of their continuing and future sustainable use. Current methods of extraction are often not economically viable for low concentrations of critical metals, resulting in wide variations in recycling percentages for different metals.[187-191] As discussed, in the introduction (chapter 1.2), conventional methods of recovery such as chemical precipitation, adsorption/biosorption, and ion exchange are limited by large reagent consumption, secondary pollution generation, and high operating costs.[192-195]Therefore, electrochemical methods such as electrodeposition, electrosorption, and electrodialysis,[196] would appear to be well-suited for the recovery and recycling of many metals, provided a suitable solvent and reduction potential is used. The primary advantage of these techniques

are the high efficiency, operational feasibility and cost effectiveness.[197-199] Electrodeposition is considered a practical metal recovery technique with broad industrial applications as it has the capability of enabling selective metal recovery from aqueous solutions under mild conditions.[195,200-204] However, the removal of the deposited metal from the cathode is normally required for onward processing and can create complications. Impact electrochemistry has several potential advantages, for example the particle size enables a high rate of mass transport to the nanoparticle surface. Furthermore, this method offers the ability to choose a suitable core particle on which to deposit the metal being recovered in such a way as to either separate for onward processing or directly produce desirable catalysts with core-shell architectures. The former case does not afford significant advantages over the existing method of deposition onto a cathode since the recovered metal still needs separation from the nanoparticle material; but the second scenario would hold significant benefits on the overall recovery-recycling process, and it is this long-term aim of the use of impacts for recovery/recycling. Impact electrochemistry also uses a large (tunable) number of nanoparticles which in some circumstances may be less susceptible to becoming fouled by contaminants than a single large electrode.

The electrodeposition of metals onto particles via impact electrochemistry has been reported in the literature, with examples including underpotential deposition (upd) and bulk deposition.[137,161,163] Initially these studies focussed primarily on metallic core particles (Ag, Au) but since has expanded to non-metallic cores. The use of non-precious metal cores would promote long-term sustainability and potential economic viability of any application in recovery/recycling and so there is great interest in the possibility of using lower value (especially 'waste') materials as core particles.

Cenospheres are a component of coal fly ash (CFA) which is generated as a waste by-product in large quantities during the combustion of pulverised coal. The combustion process as well as the total mineral content of the coal feed heavily influences the physical and chemical characteristics of the cenospheres formed. Primarily, cenospheres consist of aluminosilicates (29-90%), with moderate

amounts of calcium, iron, potassium, and magnesium oxides. Although coal is widely used globally as a fuel for energy generation, it is associated with several major environmental concerns due to greenhouse gas emissions and waste management challenges. For instance, approximately 750 million tonnes of fly ash are produced annually with significant quantities disposed of in landfill or ash lagoons. Due to the cost associated with landfill disposal, and the beneficial properties associated with cenospheres, there has been an increased interest in identifying potential applications. Cenospheres are lightweight hollow spheres with a good thermal resistance, high compressive strength and are chemically inert. Given these properties, cenospheres could be a useful functional recovered waste material. These properties make them potentially suitable for a range of industrial applications such as additives in lightweight cementitious products with reduced water release or in the production of automotive brake rotors.[205,206]

Additionally, cenospheres have been reported as a substrate for metal deposition, with Shukla et al. investigating the electroless deposition of Cu onto cenospheres via a layer of Pd clusters,[207] with the primary objective of increasing conductivity and producing light weight metal matrix composites. Their low density makes their separation from the reaction solution relatively simple (via filtration or centrifugation, etc.). Suggested applications for copper coated cenosphere particles involve the fabrication of conducting polymers, lead base composite material and electromagnetic interference shielding materials.[207,208] Their conductive and light weight properties make them suitable for electronic applications where weight reduction is critical. The modification of cenospheres using other techniques such as precipitation and fluidised-bed chemical vapour deposition have also been documented. However, their suitability as substrate for direct electrochemical deposition is unclear due to their varying composition that is typically dominated by aluminosilicates and metal oxides. A detailed characterisation is therefore required in each circumstance to determine factors such as chemical composition, morphology, and size distribution.[209-211]

To investigate the suitability of impact electrochemistry for recycling applications, it was decided to study the deposition onto metallic nanoparticles, such as gold and silver nanoparticles (AuNPs, AgNPs), before extending the investigation to include the non-metallic recovered waste material, fly-ash cenospheres (FACs). Copper was selected as an electrochemically recyclable commodity metal with a relatively well-established voltammetry exhibiting a well-known upd region on gold hence enabling demonstration of the technique.[212-219] In addition to this, copper is considered a vital resource deemed essential for modern society due to characteristics such as its electrical properties and durability making it versatile difficult to substitute. Although materials such as steel, plastics, graphene, and optical fibre can replace copper in various applications, they exhibit comparatively inferior performance in key end of use categories that account for 70% of copper applications.[220,221]

3.3 Experimental

All chemicals used were obtained commercially and used without further purification, namely: copper (II) sulphate (98%, Sigma Aldrich), potassium sulphate (99.0%, Sigma Aldrich) sulphuric acid (95.0–98.0%, Alfa Aesar), hexaammineruthenium (III) chloride (99.0%, Sigma Aldrich), potassium chloride (99.0–100.0%, Alfa Aesar), nitric acid (70.0%, Fisher Scientific), 60 nm citrate capped silver nanoparticles (AgNPs, Nanocomposix Inc, USA), 50 nm and 60 nm citrate capped gold nanoparticles (AuNPs, Nanocomposix Inc) and fly-ash cenospheres (FACs, RockTron International Ltd). All solutions were made using ultrapure water of resistivity = 18.2 MΩ cm (MilliQ, Millipore).

Electrochemical experiments were performed using a three-electrode cell in a Faraday cage as described in the general experimental section 2.1. A glassy carbon (GC, diameter = 3 mm, BASi Inc) macroelectrode, and carbon fibre (CF) microelectrodes of different sizes (diameter = 9, 11, or 33 µm) were used as working electrodes. Carbon substrate electrodes were used for impact studies since they have a high overpotential for hydrogen evolution (unlike Pt), are not easily oxidised (cf. Ag), and Cu does not readily deposit onto it (cf. Au). The 9 µm electrodes were made in-house using pitch-derived

carbon fibres (Goodfellow Cambridge Ltd), whilst the 11 µm and 33 µm electrodes were purchased (BASi Inc and ALS Inc respectively). Working electrodes were prepared by polishing the surface with alumina suspensions of 1 µm, 0.3 µm and 0.05 µm sequentially, on a micro-cloth pad (all from Buehler Inc, USA). A mercury sulphate electrode (MSE, IJ Cambria Ltd) was used as a reference electrode and a graphite rod (3 mm diameter, Goodfellow Cambridge Ltd) as the counter electrode. For nanoparticle experiments, the MSE reference electrode was placed in a separate fritted compartment to avoid possible cross-contamination when conducting the nanoparticle free blank investigation. Unless otherwise stated a solution of 19 mM potassium sulphate, 1 mM sulphuric acid and, when required, an additional 0.5 mM copper sulphate was used. Solutions were thoroughly degassed using nitrogen gas (oxygen-free, BOC Gases plc) and a nitrogen atmosphere maintained throughout the experiments. Standard electrochemical measurements were conducted using an Autolab 128N (Metrohm-Autolab BV, Netherlands) potentiostat controlled via a PC running NOVA 2.1 software conducting both linear sweep voltammetry and chronoamperometry scans. Impact chronoamperometric scans were measured using a bespoke low noise potentiostat analogous to that described in literature.[178] The data was processed using a combination of Microsoft Excel and Origin Pro 2021. Unless stated otherwise, impact electrochemical data has been analysed following electronic filtration (digital) at 250 Hz in order to improve the signal-to-noise ratio and facilitate analysis (see General Experimental 2.2). Where closer analysis was required, the 'raw' data was then reviewed when considering duration or peak current and literature.[180] Interpretation of quantitative data, in particular related to absolute peak currents requires appropriate caution since data acquisition is limited by the sampling rate (here 100 kS s^{-1}). Hence, the use has been limited to comparing between for example, deposition on AuNPs and AgNPs in a relative sense rather than relying on interpreting absolute values. The design of the potentiostat is such that charge is conserved by the filter and so analysed charges can be interpreted with more confidence.[179,180]

The cenospheres were characterised using a handheld X-ray fluorescence spectrometer (hXRF),[222] scanning electron microscopy (SEM) with energy dispersive X-ray (EDX) analysis and inductively

coupled plasma mass spectrometry (ICP-MS). For the SEM/EDX characterisation, 5 mg of cenospheres were added to the surface of a carbon tape (Agar Scientific) then examined using a Hitachi TM3030 electron microscope. To analyse cenospheres where deposition had occurred, the solution post-chronoamperometric experiment was taken and drop-casted onto glassy carbon stubs, dried, rinsed thoroughly with deionised water and dried again to be studied in the same way with the SEM/EDX. Additional experiments were conducted where modified cenospheres processed as described below for ICP-MS were taken dried and analysed directly with the SEM/EDX.

ICP-MS analysis was conducted on both unmodified cenosphere particles and cenosphere particles that had been modified via a 12h chronoamperometric scan in 0.5 mM copper sulphate, 19 mM potassium sulphate and 1 mM sulphuric acid. The modified cenosphere sample was repeatedly centrifuged (SIGMA 3k30 centrifuge) at 5000 rpm for 10 min, rinsed with ultrapure water and sonicated (U-series, Ultrawave), then repeating the washing cycle, before allowing to dry. Both samples were prepared for ICP-MS by dissolving in 2% nitric acid at a concentration of 1 ppm (cenosphere content) for 48h before filtration with 0.45 µm syringe filters (Starlab Group Ltd). The solution was then analysed using an ICP-MS (Nexion 300X ICP-MS, Perkin Elmer) with a limit of detection of 0.174 ppb. A calibration curve was generated with 1 ppm copper standard for ICP-MS, (TraceCERT Sigma Aldrich) in ultrapure water at concentrations of 0.001 ppm to 0.01 ppm. The sample was then analysed, and the concentration of copper read from the calibration curve.

3.4 Results and discussion

3.4.1 Deposition of Cu (macro and micro studies)

Macro and microelectrode studies were conducted to determine the onset potential of copper deposition onto GC and CF electrodes, as well as AuNP-modified GC and AgNP-modified GC electrodes before studying deposition onto FACs. Cyclic voltammograms (CVs) were taken of each electrode in a solution containing 0.5 mM copper sulphate, 19 mM potassium sulphate and 1 mM sulphuric acid at

a voltage scan rate of 100 mV s^{-1}. For bare GC, CF, and AuNP-modified GC electrodes a start potential of 0.0 V vs. MSE was applied. Whereas, for the AgNP-modified GC the voltammetry scan started at −0.1 V vs. MSE to prevent the stripping of the AgNPs from the electrode surface. The onset potential (visually determined from Figure 19) can be defined as an adequately negative potential able to initiate a current response,[223-225] in this case a current density of −0.025 A m^{-2} is used to determine onset potential.

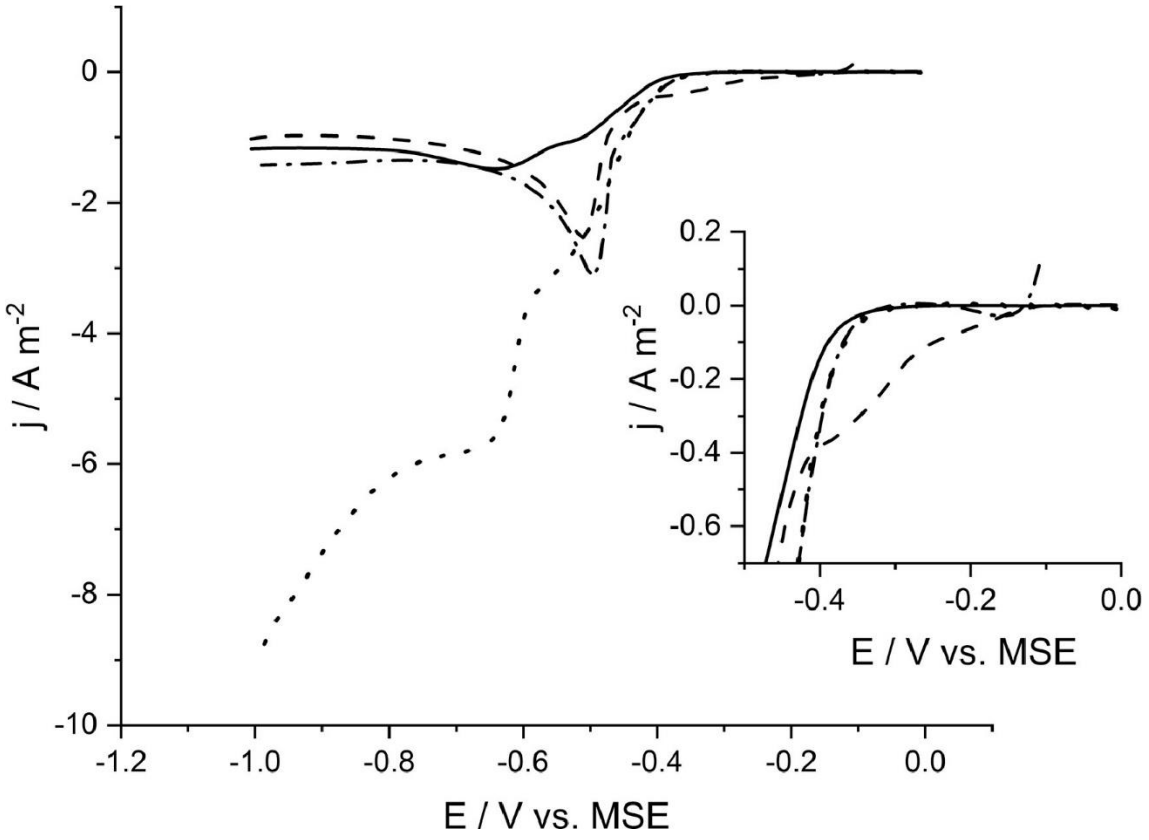

Figure 19 depicts the reductive CV segments of copper deposition on the surface of 3 mm bare GC (—), 50 nm AgNP modified GC (-·-·-), 50 nm AuNP modified GC (——) and 33 µm bare CF (·····). This was conducted in the standard copper plating solution of 0.5 mM $CuSO_4$, 1 mM H_2SO_4 and 19 mM K_2SO_4 using a scan rate of 100 mV s^{-1} in all cases.

Figure 19 illustrates the reductive scans for GC, AuNP/GC, AgNP/GC, and CF working electrodes. Both the AuNP/GC and AgNP/GC surfaces were prepared via a drop-cast method also used by Tschulik et al.[226] where 5 µL of a suspension containing 50 nm AuNPs (or 50 nm AgNPs) was added to a polished

GC surface. It can be observed that copper deposition on the gold-modified GC surface commences at a potential of −0.1 V vs. MSE whereas the onset onto other materials occurs at more negative potentials. This is due to underpotential deposition (upd) indicated by the characteristic initial peak at ca. −0.30 V vs. MSE, in agreement with the upd peak potential 0.05 V vs. Cu/Cu^{2+} onset reported in literature,[214,216] where $E_{Cu/Cu2+} = E_{SHE} + 0.28$ V,[214] and $E_{SHE} = E_{MSE} - 0.64$ V giving a potential of −0.31 V vs. MSE. The deposition of copper onto a gold surface is well-documented and is categorised into four stages,[216,225,227,228] namely the adsorption of copper and sulphate ions onto the gold surface, leading to a honeycomb ad-layer, then a full copper upd monolayer, and finally bulk deposition. Figure 19 is broadly in agreement with this, with the upd peak at ca. −0.3 V (vs. MSE) and bulk deposition occurring at potentials more negative than ca. −0.4 V (vs. MSE). From the upd peak an estimated AuNP surface coverage of ca. 0.5-layer equivalents was calculated based on the maximum possible available NP surface area as seen:

$$S = 4\pi R^2 \qquad \text{Equation 90}$$

$$S_{total} = S\, N_{NP} \qquad \text{Equation 91}$$

where S is the nanoparticle surface area, R the NP radius, S_{total} the total surface area of all NPs added via drop-cast, and N_{NP} the total number of NP added. The charge transferred can then be determined via the integration of the upd region using the potential window 0.0 V to -0.35 V (vs. MSE):

$$Q = \frac{\int IdV}{v} \qquad \text{Equation 92}$$

$$N = \frac{Q}{ez} \qquad \text{Equation 93}$$

$$N_{mono} = 0.7405\ \frac{S_{total}}{\pi r^2} \qquad \text{Equation 94}$$

$$\theta = \frac{N}{N_{mono}}$$ Equation 95

where here Q is the associated reductive charge, V the potential, v the scan rate, e the electronic charge, z = 2 the number of exchanged electrons per reduced copper atom,[144] θ the coverage, r the copper atomic radius, N the number of reduced copper atoms, and N_{mono} the number of copper atoms in a monolayer equivalent based on a 74.05 % fcc surface coverage.[229] Table 2 displays calculated values using Equation 90-Equation 95 for the surface area, total AuNP surface area in drop-cast, number of 50 nm AuNP in drop-cast, charge at upd, number of Cu deposited, number of Cu in monolayer and coverage equivalent.

Table 2: Calculated values for upd copper coverage on AuNP/GC electrode

Parameter / unit	Calculated values
S / m^2	7.9×10^{-15}
S_{total} / m^2	1.6×10^{-6}
N_{NP}	2.0×10^{8}
Q / C	-3.7×10^{-6}
N	1.2×10^{13}
N_{mono}	2.2×10^{13}
θ	0.5

3.4.2 Impact deposition of Cu onto Ag metallic nanoparticles

To investigate whether electrochemical impact events for copper deposition occurs, chronoamperometry was conducted with and without the addition of nanoparticles to the copper sulphate solution described above for the same potentials. Figure 20A depicts a 20 s segment of the chronoamperometric scans where peaks can be observed. This scan was first performed at −0.8 V (vs. MSE) before the addition of silver nanoparticles as a controlled experiment. Upon the addition of silver nanoparticles, reductive transient peaks can be observed (see Figure 20B) suggesting the occurrence of copper deposition during impact events at this potential. It was also noted that the background

current varies quite widely, especially at more negative potentials, which has been postulated to be due to small numbers of adsorbed nanoparticles and the deposition behaviour of copper. A study was performed using both 11 µm and 33 µm carbon fibre electrodes at a range of potentials (vs. MSE) to quantify this effect.

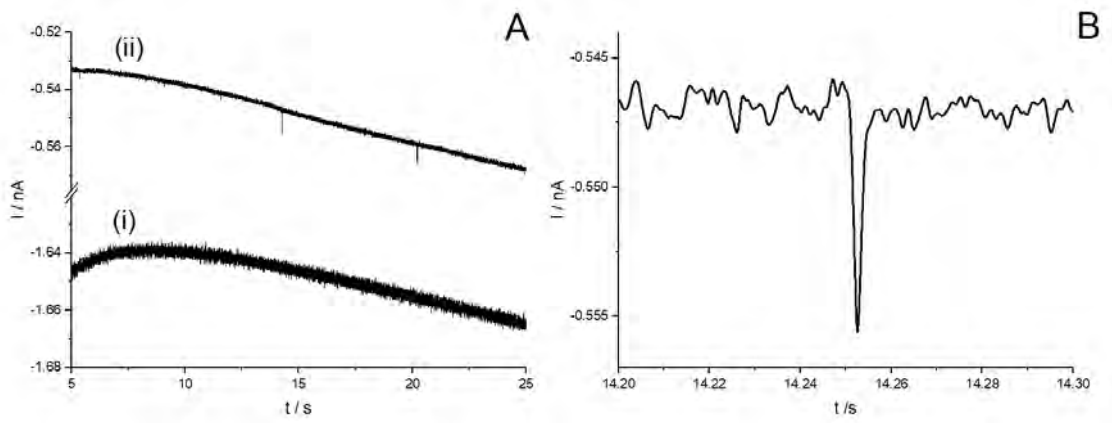

Figure 20 A shows an illustrative depiction of a typical 20 s segment of chronoamperometric scans at −0.8 V vs. MSE before (i) and after (ii) the addition of 60 nm silver nanoparticles. Figure 20B presents a magnified reductive peak from scan A (ii) at 14.25 s. All experiments were conducted in a 5 mL solution of 0.5 mM $CuSO_4$, 1 mM H_2SO_4 and 19 mM K_2SO_4 using a CF working electrode, a mercury sulphate reference electrode with a glass frit and a graphite rod counter electrode.

In order to compare the background current between the chronoamperogram depicted in Figure 21 an arbitrary time (t=25 s) was selected for all scans. A variation in magnitude of the background current can be observed as the potential becomes increasingly negative, and the variation appears to increase with electrode size Figure 22. For example, for blank solutions (containing no NPs) the current ranged from -0.26 nA to -0.66 nA for 11 µm CF and -0.25 nA to -2.24 nA for 33 µm CF. For solutions containing NPs, the current ranged from -0.61 nA to -0.73 nA for 11 µm CF and -1.15 to -3.53 nA for 33 µm CF.

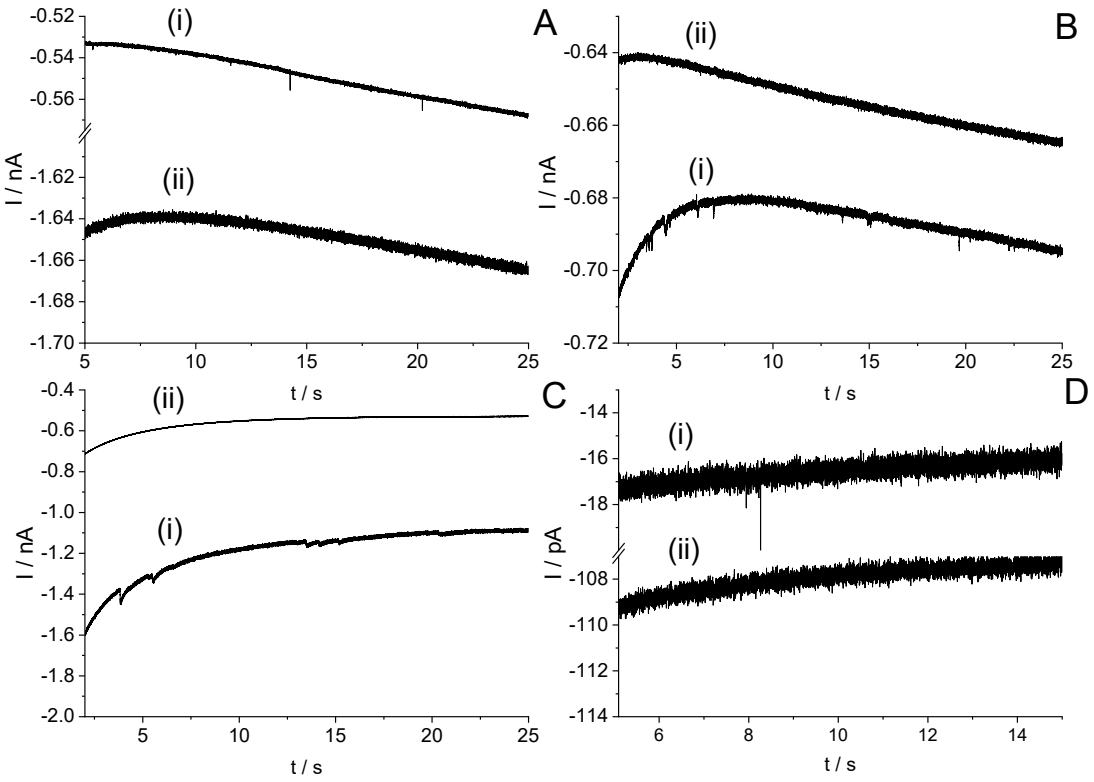

Figure 21 Comparison of chronoamperometric scans before and after the addition on AgNPs at -0.8 V, -0.7 V and -0.55 V (vs. MSE). (A) scans at -0.8 V vs. MSE with (i) and without (ii) the addition of 20 pM 60 nm AgNPs using an 11 µm CF electrode. (B) scans at -0.7 V vs. MSE with (i) and without (ii) the addition of 20 pM 60 nm AgNPs using an 11 µm CF electrode. (C) scans at -0.7 V vs. MSE with (i) and without (ii) the addition of 20 pM 50 nm AgNPs using a 33 µm CF electrode. (D) scans at -0.55 V vs. MSE with (i) and without (i) the addition of 40 pM 20 nm AgNPs using an 11 µm CF electrode.

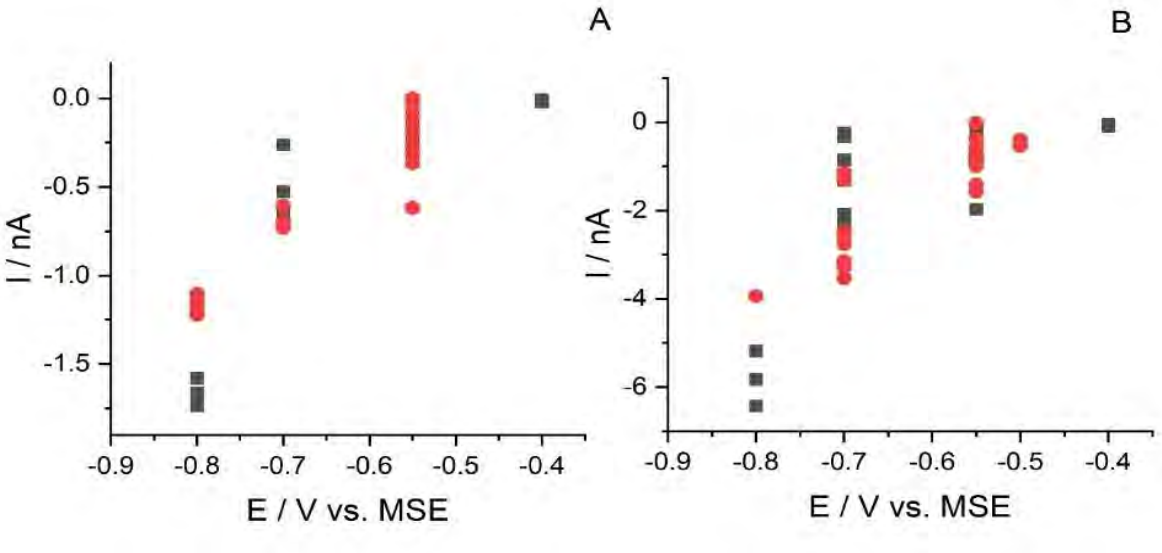

Figure 22 Variation of background current across different potentials in solutions containing no nanoparticles (■) and solutions containing Ag nanoparticles (●) for carbon microelectrodes of diameter 11 µm (A) and 33 µm (B).

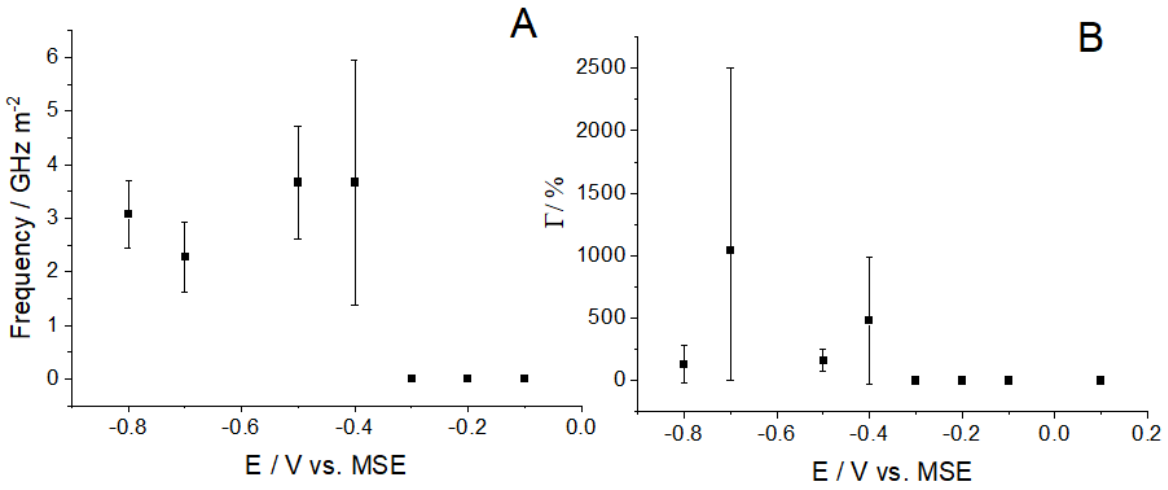

Figure 23A Frequency of impacts, normalised for electrode area, detected during 30 s chronoamperometric scans using a 20 pM suspension of 60 nm AgNPs at different potentials. Figure 23B displays the calculated average coverage of impacting AgNP at varying potentials where copper deposition occurred on nanoparticle collisions occurring at a potential negative of −0.3 V vs. MSE. All experiments were conducted in a 5 mL solution of 0.5 mM $CuSO_4$, 1 mM H_2SO_4 and 19 mM K_2SO_4 using a CF working electrode, a mercury sulphate reference electrode with a glass frit and a graphite rod counter electrode.

Further investigations were then conducted to determine the potential window at which the impact events could be observed, by recording chronoamperograms at a range of potentials under potentiostatic control. Figure 23A shows the frequency of reductive peaks detected at the different potentials ranging from −0.8 V to −0.1 V (vs. MSE), with the average frequencies at each potential where impacts were observed being in the range 2.3 to 3.7 GHz m^{-2}. At potentials more negative than −0.3 V vs. MSE, reductive peaks can be observed. This agrees with the data shown in Figure 19 (and in literature)[213,230] indicating that the onset of bulk copper deposition on the surface of silver is approximately −0.33 V (vs. MSE). The reductive peaks identified were used to determine the charge transferred during each impact event. Further details of the frequency vs. potential analysis shown in Figure 23A are provided in Figure 24 and Table 3 where additional details of the step-by-step analysis is shown. An example of the chronoamperometric scan conducted at -0.8 V (vs. MSE) used for the analysis has been provided where some peaks have been isolated and presented for clarity. Additionally, a table documenting the frequency calculated for each scan is provided.

As an example of the peak analysis, the chronoamperometric scan displayed in Figure 20A was considered and reproduced as Figure 24A. Closer inspection of the I-t curve within the 5-20 sec period of the scan shows 4 impact signals, labelled (i)-(iv), which are shown in greater detail in Figure 24B . The impact frequency for the scan can be calculated simply as the number of impacts recorded during the time length of the scan. Analysing all the chronoamperograms recorded for the potentials ranging from 0.1 V to -0.8 V (vs. MSE), an overall average impact frequency can be derived at each potential. These are given below in Table 3, where all scans were conducted in a solution of 0.5 mM $CuSO_4$, 1 mM H_2SO_4 and 19 mM K_2SO_4 in the presence of 60 nm AgNPs using 33 µm, 11 µm, and 9 µm CF working electrodes.

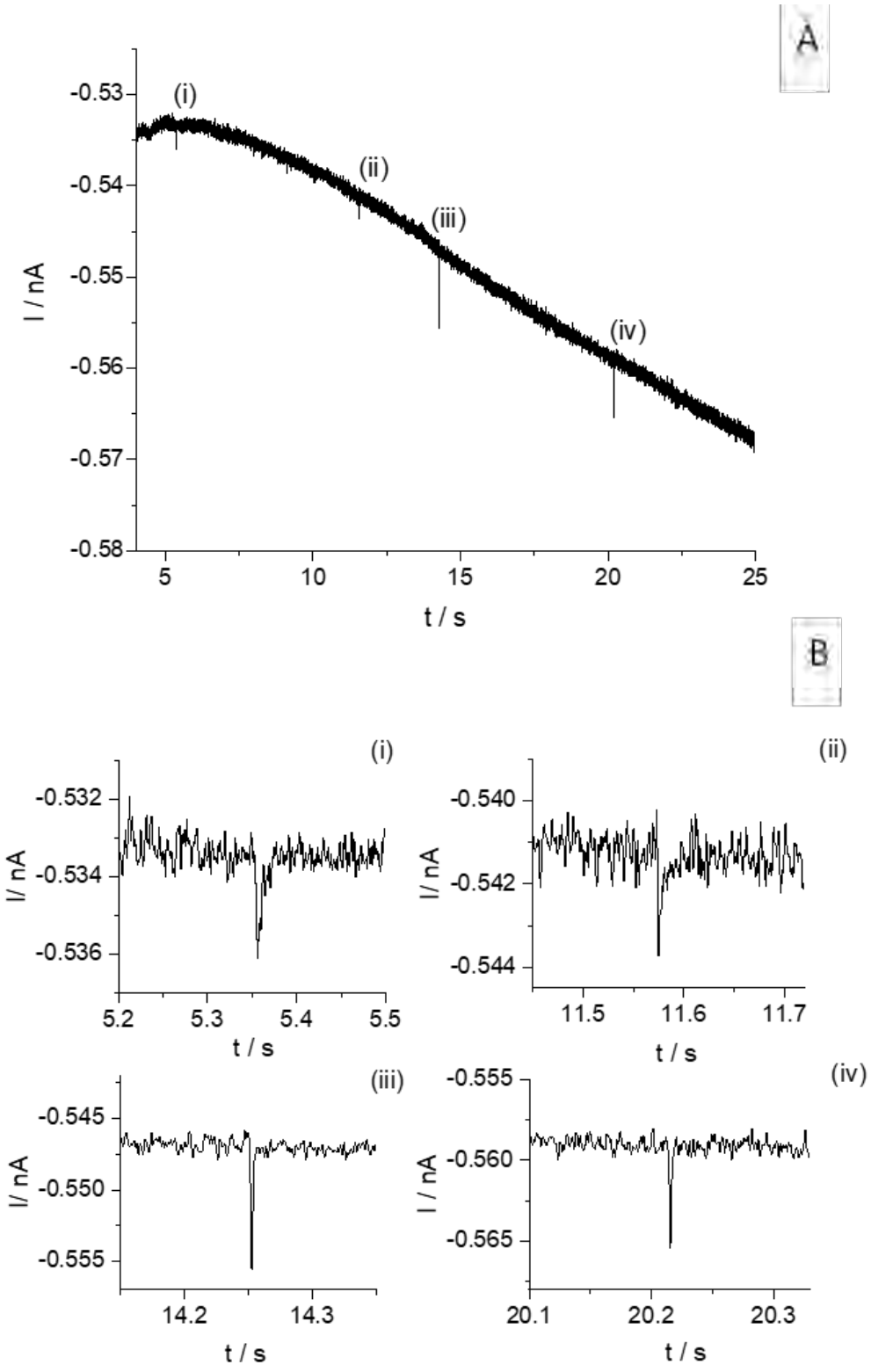

Figure 24 A Chronoamperogram showing impacts of 60 nm AgNPs in a solution containing 0.5 mM $CuSO_4$, 1 mM H_2SO_4 and 19 mM K_2SO_4 measured at -0.8 V (vs. MSE) with peaks labelled (i)-(iv); and Figure 24B showing the magnified peaks (i)-(iv) from (A).

Table 3 showing frequency of reductive peaks at different potentials ranging from 0.1 V to -0.8 V (MSE), where the average frequency of peaks has been averaged across multiple as shown.

Potential / V	No. of peaks	Frequency of peaks on scan / GHz m^{-2}	Average Frequency / GHz m^{-2}
-0.8	7	2.5	3.1 $\pm$ 0.6
-0.8	10	3.5	
-0.8	11	3.9	
-0.8	7	2.5	
-0.7	6	3.1	2.3$\pm$ 0.7
-0.7	4	2.1	
-0.7	3	1.6	
-0.5	5	2.6	3.7$\pm$ 1.0
-0.5	9	4.7	
-0.4	7	3.7	3.7$\pm$ 2.3
-0.3	0	0	0
-0.2	0	0	0
-0.1	0	0	0
0.1	0	0	0

The copper coverage of individual impacts was calculated using the charge determined from the integrated area of each peak.

$$S = 4\pi R^2 \qquad \text{Equation 96}$$

$$Q = \int I dt \; = ezN \qquad \text{Equation 97}$$

$$\theta = \frac{Q}{5.924}\left(\frac{r}{R}\right)^2 \qquad \text{Equation 98}$$

where S is the nanoparticle surface area, R the NP radius, Q the associated reductive charge, t the spike duration, e the electronic charge, z = 2 the number of exchanged electrons per reduced copper atom,[144] θ the coverage, r = 1.96 Å the copper atomic radius,[231] N the number of reduced copper atoms. The average coverage was calculated for impacts at different potentials (see Figure 23B). The data suggests that coverage greater than a monolayer equivalent occurs once the applied potential is

negative of the 'switch on' potential, for example at −0.4 V vs. MSE, an average coverage of 479% was observed. Table 4 shows a calculated example of copper coverage on the surface of an impacted AgNP. The calculated values for the AgNP surface area, reductive peak charge, number of Cu deposited, number of Cu in monolayer (Equation 94) and coverage equivalent are shown.

Table 4 Example of Cu coverage calculation associated with deposition onto an impacting AgNPs

Parameter / unit	Calculated values
S / m^2	1.1×10^{-14}
Q / C	-4.2×10^{-14}
N	1.3×10^{5}
N_{mono}	7.0×10^{4}
θ	1.9

3.4.3 Impact deposition of Cu onto Au metallic nanoparticles

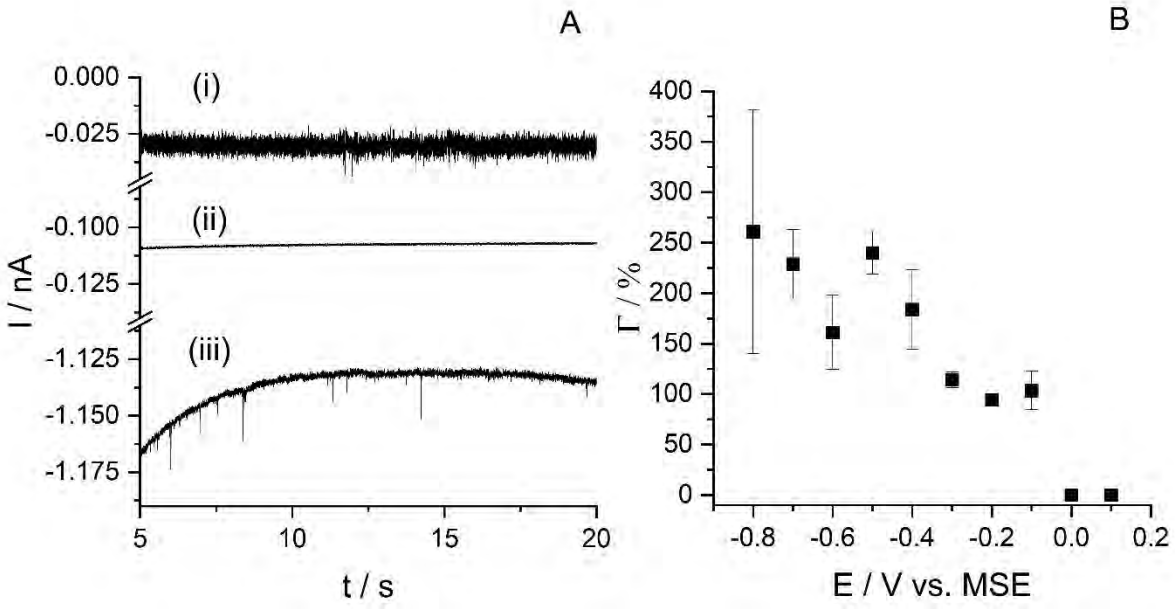

Figure 25A depicts a 15 s segment of three 30 s chronoamperometric scans (i) a chronoamperometric scan at -0.3 V using a 9 µm CF after the addition of AuNPs (ii) a scan conducted at a potential of -0.55 V using a 11 µm CF electrode before the addition of AuNPs (iii) a scan at -0.8 V using 11 µm CF after the addition of 60 nm AuNPs . Figure 25B shows the calculated average percentage coverage (θ) of individual 50 nm AuNP impacts at different potentials ranging from 0.1 V to -0.8 V vs. MSE. A series of 30 s chronoamperometric scans were conducted in a 5 mL solution of 0.5 mM Cu_5O_4, 1 mM H_2SO_4 and 19 mM K_2SO_4 using a CF working electrode, a mercury sulphate reference electrode with a glass frit and a graphite rod counter electrode.

Analogous impact experiments were then conducted using a 20 pM suspension of AuNPs to study whether impacts were observed in the upd and bulk deposition regions in Figure 19. Similar to the AgNP system, upon the addition of AuNPs, reductive transient peaks could be observed for a range of potentials (vs. MSE). Figure 25A displays the chronoamperometric scans before and after the addition of gold nanoparticles conducted at −0.3 V (upd region) and at −0.8 V (bulk deposition region). It can be observed that before the addition of AuNPs the scan is void of transient peaks, however upon the addition of gold nanoparticles reductive peaks are observed at both −0.3 V and −0.8 V (vs. MSE.), in the upd and bulk deposition regions.

The impact 'spikes' were integrated to obtain the charge passed during each impact, allowing calculation of the percentage coverage of the deposit, assuming a spherical NP, using Equation 96-Equation 98.[137,159,161] Figure 25B illustrates the calculated percentage coverage of impacting AuNP at varying potentials ranging from −0.8 V to 0.1 V (vs. MSE). Peaks begin to occur at potentials more negative than −0.1 V vs. MSE. This is in good agreement with the onset potential determined (see Figure 19) and the upd region reported in literature.[215] The data shows that at potentials where upd is expected, the impacts observed correspond to an average coverage of ca.103% ± 8%, the theoretical monolayer coverage. On the other hand, at more negative potentials where bulk deposition would occur, the maximum percentage coverage is higher with an average coverage of 215% ± 37%, significantly exceeding the equivalent of monolayer coverage.

A comparison of the AgNP and AuNP coverage (Figure 23B and Figure 25B) indicates a significantly higher copper coverage for the AgNP impacts. Given the similarity between bulk deposition onset, particles sizes (50–60 nm), and sticking coefficients for the AgNPs and AuNPs (0.15 for AgNPs ,[166] and 0.19 for AuNPs,[133] reported for particles of mean radii ca. 10–13 nm), it might be expected that the coverages should also be similar provided that the bulk deposition kinetics of Cu were not markedly different on Ag and Au. The observed difference in deposition amounts has been postulated to be due to the degree of aggregation in the NPs, with AgNPs in particular, known to have rapid aggregation

kinetics.[141] Since the coverage calculations are based on a single particle of mean diameter, they are highly sensitive to aggregation. Closer examination of the data indicates that the apparent coverages on Ag are skewed by several significantly larger impact spikes, which are consistent with the impacts of larger aggregates of NPs. Removal of these larger impacts yields coverages in the range 60–170% of a monolayer, which is comparable with the AuNP result.

3.4.4 Impact deposition of Cu onto fly-ash cenospheres (FACs)

After demonstrating the deposition of copper onto metallic nanoparticles, the reduction of copper onto cenosphere particles was investigated. Cenospheres were chosen as a core material for deposition as they are considered a waste product of the coal combustion process, additionally these are predominantly non-metallic particles. As previously stated, the composition of cenospheres varies and is influenced by the combustion conditions and coal composition.[205,209] As such, the cenosphere were characterised using SEM/ EDX, which enabled an approximate size distribution and composition to be obtained. Figure 26 shows the particle size distribution produced from SEM images of the cenosphere sample and highlights a population centred around 1 µm in size, though a very large range of sizes can be observed. The size distribution histograms were obtained from numerical analysis using GIMP software on SEM images at 50x, 200x, and 2500x magnification of virgin and treated cenospheres as shown in Figure 27 and Figure 28. The SEM was conducted using dried cenosphere powder before and after the impact investigation. The images taken are analysed with Pythagoras using co-ordinates plotted for each particle to calculate diameter.

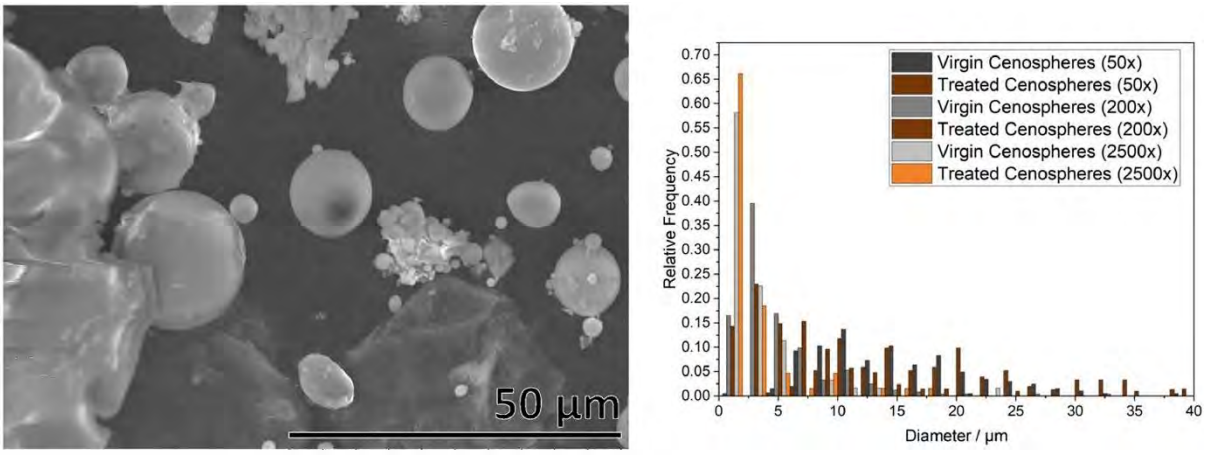

Figure 26 A SEM image of impacted cenosphere particles with higher copper content. Figure 26B Size distribution of FACs from SEM images using a magnification of 50x, 200x and 2500x, analysed using GIMP software. Number of particles analysed, N = 976.

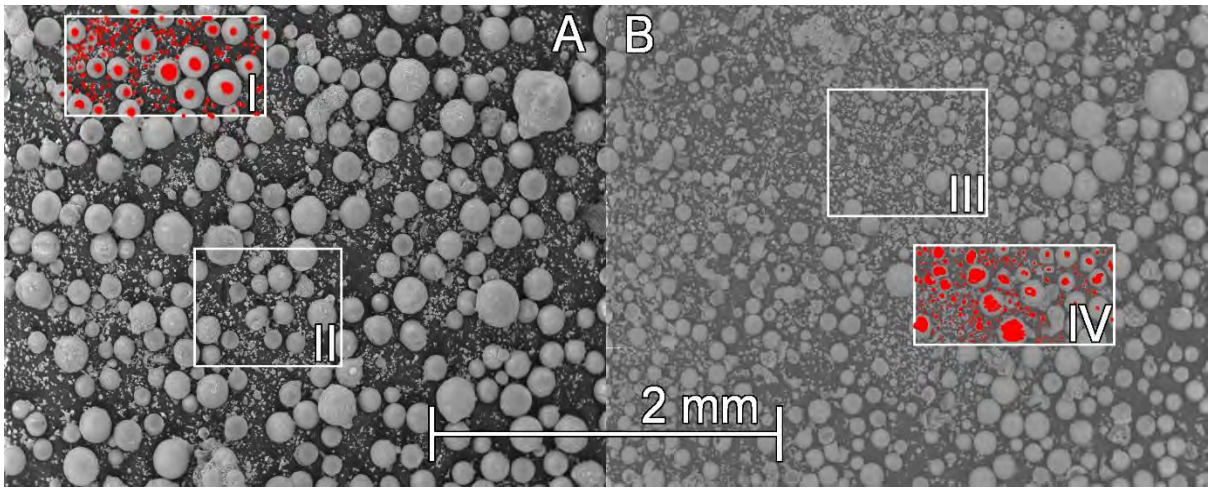

Figure 27 SEM analysis at 50x magnification of virgin (A) and treated (B) cenospheres taken as dry powders for analysis where the treated sample has been used in impact investigations. Area I and IV are areas analysed for cenosphere size with counted particles highlighted red. Areas II and III are areas further investigated at higher magnification.

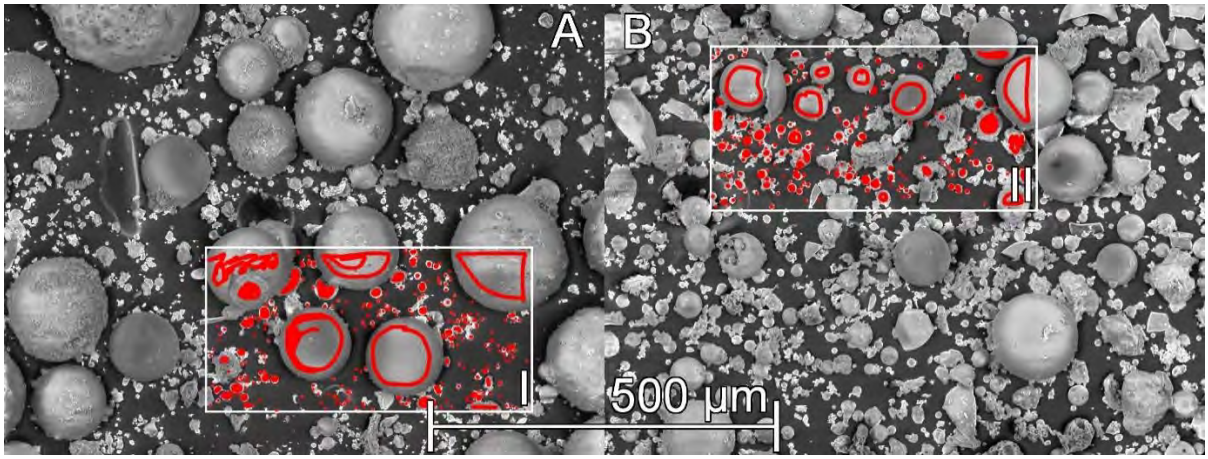

Figure 28 SEM analysis at 200x magnification of virgin (A) and treated (B) cenosphere taken as dry powders for analysis. Area I and II are areas analysed for cenosphere size with counted particles highlighted red.

Impact electrochemistry primarily focuses on particles on the nanoscale. Within literature it has been observed that the impact electrochemistry technique is able to facilitate the detection of a wide variation of particles sizes with 6 nm reported as the lower limit of detection.[232] With regards to the upper limit, it has been suggested the application of direct impact is possible for sizing aggregated particles beyond the upper nanoparticle limits (100 nm) as seen in literature.[141,145,157] The variation in cenosphere size and complex composition may affect the impact deposition process, as a result of the differing particle hydrodynamics under Brownian motion and settling properties.[233] Additionally, observations have been made suggesting an increase in the peak current with increasing particles size.[234] According to Zhou et al.[133,166,] sticking potential is not significantly affected by size however does vary with the impacting material and substrate electrode.[164,235]

To further analyse the cenosphere particles a basic XRF analysis (Table 5) was conducted to determine the cenosphere composition as this is influenced by the combustion conditions and coal composition. Additional analysis using SEM/EDX shown in Table 6 was also conducted to further characterise the particles and is in agreement with both the XRF data obtained and literature reports that cenospheres are mainly comprised of metal oxides, with varying compositions reflecting those of their starting materials .[206,211]

Table 5 displays the elemental composition of the cenosphere particles determined using the handheld X-ray fluorescence spectrometer (hXRF). This table indicates high content of Si and Al as suggested by the SEM/ EDX analysis.

Element	Mass / %	Element	Mass / %
Si	21.9	As	0.0
Al	9.3	Se	0.0
Mg	1.1	Rb	0.0
P	0.2	Sr	0.1
S	0.2	Zr	0.0
Cl	0.0	Nb	0.0
K	2.8	Mo	0.0
Ca	5.0	W	0.0
Ti	0.6	Pb	0.0
Cr	0.0	Th	0.0
Fe	3.1	U	0.0
Cu	0.0	Pr, Au, Ag, Nd, Ce, La, Sb, Cd, Sn, V, Mn, Y, Co and Ni	0.0
Zn	0.0		

*Table 6 Average compositions by mass of FACs determined by SEM/EDX (*N *= 7).*

Element	Average composition / %
Silicon	52.3
Aluminium	29.4
Iron	9.0
Calcium	6.7
Magnesium	2.3
Copper	0.2

To determine the suitability of the cenospheres for electrochemical impact experiments, the deposition of copper onto the cenosphere particles were investigated by drop-casting to produce a cenosphere-modified GC macro electrode (d = 3 mm) with ca. 1900% coverage, based on calculation assuming even distribution.[226] Figure 29 illustrates the reductive linear sweep voltammograms recorded for the bare GC and the FAC-modified GC electrode in a solution of 0.5 mM copper sulphate, 19 mM potassium sulphate and 1 mM sulphuric acid at a voltage scan rate of 100 mV s^{-1}. According to both

Danilov et al. and Bimaghra and Crousier,[236,237] the 2-electron deposition of copper onto carbonaceous materials occurs via the Volmer-Weber mechanism resulting in three-dimensional nucleation. Briefly, upon the establishment of the electric double layer, both copper metal adatoms and univalent copper ions accumulate near the electrode surface via the reactions:

$$Cu^{2+} + e \rightarrow Cu^{+} \qquad \text{Equation 99}$$

$$Cu^{+} + e \rightarrow Cu_{ad} \qquad \text{Equation 100}$$

where a quasi-equilibrium occurs between the Cu^{+} ions and free unbound Cu_{ad}. As copper nuclei form at the surface of the electrode, the corresponding reductive current is influenced by cathodic overpotential, active surface area of the deposit and the mass transport of ions to the electrode/ solution and nuclei/solution interface. The cyclic voltammetry (see Figure 29) for the bare GC depicts two peaks with currents of −7.2 µA and −2.1 µA where the first peak is ascribed to copper deposition on the bare GC (peak 1) followed by deposition on the copper-modified GC surface (peak 2).

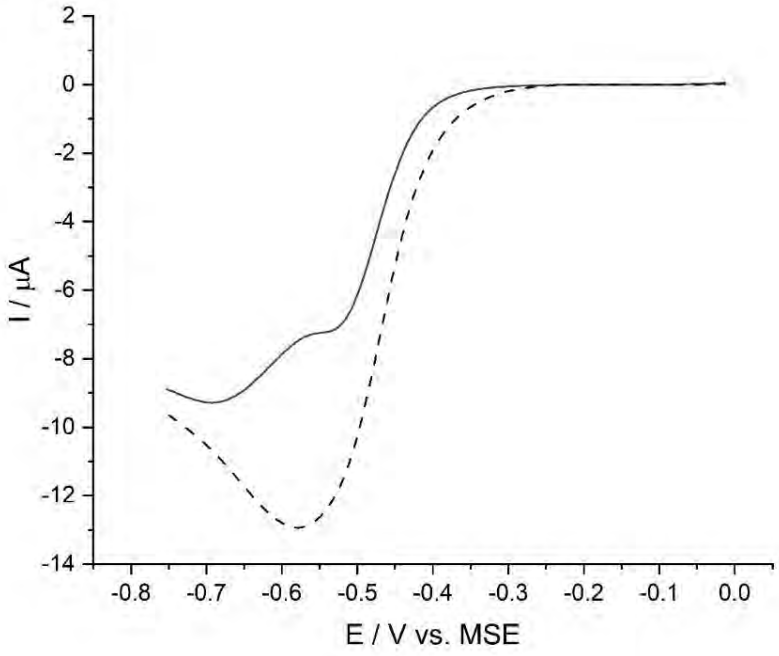

Figure 29 illustrates the reductive scans of copper deposition on the surface of 3 mm Bare GC (—) and a cenosphere modified GC surface (––). A 100 mV s^{-1} voltage scan rate was used between the potential window 0.0 V to −0.75 V (vs. MSE) in a solution of 0.5 mM $CuSO_4$, 1 mM H_2SO_4 and 19 mM K_2SO_4.

The conductivity of the cenospheres particles were investigated via a capacitance and blocking effect study. The capacitance of the cenosphere-modified GC electrode was investigated using voltammetry. The electrochemically active surface area of a cenosphere-modified GC electrode was compared to that of a bare (unmodified) GC electrode. For this, a series of cyclic voltammograms were recorded at the electrode in a thoroughly de-oxygenated solution containing 5 mM hexammineruthenium (III) chloride and 0.1 M potassium chloride. This was repeated at a range of voltage scan rates from 50 to 250 mV s^{-1} for both bare and cenosphere-modified GC electrodes. A plot of the reversible Randles-Ševčík equation (Equation 47) is given in Figure 30A, with gradients of -2.64×10^{-4} A $s^{1/2}$ $V^{-1/2}$ and -2.50×10^{-4} A $s^{1/2}$ $V^{-1/2}$ was determined for the modified and unmodified GC surface respectively. Given the outlying data point in Figure 30A, the gradients are within experimental error and active surface area is effectively unchanged.

Next, the capacitance of the modified and unmodified GC electrodes was measured by recording cyclic voltammograms over a range of voltage scan rates up to 200 mV s^{-1} in a solution containing 0.02 M potassium sulphate only (to match the ionic strength of impact experiments), with the scan centred at 0 V vs. MSE. The hysteresis between forward and reverse scans was measured and half of it plotted against scan rate in Figure 30B. Both cenosphere-modified and bare GC electrodes show a linear relationship with gradients of 0.80 μF and 1.32 μF respectively.

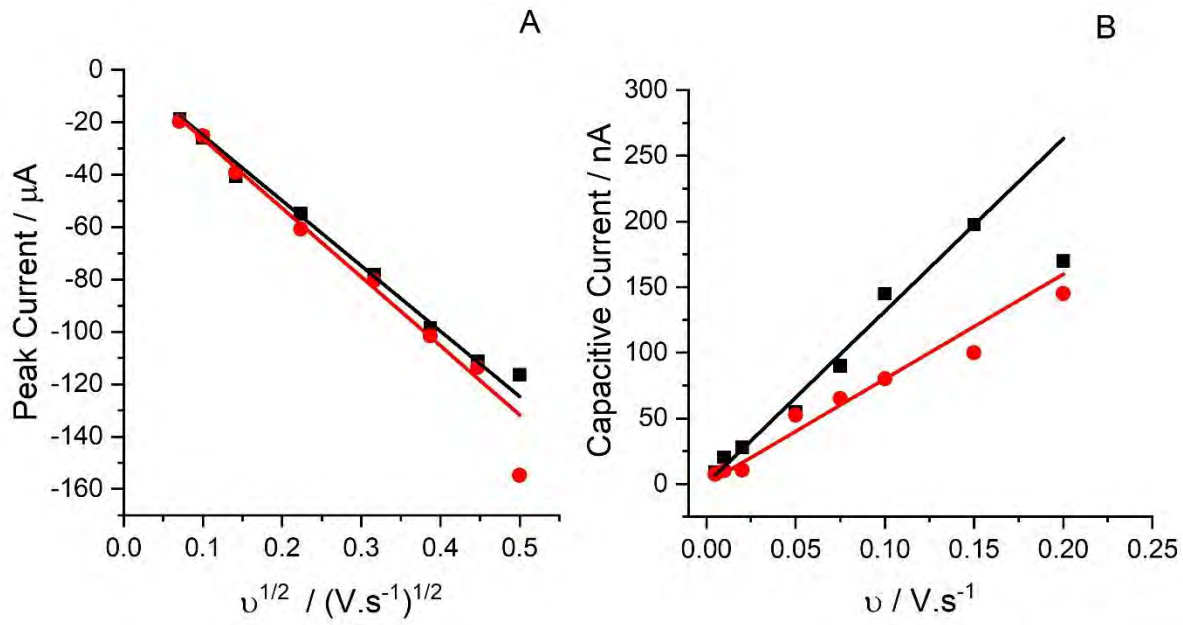

Figure 30(A) Randles- Sèvčík plot for cenosphere-modified GC (●) and bare GC (■) electrodes in a solution containing 5 mM $Ru(NH_3)_6Cl_3$ and 0.1 M KCl. (B) Plot of capacitive current vs voltage scan rate for cenosphere-modified GC (●) and bare GC (■) electrodes in a solution containing 0.02 M KCl.

Upon modification of the bare GC with cenosphere particles, the cenosphere-modified electrode has increased reductive current without any discernible increase in capacitance. This indicates the cenospheres have sufficient electrical conductivity such that the increased surface area of the electrode leads to an increased current response. In addition, Figure 29 identifies the onset potential of copper deposition onto the surface of the cenosphere particles. From this it was determined peaks may be observed upon impact with the substrate electrode at a potential negative of −0.3 V (vs. MSE).

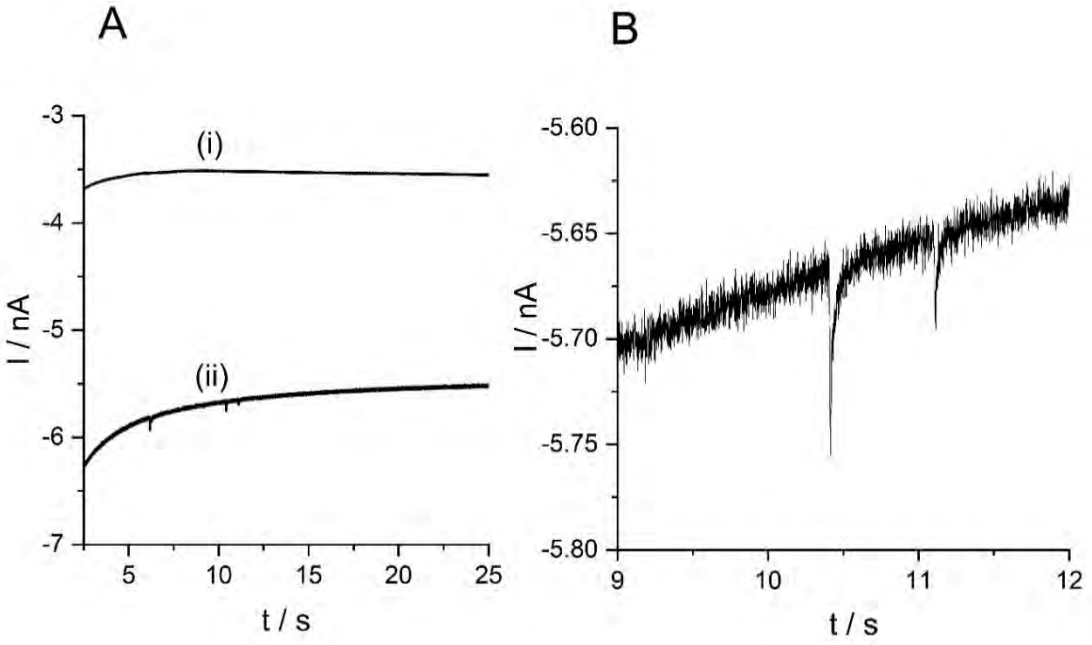

Figure 31 A illustrates two chronoamperometric scans conducted in a 5 mL solution of 0.5 mM $CuSO_4$, 1 mM H_2SO_4 and 19 mM K_2SO_4 before (i) and after (ii) the addition of cenosphere particles. Both were performed at a potential of −0.75 V vs. MSE for 30 s. (B) highlights reductive peaks observed upon the addition of the cenosphere particles.

Next, 0.05 g of FACs were added to 5 mL of a solution of 0.5 mM copper sulphate, 19 mM potassium sulphate, and 1 mM sulphuric acid resulting in a (number) concentration of 0.01 pM (and agitated using the degassing nitrogen stream. The number concentration of cenospheres was calculated as follows:

Equation 101

$$N_{ceno} = \frac{m}{\frac{4}{3}\pi\rho r_{mean}^3}$$

where N_{ceno} is the number of cenospheres in the sample, m is the mass of cenospheres in the sample, and the denominator represents the mass of an average cenosphere where ρ is the density of a cenosphere (0.857 g cm^{-3}),[206] and r_{mean} is the average radius (8 $\times 10^{-4}$ cm). Then,

Equation 102

$$NC_{ceno} = \frac{3m}{4\pi N_A V \rho r_{mean}^3}$$

where NC_{ceno} is the number concentration of cenospheres, N_A is Avogadro's constant, and V is the volume of solution that the cenospheres are suspended in. For the experiments described, m = 0.050 g and V = 5.0 mL, which yields a number concentration of cenospheres in suspension of 0.01 pM.

A carbon fibre working electrode (33 µm) was used to investigate whether FAC impacts relating to Cu deposition could be observed. Figure 31A displays typical chronoamperometric scans at −0.75 V vs. MSE in the copper solution before and after the addition of the cenosphere particles showing the emergence of reductive events on the addition of cenospheres to the system (see Figure 31B). Note that positive-direction spikes that would be associated with the partial blocking of the background reductive current at the CF electrode are not observed.[238] Additional chronoamperometric scans were conducted in a solution containing only 19 mM potassium sulphate and 1 mM sulphuric acid before and after the introduction of cenosphere particles as shown in Figure 32 . The absence of reductive transient peaks in both scans suggest the peaks observed in Figure 32 in the presence of copper is due to copper deposition onto the cenosphere, rather than a characteristic of the cenosphere particle.

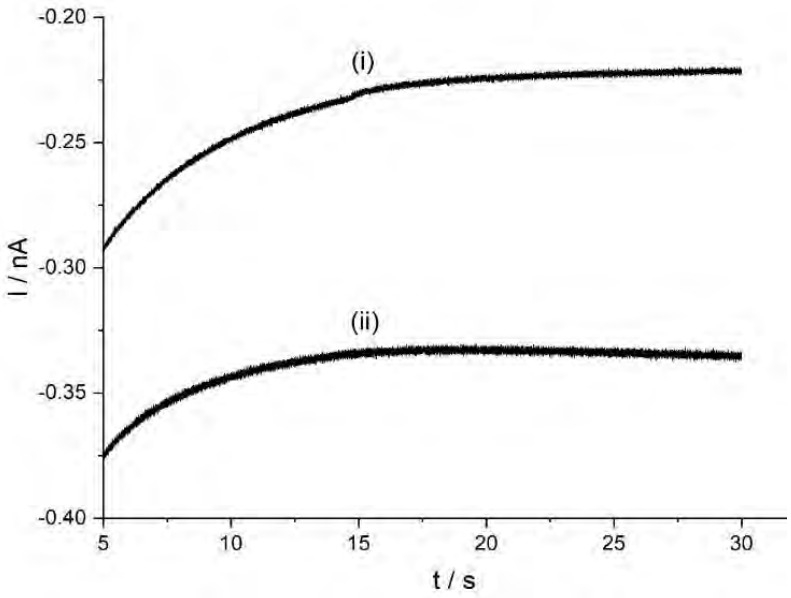

Figure 32 shows 25 s segment of a 30 s chronoamperometric scan in 19 mM potassium sulphate and 1 mM sulphuric acid solution before (i) and after (ii) the addition of cenosphere particles where no impact spikes were observed.

The blocking effect of the cenosphere particles were further investigated by conducting chronoamperometric scans in a solution of 0.5 mM $Ru(NH_3)_6Cl_3$, 1 mM H_2SO_4 and 19 mM K_2SO_4 with a 33 µm CF at −0.6 V (vs. SCE) before and after the addition of cenosphere particles as shown in Figure 33. During the investigation it was possible to obtain a blank chronoamperometric scan without transient peaks before the addition of particles. Upon the addition of cenosphere particles a reductive peak could be observed suggesting an increase in current rather than a blocking effect. Again, positive-direction spikes corresponding with the partial blocking of current by the cenospheres particles are not observed. The conclusion is therefore made that the reductive peaks observed in Figure 31B are due to the deposition of copper on the impacting cenosphere particles.

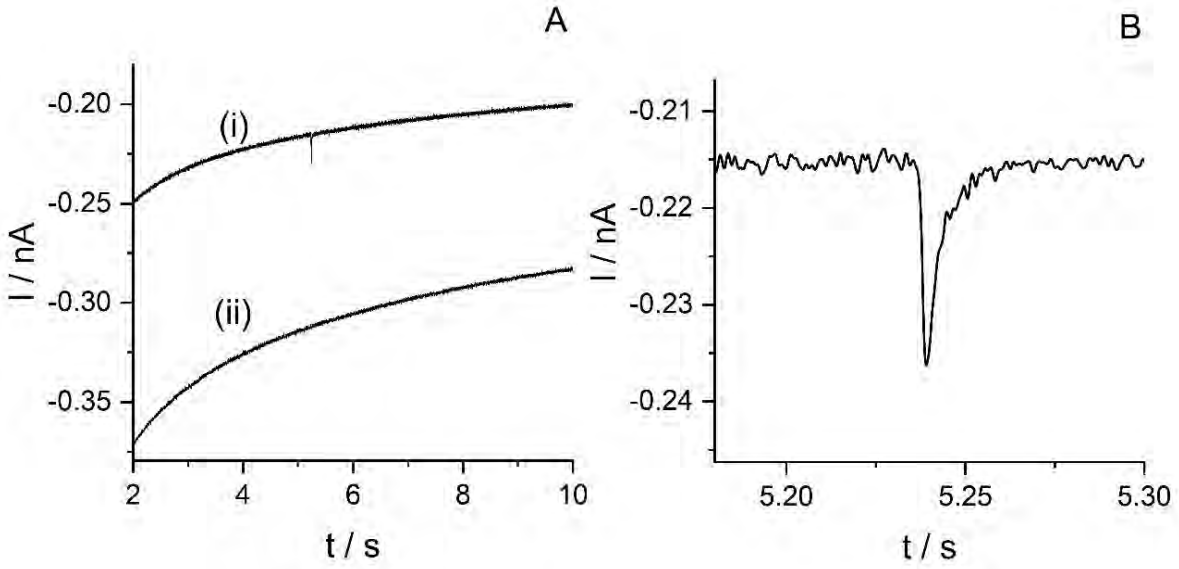

Figure 33A shows 8 s segment of a 30 s chronoamperometric scan conducted in a solution of 0.5 mM $Ru(NH_3)_6Cl_3$, 1 mM H_2SO_4 and 19 mM K_2SO_4 with a 33 µm CF at -0.6 V vs. SCE; where (i) was conducted after the addition of 0.06 g cenosphere particles (0.01 pM) and (ii) was conducted in a solution containing no cenosphere particles. The reductive peak from Figure 33 A has been isolated and displayed in Figure 33B.

To obtain direct evidence of Cu deposition onto the FACs, a 12h chronoamperometric scan was conducted using a 3 mm GC electrode at −0.75 V vs. MSE in a solution containing 0.5 mM copper sulphate, 19 mM potassium sulphate, 1 mM sulphuric acid and 0.05 g cenosphere particles. This solution was then agitated briefly using the degassing nitrogen gas stream before commencing the chronoamperometric scan. Upon completion, 5 µL of the reacted suspension solution was extracted from the reaction cell, drop-cast onto a polished GC stub and then analysed using SEM/EDX to

determine the copper content of the cenospheres (additional experiments used dried cenospheres obtained through rinsing cycles and centrifugation as described in ICP-MS sample preparation).

Table 7 displays the copper content determined by SEM/ EDX analysis of the background (GC stub), the unmodified cenosphere particles and impacted cenosphere particles. Copper content is presented as a ratio of copper and silicon count and error given by standard deviation.

Sample	**Percentage copper content / %**
Background (GC stub surface)	0
Pristine cenosphere particles	0.07 ± 0.07
Impacted cenosphere particles	7.43 ± 2.47

Table 7 displays the copper content determined by SEM/ EDX analysis of the background (GC stub), the unmodified cenosphere particles and impacted cenosphere particles. Copper content is presented as a ratio of copper and silicon count This shows the average copper content of the impacted cenospheres determined using SEM/ EDX analysis confirming that the average Cu content of impacted FACs is significantly higher than for non-impacted (pristine) FACs, with an average Cu content of 7.43 ± 2.47% compared to 0.07 ± 0.08% (by count, N = 7). Note that these values are quoted relative to the measured silicon (Si) content of the same FAC particle, to account for the variation in particle size and composition. Detecting cenospheres with copper deposition in the solution sample demonstrates that after impacting the GC electrode some particles can detach from the surface. An SEM analysis of the GC stub was also conducted and indicated a build-up of copper deposition with cenosphere inclusions. Figure 34 SEM analysis of GC stub and imbedded cenosphere particle depicts an SEM analysis of the GC stub used as the substrate during an impact investigation with cenosphere particles. Additionally, SEM studies of cenosphere particles before and after modification using impact investigation has been documented where an increase in copper content can be seen.

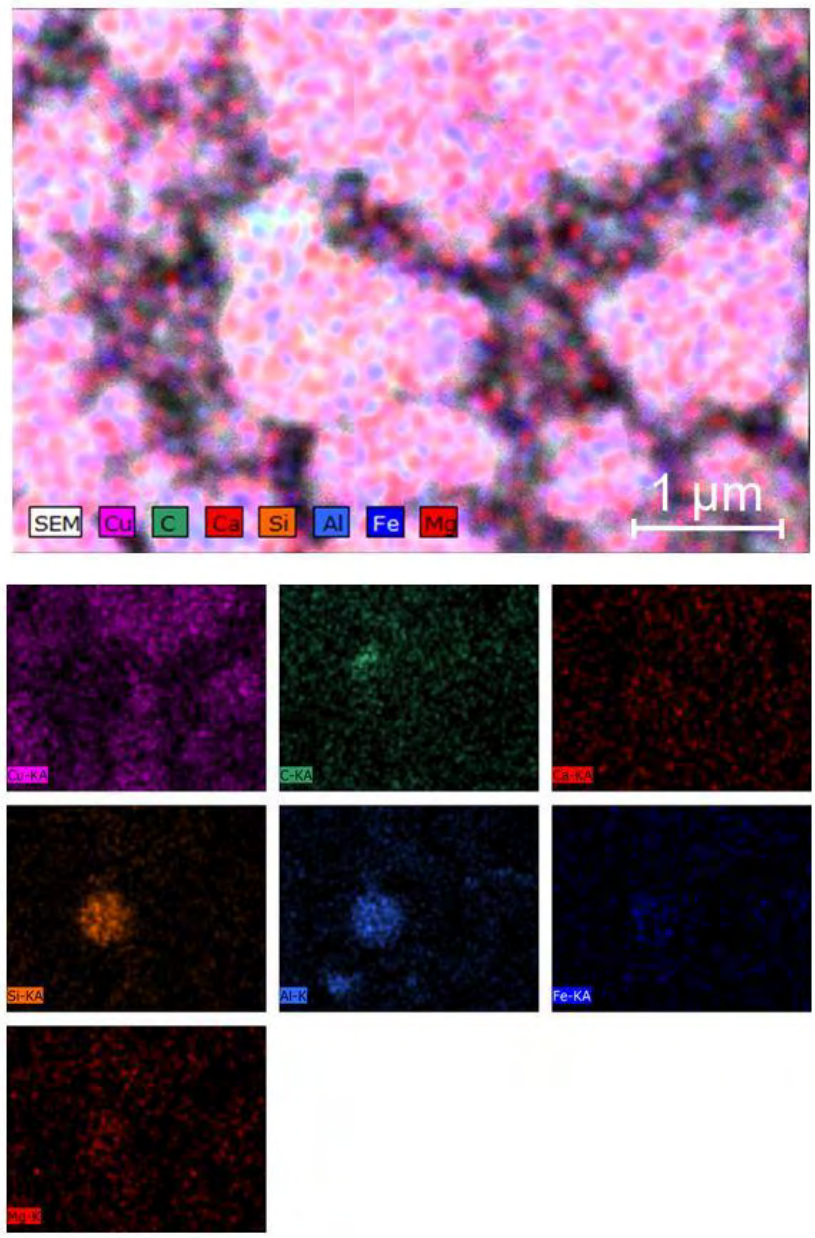

Figure 34 SEM analysis of GC stub and imbedded cenosphere particle

The degree of deposition of Cu onto the GC substrate, will clearly be dependent on the potential at which the impact experiment was conducted, and here was expected due to the choice of deposition potential. Detailed quantitative analysis of the degree of deposition onto the GC stub (via XPS) was not conducted here, since this was outside the scope of this study. However, such detailed analysis of the substrate electrode would be necessary when considering quantitative application of the impact technique for scaled-up application.

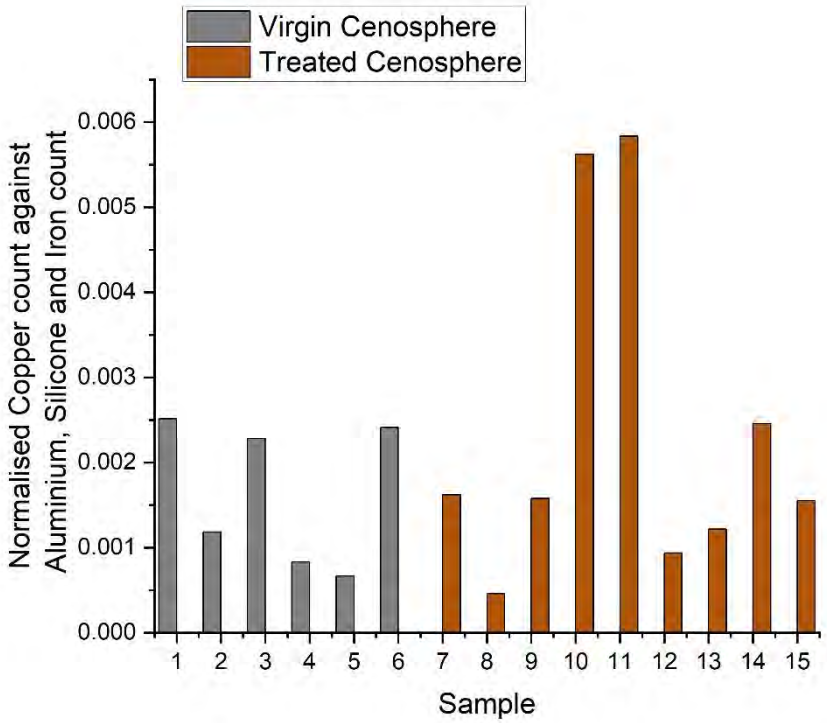

Figure 35 Chart showing relative ratio of copper in each EDX scan taken at 2500x magnification. At this magnification particles start to be isolated for the EDX inspection therefore the differential concentration of copper between particles becomes more apparent.

The SEM analysis (Figure 35) also identified some cenospheres present with a similar (near zero) level of copper content to the control, implying not all cenospheres collided with the GC electrode or else an impact occurred with little to no copper deposition. This variation is expected as the impact deposition process is uncontrolled, and the cenosphere composition (and hence conductivity) is not uniform.

In addition to the SEM/EDX analysis, ICP-MS analysis of both the impacted and the unmodified cenosphere particles was conducted. The analysis showed that the unmodified cenosphere had a copper content in the sample of 1.0 ppb and the modified cenosphere sample had double the copper content at 2.0 ppb. These values are well above the detection limit (0.174 ppb) of the ICP-MS and as such provides further evidence of impacting cenosphere increasing in concentration of copper.

3.5 Conclusion

The macro- and microelectrode studies demonstrated that the onset for copper deposition varied depending on the substrate material agreeing with previous literature.[217] A drop-casting technique was employed to show upd occurred for copper on gold further agreeing with literature.[216] Using impact voltammetry, copper deposition was observed during silver nanoparticle impacts, where the switch on/ off potential aligned with the onset potential previously mentioned at −0.4 V vs. MSE. Studies with AuNPs indicated the impact switch on/ off for copper deposition on gold shifted positively thus reflecting the upd onset predicted (to −0.1 V vs. MSE). Evidence was found suggesting peaks occurring in the upd region resulted in particle coverage of approximately a monolayer (with an average of ca. 103% ± 8%) while peaks in the bulk region showed indication of a higher coverage (with an average of ca. 215% ± 37%).

Cenospheres were tested for use as a functional recovered waste material, the particles were characterised showing significant amounts of silicon and aluminium with lower amounts of iron, calcium, magnesium, and copper agreeing with previous literature. A size distribution analysis was conducted indicating a wide range of sizes from 100 s of nanometres to 100 s of microns with a population centred at 1 µm. The same drop-cast method was applied and showed that the cenosphere particles were electrochemically active. During impact voltammetry cenospheres exhibited transient spikes and evidence of copper deposition. This was supported by direct evidence found via SEM/ EDX and ICP-MS analysis showing copper had been deposited onto the cenosphere.

4. Palladium deposition on carbon nanoparticles via impacts

4.1 Abstract

The recycling of critical materials, regeneration of waste, and responsible catalyst manufacture has been repeatedly documented as essential for a sustainable future with respect to the environment and energy production. Electrochemical methods have become increasingly recognized as capable of achieving these goals, and "impact" electrochemistry, with the advantages associated with dynamic nanoelectrodes, has recently emerged as a prime candidate for the recovery of metals from solution. In this chapter, the nano-impact technique is used to generate carbon-supported palladium catalysts from low-concentration palladium (II) chloride solutions (i.e., a waste stream mimic) as a proof of concept. Subsequently, the catalytic properties of this material in both synthesis (Suzuki coupling reaction) and electrocatalysis (hydrogen evolution) are demonstrated without further processing or treatment. Transient reductive impact signals are shown and analysed at potentials negative of +0.4 V (vs. SCE) corresponding to the onset of palladium deposition in traditional voltammetry. Direct evidence of Pd modification was obtained through characterization by environmental scanning electron microscopy/energy-dispersive X-ray spectroscopy, inductively coupled plasma mass spectrometry, X-ray photoelectron spectroscopy, transmission electron microscopy, and thermogravimetric analysis of impacted particles. This showed the formation of deposits of Pd partially covering the 50 nm carbon black particles with approximately 14% Pd (wt %) under the conditions used. This material was then used to demonstrate the conversion of iodobenzene into its biphenyl product (confirmed through nuclear magnetic resonance) and the successful production of hydrogen as an electrocatalyst under acidic conditions (under cyclic voltammetry).

4.2 Introduction

Platinum group metals (PGMs) are significant critical metals because of their wide range of applications, most notably as catalysts.[1,4,190] Palladium is a common catalyst, utilized in many

applications and processes such as environmentally important automotive catalytic converters, future energy use in hydrogen storage and production, and large-scale chemical synthesis.[239-250]The Suzuki coupling reaction for example is an industrially important reaction frequently used in pharmaceutical drug synthesis, the formulation of agrochemicals, and polymer production.[251-259]

To improve both performance and economic use, PGM catalysts are often used as supported nanoparticles (NPs), where the support particles disperse the catalytic material to a greater extent, increasing exposure of the catalytic surface area. Carbon materials such as carbon black (CB), graphite, and graphene have been extensively studied as supports,[241-263] as they are inexpensive and possess useful properties such as a high electrical conductivity and large surface areas while being mechanically and chemically stable.[264-270]

Pd-modified carbon nanostructured catalysts are extensively used in a range of applications: from electrochemical sensors and organic synthesis to the oxidation of formic acid and reduction of oxygen in fuel cells.[271-278] However, the use of Pd can lead to environmental pollution via release of contaminated waste solutions and particles.[279-283] For example, the World Health Organization has reported concentrations of 260 μg kg^{-1} in sewage sludge and up to 4.7 mg kg^{-1} in waste discharged from the jewellery industries.[284] Other sources of soluble palladium (often $PdCl_2$) such as e-waste (electroplating and printed circuit boards) can result in concentrations of 1500 mg L^{-1} in waste streams.[285] Concentrations in natural waters are significantly lower, with Pd concentrations of 22 ng L^{-1} and 70 pg L^{-1} being detected in fresh water and sea water, respectively.[286] Palladium metal has historically been considered relatively low in toxicity; however, its compounds such as palladium (II) chloride are highly toxic and carcinogenic to wildlife even in minute amounts. For example, a minimum 24 h lethal concentration of 7 mg has been reported for the freshwater fish medaka, and LD_{50} values in rats reach between 0.02 and 1.13 mmol kg^{-1} bodyweight;[286,287] hence, it is important to maximize recovery and clean waste already existing for both environmental and economic reasons.

The primary method used to recover spent Pd catalysts is hydrometallurgy which is limited because of the significant volumes of toxic and expensive reagents needed and the further production of hazardous waste such as nitric oxides.[239,288-293] These methods, often requiring the pre-treatment of Pd, have been able to achieve recovery within the range of 58–97%[294-302] but are considered ineffective for the removal of metals from waste solutions at low concentrations resulting in waste storage challenges and reduced profit.[285,303,304] Therefore, more environmentally sustainable methods of Pd nanoparticle synthesis and recovery have been investigated.[285,305-307] Electrodeposition is considered a practical method for metal recovery because of its operational feasibility, with the deposition controlled through the potential applied and metal ion concentration,[197-199,308] and traditional electrodeposition methods have many industrial applications.[60,309-313]The use of electrochemical systems such as galvanic reduction and recovery from ionic liquids after solvent extraction have been explored within the literature as a method of Pd extraction achieving a recovery of 90–99%.[285,314] Higher recoveries were observed in systems increasing mass transport via the use of rotating electrodes or flow of the plating solution.[315-316] However, overall recovery or recycling efficiency is not necessarily easily compared because studies often focus on one part of the recycling process (usually recovery, rather than separation, dissolution, etc.).

In this chapter, the recovery process from solution is considered: particle impact electrochemistry has been investigated as a method for in situ synthesis of Pd-modified carbon black nanoparticles (Pd/CB NPs) from the recovery of palladium from solutions containing low concentrations of $PdCl_2$ as a proxy for industrial waste streams. Impact electrochemistry has previously been reported as a method of reducing metallic ions onto metallic nanoparticles (or cores) via both bulk and underpotential deposition processes.[137,161,163] However, the deposition onto non-metallic cores (for metal recovery) via impact electrochemistry has only recently been described, for the deposition of copper ions onto fly-ash cenosphere particles.[137]The use of non-metallic materials potentially increases the economic viability, flexibility, and sustainability of this technique as it reduces reliance on expensive and potentially critical core materials.

In this chapter, the first metal on carbon deposition by impact electrochemistry for the case of Pd on CB, using the method to fabricate Pd/CB nanoparticles has been reported. The fabricated Pd/CB nanoparticles were then characterized and directly used, as a proof of concept, to catalyse the hydrogen evolution and Suzuki coupling reactions. Under nonoptimized conditions, the fabrication process recovered >85% of Pd from solution in 26 h, suggesting the viability for this technique in recovery/recycling of metals.

4.3 Experimental

All chemicals used were obtained commercially and used without further purification, namely, palladium chloride (99.99%, Sigma-Aldrich), potassium chloride (99.0–100.5%, Alfa Aesar), potassium sulfate (99.0%, Alfa Aesar), sulfuric acid (95.0–98.0%, Sigma-Aldrich), hydrochloric acid (37.0%, Honeywell), and 50 nm-diameter CB nanoparticles (Fuel cell store). All solutions were made using ultrapure water of resistivity =18.2 MΩ cm (MilliQ, Millipore).

4.3.1. Electrochemistry

Electrochemical experiments were performed using a three-electrode cell in a Faraday cage. The working electrodes used were a glassy carbon macroelectrode (GC, 3 mm diameter, BASi Inc) and carbon fibre (CF) microelectrodes of diameters 33 µm (ALS Inc.) and 9 µm (made in-house using pitch-derived CF from Goodfellow Cambridge Ltd). All working electrodes were thoroughly polished with 3 µm diamond paste and alumina suspensions of 1, 0.3, and 0.05 µm sequentially, on a microcloth pad (all from Buehler Inc., USA). A saturated calomel electrode (SCE, ALS Inc) was used as a reference electrode and a graphite rod (3 mm diameter, Goodfellow Cambridge Ltd.) as the counter electrode. For impact studies, the SCE reference electrode was placed in a separate fritted compartment to prevent cross-contamination. Unless otherwise stated, a solution containing 0.01 M potassium chloride, 0.01 M hydrochloric acid, and 0.5 mM palladium (II) chloride was used.

In the reaction solution containing 0.5 mM of $PdCl_2$ and 0.02 M of HCl, the most prominent palladium species are: $[Pd(H_20)_6]^{2+}$, $[Pd(H_20)_5Cl]^{+}$, $[Pd(H_20)_4Cl_2]$, $[Pd(H_20)_3Cl_3]^{-}$, and $[Pd(H_20)_2Cl_4]^{2-}$ due to the relatively low chloride concentration. The approximate equilibrium concentrations of the species can be calculated via their respective stability constants,[244,245] given the mass balance requirement that the total Pd (II) and Cl^- concentrations must add up to 0.5 mM and 0.021 M respectively.

Table 8 Complexation equilibria, associated stability constants and calculated equilibrium concentrations of Pd-chloro complexes in the reaction solution. Where β_n is the accumulative complex stability constant. For more detail see Appendix A.

	$Log_{10}\beta_n$	Species	Calculated Equilibrium Concentration / mol dm^{-3}
$[Pd(H_20)_6]^{2+} + Cl^- \rightarrow [Pd(H_20)_5Cl]^+ + H_2O$	4.47	$[Pd(H_20)_5Cl]^+$	1.57×10^{-6}
$[Pd(H_20)_6]^{2+} + 2Cl^- \rightarrow [Pd(H_20)_4Cl_2] + 2H_2O$	7.74	$[Pd(H_20)_4Cl_2]$	5.68×10^{-5}
$[Pd(H_20)_6]^{2+} + 3Cl^- \rightarrow [Pd(H_20)_3Cl3]^- + 3H_2O$	10.20	$[Pd(H_20)_3Cl3]^-$	3.19×10^{-4}
$[Pd(H_20)_6]^{2+} + 4Cl^- \rightarrow [Pd(H_20)_2Cl_4]^{2-} + 4H_2O$	11.50	$[Pd(H_20)_2Cl_4]^{2-}$	1.23×10^{-4}
		$[Pd(H_20)_6]^{2+}$	2.74×10^{-9}
		Cl^-	0.0194

A bulk solution of CB NPs was prepared by adding CB NPs to ultrapure water and sonicating for 1 h before use. The desired CB NP concentration of 50 pM was prepared using aliquots of the CB NP bulk solution. Solutions were thoroughly degassed using nitrogen gas (oxygen-free, BOC Gases plc), and a nitrogen atmosphere was maintained throughout the experiments. For impact experiments, the solution was bubbled with nitrogen regularly to agitate the particle suspension and inhibit aggregation. For particle-modified GC voltammetry, the GC electrode was prepared via a drop-cast method where 5 µL of the relevant NP suspension was added to a polished GC electrode surface and allowed to dry under nitrogen.

Standard electrochemical measurements were conducted using an Autolab 128 N (Metrohm-Autolab BV, Netherlands) potentiostat controlled via a PC running NOVA 2.1 software conducting both linear

sweep voltammetry and chronoamperometry scans. Particle impact chronoamperometric scans were performed using a bespoke low noise potentiostat,[317] with a sampling rate of 100 kHz. All data were processed using a combination of Microsoft Excel and Origin Pro 2021. Unless stated otherwise, impact electrochemical data were analysed following electronic filtration (digital) at 250 Hz in order to improve the signal-to-noise ratio and facilitate analysis. Further discussion on the design of the potentiostat can be found in chapter 2.2.

For the bulk synthesis of Pd-modified carbon nanoparticles (Pd/CB) using impact electrochemistry, a polished graphite plate working electrode (6.25 cm^2) with a larger area graphite counter electrode (Alfa Aesar) and a SCE reference electrode were used. Long-term chronoamperometry (potential held at −0.1 V) was conducted in 500 mL of palladium solution with 20 nM 50 nm CB NPs to produce Pd/CB NP samples that had been modified for 168 h for imaging and testing for catalytic activity. The reacted Pd/CB samples were filtered using 0.02 µm anodisc membrane filters (Cytiva) and repeatedly rinsed with ultrapure water before drying. An analogous experiment was conducted for 24 h to fabricate Pd/CB nanoparticles which were tested electrocatalytically via the hydrogen evolution reaction (HER) by drop casting 5 µL (giving a catalyst mass loading of 8.5 g m^{-2}) onto a bare GC electrode.[226,317] To prepare the three catalyst inks, unmodified CB NPs, Pd/CB NPs (modified via impacts), and commercial 10% Pd on CB nanoparticles (Sigma-Aldrich) were added to ultrapure water respectively. This was followed by the addition of Nafion™ dispersion D1021 (Fuel Cell Store) to each catalyst ink to achieve 10% of total mass (i.e., carbon plus Pd). Cyclic voltammetry (CV) scans were then conducted at 100 mV s^{-1} in a solution of 0.01 M H_2SO_4 and 0.09 M K_2SO_4 in the potential window of 1.0 to −1.7 V vs. SCE using a graphite rod as the counter electrode.

To analyse the rate of Pd recovery, experiments were conducted for 26 h, as above, with and without the addition of CB NPs where the nitrogen flow rate was kept constant at 5 L min^{-1}, and 3 mL aliquots were extracted at designated time intervals. The samples were filtered and diluted with ultrapure water for inductively coupled plasma optical emission spectrometry (ICP-OES) using a PerkinElmer

Optima 8000. A calibration curve was generated with a 10 ppm multielement calibration standard for ICP (Agilent), in ultrapure water at concentrations of 5–0.01 ppm (see Appendix B). The samples were then analysed, and the concentration of palladium was read from the calibration curve which has an upper concentration limit of 500 ppm.

4.3.2. Material Characterization of Pd-Modified CB NPs

Modified and unmodified CB nanoparticle samples were characterized using environmental scanning electron microscopy (ESEM) with energy-dispersive X-ray spectroscopy (EDX), transmission electron microscopy (TEM) with EDX, X-ray photoelectron spectroscopy (XPS) analysis, and inductively coupled plasma mass spectrometry (ICP-MS). For the ESEM/EDX characterization, 5 mg of CB nanoparticle samples were added to the surface of carbon tape (Agar Scientific) and then analysed using a Philips XL30 FEG ESEM. For TEM, samples were drop-cast onto grids and imaged using a JEM-2100F Field Emission Electron Microscope operated at 200 kV, equipped with a Gatan Orius SC1000 CCD camera (performed at NMRC, University of Nottingham). HAADF-STEM data were acquired using JEOL DF detectors, and EDX data were acquired using an Oxford Instruments X-Max 80 EDX detector. For the XPS characterization, the samples were analysed (at NMRC, University of Nottingham) using a Kratos Liquid Phase Photoelectron Spectrometer (LiPPS, in dry sample mode) with monochromated Al Kα X-ray source (1486.6 eV). This was operated at 10 mA emission current and 12 kV anode potential (120 W). For the wide scan, a pass energy of 80 eV was used (run with a step size of 0.5 eV) while the high-resolution scan was conducted with a pass energy of 20 eV (with a step size of 0.1 eV). Data processing was conducted using CASAXPS software (version 2.3.20) with Kratos sensitivity factors (RSFs) to determine the atomic percentage values from the peaks.

For the ICP-MS analysis, three samples were dissolved in aqua regia, then diluted using ultrapure water to obtain 1% aqua regia at a concentration of 1 ppm (CB content) and filtered with 0.45 µm syringe filters (Starlab Group Ltd). The samples were then analysed using ICP-MS (Nexion 300X ICP-MS,

PerkinElmer) with a limit of detection of 10 ppt. A calibration curve was generated as described for the ICP-OES analysis ranging from 1 ppb to 1 ppm.

Thermogravimetric analysis (TGA) (sample weight 8.61 mg) was performed using NETZSCH TG 209 F1 in an aluminium oxide crucible at a heating rate of 10 °C min^{-1} from 25 to 900 °C under nitrogen purging (10 mL min^{-1}), and sample weights were additionally measured using the nanobalance (Sartorius) before and after thermal treatment.

4.3.3 Catalysis of the Suzuki Coupling Reaction

For the Suzuki coupling reaction, a solution of 184 mg of phenylboronic acid (≥97.0%, Sigma-Aldrich), 426 mg of potassium phosphate tribasic (≥ 98.0%, Sigma-Aldrich), and 20 mL of ultrapure water was added to a three-necked round bottom flask and stirred (450 rpm) for 20 min. To this mixture 115 µL of iodobenzene (98.0%, Sigma-Aldrich) and ca. 30 mg of Pd-modified carbon nanoparticles were added while stirring. The mixture was stirred and refluxed in a silicone oil bath at 80 °C for 6 h. After cooling, the organic phase was extracted three times using 20 mL of ethyl acetate (Sigma-Aldrich) and then dried using anhydrous sodium sulphate (Sigma-Aldrich). The sodium sulphate was removed from the organic phase using 5–13 µm filter paper (Fisherbrand), and then the ethyl acetate was evaporated. The powdered sample was dissolved in $CDCl_3$ for 1h NMR analysis using a Bruker 400 MHz NMR spectrometer where four scans were conducted with an acquisition time of 4.7 s and relaxation delay of 2 s. Data were analysed using Mestrenova software (version 14.0.0).

4.4 Results and discussion

4.4.1 Impact Deposition of Pd onto CB Nanoparticles

First, preliminary experiments were performed to confirm the deposition of Pd onto carbon surfaces and to determine at which potentials the deposition onto CB NPs during impacts might occur. To do this, the deposition of Pd from a solution containing 0.5 mM $PdCl_2$, 0.01 M KCl, and 0.01 M HCl was investigated using macroelectrode CV at a voltage scan rate of 100 mV s^{-1} to determine the onset

potential on the bare GC electrode, where onset is defined here as the potential at which the measured current density was −0.5 mA m^{-2}.[223-225]

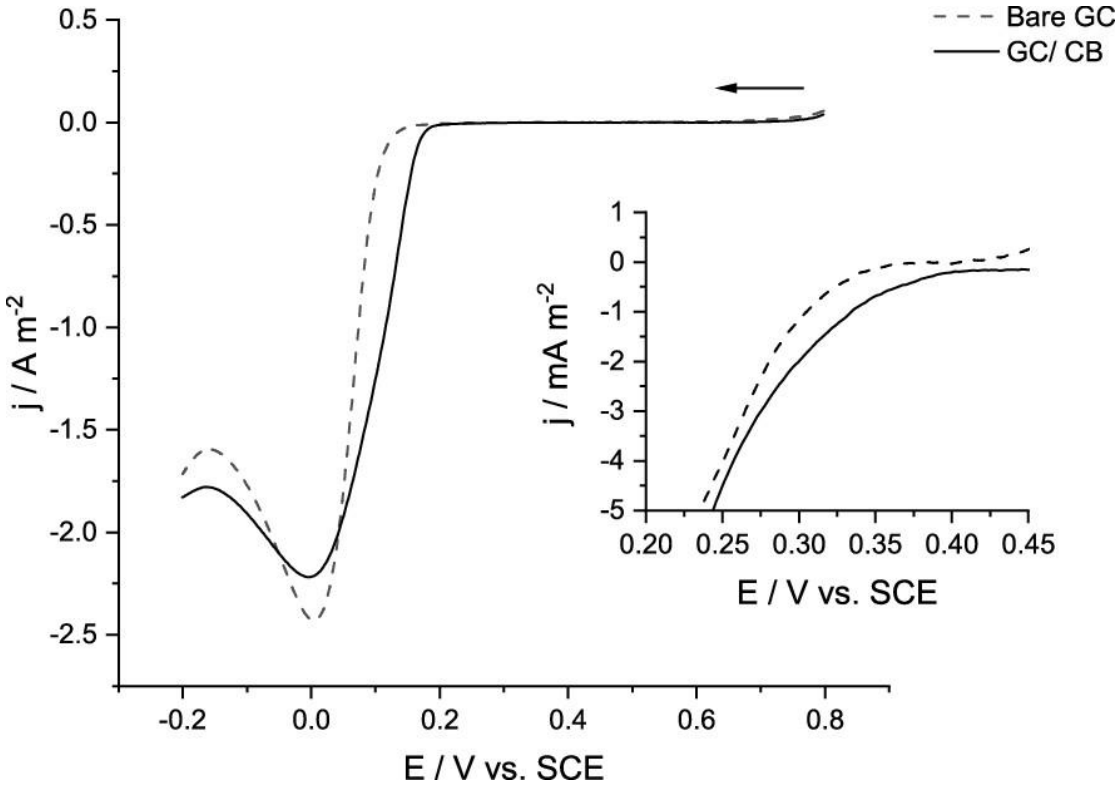

Figure 36 Reductive voltammetric scans of Pd deposition from a solution of 0.5 mM PdCl2, 0.01 M KCl, and 0.01 M HCl onto the surface of 3 mm bare GC (·····) and 50 nm CB NP-modified GC (–) electrode where the inset shows the magnified onset potentials where Pd deposition commences. The voltage scan rate was 100 mV s^{-1} for all scans.

Figure 36 shows the reductive segments of CV scans showing the deposition of palladium on the surface of 3 mm bare GC and 50 nm carbon black-modified GC electrodes. The CB-modified GC electrode was prepared via a drop-cast method where 5 µL of the CB NP suspension was added to a polished GC electrode surface and allowed to dry, resulting in a surface (particle) concentration of 66 pmol m^{-2}. The deposition of palladium is known to be a two-electron transfer:[271,318]

$$Pd^{2+} + 2e^{-} \rightarrow Pd \qquad \text{Equation 103}$$

where the nucleation mechanism and morphology of the deposited Pd are influenced by deposition conditions such as applied potential and Pd concentration. The literature records the bulk deposition process to occur at potentials lower than ca. +0.3 to +0.4 V (vs SCE) depending on the carbonaceous

material.[308,319] This is in good agreement with the recorded data (Figure 36) showing the onset at +0.29 V (vs. SCE) for the bare GC and +0.38 V (vs. SCE) on the CB NP-modified GC. The proximity of these onset potentials suggests that it is unlikely that Pd will deposit onto CB NPs during impacts without some degree of background deposition onto the substrate GC electrode. It has previously been shown that at more positive potentials (lower overpotential) the electro nucleation of Pd occurs via a 3D instantaneous mechanism while more negative potentials (higher overpotential) result in a 3D progressive nucleation mechanism[308,320,321]

Having determined the onset potentials for Pd deposition on GC and CB NPs under these conditions, chronoamperometric scans were conducted in the presence and absence of nanoparticles to investigate whether transient impact events occurred. The chronoamperometric scans were conducted using a three-electrode cell in a 0.5 mM palladium solution (as described previously) where either a 9 µm or a 33 µm diameter CF electrode acted as the substrate surface.

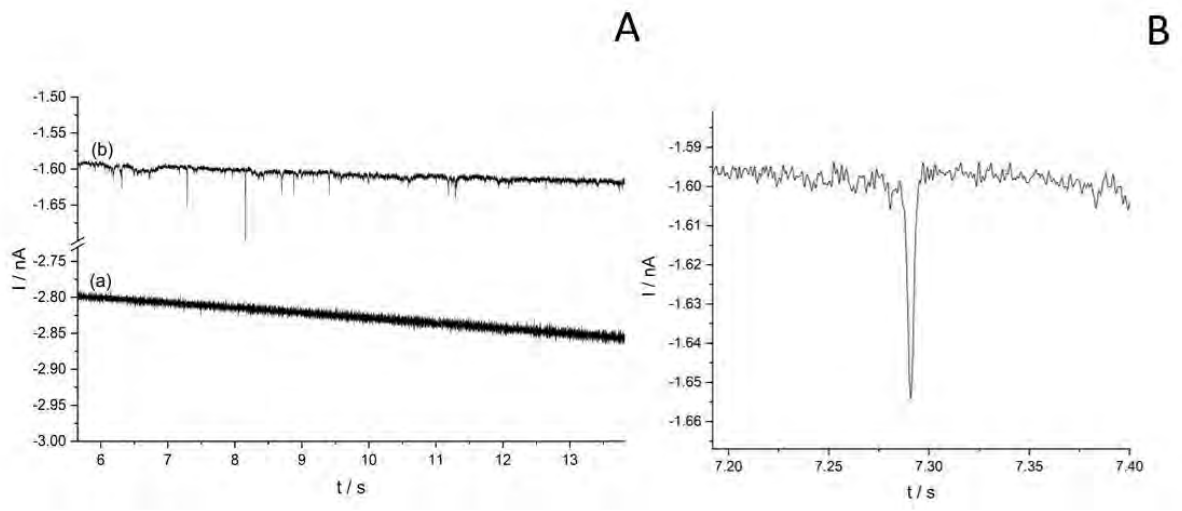

Figure 37A Typical segments of chronoamperometric scans conducted at −0.1 V vs. SCE using a 9 µm CF electrode: (a) before and (b) after the addition of 50 pM 50 nm CB nanoparticles to a solution of 0.5 mM $PdCl_2$, 0.01 M KCl, and 0.01 M HCl. Figure 37B shows the magnified reductive signal from scan (b) at t = 7.29 s.

Figure 37A displays two chronoamperometric scans conducted using a 9 µm CF microelectrode at −0.1 V vs SCE before (a) and after (b) the addition of CB nanoparticles, where scan (a) acts as the controlled

experiment and is void of reductive peaks. Upon the addition of nanoparticles, peaks were observed indicating the deposition of palladium onto the CB NPs upon impact. At this potential, Pd deposition may occur at CB NPs as well as the substrate GC electrode (see Figure 36), and so the measured currents reflect the capacitance of the GC substrate as well as any faradaic currents because of Pd deposition. The difference in currents of (a) and (b) is ascribed to fluctuations because of natural convection given the length of each chronoamperometric scan. Impact studies were conducted on both 9 and 33 µm CF electrodes: the former was used predominantly for potentials close to the onset of deposition, where transient signals were small, and optimal signal-to-noise ratios were required. Although the smaller electrode provided lower noise levels due to lower capacitance, its smaller area also led to less frequent transient signals. Hence, larger microelectrodes were used at more reductive potentials with the associated benefit of a larger surface area thus a higher number of transient events. This provides a greater quantity of data more rapidly, however, this also resulted in a higher background current thus decreasing the signal to noise ratio.

Figure 37A displays two chronoamperometric scans conducted using a 9 µm CF microelectrode at −0.1 V vs SCE before (a) and after (b) the addition of CB nanoparticles, where scan (a) acts as the controlled experiment and is void of reductive peaks. Upon the addition of nanoparticles, peaks were observed indicating the deposition of palladium onto the CB NPs upon impact. At this potential, Pd deposition may occur at CB NPs as well as the substrate GC electrode (see Figure 36), and so the measured currents reflect the capacitance of the displays typical examples of unfiltered peaks isolated from chronoamperometry scans conducted at the same potential (-0.1V vs. SCE). Analysis of the peaks conducted with 50 pM of 50 nm CB NPs on the 9 µm and 33 µm CF electrodes using the unfiltered data indicated individual peaks were virtually identical in height with an average peak current of (-0.13 ± 0.03) nA and (-0.11 ± 0.07) nA respectively.

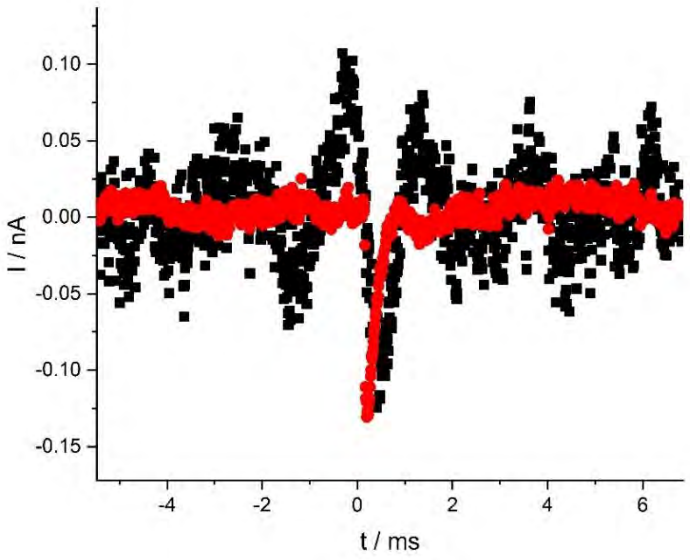

Figure 38 unfiltered peaks conducted on a 9 µm (•) and 33 µm (▪) carbon fibre electrodes during a 30 s chronoamperometric scan held at -0.1 V vs. SCE. The peaks have been time and background current corrected to show the similarity in peak heights occurring on a 9 µm and 33 µm CF electrode. All scans were conducted in a solution containing 0.5 mM $PdCl_2$, 0.01 M KCl and 0.01 M HCl.

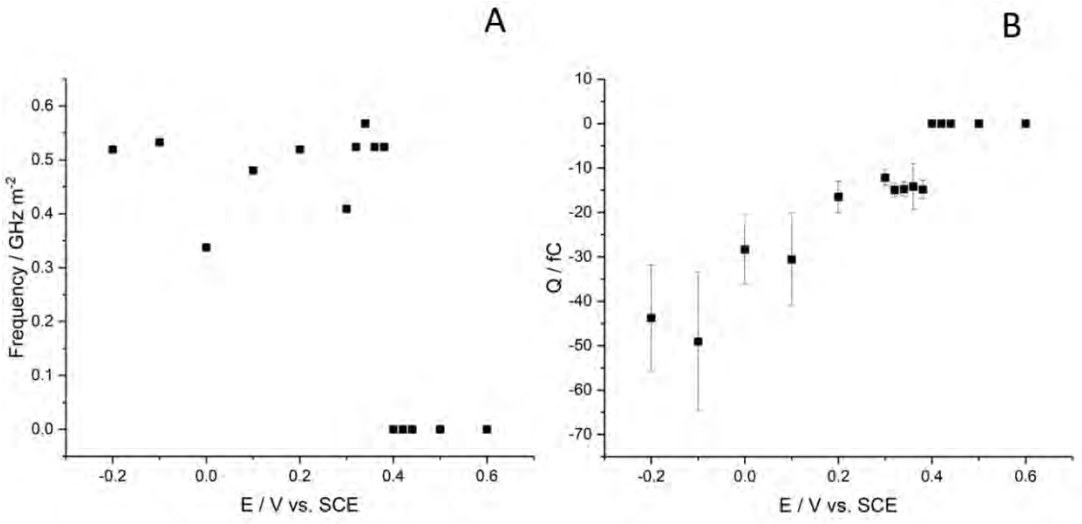

Figure 39A shows the frequency of reductive transient peaks detected during 30 s chronoamperometric scans at different potentials ranging from +0.6 to −0.2 V vs SCE using both 33 and 9 µm CF electrodes. Figure 39B displays the mean calculated charge passed during transient deposition events analysed using unfiltered peaks. All scans were conducted in a 5 mL solution of 0.5 mM $PdCl_2$, 0.01 M KCl, and 0.01 M HCl.

Further impact studies were conducted by performing multiple chronoamperometric scans using 50 pM CB NPs at potentials between +0.6 and −0.2 V vs SCE. The impact frequency was determined at

each potential by dividing the total number of observed impact signals by the total time of all scans, as seen in Figure 39A and was in the range of 0.34–0.57 GHz m^{-2} (within the literature a frequency range of 0.7–3.7 GHz m^{-2} is documented for metal deposition impacts using *ca*. 20 pM metallic cores.[163,317] From Figure 39A, reductive peaks can be observed at potentials negative of +0.4 V vs SCE, consistent with the onset observed in Figure 36. At all potentials, the impact signals had a similar duration, indicating that deposition of Pd occurred during approximately elastic collisions with the electrode (if deposition occurred at NPs that had pre-adsorbed to the GC surface, then step-like signals would be observed, see Figure 16 for a schematic). The role of pre-adsorbed Pd^{2+} is less straightforward to quantify and may well prove to be key to electrodeposition during impacts, especially where reduction kinetics may be less than reversible.

Similar to the copper study, the integration of the CB NP reductive transients produced the charge associated with Pd deposition on individual nanoparticles (Equation 97). Figure 39B shows the average charge of impacting CB NPs at different potentials ranging from +0.6 to −0.2 V vs SCE where at potentials more reductive than +0.4 V, charge ranging from −12.2 to −49.0 fC is observed, seemingly increasing with increased overpotential. The theoretical Pd coverage can be calculated based on the charge transferred during impacts using Equation 9 where r = 2.10 Å the palladium atomic radius.[231] An example of this calculation is shown in Table 9 using a peak isolated on a chronoamperometry scan conducted at -0.1 V vs. SCE. For this example, a charge of -4.02×10^{-14} C was determined resulting in a coverage equivalent of 300%. Figure 39B shows at +0.38 V (vs SCE) an average charge of −14.8 ± 2.1 fC corresponds to a coverage of 110 ± 15%, increasing to 365 ± 116% at a more reductive potential of −0.1 V (vs. SCE) where the charge was −49.0 ± 15.6 fC.

Table 9 Example calculation of palladium coverage on the surface of CB NPs. The calculated values for the NP surface area, reductive peak charge, number of Pd deposited, number of Pd in monolayer and coverage equivalent are shown. This calculation was conducted using unfiltered raw peak data.

Parameter / unit	CB NP (-0.1 V vs. SCE)
S / m^2	7.85×10^{-15}
Q / C	-4.02×10^{-14}
N	1.26×10^{5}
N_{mono}	4.20×10^{4}
θ / %	300

4.4.2 Characterization of Pd-Modified CB NPs

To confirm palladium deposition on the CB nanoparticles, a 24 h impact experiment was conducted using a graphite plate electrode (area 6.25 cm^2) held at a potential of −0.1 V (vs SCE) in 500 mL of a solution containing 0.5 mM $PdCl_2$, 0.01 M KCl, and 0.01 M HCl. The upscaling of the experiment was required to produce sufficient mass of impacted CB NPs to analyse. A concentration of 20 nM CB NPs was added to the solution and agitated continually with a nitrogen gas stream for the 24 h period. An analogous experiment was conducted at +0.6 V vs SCE, where no transient impact peaks due to Pd reduction were expected. The two samples held at −0.1 V and +0.6 V were rinsed thoroughly with deionized water during filtration using 0.02 µm anodisc inorganic membrane filters before drying.

The samples in addition to unmodified CB NPs were characterized using ESEM/EDX and ICP-MS with results shown in Table 10. The ESEM/EDX analysis indicated that no palladium was detected in the unmodified sample, as expected as it had not been in contact with the $PdCl_2$ solution. The sample held at −0.1 V exhibited the highest average weight % ratio Pd/C of 0.09 ± 0.009 followed by the sample held at +0.6 V with an average weight % ratio Pd/C of 0.03 ± 0.005. Analysis by ICP-MS showed a similar trend with the measured Pd concentration of 0.01, 2.75, and 17.67 ppm for the samples of unmodified CBNPs, held at 0.6 V vs SCE during chronoamperometry and at −0.1 V vs SCE, respectively.

Table 10 SEM Image of Aggregated CBNPs Obtained from a 24 h Chronoamperometric Scan Conducted at −0.1 V (vs SCE) in a Solution of 0.5 mM $PdCl_2$, 0.01 M KCl, and 0.01 M HCl. The table displays palladium content determined by SEM/ EDX and ICP-MS analysis of the unmodified CBNPs, the sample held at +0.6 V vs SCE during chronoamperometry, and the sample held at −0.1 V vs SCE.

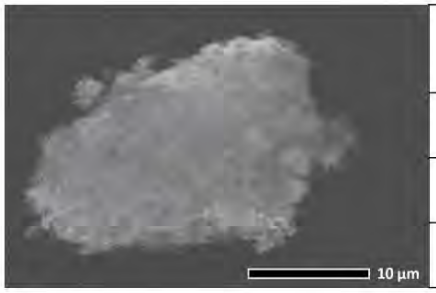

CBNP Samples	SEM/ EDX Average weight% ratio Pd/CB	ICP-MS Pd Conc. (ppm)
Unmodified	0	0.01*
0.6V vs. SCE	0.03 ± 0.005	2.75
-0.1V vs. SCE	0.09 ± 0.009	17.67

*Measurement equivalent to zero within error.

The Pd detected in the sample held at +0.6 V reflects the residual trace adsorbed palladium (II) left after the washing procedure. This level of Pd (II) appears to remain regardless of the extent of washing, suggesting adsorption to the CB surface, possibly via oxygen moieties. To further analyse the samples and determine the oxidation state of the Pd detected, XPS analysis was conducted on +0.6 and −0.1 V modified samples, shown in Figure 40. The data suggest that trace palladium was detected on the unmodified sample similar to results determined by the ESEM/EDX and ICP-MS analysis. The Pd 3d XPS characterization of the sample held at −0.1 V vs SCE indicated the presence of both Pd^0 and Pd^{2+}, with the latter associated with both $PdCl_2$ and PdO. The peak with a lower binding energy (Pd $3d_{5/2}$) of 335.49 eV is assigned to the metallic palladium (Pd^0) content while the peaks with a binding energy of 336.14 and 338.10 eV indicate the presence of PdO and $PdCl_2$ respectively.[322-328]The presence of Pd^0 suggests that during impact events the potential was sufficiently negative to facilitate the reduction of Pd^{2+} to Pd^0, which may have later (partially) oxidized to form PdO. Analysis of the sample held at +0.6 V vs SCE demonstrated the presence of Pd^{2+} as $PdCl_2$ (with binding energies 337.94 and 343.96 eV) but no Pd^0. This supports the earlier conclusion from the ESEM/EDX and ICP-MS data that

some residual $PdCl_2$ persisted after washing and no palladium deposition had occurred during collision at +0.6 V vs SCE.

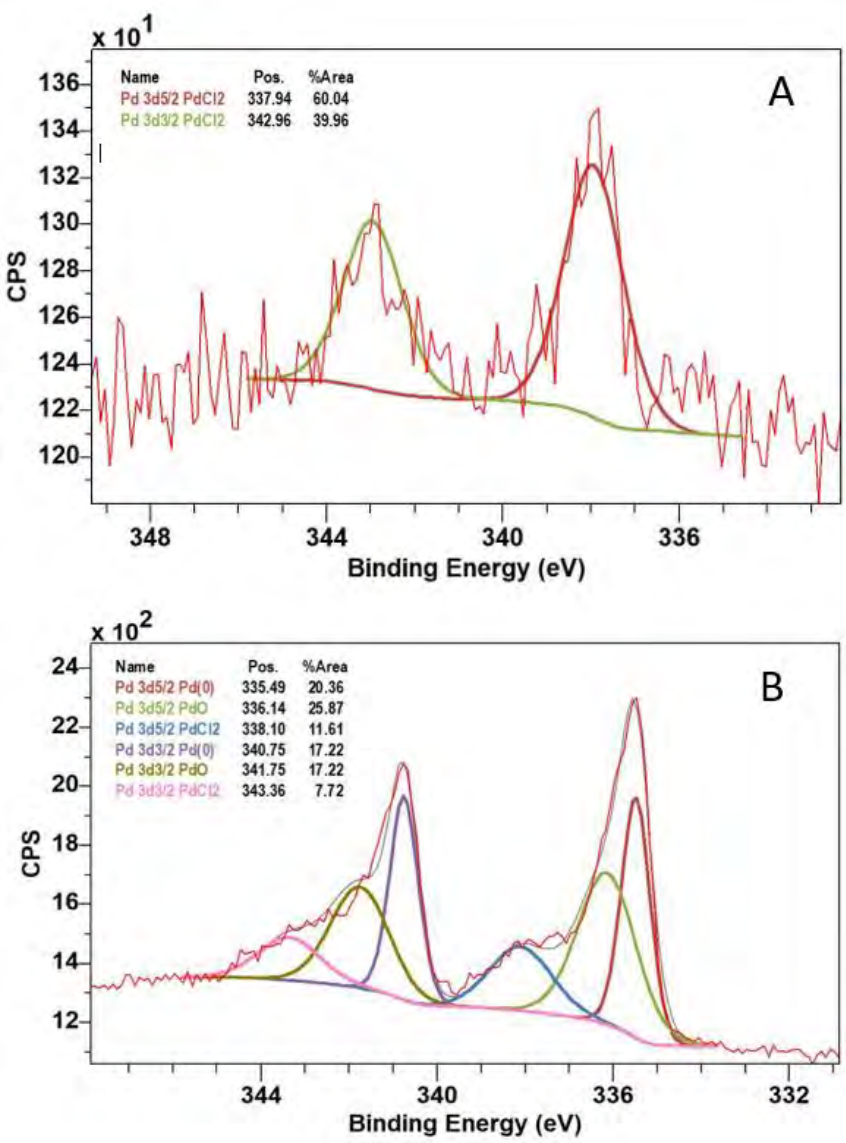

Figure 40 XPS spectra (Pd $3d_{5/2}$ and Pd $3d_{3/2}$) of (A) +0.6 V vs SCE modified CB NPs and (B) −0.1 V vs SCE modified CB NPs where the peaks with a binding energy of 335.49 eV (Pd $3d_{5/2}$) and 340.75 eV (Pd $3d_{3/2}$) indicate Pd^0.

4.4.3 Synthesis and Testing of Pd/CB NP Catalysts

To sufficiently scale-up the quantity of Pd/CB NPs fabricated for testing in the hydrogen evolution and Suzuki coupling reactions, a batch of Pd/CB NPs was produced from a longer-term, 24 h, and 168 h deposition experiment (section 4.3.1). Thermogravimetric (TGA) analysis was conducted on the Pd

modified CB NPs obtained from the 168h impact investigation. This was conducted by heating the sample in an aluminium oxide crucible at a heating rate of 10 °C min^{-1} from 25 to 900 °C under nitrogen purging at 10 mL min^{-1}. Figure 41 shows the thermogram obtained which suggested that the Pd/CB NPs contained 14% by mass of Pd.

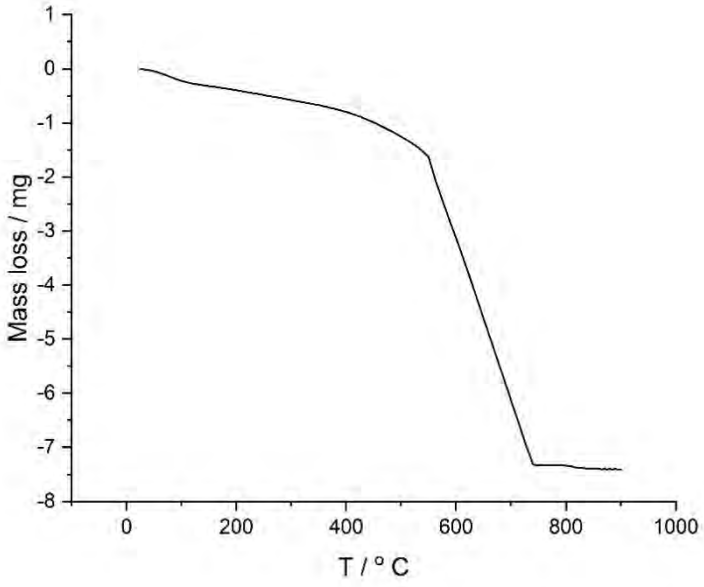

Figure 41 TGA thermogram of the 168-hr palladium modified carbon nanoparticles. From this, a 13.9% palladium coverage was determined based on a mass change from 8.6 mg to 1.2 mg upon reaching 900 °C.

The TEM images (Figure 42A-F) further highlighted the presence of palladium metal on some particles evident in the contrasting darker regions seen on the carbon core, confirmed with EDX mapping (Figure 43). Deposition did not occur consistently across all Pd/CB NPs as some CB NPs were void of Pd suggesting that not all CB NPs collided with the GC electrode during the investigation or alternatively some collisions resulted in little to no Pd deposition.

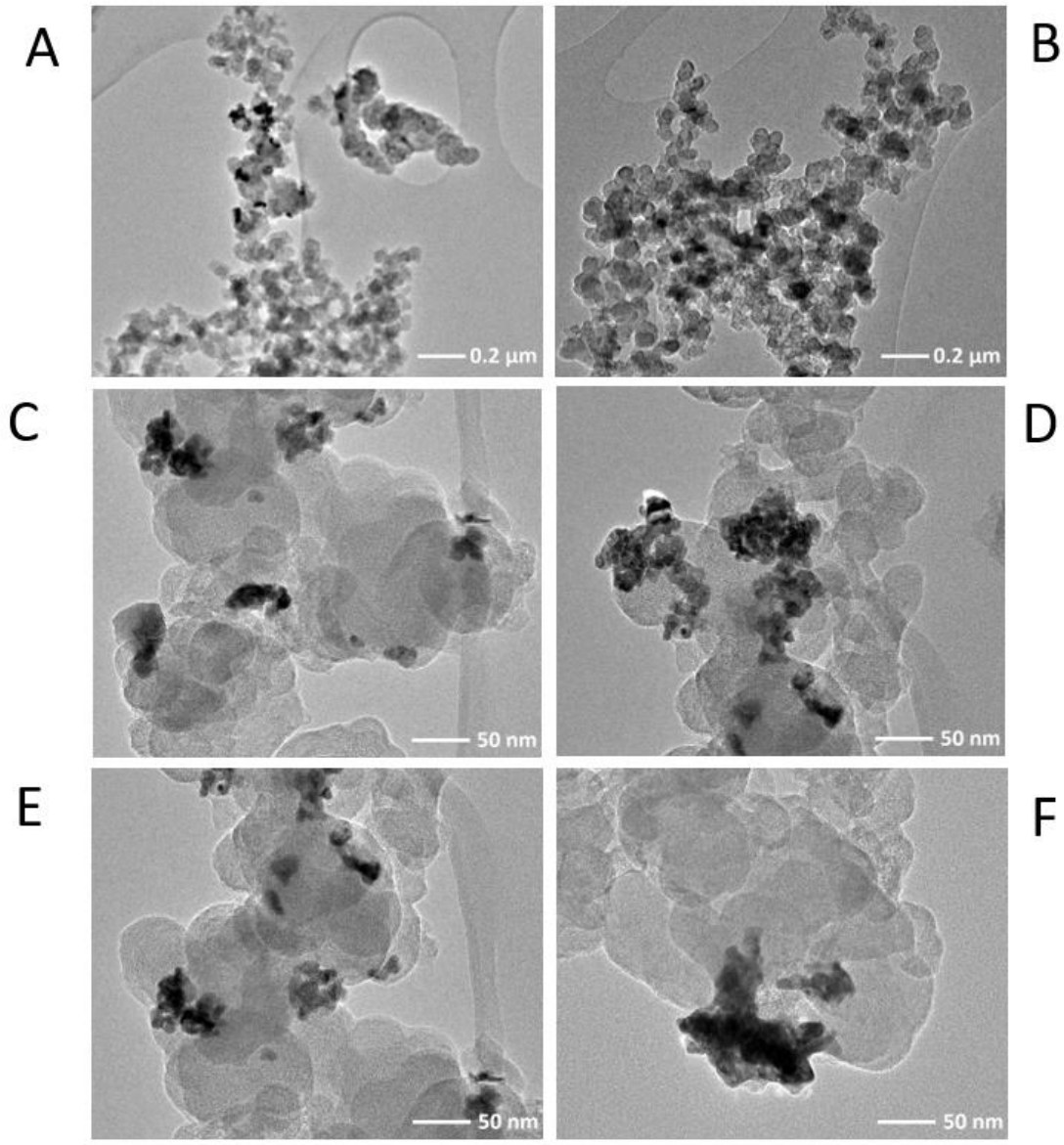

Figure 42 Typical TEM images (A–F) of the 168-h palladium-modified carbon nanoparticles where the darker regions represent deposited Pd metal.

Figure 42 (TEM images of the impacted particles) suggests that the Pd deposits formed were not singular nanoparticles evenly distributed across the surface of the CB particles, but rather deposits covering sections of the impacting particle. Using the tilt function of the TEM, it was observed that these growths followed the curvature of the carbon particle rather than directly protruding out from the particle surface (Figure 42D), and future work will explore further details of the Pd deposition to shed light on the mechanism of metal deposition during impact.

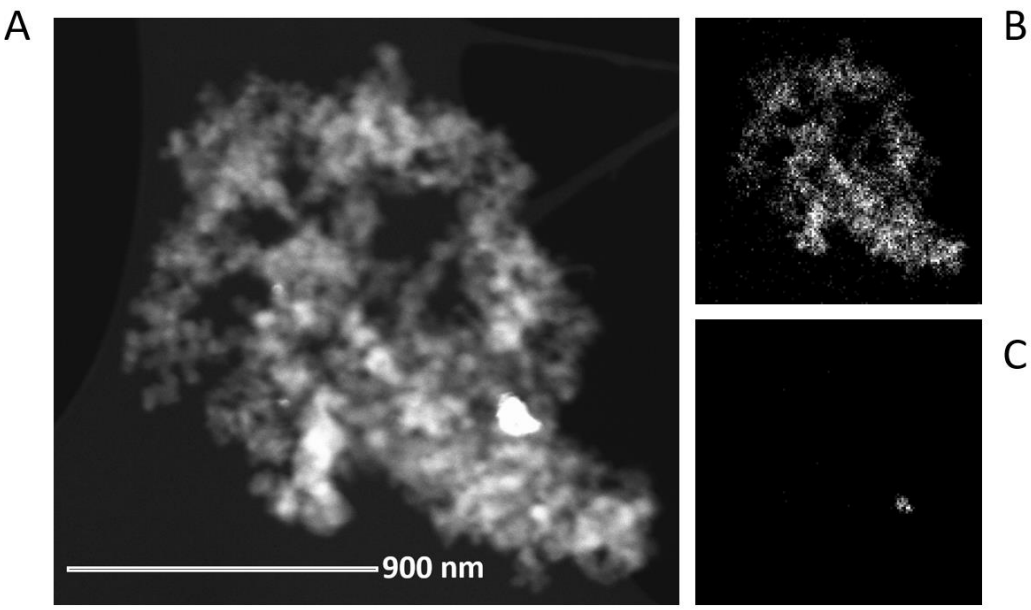

Figure 43A TEM showing an agglomerated Pd/CB NPs where the CBNPs (B) and Pd deposition (C) have been identified using EDX mapping.

As a simple test of the catalytic capabilities of the Pd/CB NPs as catalysts without further treatment, samples were used for both hydrogen evolution and Suzuki coupling reactions. For the HER, 24 h modified Pd/CB NPs were compared with commercial 10 wt % Pd on CB catalyst. The 3 mm GC working electrodes were prepared by dropcasting Pd/CB NPs onto the electrode surface before performing cyclic voltammetry in a solution of 0.1 M H_2SO_4 and 0.09 M K_2SO_4 in a three-electrode cell with a SCE reference and a graphite rod counter electrode. Figure 44 shows initial 100 cycle electrochemical cleaning scans performed at a scan rate of 500 mV s^{-1} between 0.80 V to -0.27 V vs. SCE before conducting HER CVs to remove surface contaminants shows the resulting voltammograms recorded using GC electrodes which were modified with CB NPs, Pd/CB NPs, and commercial 10% Pd/CB catalyst where the characteristic proton reduction profile for both the commercial standard and the impact synthesized sample can be observed.

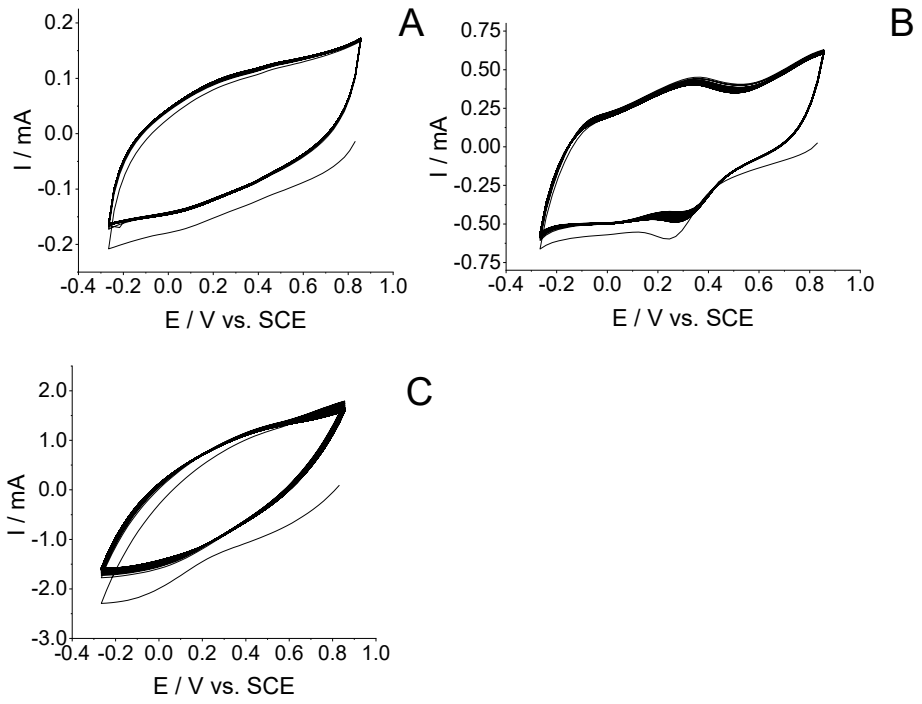

Figure 44 The 100 cycle CV cleaning scans conducted for (A) unmodified CBNPs/ GC, (B) -0.1 V vs. SCE modified GC and (C) commercial 10% Pd modified CBNPs/ GC. A scan rate of 500 mV s^{-1} was used between the potential window 0.8 V to -0.27 V vs. SCE in a solution of 0.1 M sulfuric acid and 0.09 M potassium sulphate.

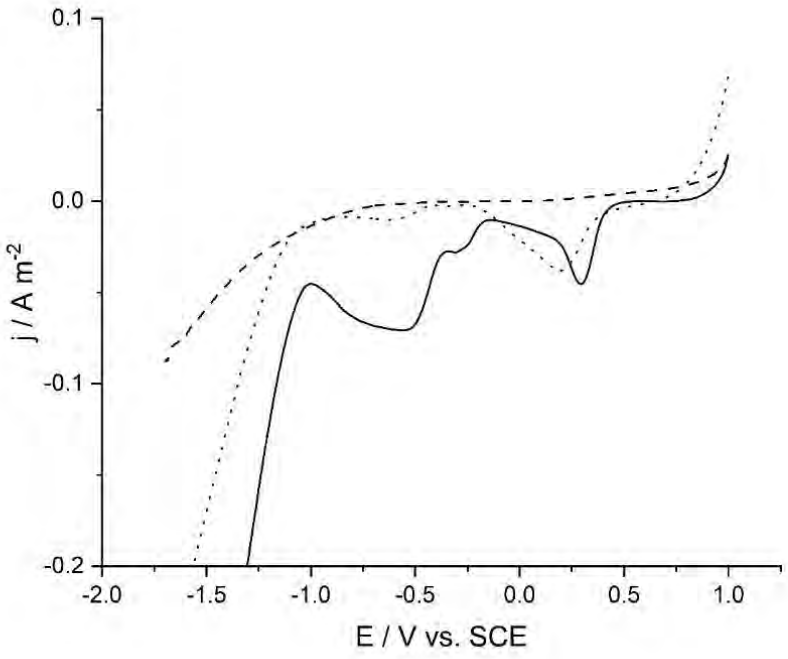

Figure 45 Reductive cyclic voltammetry scans conducted between 1.0 V to -1.7 V vs. SCE at a scan rate of 100 mV s^{-1} on the surface of unmodified CBNPs/GC (----), -0.1 V (vs. SCE) modified CBNPs/ GC (—)and commercial 10 % Pd modified CBNPs/ GC (····). This was conducted in a solution of 0.01 M H_2SO_4 and 0.09 M K_2SO_4 after an initial 100 cycle cleaning scan conducted at 500 mV s^{-1}.

Figure 45 indicates that a higher overpotential is required for the reduction of protons on the surface of the unmodified CB NPs with onset at ca. -1.0 V (vs. SCE). However, for both the Pd/CB NPs and commercial 10 % Pd/CB NPs a more positive initial peak at ca. 0.4 V (vs. SCE) associated with the reduction of oxide layers can be identified. A feature at ca. -0.2 V (vs. SCE) associated with hydrogen adsorption,[241,248,263]and the similarity of the CV response for both samples further suggests that the impact voltammetry technique was sufficiently able to modify the CB NPs at -0.1 V vs. SCE and significantly that these modified particles show electrocatalytic activity. The onset of hydrogen evolution on the Pd modified surfaces can be observed at ca. -0.3 V followed by additional HER occurring on the GC surface at -0.1 V vs. SCE.[308]

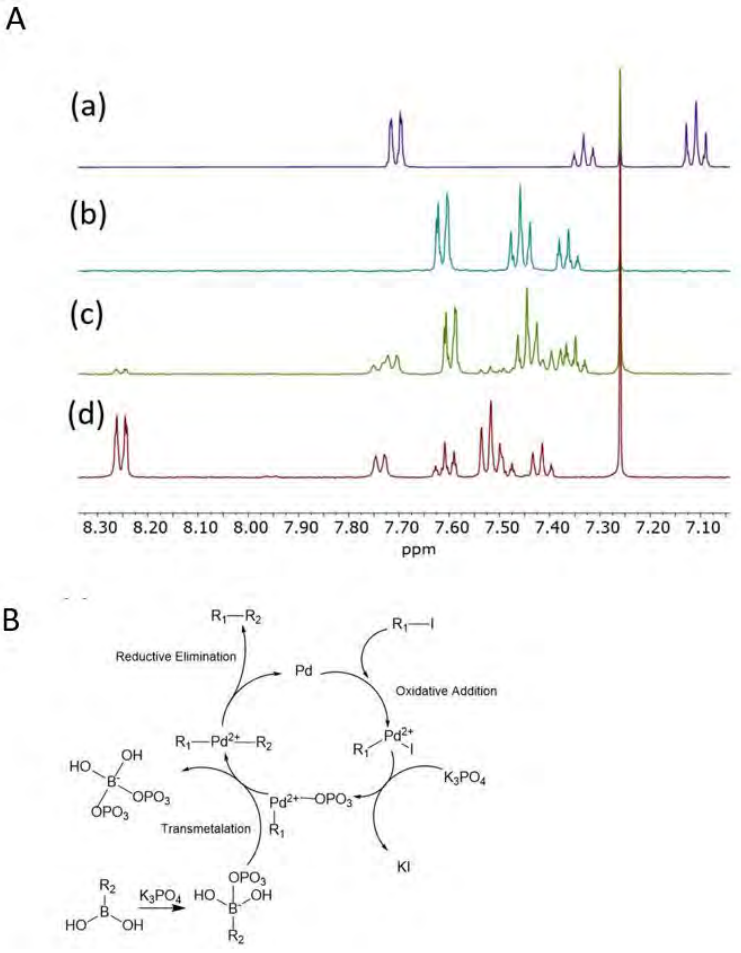

Figure 46A ^{1}H NMR spectrum of (a) iodobenzene, (b) biphenyl product taken from doi:10.13018/BMSE000506) (c) product extracted during the Suzuki reaction using Pd/CB NPs, and (d) displaying the ^{1}H NMR analysis of the benzeneboronic acid reactant used in the investigation. The ^{1}H NMR was performed using $CDCl_3$ identified by the singlet at 7.26 ppm. Figure 46B schematic of the Suzuki reaction mechanism.[317]

For the Suzuki reaction, 30 mg of 168 h modified Pd/CB NPs was used to catalyse the reaction between benzeneboronic acid (phenylboronic acid), iodobenzene, and potassium phosphate to produce biphenyl.[251,252,305]This was achieved under 80 °C reflux where the resulting product was identified using ^{1}H NMR. It should be noted that the quantity of Pd/CB NPs used is not optimized: at 14 wt % Pd this quantity of NPs provides *ca*. 4.2 mg of Pd, chosen to produce sufficient product for convenient handling and analysis.[305] It was determined that the Pd/CB NPs had successfully catalysed the reaction producing a mixture of biphenyl and residual benzeneboronic acid, evidenced by ^{1}H NMR spectra of the product mixture (Figure 46A, spectrum (c)) which indicated that the iodobenzene had reacted and was no longer present in the final product as the signals at 7.10 ppm (spectrum (a)) are no longer observed. The multiplets at 7.60, 7.45, and 7.35 ppm in both the reference spectrum (b) and the product spectrum (c) suggest the presence of biphenyl. The additional signals can be attributed to the excess benzeneboronic acid initially used in the reaction.

4.4.4 Palladium Recovery from Low Concentration of $PdCl_2$

Finally, the use of the impact method to recover Pd from solution was studied. To examine the change in $PdCl_2$ concentration during the impact deposition process, and hence Pd recovery from solution, 26 h chronoamperometric scans were conducted with and without CBNPs where a flow rate of nitrogen at 5 L min^{-1} (selected due to the range of flow rate gauges available) was maintained to ensure the same level of agitation. A 500 mL solution containing 0.01 M potassium chloride, 0.01 M hydrochloric acid, and 0.4 mM palladium (II) chloride (determined by ICP-OES) was used. The lower initial concentration determined by ICP-OES may be due to the presence of high levels of potassium ions in the samples causing a suppression of the Pd signal.[184,329] At regular intervals throughout the experiments, 3 mL aliquots were extracted and filtered with 0.45 µm syringe filters to prepare samples for ICP-OES analysis.

Figure 47A shows the percentage of Pd^{2+} recovered during a 26 h chronoamperometric scan with and without the addition of CB NPs. Figure 47A was determined by subtracting the sample concentration

from the stating concentration as determined by the ICP analysis. Figure 47B shows the depletion in Pd^{2+} concentration in logarithmic form: the NP-mediated experiment showing an enhancement in the recovery rate of a factor of approximately 1.7, for these nonoptimized conditions. Despite each individual nanoimpact resulting in the deposition of *ca*. 10^5 Pd atoms, the high number of impacts has a significant effect on the overall rate of removal of Pd from solution. Future work will seek to quantify the relationship between the experimental parameters and recovery rate.

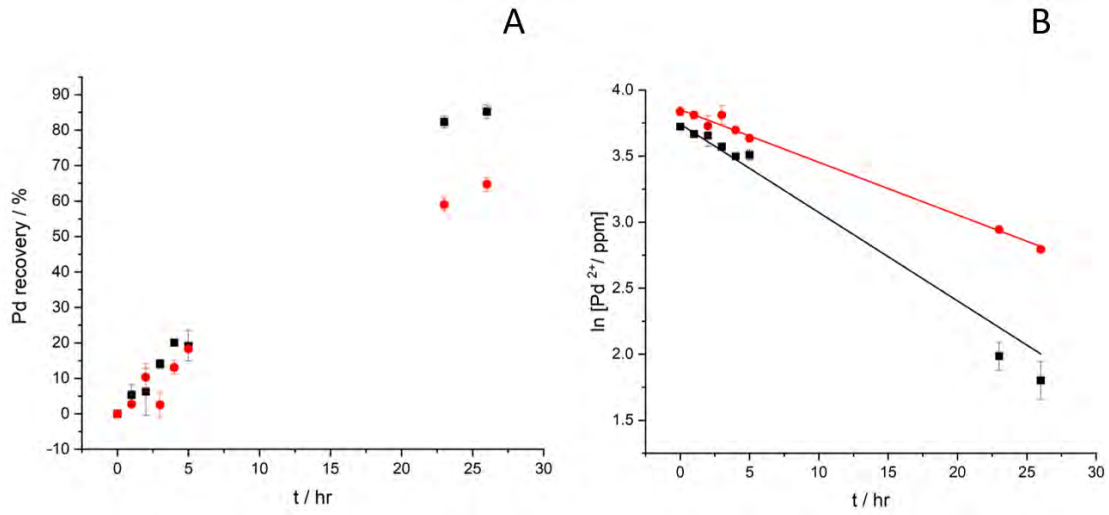

Figure 47A Percentage of Pd recovered from $PdCl_2$ during a 26 h chronoamperometric scan conducted with (■) and without (●) CB NP particles. Figure 47B ln[Pd^{2+}] vs time based on the data in Figure 47A where the best fit lines from linear regression are given by ln[Pd^{2+}/ppm] = 3.74–0.067t for (■) and ln[Pd^{2+}/ppm] = 3.85–0.04t for (●)

The deposition of palladium on the graphite substrate electrodes used during impact electrochemistry investigations (with and without nanoparticles) was studied. ESEM/EDX was used to analyse a polished graphite plate substrate electrode and electrodes after use in the 168h chronoamperometric scan.

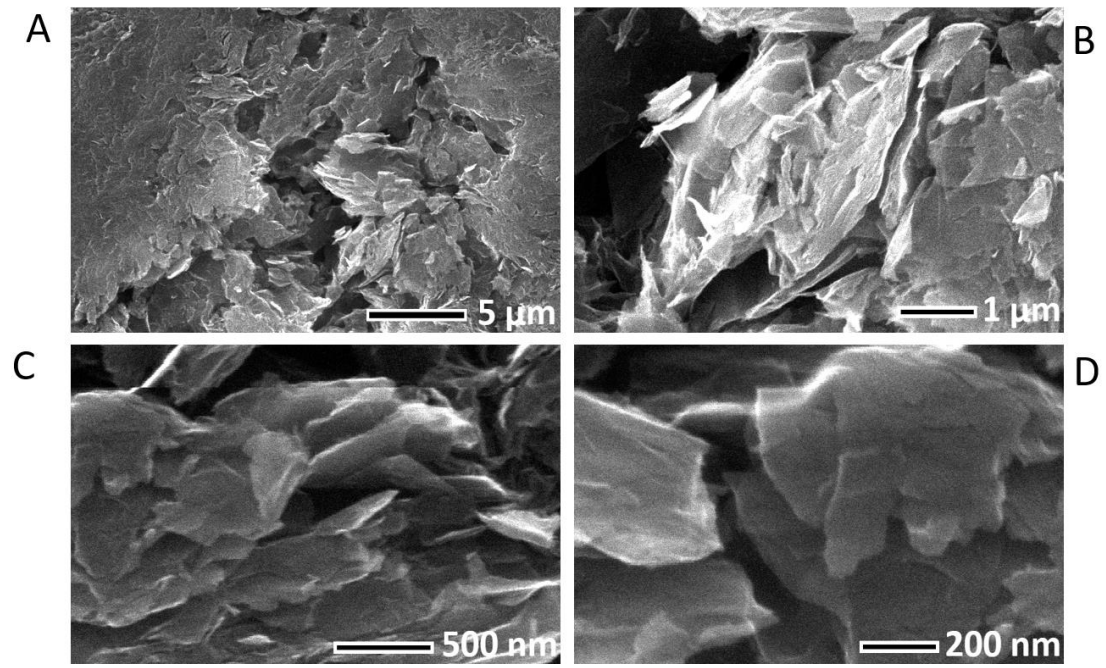

Figure 48 ESEM images of a polished graphite electrode at magnification factors of (A) 5 × 10^3, (B) 2 × 10^4, (C) 5 × 10^4, and (D) 10^5. This electrode was polished using a diamond paste 3 µm and alumina suspensions of 1 µm, 0.3 µm and 0.05 µm sequentially, on a micro-cloth pad.

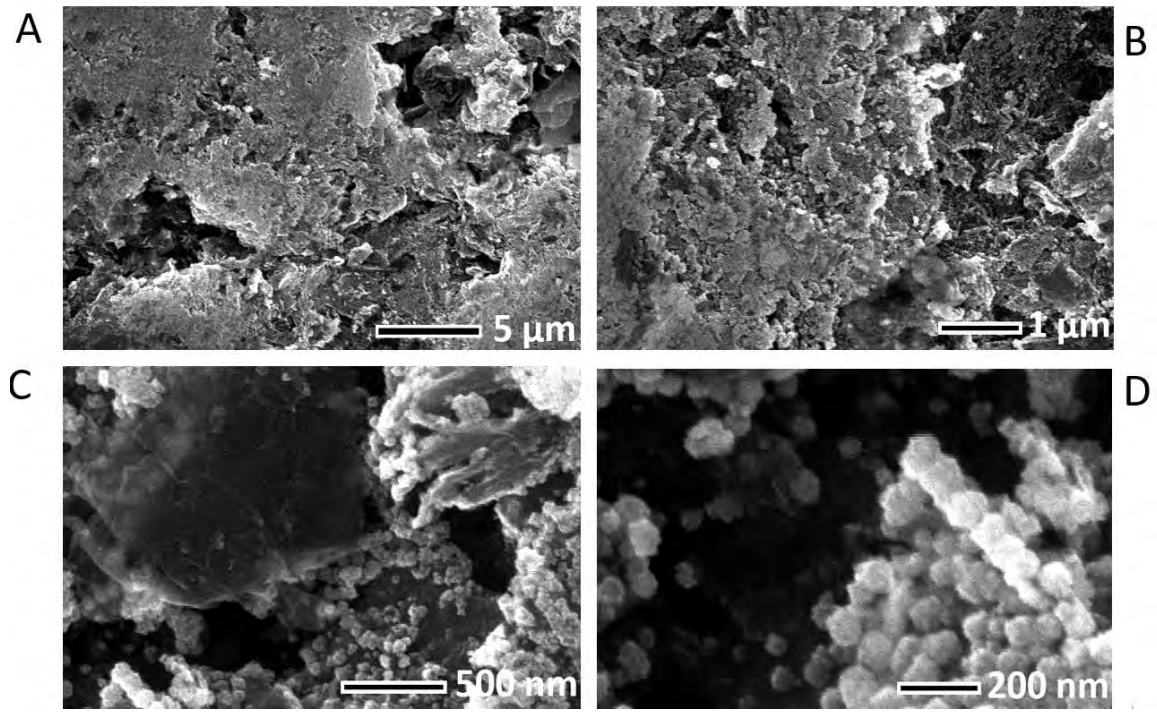

Figure 49 displays ESEM analysis of a modified graphite electrode after use in a 168 h chronoamperometry scan at magnification factors of (A) 5 × 10^3, (B) 2 × 10^4, (C) 5 × 10^4, and (D) 10^5. The chronoamperometry scan was conducted at -0.1 V vs. SCE in a palladium plating solution without CB NPs.

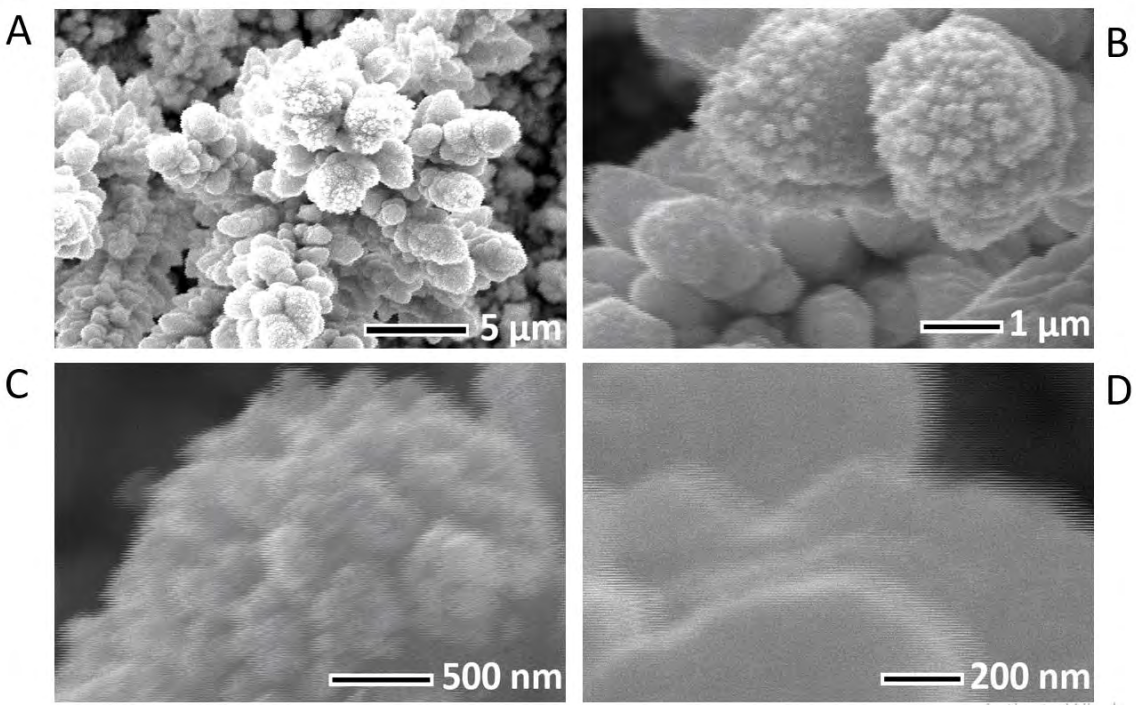

Figure 50 ESEM images of a modified graphite electrode after use in a 168h chronoamperometry scan at magnification factors of (A) 5 × 10^3, (B) 2 × 10^4, (C) 5 × 10^4, and (D) 10^5. The chronoamperometry scan was conducted at -0.1 V vs. SCE in a palladium plating solution in the presence of 20 nM CB NPs.

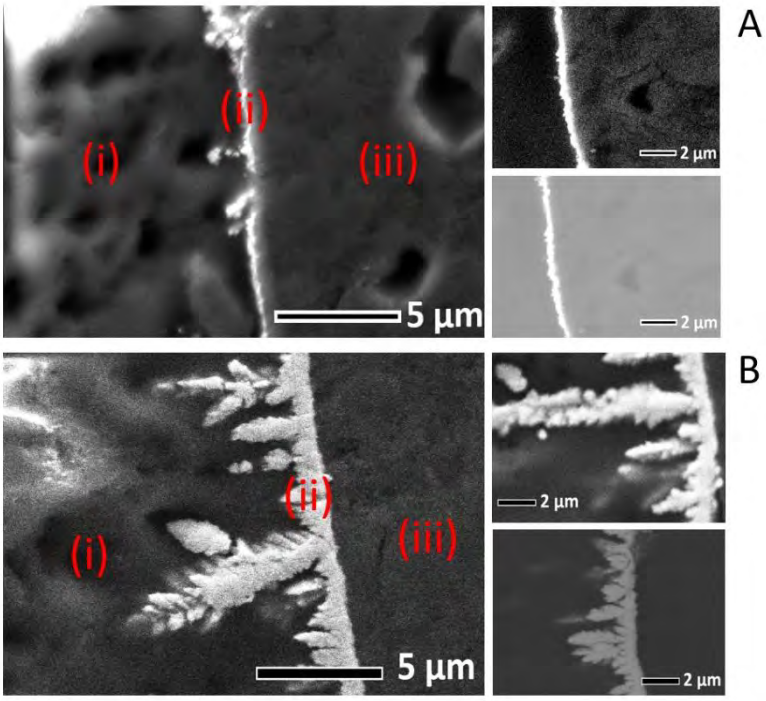

Figure 51 displays SEM/EDX analysis of a modified graphite electrode after use in a 168 h chronoamperometry. Figure 51A representing sample A was conducted in the presence of NPs and Figure 16B representing sample B was conducted without the presence of 20 nM CBNPs. Region (i), (ii) and (iii) indicate the epoxy, Pd deposition and graphite region respectively where EDX was performed to determine the Pd content.

A comparison of Figure 48 displaying a polished graphite electrode with Figure 50 and Figure 49 showing an electrode held in solution under potential for as long as 168 h confirms that Pd deposition occurs on the electrode resulting in a heavily modified surface. Figure 51 shows a side profile of both graphite electrodes (modified with and without CBNPs) indicating that the extent of Pd deposition on the background electrode is more prominent without the presence of particles. An average Pd thickness of 2.2 µm with larger growths (some exceeding 10 µm) was seen on the electrode without CBNPs in comparison to an average thickness of 0.5 µm seen on the electrode used with CB NPs present. A lower Pd weight% of 27% was detected on the electrode surface where CB NPs were used in comparison to deposition occurring without particles where a 99.6% Pd weight% was detected. The epoxy regions of both samples had much lower Pd content of 0% (-0.4%) for sample A and 11.6% for sample B and graphite region (iii) indicated 0.19 % and 1.39 % in sample A and B respectively.

4.5 Conclusion

Initial deposition studies conducted on glassy carbon showed that bulk deposition of Pd occurred at potentials negative of ca. +0.4 V (vs SCE), in good agreement with the literature.[308,319,321] Subsequent impact electrochemistry studies with CB NPs showed that transient impact events resulting in Pd deposition also commenced at ca. +0.40 V (vs SCE). Analysis of the resulting transient peaks determined an average charge of −14.8 ± 2.1 fC was observed at the “switch on/off potential” of +0.38 V (vs SCE) increasing to −49.0 ± 15.6 fC at a potential of −0.1 V (vs SCE).

Direct evidence of impact-mediated Pd deposition on the CB NPs was obtained via ESEM, EDX, TEM, ICP-MS, and XPS analysis of the Pd/CB NP sample. The impact experiment was successfully scaled up to produce enough Pd/CB NPs to test as a catalyst through large-volume long-term chronoamperometry, and synthesized Pd/CB NPs were characterized using TEM and TGA confirming a metal loading of 14 wt % Pd. The particles were then used to demonstrate direct catalytic application via the hydrogen evolution and Suzuki coupling reactions.

Finally, Pd recovery via nanoimpacts was investigated. Although not optimized to recover the maximum amount of Pd from solution, it was found that comparing Pd recovery with and without CB NPs over a 26-h period, the NP-mediated method increased recovery from ca. 65% to ca. 85%. This demonstrates the potential for single-entity electrochemistry to be a useful recovery method for metals, and future work will investigate its optimization and develop semiempirical equations for practical use as well as exploring applications for the deposited metal such as using 3D structured substrate electrodes that could be used for energy storage (e.g., recovered Ni, Mn, and Co for battery materials).

5. Platinum deposition on carbon nanoparticles via impacts

5.1 Abstract

Pt is a scarce and expensive metal with major economic significance due to its fundamental role in multiple global industries owing to its unique catalytic and physical properties. In order to meet increasing demands and, for nations to meet their ambitious climate targets, the sustainable recovery and reuse of this critical metal is essential. Impact electrochemical deposition methods have been highlighted for the recovery of critical metals from low concentration metal solutions, such as wastes, and in-situ catalyst synthesis. Pt/CB nanoparticles (NPs) are of particular interest as a target for in-situ synthesis due to their ubiquity as a fundamental material across the hydrogen value chain used within fuel cells, electrolysers and electrochemical compressors.

In this impact electrochemistry study, the recovery of Pt from low concentrations of hexachloroplatinic acid (0.5 mM) directly fabricating Pt modified carbon nanoparticles (Pt/CB NPs) has been demonstrated and investigated. Transient impact signals indicating the reduction of Pt on the surface of carbon black nanoparticles (CB NPs) are shown to occur at potentials negative of +0.38 V vs. SCE (satd KCl) corresponding to the onset potential identified via deposition on the surface of CBNP-modified glassy carbon (GC) electrodes. Analysis of these transient signals showed an average charge passed ranging from -6.9±1.3 fC to -15.2± 9.0 fC, corresponding to the reduction of Pt (IV) to Pt (0). Additionally, further evidence of Pt deposition was obtained via characterization using scanning electron microscopy/energy-dispersive X-ray spectroscopy, inductively coupled plasma optical emission spectrometry, X-ray photoelectron spectroscopy, transmission electron microscopy, and thermogravimetric analysis of modified particles. This indicated the formation of Pt (0) on the surface of the impacted 50 nm carbon black particles with approximately 14.9 % Pt (wt %) under the conditions used. The catalytic performance of the synthesised Pt/CB NPs was tested without any further modification via the hydrogen evolution reaction (HER) and oxygen reduction reaction (ORR).

5.2 Introduction

Hydrogen technology is essential for future sustainable energy economy and for international governments to reach their ambitious climate and carbon goals. As such, proton exchange membrane fuel cells, electrolysers (for hydrogen production) and ancillary technologies (such as electrochemical compression) are major topics of industrial and academic interest.[330] There is significant research focused on reducing the quantity of platinum required within these devices due to high manufacturing costs attributed to the use of Pt catalyst.[331] Despite this, Pt is used extensively across the hydrogen value chain as it is pivotal to several reactions including hydrogen evolution in electrolysers and oxygen reduction in proton exchange membrane fuel cells.[105,119,332-335]

To reduce Pt loading and increase the stability of the catalyst, Pt nanoparticles are dispersed onto the surface of support materials such as carbon black nanoparticles (CB NPs), carbon nanotubes, graphene, and carbon nanofibers.[121,336-340] Carbon black substrates are widely used as they are inexpensive and have useful properties such as a high surface area, good electrical conductivity, and chemical stability.[341] These supported catalysts are traditionally prepared via methods such as hydrothermal techniques, impregnation, and the chemical deposition of Pt onto the carbon substrate using various precursor such as hexachloroplatinic acid.[342-346] Within literature, there is debate regarding the reduction mechanism of the platinum chloride complexes. Some studies indicate a four-electron transfer from Pt (IV) in the form of $PtCl_6^{2-}$ to Pt (0) without the formation of stable Pt (II) intermediates. Alternatively, some studies indicate an initial reduction of Pt (IV) to Pt (II) before a further reduction to form Pt. Although the synthesis of Pt/CB NPs via wet chemical processes is relatively simple and requires the use of inexpensive equipment; it is considered labour intensive and results in limited control over the size distribution of the nanoparticles without the use of capping agents (e.g., surfactants, citrate, etc). Additionally, the presence of

surfactants results in their adsorption, which may adversely affect the properties of the Pt/CB NPs.[346,347]

Due to the scarcity and expense of Pt (along with other PGMs), the ability to recover spent Pt is essential for its continuous long-term sustainable use as global demands increase. Currently, spent Pt is recovered using both pyrometallurgical and hydrometallurgical methods which entails thermal treatment, chemical leaching, precipitation, or solvent extraction. These methods are limited by their adverse environmental impacts associated with high energy consumption and the generation of large volumes of chemical waste.[170,292,346,348]

The use of electrochemical techniques such as impact electrochemistry as a method for both metal recovery and in situ catalyst synthesis is an emerging area of interest due to its operational advantages. Like bulk deposition, impact electrochemistry is potentially a cost effective and facile approach enabling good control of the deposition process via changes to the voltage or current density.[349] The use of nanoparticles has been demonstrated to have a higher recovery rate than bulk electrodeposition (to a planar electrode) due to higher mass transport to the nanoparticle. As discussed in chapter 1, impact electrochemical deposition occurs when nanoparticles suspended in a solution moving under Brownian motion (or convection, if the experiment is designed appropriately) interacts or collides with a substrate electrode held at a suitable potential.

In this chapter, the use of impact electrochemistry using carbon black nanoparticles as a method of Pt metal recovery from low concentrations of Pt solution (0.5 mM) and in situ synthesis of Pt/CB NPs under non optimised conditions was investigated. The extent of the Pt deposition on the surface of the carbon black nanoparticles was characterised via SEM/EDX, TGA, XPS and ICP-OES. In addition, the electro-catalytic performance of the generated Pt/CB NPs was investigated via direct use as a catalyst for the hydrogen evolution reaction (HER) and oxygen evolution reaction (ORR).

5.3 Experimental

Chemicals were obtained commercially and used without further purification, namely: hexachloroplatinic acid solution (8 wt% in H_2O, Sigma-Aldrich), potassium chloride (99.0- 100.5 %, Alfa Aesar), potassium sulphate (99.0 %, Alfa Aesar), sulfuric acid (95.0-98.0 %, Sigma-Aldrich), hydrochloric acid (37.0 %, Honeywell), 10% Pt-modified CB NPs (Sigma Aldrich) and 50 nm diameter carbon black nanoparticles (Fuel cell store). All solutions were prepared using ultrapure water of resistivity = 18.2 MΩ cm (MilliQ, Millipore).

5.3.1 Electrochemistry

Pt metal electrochemical deposition onto carbon substrates was investigated using a three-electrode cell within a Faraday cage. The working electrodes used were a glassy carbon macroelectrode (GC, 3 mm diameter, BASi Inc), GC modified with 50 nm carbon black nanoparticles via drop casting[226,317,350] and 9 µm carbon fibre (made in-house using pitch-derived carbon fibre from Goodfellow Cambridge Ltd). The electrode size has been electrochemically confirmed using a thoroughly de-oxygenated solution containing 5 mM hexammineruthenium (III) chloride and 0.1 M potassium chloride. All working electrodes were prepared by polishing with alumina suspensions of 1 µm, 0.3 µm and 0.05 µm sequentially, on a micro-cloth pad (all from Buehler Inc, USA). A saturated calomel electrode (SCE, ALS Inc) and a graphite rod (3 mm diameter, Goodfellow Cambridge Ltd) were used as the reference and counter electrodes respectively. The SCE reference electrode was placed in a separate fritted compartment during the impact investigation to prevent cross-contamination. Both macro and impact electrochemical investigations were conducted in a solution consisting of 0.01 M hydrochloric acid, 0.01 M potassium chloride and 0.5 mM hexachloroplatinic acid solution (to provide adequate electrolyte support ratio whilst maintaining the suspension stability over experimental timescales.[178,351] Unless stated otherwise, for impact studies, 50 pM of CB NPs were added to the

reaction-solution from a bulk solution of CB NPs prepared by adding CB NPs to ultrapure water and sonicated for 1h before use. All solutions were deoxygenated by thoroughly degassing using nitrogen gas (oxygen-free, BOC Gases plc) and a nitrogen atmosphere was maintained throughout. Macro-electrode studies were performed using a PC controlled Autolab 128N (Metrohm-Autolab BV, Netherlands) potentiostat running NOVA 2.1 software conducting both cyclic voltammetry and chronoamperometric scans. Particle impact chronoamperometric scans were measured using a bespoke low noise potentiostat as described in chapter 2, and all data was processed using a combination of Microsoft Excel and Origin Pro 2021. Impact transient peaks were analysed without additional electronic filtration (digital).

Bulk synthesis of Pt-modified carbon black nanoparticles was conducted to generate sufficient sample for characterisation and electrocatalytic studies. This was achieved through a 48-h chronoamperometric scan held at -0.1 V and +0.6 V (vs. SCE) as described previously in chapter 4. This was conducted in a 500 mL solution of 0.01 M hydrochloric acid, 0.01 M potassium chloride and 0.5 mM hexachloroplatinic acid solution and 20 nM of 50 nm CB NPs was added. An inert atmosphere and agitation of the solution was maintained throughout using a nitrogen gas stream with a flow rate of 5 L min^{-1}. An additional control experiment was conducted at -0.1 V vs. SCE without the addition of carbon black nanoparticles. For all experiments, 3 mL samples were collected at designated periods during the chronoamperometry scan. The samples were analysed using inductively coupled plasma optical emission spectrometry (ICP-OES, Perkin Elmer Optima 8000) with a limit of detection of 1 ppb. A calibration curve ranging from 0.01 ppm to 100 ppm was produced using a Pt standard solution (VWR ARISTAR) and all samples were filtered and diluted with ultrapure water before analysis (see Appendix B). The modified particles produced during the chronoamperometry scan was extracted and repeatedly rinsed with ultrapure water for characterisation and catalytic studies.

5.3.2 Material Characterisation of Pt- modified CB NPs

Commercial unmodified CB NPs, CB NPs modified with Pt (Pt/CB NPs) via a -0.1 V and +0.6 V chronoamperometric scans as previously stated were characterised using scanning electron microscopy with energy dispersive X-ray spectroscopy (SEM/EDX). Inductively coupled plasma optical emission spectroscopy (ICP-OES) and X-ray photoelectron spectroscopy (XPS) analysis was also performed on these particles. Additional characterisation of -0.1 V Pt-modified particles was achieved using transmission electron microscopy (TEM), and thermogravimetric (TGA) analysis.

The SEM/ EDX analysis was conducted at a magnification of 4000× using the Hitachi TM3030 electron microscope. Three samples were prepared by adding 5 mg of CB NPs modified at a potential of -0.1 V, CB NPs modified at a potential of +0.6 V, and unmodified carbon black nanoparticles to carbon tape (Agar Scientific). SEM/EDX was also used to analyse the extent of background deposition on the surface of the graphite substrate electrode after use in the 48-h chronoamperometric scans. For the ICP analysis of the particles, Pt-modified nanoparticles and unmodified CB NPs were digested in 3 mL aqua regia for 10 days. The particles were removed from the solution using 0.45 µm syringe filters (Starlab Group Ltd) then diluted with ultrapure water in preparation for ICP-OES analysis. XPS and TEM analysis of the particles were conducted at the University of Nottingham interface and surface analysis centre (ISAC). For the XPS analysis, the samples were analysed using a Kratos Liquid Phase Photoelectron Spectroscopy (LiPPS) with a mono-chromated Al kα X-ray source (1486.6eV) operated at 10 mA emission current and 12 kV anode potential (120 W). The pass energy was 80 eV for wide scans and 20 eV for high resolution scans and wide scans were conducted with a step size of 0.5 eV and high-resolution scans were run with a step size of 0.1 eV. CASAXPS software (version 2.3.20) with Kratos sensitivity factors (RSFs) was used to determine atomic % values from the peak areas. For the TEM, the -0.1 V modified Pt/CB NPs were prepared as a dry sample onto a carbon film on a Cu support grid (Agar Scientific). The TEM analysis was conducted using the JEOL 2100Plus operated at 200 kV and Oxford Instruments AZtec 3.1 for EDX. The microscope was equipped with a Gatan OneView CMOS

camera, JEOL and Gatan Annular Dark Field detectors and an Oxford Instruments X-Max 100 TLE EDS detector. Gatan Microscopy Suite 3.43 software was used for imaging and STEM. Thermogravimetric analysis (TGA) of the -0.1 V (vs. SCE) modified sample was performed using NETZSCH TG 209 F1 where 8.6 mg of the sample was added to an aluminium oxide crucible. The sample was heated from 25 °C to 900 °C at a rate of 10 °C min^{-1} under nitrogen purging (10 mL min^{-1}). The change in sample mass was additionally measured using the nano balance (Sartorius) before and after thermal treatment.

5.3.3 Catalytic studies

The electrocatalytic performance of the -0.1 V modified CB NPs, 10% Pt-modified CB NPs (Sigma Aldrich) and unmodified carbon nanoparticle samples were studied for the hydrogen evolution reaction (HER), oxygen reduction reaction (ORR) with the electrochemically active surface area (ECSA) analysed using an Ivium compactstat.e pc-controlled potentiostat. Three catalytic inks were prepared using 8.9 mg of the -0.1 V modified CB NPs, 12.7 mg of the 10% Pt-modified CB NPs and 7.5 mg of the unmodified CBNPS. Each ink also contained Nafion^{TM} dispersion D1021 (Fuel Cell Store) to achieve 10% of total catalyst mass, 1.2 mL propan-2-ol (Fisher Scientific) and ultrapure water resulting in a total volume of 5 mL. This was sonicated for 1h before use. The HER was conducted in a solution of 0.01 M sulfuric acid and 0.09 M potassium sulphate using a SCE and graphite rod as the reference and counter electrodes respectively. An inert atmosphere was maintained throughout using nitrogen gas. A 3 mm GC electrode was used as the working electrode and was prepared by polishing with 3 µm diamond paste and alumina suspensions of 1 µm, 0.3 µm and 0.05 µm as previously described before modification using the catalytic inks. The surface of the GC electrode was modified using the rotational air-drying method by drop casting the catalytic ink during the rotation of the electrode (700 rpm) then dried for 15 min using a lamp as a heat source. An initial cyclic voltammogram (CV) was conducted from +0.95 V to -1.7 V (vs. SCE), followed by a further 100-cycle cleaning scan performed at a scan rate of 500 mV s^{-1} from +0.8 V to -0.27 V (vs. SCE) then a final CV scan from +0.95 V to -1.7 V (vs. SCE). [352,354]

ECSA and ORR studies were conducted in 0.1 M perchloric acid solution using a reversible hydrogen electrode (RHE) (BioLogic) and graphite rod as the reference and counter electrodes. For the ECSA, an initial CV (scan rate of 20 mV s^{-1}), 100-cycle cleaning CV (scan rate of 500 mV s^{-1}) and final CV (scan rate of 20 mV s^{-1}) was conducted in a nitrogen atmosphere using a potential window of +0.025 V to +1.0 V (vs. RHE). The perchloric acid solution was then saturated with oxygen before conducting linear sweep voltammetry (LSV) at a scan rate of 20 mVs^{-1} and potential window of -0.01 V to +1.1 V for the ORR studies where a range of rotational speeds from 400 to 2400 rpm were investigated.

5.4 Results and Discussion

5.4.1 Fabrication of Pt-modified CB NPs using impact deposition

Initial macro-electrode studies were conducted to determine the onset potential of Pt deposition on the surface of bare GC and CB NPs modified GC by drop casting 50 nm CB NPs (0.86 pmol m^{-2}) onto a 3 mm GC working electrode. The onset potential refers to an adequately negative potential able to initiate a sufficient current response and for this investigation this has been defined as -0.5 µA. Cyclic voltammograms were recorded for these electrodes in a solution of 0.01 M hydrochloric acid, 0.01 M potassium chloride and 0.5 mM hexachloroplatinic acid at a scan rate of 100 mV s^{-1} using a potential window of +0.6 V to -0.4 V vs. SCE. This potential window was selected as proton reduction commences at potentials negative of -0.25 V vs. SCE.[355] Figure 52 shows the reduction of Pt on the surface of bare GC (----) and CB-modified GC (—) where a sufficient increase in reductive current (-0.5 µA) is observed at ca. +0.20 V and ca. +0.38 V (vs. SCE) respectively. This is in broad agreement with literature indicating that the onset of platinum deposition occurs at a potential of ca. +0.15 V (vs SCE) on GC electrode and ca. +0.4 V (vs SCE) on highly oriented pyrolytic graphite electrode where it was observed Pt deposition on defects were characterised by a lower nucleation overpotential. Within literature it has also been observed that the Pt reduction onset potential is influenced by various electroplating conditions such as the electrode surface and electrolyte composition. A notable example of this is the presence of

chloride which has been documented to result in a more reductive onset potential as it inhibits the deposition of Pt by adsorbing to the substrate surface. [91,356]

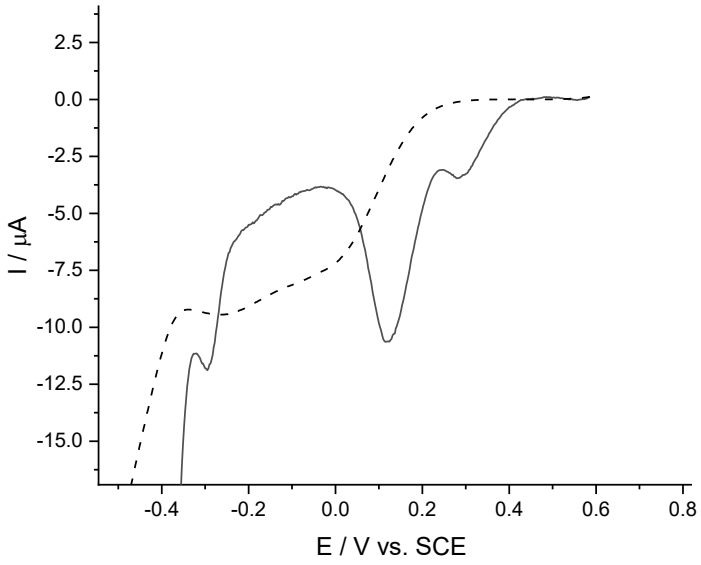

Figure 52 Reductive voltammetry indicating the deposition of Pt on bare GC (—) and 50 nm CB NPs modified GC (---) working electrodes. Cyclic voltammetry was conducted at a scan rate of 100 mVs^{-1} in a solution of 0.01 M hydrochloric acid, 0.01 M potassium chloride and 0.5 mM hexachloroplatinic acid solution.

In general, the deposition of Pt on carbon from a Pt chlorine complex occurs via initial adsorption to the electrode surface followed by the generation of ad-ions. The ad-ions form ad-atoms after a 4-electron transfer resulting in nuclei formation at the surface of the electrode where Pt nuclei results in Pt clusters. [341]

Within literature there are two primary mechanisms highlighted to describe the reduction of platinum (IV) ions to platinum metal with regards to electron transfer. The first mechanism suggests the two or more peaks observed in the voltammetry are associated with the deposition of Pt on carbon surfaces via a two-stage electron transfer (Equation 18 and Equation 19) where Pt (IV) is initially reduced to Pt (II) before forming Pt (0).[91,357,358] An alternative mechanism proposed is the direct reduction of Pt (IV) to Pt (0) (Equation 20) without the generation of a stable Pt (II) intermediate.[359] Based on this

mechanism, the multiple waves are thought to be associated with the reduction of Pt chloride complexes ($PtCl_6^{2-}$, $PtCl_5^{2-}$ and $PtCl_5(H_2O)$) within the solution.[91]

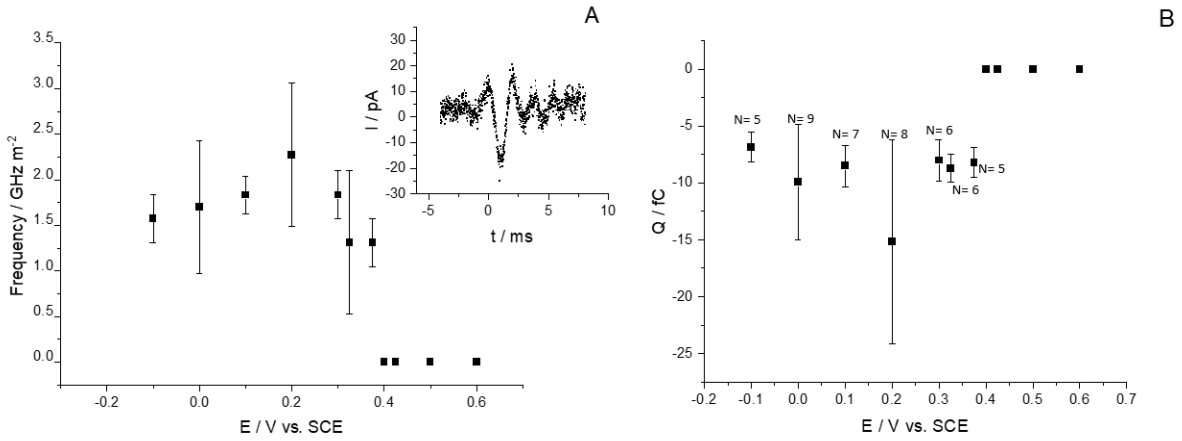

Figure 53 (A) Frequency of reductive peaks detected during 30 s chronoamperometric scans between the potential window +0.6 V to -0.1 V vs. SCE using 9 µm CF electrodes. The insert displays an illustrative example of a transient peak produced from the average of multiple peaks detected at 0.0 V (vs. SCE) where no additional electronic filtration was applied. The peaks have been time and background corrected to allow comparison between the peaks isolated. Figure 53(B) Mean average charge associated with the reductive peaks at different potential analysed using unfiltered peaks, where N is the number of peaks analysed.

Upon establishing the onset potential, impact studies were conducted to further investigate the deposition Pt on the surface of carbon black nanoparticles during impact electrochemistry. This was achieved by conducting chronoamperometric scans in a 5 mL solution of 0.01 M hydrochloric acid, 0.01 M potassium chloride and 0.5 mM hexachloroplatinic acid with and without the addition of 50 pM 50 nm CB NPs, where 9 µm CF electrodes were used as the substrate surface. Figure 53(A) shows the average frequency of reductive transient peaks detected during 30 s chronoamperometric scans conducted using a bespoke low noise potentiostat. This was determined by dividing the total number of observed impact signals during each chronoamperometric scan by the scan duration and electrode area. Figure 53(A) suggests that reductive peaks can be observed at potentials reductive of +0.38 V (vs. SCE) which is in good agreement with the onset potential determined via the macro studies (Figure 52). The average peak frequency detected ranged from 1.3 ± 0.8 GHz m^{-2} to 2.3 ± 0.8 GHz m^{-2} which is within range of literature records (0.3 to 3.7 GHz m^{-2}).[163,317,350] Figure 53(B) shows the average charge

of the peaks calculated using the integrated reductive transient peaks with no additional filtration as describe. Figure 53(B) indicates the charge ranges from -6.9±1.3 fC to -15.2± 9.0 fC suggesting an equivalent coverage of 53.8±0.1% to 119±71%. Within literature it has been noted that Pt growth requires large overpotentials due to sluggish nucleation kinetics in the presence of chlorides and occurs as isolated, hemispherical centres with nuclei formation occurring at specific sites on the carbon surface.[91] Figure 53(B) indicates an equivalent coverage of approximately a single monolayer or lower which potentially can be attributed to the slow Pt nucleation.

5.4.2 Characterisation

Table 11 SEM Image of aggregated CBNPs obtained from a 48 h chronoamperometric scan conducted at −0.1 V (vs. SCE) in a solution of 0.5 mM H_2PtCl_6, 0.01 M KCl, and 0.01 M HCl.

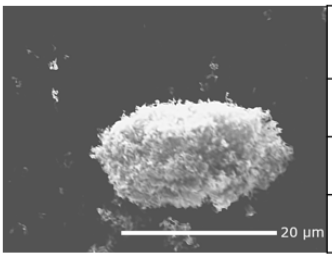

CBNP Samples	SEM/ EDX Average weight % ratio Pt/CB	ICP-MS Pt Conc. (ppm)
Unmodified	0	0
0.6 V vs. SCE	0.002 ± 0.000	47.7
-0.1 V vs. SCE	0.067 ± 0.022	821.6

The deposition of Pt on CB NPs during impact electrochemistry was further studied via a 48h chronoamperometry experiments conducted using a graphite plate electrode (area 6.25 cm^2) held at a potential of −0.1 V (vs SCE). The setup was scaled up to increase the amount of Pt-modified CBNPs generated for analysis therefore, a 500 mL solution containing 20 nM CB NPs, 0.5 mM H_2PtCl_6, 0.01 M KCl, and 0.01 M HCl was used. The solution was continuously agitated using a nitrogen gas stream (5 L min^{-1}) for the duration of the 48-h scan. A comparable experiment was conducted at +0.6 V vs. SCE which is sufficiently positive of the onset potential therefore reductive transient impact peaks are not expected. The two samples held at −0.1 V and +0.6 V were rinsed thoroughly with deionized water during filtration (using 0.02 µm anodisc inorganic membrane filters) then dried for SEM/EDX and ICP characterisation. Table 11 shows the SEM/EDX and ICP-OES analysis of unmodified CB NPs, CB NPs modified at -0.1 V, and CB NPs modified at +0.6 V. The -0.1 V modified CB NPs sample indicated the highest presence of Pt with an average weight % ratio Pt/CB of 0.067 ± 0.022 whereas the +0.6 V

sample and unmodified sample exhibited an average weight % ratio Pt/CB of 0.002 ± 0.000 and 0 respectively. This was in good agreement with the ICP-OES analysis indicating the highest Pt concentration of 821.6 ppm was detected in the -0.1 V modified sample followed by the +0.6 V sample where 47.7 ppm was detected. Similar to the SEM analysis, 0 ppm was detected in the unmodified sample which is expected as it had not been in contact with the H_2PtCl_6 solution. The Pt detected in the +0.6 V CB NPs sample is attributed to residual trace adsorbed Pt ions which remained after extensive washing.

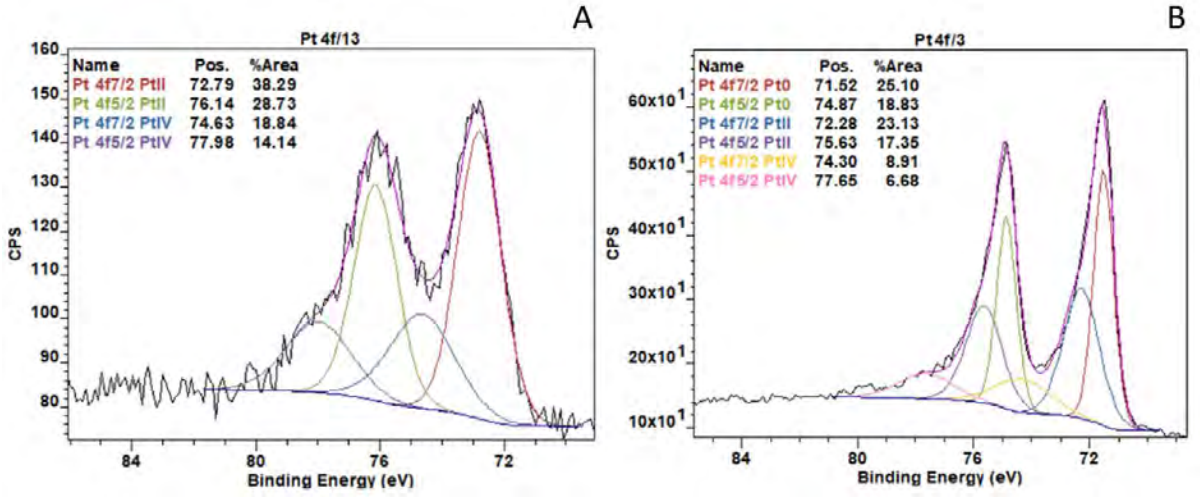

Figure 54 . XPS spectra (Pt 4f7/2 and Pt 4f5/2) of (A) +0.6 V vs SCE modified CB NPs and (B) −0.1 V vs. SCE modified CB NPs where the peaks with a binding energy of 71.52 eV (Pt 4f7/2) and 74.87 eV (Pt 4f5/2) indicate Pt (0).

XPS characterisation, shown in Figure 54, was conducted to determine the oxidation state of Pt detected in both the -0.1 V and 0.6 V modified samples. XPS analysis of both samples indicate the presence of Pt (IV) in both samples suggested by the peaks with a binding energy of 74.30 eV (Pt $4f_{7/2}$) and 77.65 eV (Pt $4f_{5/2}$) for -0.1 V sample and 74.63 eV (Pt $4f_{7/2}$) and 77.98 eV (Pt $4f_{5/2}$) for the +0.6 V sample. Figure 54 also indicates the presence of Pt (II) in both samples identified by the peak at 72.79 eV (Pt $4f_{7/2}$) and 76.14 eV (Pt $4f_{5/2}$) for the -0.1 V sample and peaks at 72.28 eV (Pt $4f_{7/2}$) and 75.63 eV (Pt $4f_{5/2}$) for the +0.6 V sample. This in good agreement with Pt $4f_{7/2}$ XPS values documented in

literature, which indicated a range of 70.0 to 71.6 eV, 72.3 to 74.6 eV and 74.0-75.6 eV for Pt (0), Pt (II) and Pt (IV) respectively.[360-362]

The presence of Pt (IV) can be attributed to the use of H_2PtCl_6 solution as the Pt salt while Pt (II) is associated with a spontaneous redox reaction resulting from the energy difference between the Pt^{4+} and carbon nanoparticles.[363,364] A distinct difference between the -0.1 V and +0.6 V modified sample is the presence of Pt (0) identified by peaks at 71.52 eV (Pt $4f_{7/2}$) and 74.87 eV (Pt $4f_{5/2}$) which was detected only in the -0.1 V modified CB NPs. This supports earlier conclusions made based on initial onset studies, SEM/EDX and ICP-OES analysis indicating that 0.6 V vs. SCE is not sufficiently reductive to facilitate the reduction of Pt ions to Pt metal.

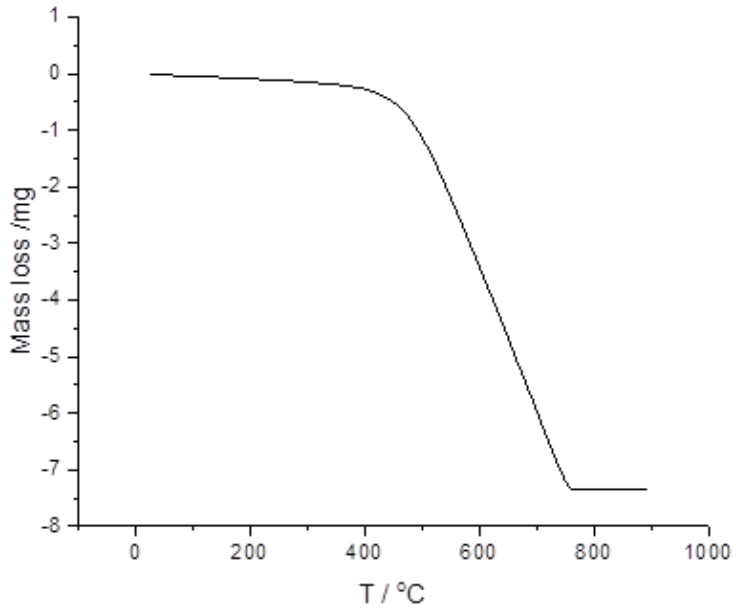

Figure 55 TGA thermogram of the -0.1 V vs. SCE modified CB NPs prepared during a 48-h chronoamperometric scan. From this, a 14.9 % platinum coverage was determined based on a mass change from 8.6 mg to 1.29 mg upon reaching 900 °C.

To further confirm the deposition of Pt metal on the surface of CB NPs during impact events at -0.1 V (vs. SCE), both TGA and TEM analysis were conducted using the 48-h -0.1 V modified CB NPs sample. The thermogravimetric (TGA) analysis of the sample (Figure 55) indicated the Pt/CB NPs contained 14.9% by mass of Pt. Furthermore, the TEM images shown in Figure 56A-F provides images of the

deposited Pt metal depicted by the darker regions observed on the CB NP support material. This was also confirmed via additional EDX mapping seen in Figure 57. The TEM images show the impacts do not result in the formation of a complete layer or evenly distributed clusters of Pt, but instead appear as growth limited to particular sites of the particle similar to that observed in Figure 42 for Pd deposits on carbon black nanoparticles.

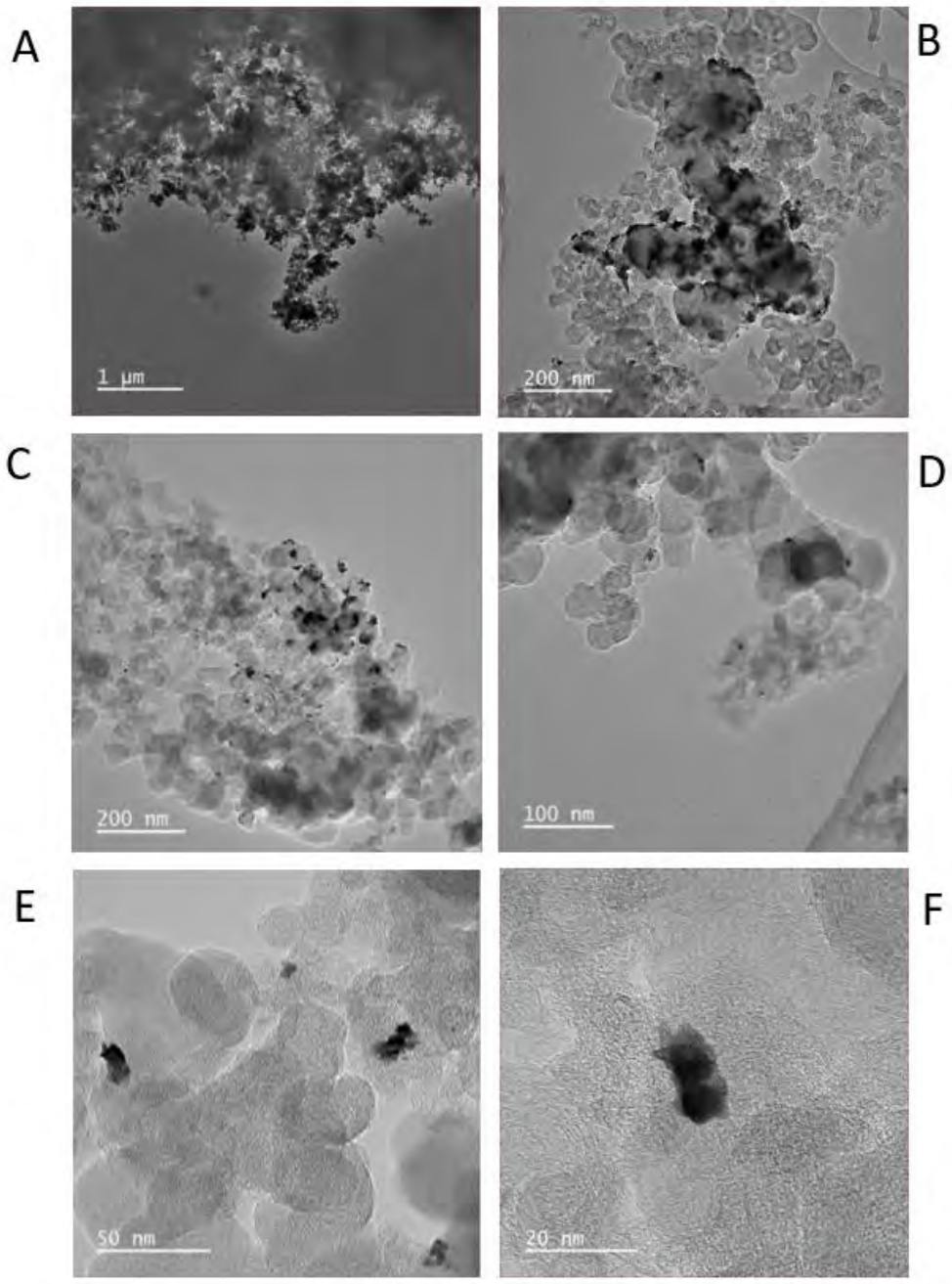

Figure 56 Typical TEM images (A–F) of the 48 h Pt-modified carbon nanoparticles where the darker regions represent deposited Pt metal.

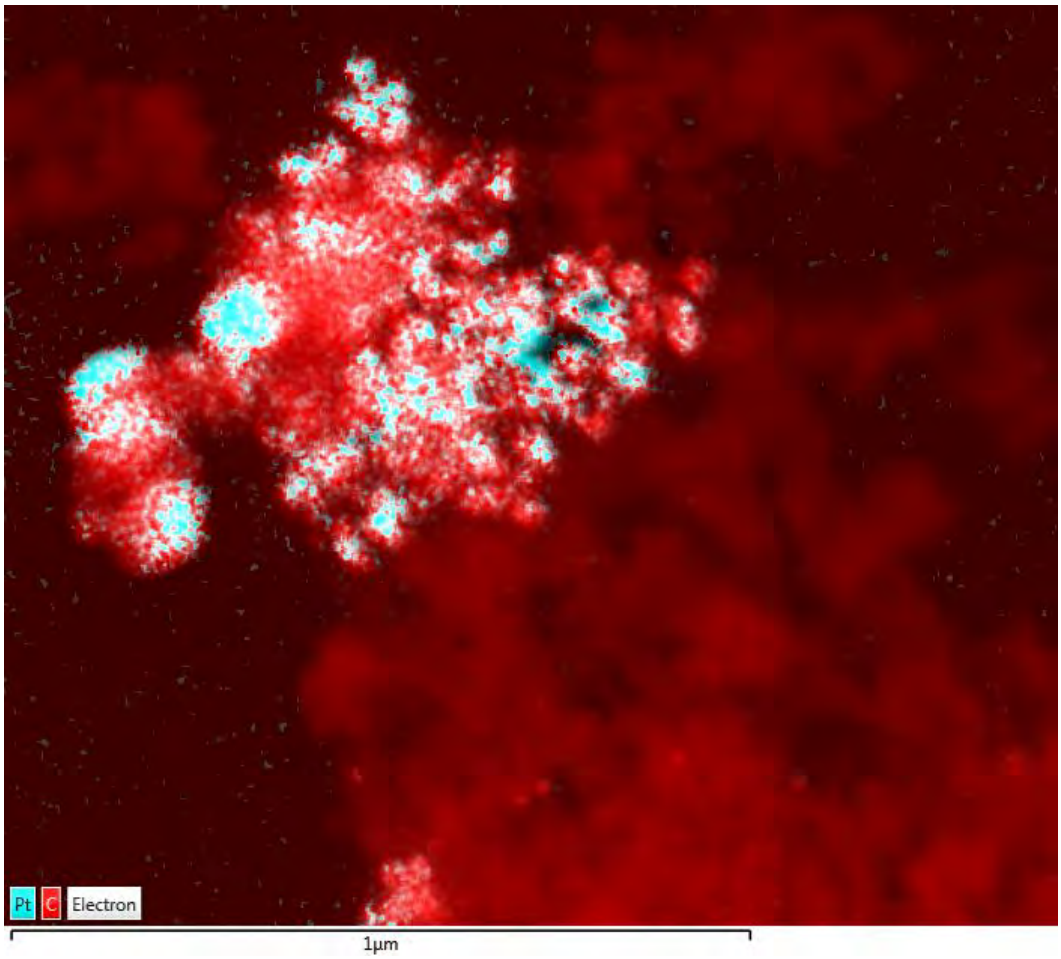

Figure 57 EDX mapping of -0.1 V modified sample highlighting the presence of Pt deposition on the surface of carbon nanoparticles where the blue region indicates Pt metal, and the red region indicates carbon.

5.4.3 Application of Pt/CB NPs for HER and ORR

The electro-catalytic performance of the -0.1 V modified CB NPs sample was studied via the hydrogen evolution reaction (HER), and oxygen reduction reaction (ORR), and the electrochemically active surface area (ECSA) determined via hydrogen adsorption. Three catalyst inks were prepared (see Experimental) using the -0.1 V sample, 10 % Pt-modified CB NPs (commercially obtained as a comparison), and unmodified CB NPs. The inks were used to modify the surface of the bare GC working electrode via the drop cast method before use in the study. An initial HER study was conducted via CV scans in a de-oxygenated solution of 0.1 M sulfuric acid and 0.09 M potassium sulphate to determine if the -0.1 V modified ink showed any catalytic properties. An initial CV scan (potential window 0.95 V

to -1.7 V vs. SCE) was employed to determine the HER performance before cleaning, followed by a 100-cycle cleaning CV scan between the potential 0.8 V and -0.27 V (vs. SCE) at a scan rate of 500 mV s^{-1} to remove impurities.[102] Figure 58 shows the reductive segment of the HER on the surface of bare GC, GC modified with CB NPs, GC modified with commercial Pt/CB NPs, and GC modified with the -0.1 V deposited Pt/CB NPs. Catalyst inks free of Pt (bare GC and GC/unmodified CB NPs) exhibit poor HER activity consistent with other studies.[365,366] The scans obtained using the GC/-0.1 V modified Pt/CB NPs and GC/commercial Pt/CB NPs electrodes show a similar current response, where a more oxidative HER onset of ca. -0.25 V and ca. -0.23 V (vs. SCE) respectively (observed at -0.5 μA). This further demonstrates the presence of Pt on the -0.1 V modified CB NPs as the HER kinetics is strongly dependent on the electrode material.[367,368]

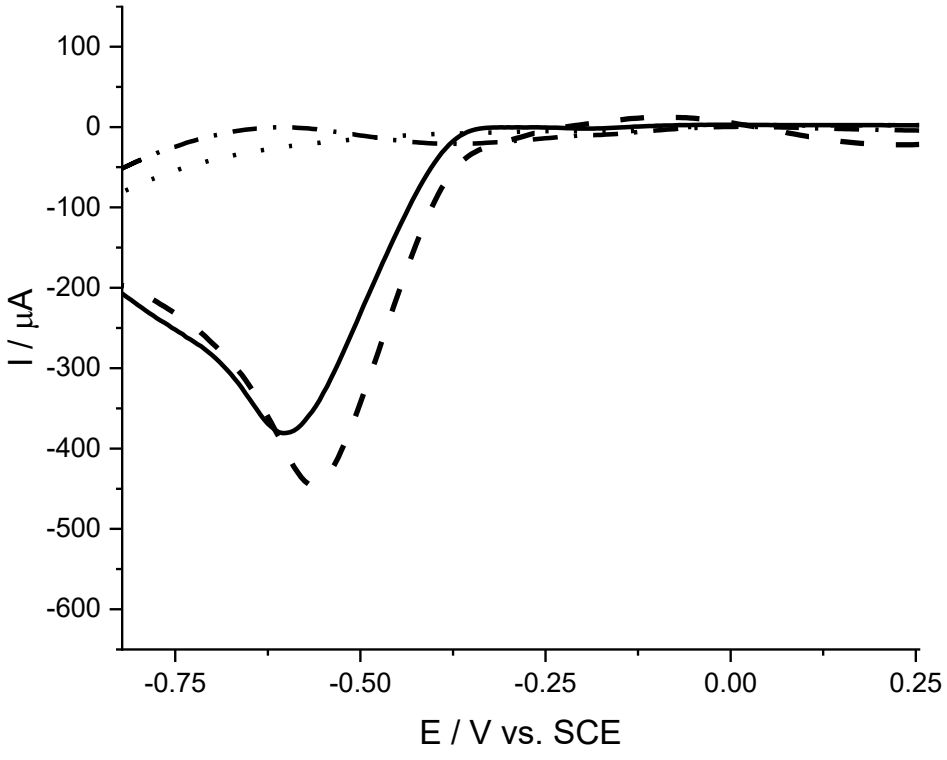

Figure 58 HER performance on the surface of bare GC (….), GC/ CB (-.-.), GC/ 10% Pt-CB commercially obtained (----) and GC/ -0.1 V modified CB NPs (—). This investigation was conducted in a solution of 0.1 M sulfuric acid and 0.09 M potassium sulphate.

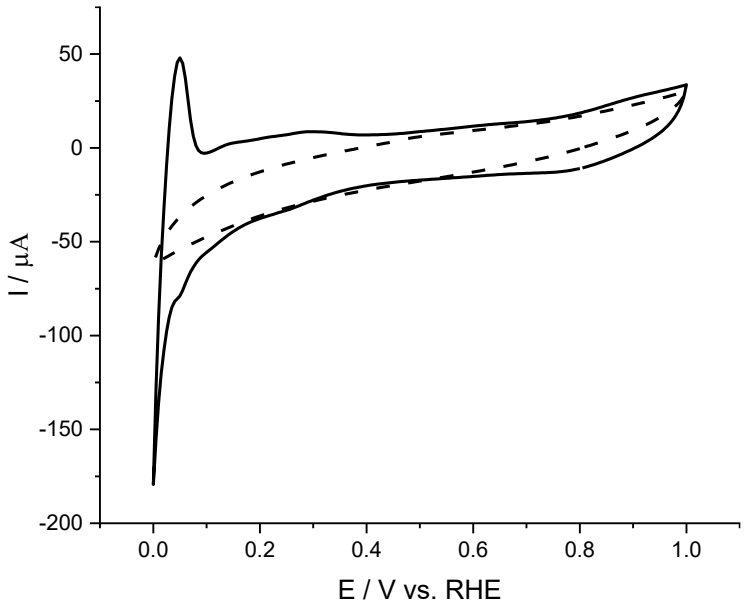

Figure 59 Cyclic voltammetry performed to determine the ECSA of the -0.1 V modified CB NPs. This was conducted in a solution of 0.1 M perchloric acid on the surface of Bare GC electrode and GC modified with -0.1 V modified CB NPs after a 100- cycle cleaning scan.

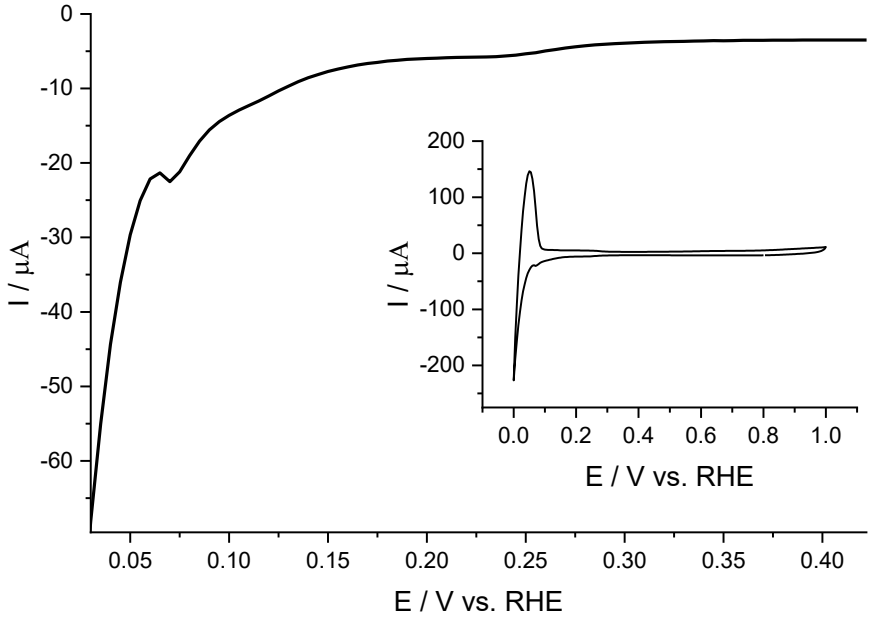

Figure 60 Reductive segment of CV scan conducted in a solution of 0.1 M perchloric acid using GC/10% Pt-CB NPs electrode before the cleaning cycle. The Inset shows the full potential window, where the hydrogen adsorption region has been used to determine the ECSA of the catalyst surface.

Next, the electrochemically active surface area (ECSA) was investigated in a de-oxygenated solution of 0.1 M perchloric acid between the potential window 0.025 V to 1.0 V (vs. RHE). Figure 59 shows the cyclic voltammetry scan conducted on the surface of bare GC and GC modified with -0.1 V modified Pt/CB after conducting an initial 100-cycle cleaning scan, where the initial ECSA can be seen in Figure 60. Figure 59 displays the characteristic peaks typically associated with hydrogen underpotential deposition and hydrogen evolution thus closely aligns with other cyclic voltammetry scans shown in literature.[369,370] This further indicates successful modification of the CB NPs during the impact events. The estimated ECSA of both the -0.1 V modified CB NPs and 10% Pt-CB NPs were calculated via the charge associated with the hydrogen adsorption region (Equation 104)[364,371,372], where the average ECSA values were 36 ± 13 $m^2 g^{-1}$ and 31 ± 13 $m^2 g^{-1}$ respectively.

$$ECSA = \frac{Q_H}{0.21\ m_{Pt}} \qquad \text{Equation 104}$$

Where Q_H represents the integrated charge associated with the hydrogen adsorption region of the voltammetry (see Figure 59 and Figure 60). The constant 0.21 (mC cm^{-2}) is the value of Q_H per cm^2 of Pt while m_{Pt} is the platinum loading on the surface of the CB NPs (g cm^{-2}). The higher ECSA attributed to the -0.1 V CB NPs is likely due to having a higher Pt loading of 15% determined by the TGA analysis.

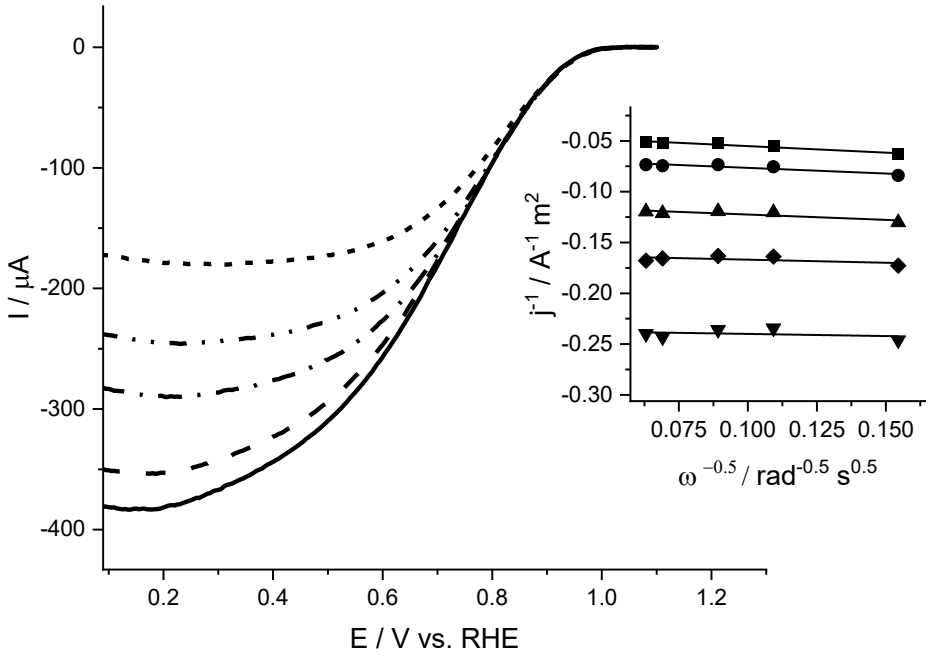

Figure 61 Linear sweep voltammetry conducted in a solution of 0.1 M perchloric acid using a rotating GC electrode modified with the -0.1 V modified Pt/CB NPs catalyst ink. This was conducted at a rotation speed of 400 rpm (····), 800 rpm (-····) , 1200 rpm (-·-··), 2000 rpm (-----) and 2400 rpm (——), where the Inset shows the Koutecky-Levich plot at 0.75V (■), 0.80 V (●), 0.85 V (▲), 0.875V (◆) and 0.9V (▼) from the ORR polarisation curves. The linear sweep voltammetry was background current corrected before use for the Koutecky-Levich.

The catalytic behaviour of the -0.1 V modified CB NPs towards the oxygen reduction reaction was then investigated via linear voltammetry sweeps (LVS) using an RDE at different electrode rotational speeds. The ORR is a complex 4-electron reaction involving multiple steps where there are several proposed mechanisms for the overall reaction. The mechanism involves the adsorption of O_2 to the Pt surface resulting in $O_{2\,(ads)}$. The $O_{2\,(ads)}$ can then react via multiple mechanisms such as a direct 4-electron reduction and indirect reduction as shown by Equation 76, Equation 82 and Equation 83 on page 59-60.

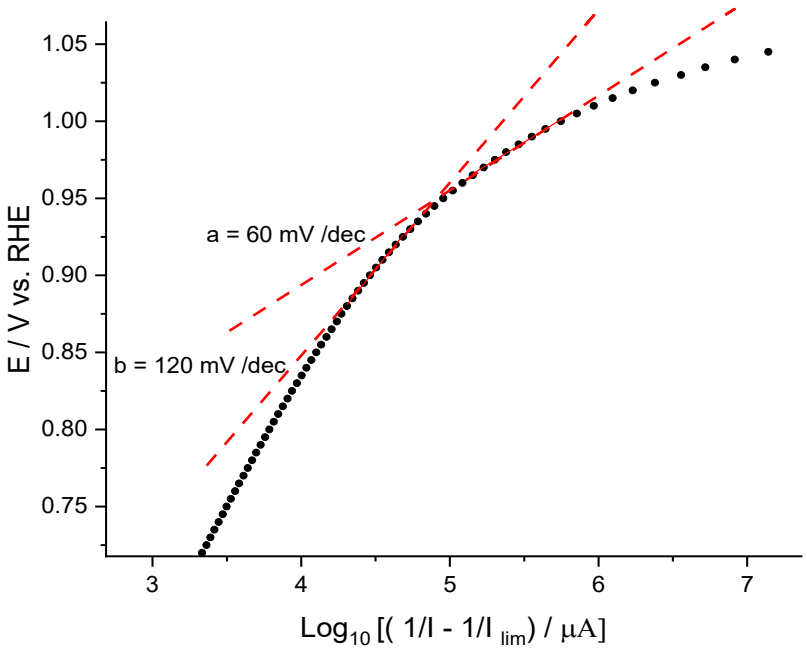

Figure 62 Tafel plot of GC modified with -0.1 V Pt/CB derived from LSV sweep at 400 RPM after additional mass transport correction. Slopes with a gradient of (a) 60 mV/dec at 0.98 and (b) 120 mV/ dec at 0.89 V.

This study was conducted in a solution of 0.1 M perchloric acid between the potential window of -0.01 V to 0.08 V (vs. RHE) using a GC electrode modified with -0.1 V deposited Pt/CB NPs catalytic ink. Figure 61 the ORR LSV scans conducted using electrode rotational speeds from 400 to 2400 rpm, and the resulting Koutecky-Levich plots (shown inset) at potential of 0.75 V, 0.8 V, 0.85 V, 0.875V and 0.9 V (vs. RHE) resulting in a kinetic current of -165 µA, -106 µA, -62 µA, -43 µA and -29 µA respectively. A mass-transport corrected Tafel plot (E vs. Log_{10} (1/ I – 1/ I_{lim}) was produced from the linear sweep voltammetry conducted at 400 RPM after mass transport correction. Figure 62 shows two Tafel slope regions are observed with a slope of ca. 60 mV dec^{-1} at more positive potentials of 0.98 V. This indicates the ORR occurs via the four-electron reduction pathway mechanism where the rate determining step involves the adsorption and activation of oxygen molecules on the electrode surface. At a more reductive potential of 0.89 V a slope of ca. 120 mV dec^{-1} was determined indicating the ORR shifting to a two-electron reduction mechanism where the reduction of hydrogen peroxide to water becomes

the rate determining step. This is in good agreement with studies investigating the electrocatalytic reaction of the ORR on the surface of Pt thus further indicating sufficient modification of the impacting carbon black nanoparticles.[346,373,374]

5.4.4 Recovery of Pt from low concentration of H_2PtCl_6

Having demonstrated the deposition of Pt on CB NPs during reductive impact events and the electro catalytic performance of the Pt/CB NPs produced; the use of the impact method to recover Pt from solutions containing low concentrations of H_2PtCl_6 was investigated. To achieve this, a 48-h chronoamperometric scan was conducted in a solution of 0.5 mM H_2PtCl_6, 0.01 M KCl, and 0.01 M HCl with and without the addition of 50 nm CB NPs. An additional 48-h investigation was conducted with CB NPs at a potential of 0.6 V vs. SCE. Throughout the investigation, 3 mL samples were extracted and filtered for ICP-OES analysis which was used to determine the Pt recovery % as shown in Figure 63(A). Figure 63(A) suggests the Pt concentration of the 0.6 V samples remained constant over the 48-h chronoamperometric scan indicating Pt deposition did not occur at this potential. For investigations conducted at -0.1 V vs. SCE with and without CB NPs, an increase in the Pt recovery % was observed suggesting the removal of Pt from the solution via nano impact and traditional deposition respectively.

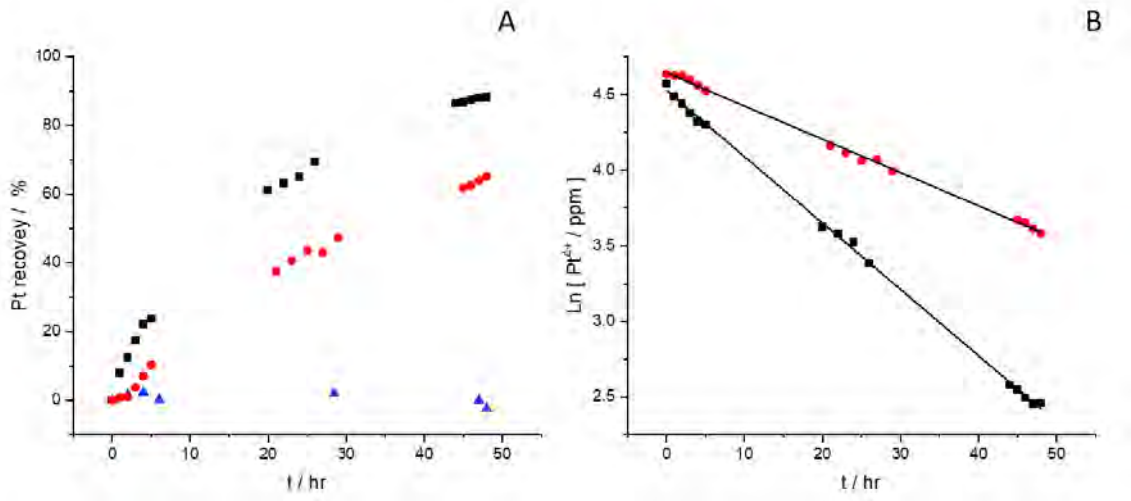

Figure 63 (A) Percentage of Pt recovered from H_2PtCl_6 during a 42-h chronoamperometric scan conducted at -0.1 V vs. SCE with (▪) and without (•) CB NPs. An additional chronometry was conducted at 0.6 V vs. SCE with CB NPs indicated by (▲). Figure 63(B) ln [Pt^{4+}] vs. time based on the data in (A) where the best fit lines from linear regression are given by ln [Pt^{4+}/ ppm] = 4.65–0.02t for (•) and ln [Pt^{4+}/ppm] = 4.52–0.04t for (▪).

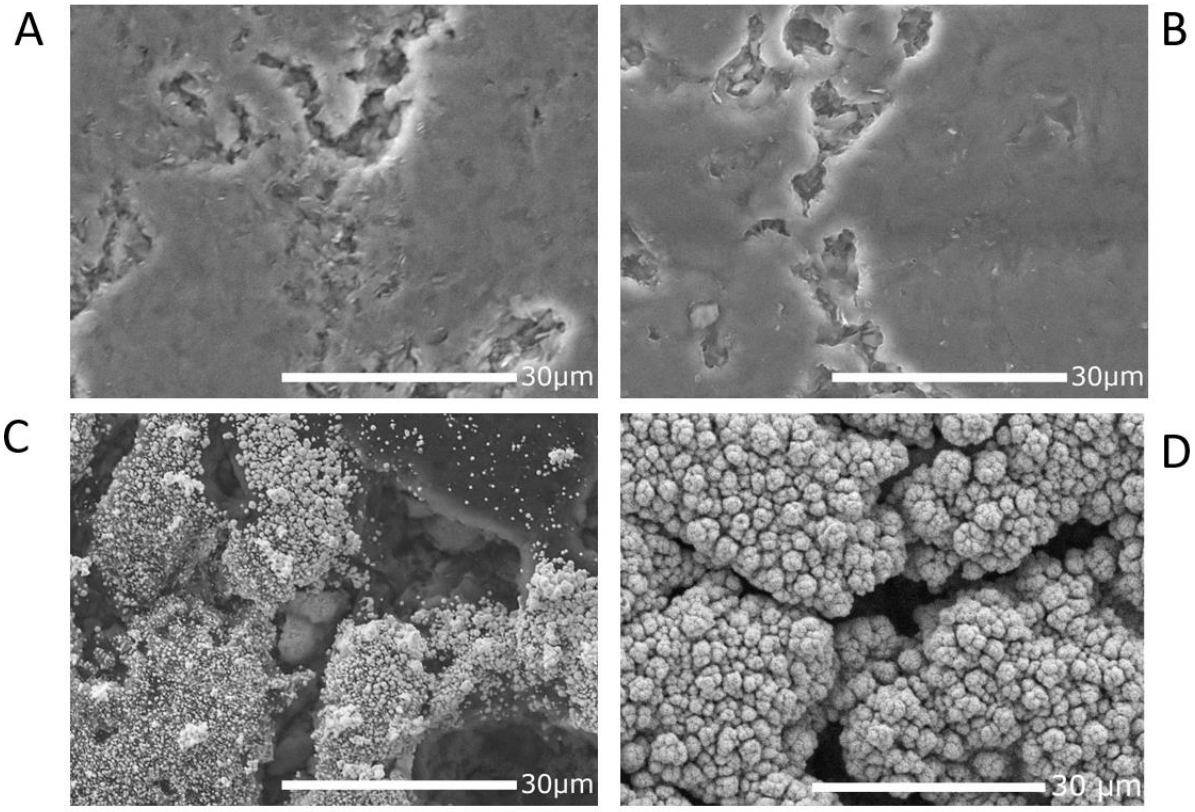

Figure 64 SEM images with a magnification of x 2.5 K showing the morphology of (A) an unmodified polished graphite electrode (B) graphite electrode after use in a 48-h chronoamperometric scan held at 0.6 V, (C) -0.1 V vs. SCE modified electrode with and without (D) the addition on of CB NPs.

The significance of background deposition during the impact events was studied via SEM/EDX of the graphite substrate electrodes after use in the 48-h chronoamperometric scans. Figure 64 indicates that both the polished unmodified graphite electrode (Figure 64(A) and 0.6 V modified graphite electrode (Figure 64(B) share similar morphologies suggesting that Pt deposition did not occur at 0.6 V vs. SCE. This is further supported by EDX analysis showing that both surfaces had an average weight % ratio Pt/CB of 0.000 ± 0.000. Figure 64(C) and (D) shows the modification of the graphite substrate electrode held at -0.1 V vs. SCE in the presence of CB NPs where there is evidence of some background deposition. There is a variation in the amount of Pt deposited on the substrate surface in the presence of CB NPs where the average weight % ratio Pt/CB ranges from 0.006 ± 0.002 to 0.030 ± 0.015. Analysis of the graphite electrode modified at -0.1 V in the absence of CB NPs showed significant surface modification with an average weight % ratio Pt/CB of 12.877 ± 0.480, thus demonstrating electrode modification attributed to background surface deposition is more prominent without the impacting particles. Figure 63(B) shows the change in Ln [Pt^{4+}] over a 48-h chronoamperometric scan held at -0.1 V with and without the addition of CB NPs. Figure 63 (B) suggests the presence of CB NPs resulted in an increased Pt recovery rate by a factor of 2 under non-optimised condition. This can be attributed to both the increased surface area of the NPs and the 3D diffusion of Pt ions to the NP surface enhancing mass transfer activities.[65,375]

5.5 Conclusion

In this chapter, the recovery of Pt metal from low concentrations of hexachloroplatinic acid (0.5 mM) and the in-situ fabrication of Pt modified carbon nanoparticles (Pt/CBNPs) was demonstrated. Initial macroelectrode studies conducted determined an onset potential of ca. +0.20 V and ca. +0.38 V (vs. SCE) on the surface of bare GC and CB-modified GC respectively. Subsequently, impact electrochemistry was conducted across the potential window +0.6 V to -0.1 V (vs. SCE) where impact indicating the deposition of Pt onto the carbon nanoparticles were observed negative of ca. +0.38 V (vs. SCE), in good agreement with the macroelectrode studies and the literature. Evaluation of the

resulting transient peaks determined an average charge of 6.9±1.3 fC to -15.2± 9.0 fC suggesting an equivalent coverage of 53.8±0.1% to 119±71%.

The deposition of Pt onto carbon black nanoparticles upon impact was further studied using characterisation methods such as SEM/EDX, ICP-OES, XPS, TGA and TEM/EDX. The ICP-OES indicated the highest presence of Pt with an average weight % ratio Pt/CB of 0.067 ± 0.022 in comparison to the +0.6 V sample and unmodified sample which had an average weight % ratio Pt/CB of 0.002 ± 0.000 and 0 respectively. The XPS analysis of the -0.1 V and +0.6 V modified samples indicated Pt (0) was only detected in the -0.1 V sample suggesting that Pt deposition had occurred on the surface of the impacted 50 nm carbon black particles resulting in approximately 14.9 % Pt (wt %) based on TGA.

The catalytic properties of the synthesised Pt carbon black nanoparticles were evaluated via the hydrogen evolution reaction (HER) and oxygen reduction reaction (ORR). For the HER stud, the GC/-0.1 V modified Pt/CB NPs and GC/commercial Pt/CB NPs electrodes both showed a more oxidative HER onset of ca. -0.25 V and ca. -0.23 V (vs. SCE) respectively further demonstrating the presence of Pt on the impact modified sample. The ECSA study determined the -0.1 V modified CB NPs and 10% Pt-CB NPs had ECSA values of 36 ± 13 $m^2 g^{-1}$ and 31 ± 13 $m^2 g^{-1}$ respectively. In addition to characterising the synthesised nanoparticles, the concentration of the hexachloroplatinic acid solution was also monitored during a 48-h chronoamperometry with and without the addition of CB NPs. This suggested the presence of CB NPs increased Pt recovery rate by a factor of 2 under non-optimised condition.

6. General conclusion

6.1 Thesis conclusion

This thesis has demonstrated the use of impact electrochemistry as a technique for the recovery of copper, palladium, and platinum from low concentrations solutions. Chapter 1 begins by introducing the challenges associated with heavy reliance on primary sources of metals as they are finite with varying abundancy and accessibility. These challenges are more evident when considering critical metals such as copper, palladium, and platinum. The extraction of these metals via mining activities are energy intensive resulting in significant adverse environmental impacts. Additionally, due to the relevance of these metals in a number of industries, waste management is a major concern with a forecasted 74 million tonnes of electronic waste expected by 2030. E-wastes are considered urban mines and are a major source of commercially valuable metals thus there are compelling environmental and economic incentives for extracting these metals.

A current challenge is the recapture of metals from low concentrations waste streams as conventional methods of recovery such as chemical precipitation, adsorption/biosorption, and ion exchange are limited by additional preconcentrating and separation steps resulting in an increased complexity and high operating costs. Impact electrochemistry emerges as a potential method for the recovery of metals from low concentration solutions due to the operational ease and high mass transport to the nanoparticle increasing the deposition rate.

This experimental work can be separated into three sections investigating the recovery of copper, palladium, and platinum. To consider the feasibility of impact electrochemistry for this application, copper deposition onto metallic gold and silver nanoparticles (AuNPs and AgNPs) was first performed in a solution of 0.5 mM copper sulphate, 19 mM potassium sulphate and 1 mM sulphuric acid. The macroelectrode studies determined the experimental onset potential for copper deposition onto AgNP-modified GC electrodes and AuNP-modified GC to be −0.4 V (vs. MSE) and −0.1 V (vs. MSE)

respectively. The deposition of copper on the gold-modified GC surface started at a more positive potential as a result of underpotential deposition (upd) indicated by the characteristic initial peak at ca. −0.3 V vs. MSE.

Individual impact studies were then performed to investigate copper deposition onto Ag NPs and then Au NPs during collision events. The reductive transient peaks observed aligned with the onset potential previously determined indicating a peak switch on/ off potential at −0.4 V vs. MSE for Ag NPs and at −0.1 V vs. MSE for Au NPs where deposition occurred negative of the stated potential. The impact studies also showed evidence suggesting impacts occurring in the upd region resulted in an average of ca. 103% ± 8% indicating coverage of approximately a monolayer. Impacts at a higher reductive potential showed a higher average coverage of ca. 215% ± 37%. For the Ag NPs impacts, once the applied potential is negative of the 'switch on' potential (−0.4 V vs. MSE), an average coverage of 479% was observed.

The copper deposition investigation was then extended to the use of non-metallic recovered waste material, fly-ash cenospheres (FACs). The use of lower value non-precious metal cores ensures the process is more practical than Ag NPs and Au NPs as this encourages long-term sustainability and economic viability of applications in recovery/recycling. Before use, the cenosphere particles were characterised using a SEM/EDX indicating significant amounts of silicon (52.3%) and aluminium (29.4%) with lower amounts of iron (9.0%), calcium (6.7%), magnesium (2.3%), and copper (0.2%). A size distribution analysis indicated a wide range of sizes from 100 s of nanometres to 100 s of microns with a population centred at 1 μm. These particles were used to modify a 3 mm GC electrode via drop casting methods and showed that the cenosphere particles were electrochemically active. During impact voltammetry cenospheres exhibited transient spikes thus suggesting evidence of copper deposition. This was supported by direct evidence found via SEM/ EDX and ICP-MS characterisation of the cenosphere. SEM/EDX and ICP-MS analysis of both the impacted and the unmodified cenosphere particles showed the unmodified cenosphere had a copper content of 1.0 ppb and 0.07 ± 0.08 %

copper content ratio. However, the modified cenospheres had a higher copper content of 2.0 ppb and 7.43 ± 2.47 % copper content ratio thus demonstrating the successful modification of cenosphere (waste)particles via impact electrochemistry.

In chapter 4, the deposition of palladium metal on the surface of carbon nanoparticles by impact electrochemistry and the in-situ fabrication of Pd modified CB nanoparticles was reported. An initial macroelectrode study was conducted in a solution of 0.01 M potassium chloride, 0.01 M hydrochloric acid, and 0.5 mM palladium (II) chloride. This showed the deposition of Pd occurred at an onset potential of +0.29 V (vs. SCE) on the surface of bare GC and +0.38 V (vs. SCE) on the CB NP-modified GC. Multiple chronoamperometric scans were then conducted between +0.6 and −0.2 V vs. SCE to investigate deposition during impact events. This established that peaks were observed negative of the switch on potential (+0.38 V) which is in good agreement with the macro studies. Further analysis of the resulting transient peaks indicated an average charge of −14.8 ± 2.1 fC was observed at +0.38 V (vs SCE) increasing to −49.0 ± 15.6 fC at a potential of −0.1 V (vs SCE). The electrochemical impact experimental setup was then scaled from 5 mL to 500 mL to produce sufficient mass of impacted CB NPs for analysis and to also study the change in Pd concentration in the $PdCl_2$ electroplating solution over time. A potential of -0.1 V (vs. SCE) and +0.6 V (vs. SCE) was selected for the scale up to test the 'on' and 'off' impact potentials respectively. The percentage of Pd^{2+} recovered during a 26 h chronoamperometric scan with and without the addition of CB NPs showed an enhancement in the recovery rate of a factor of approximately 1.7 for the NP-mediated experiment.

Direct evidence of impact-mediated Pd deposition on the CB NPs was obtained via characterisation methods such as ESEM, EDX, TEM, ICP-MS, and XPS analysis of the Pd/CB NP samples. The ICP analysis of both samples showed a Pd concentration of 17.67 ppm and 2.75 ppm for the -0.1 V and +0.6 V modified CB NPs respectively where XPS confirmed, Pd (0) was only detected on the former. A TGA was also conducted and confirmed a metal loading of 14 wt % Pd for the -0.1 V modified sample. The

particles were then used to demonstrate direct catalytic application via the hydrogen evolution and Suzuki coupling reactions without further modification.

Chapter 5 continued the focus on platinum group metals by demonstrating the deposition of Pt onto CB NPs via electrochemical impact deposition performed in a solution consisting of 0.01 M hydrochloric acid, 0.01 M potassium chloride and 0.5 mM hexachloroplatinic acid. Macroelectrode studies conducted on the surface of bare GC and CB-modified GC indicated an experimental onset potential of ca. +0.20 V and ca. +0.38 V (vs. SCE) respectively. This was reflected in the impact studies where transient impact signals indicating the reduction of Pt on the surface of carbon black nanoparticles (CB NPs) occurred at potentials negative of +0.38 V vs. SCE. The average peak frequency detected ranged from 1.3±0.8 GHz m^{-2} to 2.3±0.8 GHz m^{-2} which is within range of literature records 0.3 to 3.7 GHz m^{-2}) and charge ranges from -6.9±1.3 fC to -15.2± 9.0 fC suggesting an equivalent coverage of 53.8±0.1% to 119±71% attributed to the sluggish nucleation kinetics in the presence of chlorides.

Analogous to the Pd investigation, the electrochemical impact experiment was scaled from 5 mL to 500 mL of 0.01 M hydrochloric acid, 0.01 M potassium chloride and 0.5 mM hexachloroplatinic acid to generate pt modified CB NPs. The concentration of the hexachloroplatinic acid solution was also monitored during a 48-h chronoamperometry with and without the addition of CB NPs. Similar to the Pd study, this suggested the presence of CB NPs increased Pt recovery rate by a factor of 2 under non-optimised condition.

The fabricated Pt/ CB NPs particles were characterised using SEM/EDX, ICP-OES, XPS, TGA and TEM/EDX where the ICP-OES analysis indicated the -0.1 V modified sample had a high amount of Pt with an average weight % ratio Pt/CB of 0.067 ± 0.022 compared to the +0.6 V sample which had an average weight % ratio Pt/CB of 0.002 ± 0.000. The XPS analysis of the -0.1 V and +0.6 V modified samples indicated Pt (0) was only detected in the -0.1 V sample suggesting the successful modification of the impacted 50 nm carbon black particles.

Approximately 14.9 % Pt (wt %) was determined using the TGA before the catalytic properties of the synthesised Pt carbon black nanoparticles were evaluated via the hydrogen evolution reaction (HER) and oxygen reduction reaction (ORR). For the HER study, the GC/-0.1 V modified Pt/CB NPs and GC/commercial Pt/CB NPs electrodes both showed a more positive HER onset of ca. -0.25 V and ca. -0.23 V (vs. SCE) respectively again indicating the presence of Pt on the impact modified sample. The ECSA study determined the -0.1 V modified CB NPs and 10% Pt-CB NPs had ECSA values of 36 ± 13 m^2 g^{-1} and 31 ± 13 m^2g^{-1} respectively.

6.2 Recommendations for further work

The present work demonstrated the deposition of copper, palladium, and platinum onto both metallic and non-metallic nanoparticles during impact events using a carbon substrate electrode. As a result, metal deposition was also observed on the background electrode.

Firstly, to optimise this process for potential scale up, when considering the electrodeposition of metal(s) onto core particles via the impact method it is recommended to investigate the use of a substrate electrode material with a significantly higher overpotential compared to that of the core particle material. Boron-doped diamond (BDD) is suggested due to its notably wide potential window and low background and capacitive current. The use of BDD offers a more reductive potential for the deposition of metals, for example, the onset of platinum deposition is -0.24 V vs. SCE on the surface of BDD. This ensures that at the appropriate potential, deposition will preferentially occur on the impacting particle and not the underlying substrate electrode increasing the amount of metal present on the nanoparticle.[376,377]

A second recommendation to support a scaled-up process is to investigate impact deposition under more optimised conditions. Currently, the movement of the nanoparticle is influenced by Brownian motion or forced convection provided by the nitrogen gas stream. Further studies on the effect of agitation on frequency and characteristics of impact is required. This can be further extended to the use of a jet stream to direct the impacting nanoparticles towards the surface of the substrate

electrode. This could further improve the recovery rate by increasing the collision frequency of impacting nanoparticles thus increasing the number of impacts resulting in metal recovery.

A further recommendation is to investigate mixed metal solutions as this is a more accurate representation of waste solutions found in industry. An investigation into the upper and lower concentration limits would also be beneficial to further understand the effect of metal concentration on the recovery rate and resulting transient peaks.

The primary product of this process would be nanoparticles modified with deposits of the desired metal which can then be directly used in other processes. This can be extended to investigate the preparation of single atom catalysts (SAC) which would consist of isolated metal atoms dispersed onto the surface of the impacting nanoparticles resulting in a well-defined and uniform catalyst with high activity and selectivity. Alternatively, the extraction of the deposited metal from the nanoparticles could be achieved with additional hydrometallurgy and pyrometallurgy processes where impact electrochemistry acts as a pre concentration step.

7. References

1. Hughes AE, Haque N, Northey SA, Giddey S. Platinum Group Metals: A Review of Resources, Production and Usage with a Focus on Catalysts. Resources. 2021 Sep 20;10(9):93.
2. ElGuindy M. Platinum Group Metals: Alloying, Properties, and Applications. In: Jürgen Buschow KH, Cahn RW, Flemings MC, Ilschner B, editors. Encyclopedia of materials: Science and technology. Oxford: Elsevier;2001. p. 7117-21.
3. Albrecht M, Bedford R, Plietker B. Catalytic and Organometallic Chemistry of Earth-Abundant Metals. Organometallics. 2014 Oct 27;33(20):5619-21.
4. Crundwell FK, Moats MS, Davenport WG, Robinson TG, Ramachandran V. Extractive metallurgy of nickel, cobalt and platinum-group materials. Oxford: Elsevier;2011. p. 395-415.
5. Cramer LA. The extractive metallurgy of south africa's platinum ores. JOM. 2001 Oct;53(10):14-8.
6. Kyriakakis G. Extraction of gold from platinum group metal (PGM) ores. Dev Miner Process. 2005;15:897-917.
7. UNEP. Environmental Risks and Challenges of Anthropogenic Metals Flows and Cycles: A Report of the Working Group on the Global Metal Flows to the International Resource Panel. van der Voet E, Salminen R, Eckelman M, Mudd G, Norgate T, Hischier R;2013.
8. Schluep M, Hagelueken C, Kuehr R, Magalini F, Maurer C, Meskers C, et al. Sustainable innovation and technology transfer industrial sector studies: Recycling-from e-waste to resources. United Nations Environment Programme & United Nations University, Bonn, Germany. 2009.
9. Ghimire H, Ariya PA. E-wastes: bridging the knowledge gaps in global production budgets, composition, recycling and sustainability implications. Sustain Chem. 2020 Sep 9;1(2):154-82.
10. Rankin WJ. Chapter 4.1 - Sustainability. In: Seetharaman S, editors. Treatise on process metallurgy. Oxford: Elsevier;2014. p. 1376-424.
11. WCED SW. World commission on environment and development. Our common future. 1987 Jan 29;17(1):1-91.
12. Zeng X, Wang F, Li J, Gong R. A simplified method to evaluate the recycling potential of e-waste. J Clean Prod. 2017 Dec 1;168:1518-24.
13. Balde CP, Kuehr R, Blumenthal K, Fondeur GS, Kern M, Micheli P, et al. E-waste statistics - Guidelines on classification, reporting and indicators. Bonn: UNU;2015.
14. Li J, Zeng X, Chen M, Ogunseitan OA, Stevels A. Control-Alt-Delete: Rebooting Solutions for the E-Waste Problem. Environ Sci Technol. 2015;49(12):7095-108.
15. Shumon MRH, Ahmed S, Islam MT. Electronic waste: present status and future perspectives of sustainable management practices in Malaysia. Environ Earth Sci. 2014;72:2239-49.
16. Nagarajan N, Panchatcharam P. Cost-effective and eco-friendly copper recovery from waste printed circuit boards using organic chemical leaching. Heliyon. 2023 Mar 1;9(3):e13806.

17. Forti V, Balde CP, Kuehr R, Bel G. The Global E-waste Monitor 2020: Quantities, flows and the circular economy potential. Bonn: UNU;2020.

18. Kuntawee C, Tantrakarnapa K, Limpanont Y, Lawpoolsri S, Phetrak A, Mingkhwan R, et al. Exposure to Heavy Metals in Electronic Waste Recycling in Thailand. Int J Environ Res Public Health. 2020;17(9):2996.

19. Guo Y, Huo X, Li Y, Wu K, Liu J, Huang J, et al. Monitoring of lead, cadmium, chromium and nickel in placenta from an e-waste recycling town in China. Sci Total Environ. 2010 Jul 15;408(16):3113-7.

20. Ebin B, Isik MI. Chapter 5 - Pyrometallurgical Processes for the Recovery of Metals from WEEE. In: Chagnes A, Cote G, Ekberg C, Nilsson M, Retegan T, editors. WEEE Recycling. Oxford: Elsevier;2016. p. 107-37.

21. Manikandan S, Inbakandan D, Valli Nachiyar C, Karthick Raja Namasivayam S. Towards sustainable metal recovery from e-waste: A mini review. SCENV. 2023;2:100001.

22. Pinho S, Ladeiro B. Phytotoxicity by Lead as Heavy Metal Focus on Oxidative Stress. J Bot. 2012 Jul 19;2012:369572.

23. Wierzbicka M. Comparison of lead tolerance in Allium cepa with other plant species. Environ Pollut. 1999 Jan 1;104(1):41-52.

24. Işıldar A, Rene ER, van Hullebusch ED, Lens PNL. Electronic waste as a secondary source of critical metals: Management and recovery technologies. Resour Conserv Recycl. 2018 Aug;135:296-312.

25. Babu BR, Parande AK, Basha CA. Electrical and electronic waste: a global environmental problem. Waste Manag Res. 2007 Aug;25(4):307-18.

26. European Commission, Directorate-General for Internal Market, Industry, Entrepreneurship and SMEs, Grohol M, Veeh C. *Study on the critical raw materials for the EU 2023: final report*. Publications Office of the European Union;2023.

27. Lottermoser BG. Mine Wastes: Characterization, Treatment, Environmental Impacts. 2nd ed. Berlin: Springer;2007.

28. Lèbre É, Corder GD, Golev A. Sustainable practices in the management of mining waste: A focus on the mineral resource. Miner Eng. 2017 Jun;107:34-42.

29. Ray DA, Baniasadi M, Graves JE, Greenwood A, Farnaud S. Thiourea Leaching: An Update on a Sustainable Approach for Gold Recovery from E-waste. J Sustain Metall. 2022 Mar 18;8:597-612.

30. Blowes DW, Ptacek CJ, Jambor JL, Weisener CG, Paktunc D, Gould WD, et al. The Geochemistry of Acid Mine Drainage. In: Holland HD, Turekian KK, editors. Treatise on Geochemistry (Second Edition). Amsterdam: Elsevier;2014. p. 131-90.

31. Khaliq A, Rhamdhani MA, Brooks G, Masood S. Metal Extraction Processes for Electronic Waste and Existing Industrial Routes: A Review and Australian Perspective. Resources. 2014;3(1):152-79.

32. Cui J, Roven HJ. Chapter 20 - Electronic Waste. In: Letcher TM, Vallero DA, editors. Waste. Cambridge: Academic Press;2011. p. 281-96.

33. D'Silva K, Fernandes A, Rose M. Brominated Organic Micropollutants—Igniting the Flame-Retardant Issue. Crit Rev Environ Sci and Technol. 2004;34(2):141-207.

34. Yang L, Liu G, Shen J, Wang M, Yang Q, Zheng M. Environmental characteristics and formations of polybrominated dibenzo-p-dioxins and dibenzofurans. Environ Int. 2021 Jul;152:106450.

35. Hocking MB. Ore Enrichment and Smelting of Copper. Modern Chemical Technology and Emission Control. Berlin: Springer;1985. p. 242-74.

36. Altinkaya P, Wang Z, Korolev I, Hamuyuni J, Haapalainen M, Kolehmainen E, et al. Leaching and recovery of gold from ore in cyanide-free glycine media. Miner Eng. 2020 Nov 1;158:106610.

37. Zhang Y, Liu S, Xie H, Zeng X, Li J. Current Status on Leaching Precious Metals from Waste Printed Circuit Boards. Procedia Environ Sci. 2012;16:560-8.

38. Leung AMR, Lu JLD. Environmental Health and Safety Hazards of Indigenous Small-Scale Gold Mining Using Cyanidation in the Philippines. Environ Health Insights. 2016 Aug 8;10:125-31.

39. Hamel J. A Review of Acute Cyanide Poisoning with a Treatment Update. Crit Care Nurse. 2011 Feb 1;31(1):72-82.

40. Jethava D, Gupta P, Kothari S, Rijhwani P, Kumar A. Acute cyanide intoxication: A rare case of survival. Indian J Anaesth. 2014 May;58(3):312-4.

41. Eisler R, Wiemeyer SN. Cyanide hazards to plants and animals from gold mining and related water issues. Rev Environ Contam Toxicol. 2004;183:21-54.

42. González-Valoys AC, Arrocha J, Monteza-Destro T, Vargas-Lombardo M, Esbrí JM, Garcia-Ordiales E, et al. Environmental challenges related to cyanidation in Central American gold mining;the Remance mine (Panama). J Environ Manage. 2022 Jan 15;302:113979

43. Abbruzzese C, Fornari P, Massidda R, Vegliò F, Ubaldini S. Thiosulphate leaching for gold hydrometallurgy. Hydrometallurgy. 1995 Oct;39(1-3):265-76.

44. Rizki IN, Tanaka Y, Okibe N. Thiourea bioleaching for gold recycling from e-waste. Waste management. 2019 Feb 1;84:158-65.

45. Ding Y, Zhang S, Liu B, Zheng H, Chang CC, Ekberg C. Recovery of precious metals from electronic waste and spent catalysts: A review. Resour Conserv Recycl. 2019 Feb 1;141:284-98.

46. Ubaldini S, Fornari P, Massidda R, Abbruzzese C. An Innovative Thiourea Gold Leaching Process. Hydrometallurgy. 1998 Mar;48(1): 113-24.

47. Juarez CM, Oliveira JF. Activated carbon adsorption of gold from thiourea solutions. Miner Eng. 1993 June;6(6): 575-83.

48. Ghosh B, Ghosh MK, Parhi P, Mukherjee PS, Mishra BK. Waste printed circuit boards recycling: an extensive assessment of current status. J Clean Prod. 2015 May 1;94:5-19.

49. Yaashikaa PR, Priyanka B, Kumar PS, Karishma S, Jeevanantham S, Indraganti S. A review on recent advancements in recovery of valuable and toxic metals from e-waste using bioleaching approach. Chemosphere. 2022 Jan 1;287:132230.

50. Asghari I, Mousavi SM, Amiri F, Tavassoli S. Bioleaching of spent refinery catalysts: a review. J Ind Eng Chem. 2013 Jul 25;19(4):1069-81.

51. Saldaña M, Jeldres M, Madrid FMG, Gallegos S, Salazar I, Robles P, et al. Bioleaching Modeling—A Review. Materials. 2023 May 18;16(10):3812.

52. Murugappan RM, Karthikeyan M. Microbe-assisted management and recovery of heavy metals from electronic wastes. In: Hussain CM, editors. Environmental Management of Waste Electrical and Electronic Equipment. Oxford: Elsevier;2021. p. 65-88.

53. Srichandan H, Mohapatra RK, Parhi PK, Mishra S. Bioleaching: A Bioremediation Process to Treat Hazardous Wastes. In: Jamil N, Kumar P, Batool R, editors. Hoboken: Wiley;2019. p. 115-29.

54. Sand W, Gehrke T, Jozsa PG, Schippers A. (Bio) chemistry of bacterial leaching—direct vs. indirect bioleaching. Hydrometallurgy. 2001 Feb 1;59(2-3):159-75.

55. Yang J, Wang Q, Wang Q, Wu T. Comparisons of one-step and two-step bioleaching for heavy metals removed from municipal solid waste incineration fly ash. Environ Eng Sci. 2008 Jun 1;25(5):783-9.

56. Bosshard PP, Bachofen R, Brandl H. Metal leaching of fly ash from municipal waste incineration by Aspergillus niger. Environ Sci Technol. 1996 Sep 26;30(10):3066-70.

57. Pradhan JK, Kumar S. Metals bioleaching from electronic waste by Chromobacterium violaceum and Pseudomonads sp. Waste Manag Res. 2012 Nov;30(11):1151-9.

58. Dusengemungu L, Kasali G, Gwanama C, Mubemba B. Overview of fungal bioleaching of metals. Environ Adv. 2021 Oct;5:100083.

59. Kanani N. Metal Finishing — A Key Technology? In: Kanani N, editors. Electroplating: Basic Principles, Processes and Practice. Oxford: Elsevier;2004. p. 1-19.

60. Jayakrishnan DS. Electrodeposition: The Versatile Technique for Nanomaterials. In: Saji VS, Cook R, editors. Corrosion Protection and Control Using Nanomaterials. Cambridge: Woodhead;2012. p. 86-125.

61. Lee S. Encyclopedia of Chemical Processing. 1st ed. Boca Raton: CRC Press;2005.

62. Vereecken PM, Binstead RA, Deligianni H, Andricacos PC. The chemistry of additives in damascene copper plating. IBM J Res Dev. 2005 Jan;49(1):3-18.

63. Moffat TP, Wheeler D, Josell D. Electrodeposition of Copper in the SPS-PEG-Cl Additive System: I. Kinetic Measurements: Influence of SPS. J Electrochem Soc. 2004 Mar 4;151(4).

64. Kanani N. Chapter 5 - Electrodeposition Considered at the Atomistic Level. In: Kanani N, editors. Electroplating: Basic Principles, Processes and Practice. Oxford: Elsevier;2004. p. 141-77.

65. Fisher AC. Electrode Dynamics. Oxford: Oxford University Press;1996.

66. Compton RG, Sanders GHW. Electrode Potentials. Oxford: Oxford University Press;1996.

67. Compton RG, Banks CE. Understanding Voltammetry. Singapore: World Scientific;2007.

68. Hamann CH, Hamnett A, Vielstich W. Electrochemistry. Weinheim: Wiley VCH;1998.

69. Montenegro I, Queirós MA, Daschbach DL. Microelectrodes: Theory and Applications. Netherlands: Kluwer Academic Publishers;1991.

70. Scharifker B, Hills G. Theoretical and experimental studies of multiple nucleation. Electrochim Acta. 1983 Jul;28(7):879-89.

71. Blum W, Beckman AO, Meyer WR. General Principles and Methods of Electroplating. Trans Electrochem Soc. 1941;80(1):249.

72. Pletcher D. A First Course in Electrode Processes. 2nd ed. Cambridge: Royal Society of Chemistry;2009.

73. Pise M, Muduli M, Chatterjee A, Kashyap BP, Singh RN, Tatiparti SSV. Instantaneous-Progressive nucleation and growth of palladium during electrodeposition. Results in Surfaces and Interfaces. 2022 Feb 1;6:100044.

74. Schlesinger ME, King MJ, Sole KC, Davenport WG. Extractive Metallurgy of Copper. 5th ed. Oxford: Elsevier;2011.

75. Gabrielli C, Moçotéguy P, Perrot H, Wiart R. Mechanism of copper deposition in a sulphate bath containing chlorides. J Electroanal Chem. 2004 Nov 1;572(2):367-75.

76. Grujicic D, Pesic B. Electrodeposition of copper: the nucleation mechanisms. Electrochim Acta. 2002 Jul 18;47(18):2901-12.

77. Anderson JL, Shain I. Cyclic voltammetric studies of the pH dependence of copper (II) reduction in acidic aqueous nitrate and perchlorate solutions. Anal Chem. 1976 Aug 1;48(9):1274-82.

78. Persson I, Persson P, Sandström M, Ullström A. Structure of Jahn-Teller distorted solvate copper (II) ions in solution, and in solids with apparently regular octahedral coordination geometry. Chem Soc. 2002 Mar 1;(7):1256-65.

79. Shtepliuk I, Vagin M, Yakimova R. Electrochemical Deposition of Copper on Epitaxial Graphene. Appl Sci. 2020 Feb 19;10(4):1405.

80. Shao W, Pattanaik G, Zangari G. Influence of chloride anions on the mechanism of copper electrodeposition from acidic sulfate electrolytes. J Electrochem Soc. 2007 Feb 5;154(4):D201.

81. Testa AC, Reinmuth WH. Chronopotentiometry with Step-Functional Change in Current. Anal Chem. 1961 Sept 1;33(10):1324-8.

82. Wagner ME, Valenzuela R, Vargas T, Colet-Lagrille M, Allanore A. Copper Electrodeposition Kinetics Measured by Alternating Current Voltammetry and the Role of Ferrous Species. J. Electrochem. Soc. 2016 Nov 5;163(2):D17.

83. Mattsson E, Bockris JOM. Galvanostatic studies of the kinetics of deposition and dissolution in the copper + copper sulphate system. Trans Faraday Soc. 1959;55:1586-601.

84. Nikolić ND, Branković G, Pavlović MG, Popov KI. The effect of hydrogen co-deposition on the morphology of copper electrodeposits. II. Correlation between the properties of electrolytic solutions and the quantity of evolved hydrogen. J Electroanal Chem. 2008 Sep 1;621(1):13-21.

85. Diculescu VC, Chiorcea-Paquim AM, Corduneanu O, Oliveira-Brett AM. Palladium nanoparticles and nanowires deposited electrochemically: AFM and electrochemical characterization. J Solid State Electrochem. 2007 Feb 14;11(7):887-98.

86. Lubert KH, Guttmann M, Beyer L. Electrode reactions and accumulation of hydrogen at carbon paste electrodes in the presence of tetrachloropalladate. J Electroanal Chem. 1999 Feb 18;462(2):174-180.

87. Li F, Zhang B, Dong S, Wang E. A novel method of electrodepositing highly dispersed nano palladium particles on glassy carbon electrode. Electrochim Acta. 1997;42(16):2563-8.

88. Pattabiraman R. Electrochemical investigations on carbon supported palladium catalysts. Appl Catal A-Gen. 1997 May 29;153(1-2):9-20.

89. Batchelor-McAuley C, Banks CE, Simm AO, Jones TG, Compton RG. Nano-Electrochemical Detection of Hydrogen or Protons Using Palladium Nanoparticles: Distinguishing Surface and Bulk Hydrogen. ChemPhysChem. 2006 May 12;7(5):1081-5.

90. Zhang W, Pesic B. Electrochemistry of $PdCl_2$ at glassy carbon electrode in 1-Ethyl-3-methylimidazolium chloride ionic liquid. Electrochim Acta. 2021 Feb 20;370:137818.

91. Yasin, HM, Denuault G, Pletcher D. Studies of the electrodeposition of platinum metal from a hexachloroplatinic acid bath. J Electroanal Chem. 2009 Aug 15;633(2):327-32.

92. Endo M, Takeda T, Kim Y, Koshiba K, Ishii K. High power electric double layer capacitor (EDLC's);from operating principle to pore size control in advanced activated carbons. Carbon Lett. 2001 Jan;1(3-4):117-28.

93. Grahame DC. The electrical double layer and the theory of electrocapillarity. Chem Rev. 1947 Dec 1;41(3):441-501.

94. Grahame DC. Mathematical theory of the Faradaic Admittance. J Electrochem Soc. 1952 Dec;52(12):370C-85C.

95. Cohen ER, editor. Quantities, units and symbols in physical chemistry. Royal Society of Chemistry;2007.

96. Guth U, Vonau W, Zosel J. Recent developments in electrochemical sensor application and technology-a review. Meas Sci Technol. 2009 Jan 27;20(4): 042002.

97. Mao G, Kilani M, Ahmed M. Review-Micro/Nanoelectrodes and Their Use in Electrocrystallization: Historical Perspective and Current Trends. J Electrochem Soc. 2022 Feb 16;169(2):022505.

98. Elliott JR, Compton RG. Local diffusion indicators: A new tool for analysis of electrochemical mass transport. J Electroanal Chem. 2022 Mar 22;908:116114.

99. Bobbert PA, Wind MM, Vlieger J. Diffusion to a slowly growing truncated sphere on a substrate. Physica A. 1987 Feb;141(1):58-72.

100. Ward KR, Lawrence NS, Hartshorne RS, Compton RG. Modelling the steady state voltammetry of a single spherical nanoparticle on a surface. J Electroanal Chem. 2012 Sept 1;683:37-42.

101. Li D, Batchelor-McAuley C, Compton RG. Some thoughts about reporting the electrocatalytic performance of nanomaterials. Appl Mater Today. 2020 Mar;18:100404.

102. Bockris JOM. The hydrogen economy: Its history. International Journal of Hydrogen Energy. 2013 Feb 27;38(6):2579-88.

103. Dou Y, Sun L, Ren J, Dong L. Chapter 17-Opportunities and future challenges in hydrogen economy for sustainable development. In: Scipioni A, Manzardo A, Ren J, editors. Hydrogen Economy (Second Edition). Academic Press;2023. p. 537-69.

104. Ren X, Wang Y, Liu A, Zhang Z, Lv Q, Liu B. Current progress and performance improvement of Pt/C catalysts for fuel cells. J Mater Chem A. 2020 Oct 20;8(46): 24284-306.

105. Fan L, Tu Z, Chan SH. Recent development of hydrogen and fuel cell technologies: A review. Energy Reports. 2021 Nov;7:8421-46.

106. Zalitis CM, Sharman J, Wright E, Kucernak AR. Properties of the hydrogen oxidation reaction on Pt/C catalysts at optimised high mass transport conditions and its relevance to the anode reaction in PEFCs and cathode reactions in electrolysers. Electrochim Acta. 2015 Sept 10;176:763-76.

107. Qiu Y, Xie X, Li W, Shao Y. Electrocatalysts development for hydrogen oxidation reaction in alkaline media: From mechanism understanding to materials design. Chinese Journal of Catalysis. 2021 Dec;42(12):2094-104.

108. Ma R, Lin G, Zhou Y, Liu Q, Zhang T, Shan G, et al. A review of oxygen reduction mechanisms for metal-free carbon-based electrocatalysts. npj Comput Mater. 2019 Jul 19;5:78.

109. Rothenberg G. Catalysis: Concepts and Green Applications. Weinheim: Wiley-VCH;2008.

110. Triki M, Minh DP, Ksibi Z, Ghorbel A, Gallezot P, Besson M. Preparation of ruthenium supported catalysts for wet air oxidation of p-hydroxybenzoic acid. In: Gaigneaux EM, Devillers M, De Vos DE, Hermans S, Jacobs PA, Martens JA, et al., editors. Studies in Surface Science and Catalysis. Oxford: Elsevier;2006. p. 609-16.

111. Climent MJ, Corma A, Iborra S. Heterogeneous Catalysts for the One-Pot Synthesis of Chemicals and Fine Chemicals. Chem Rev. 2011 Nov 24;111(2):1072-133.

112. Somorjai GA, Kliewer CJ. Reaction selectivity in heterogeneous catalysis. React Kinet Catal Lett. 2009 Apr 30;96:191-208.

113. Schlögl R. Heterogeneous Catalysis. Angew Chem Int Ed. 2015 Feb 18;54(11):3465-520.

114. Zhong L, Li S. Unconventional Oxygen Reduction Reaction Mechanism and Scaling Relation on Single-Atom Catalysts. ACS Catal. 2020 Mar 19;10(7):4313-8.

115. Holton OT, Stevenson JW. The Role of Platinum in Proton Exchange Membrane Fuel Cells. Platinum Metals Rev. 2013;57(4):259.

116. Xue Y, Shi L, Liu X, Fang J, Wang X, Setzler BP, et al. A highly-active, stable and low-cost platinum-free anode catalyst based on RuNi for hydroxide exchange membrane fuel cells. Nat Commun. 2020 Nov 6;11:5651.

117. Stratton SM, Zhang S, Montemore MM. Addressing complexity in catalyst design: From volcanos and scaling to more sophisticated design strategies. Surf Sci Rep. 2023 Aug;78(3):100597.

118. Nie Y, Li L, Wei Z. Recent advancements in Pt and Pt-free catalysts for oxygen reduction reaction. Chem Soc Rev. 2015 Feb 5;44(8):2168-201.

119. Nørskov JK, Rossmeisl J, Logadottir A, Lindqvist L, Kitchin JR, Bligaard T, Jónsson H. Origin of the Overpotential for Oxygen Reduction at a Fuel-Cell Cathode. J Phys Chem B. 2004 Oct 22;108(46):17886-92.

120. Samad S, Loh KS, Wong WY, Lee TK, Sunarso J, Chong ST, et al. Carbon and non-carbon support materials for platinum-based catalysts in fuel cells. Int J Hydrogen Energy. 2018 Apr 19;43(16):7823-54.

121. Antolini E. Carbon supports for low-temperature fuel cell catalysts. Appl Catal B Environ. 2009 Apr 29;88(1-2):1-24.

122. Das S, Pérez-Ramírez J, Gong J, Dewangan N, Hidajat K, Gates BC, et al. Core-shell structured catalysts for thermocatalytic, photocatalytic, and electrocatalytic conversion of CO2. Chem Soc Rev. 2020 May 14;49(10): 2937-3004.

123. Astruc D. Introduction: Nanoparticles in Catalysis. Chem Rev. 2020 Jan 22;120(2):461-3.

124. Ndolomingo MJ, Bingwa N, Meijboom R. Review of supported metal nanoparticles: synthesis methodologies, advantages and application as catalysts. J Mater Sci. 2020 Feb 12;55:6195-241.

125. Micka K. Depolarisation der Quecksilbertropfelektrode durch Suspensionen unlöslicher Stoffe I. Allgemeine Beobachtungen. Collect Czech Chem Commun. 1956;21(3):647-51.

126. Jones I, Kaye R. Polarography of carbon suspension. J Electroanal Chem Interf Electrochem. 1969 Feb 2;20:213-21.

127. Heyrovsky M, Jirkovsky J. Polarography and voltammetry of ultrasmall colloids: introduction to a new field. Langmuir. 1995;11(11):4288-92.

128. Heyrovsky M, Jirkovsky J, Struplova-Bartackova M. Polarography and voltammetry of aqueous colloidal TiO2 solutions. Langmuir. 1995;11(11):4300-8.

129. Heyrovsky M, Jirkovsky J, Mueller BR. Polarography and voltammetry of aqueous colloidal SnO2 solutions. Langmuir. 1995;11(11):4293-9.

130. Heyrovsky M, Jirkovsky J, Struplova-Bartackova M. Polarography and voltammetry of mixed titanium(IV) oxide/iron(III) oxide colloids. Langmuir. 1995;11(11):4309-12.

131. Pumera M. Impact Electrochemistry: Measuring Individual Nanoparticles. ACS Nano. 2014;8(8):7555-8.

132. Korshunov A, Heyrovský M, Bakardjieva S, Brabec L. Electrolytic Processes in Various Degrees of Dispersion. Langmuir. 2007 Dec 2;23(3):1523-9.

133. Zhou YG, Stuart EJE, Pillay J, Vilakazi S, Tshikhudo R, Rees NV, et al. Electrode-nanoparticle collisions: The measurement of the sticking coefficients of gold and nickel nanoparticles from aqueous solution onto a carbon electrode. Chem Phys Lett. 2012 Nov 1;551:68-71.

134. Xiao X, Pan S, Jang JS, Fan FRF, Bard AJ. Single Nanoparticle Electrocatalysis: Effect of Monolayers on Particle and Electrode on Electron Transfer. J Phys Chem C. 2009 Jul 28;113(33):14978-82.

135. Xiao X, Fan FRF, Zhou J, Bard AJ. Current Transients in Single Nanoparticle Collision Events. J Am Chem Soc. 2008 Nov 14;130(49):16669-77.

136. Hellberg D, Scholz F, Schauer F, Weitschies W. Bursting and spreading of liposomes on the surface of a static mercury drop electrode. Electrochem Commun. 2002 Apr;4(4):305-9.

137. Zhou YG, Rees NV, Compton RG. Nanoparticle-electrode collision processes: The electroplating of bulk cadmium on impacting silver nanoparticles. Chem Phys Lett. 2011 Aug;511(4-6):183-6.

138. Dasari R, Walther B, Robinson DA, Stevenson KJ. Influence of the Redox Indicator Reaction on Single-Nanoparticle Collisions at Mercury- and Bismuth-Modified Pt Ultramicroelectrodes. Langmuir. 2013 Nov 4;29(48):15100-6.

139. Robinson DA, Liu Y, Edwards MA, Vitti NJ, Oja SM, Zhang B, White HS. Collision Dynamics during the Electrooxidation of Individual Silver Nanoparticles. J Am Chem Soc. 2017 Oct 30;139(46):16923-31.

140. Saw EN, Blanc N, Kanokkanchana K, Tschulik K. Time-resolved impact electrochemistry - A new method to determine diffusion coefficients of ions in solution. Electrochim Acta. 2018;282:317-23.

141. Rees NV, Zhou Y, Compton R. The aggregation of silver nanoparticles in aqueous solution investigated via anodic particle coulometry. Chemphyschem. 2011;12(9):1645-7.

142. Haddou B, Rees NV, Compton RG. Nanoparticle-electrode impacts: the oxidation of copper nanoparticles has slow kinetics. Phys Chem Chem Phys. 2012 Aug 21;14(39):13612-7.

143. Zhou YG, Haddou B, Rees NV, Compton RG. The charge transfer kinetics of the oxidation of silver and nickel nanoparticles via particle-electrode impact electrochemistry. Physical Chemistry Chemical Physics. 2012 Sept 10;14(41):14354-7.

144. Tschulik K, Haddou B, Omanović D, Rees NV, Compton RG. Coulometric sizing of nanoparticles: Cathodic and anodic impact experiments open two independent routes to electrochemical sizing of Fe_3O_4 nanoparticles. Nano Research. 2013 Sept 3;6:836-41.

145. Nasir MZ, Pumera M. Impact electrochemistry on screen-printed electrodes for the detection of monodispersed silver nanoparticles of sizes 10-107 nm. Phys Chem Chem Phys. 2016 Oct 3;18(40):28183-8.

146. Teo WZ, Pumera M. Fate of silver nanoparticles in natural waters;integrative use of conventional and electrochemical analytical techniques. RSC Adv. 2014 Jan 2;4(10):5006-11.

147. Stuart EJ, Zhou YG, Rees NV, Compton RG. Determining unknown concentrations of nanoparticles: the particle-impact electrochemistry of nickel and silver. Rsc Adv. 2012 Jun 1;2(17):6879-84.

148. Lim CS, Pumera M. Impact electrochemistry: colloidal metal sulfide detection by cathodic particle coulometry. Phys Chem Chem Phys. 2015 Sept 28;17(40):26997-7000.

149. Kwon SJ, Bard AJ. Analysis of diffusion-controlled stochastic events of iridium oxide single nanoparticle collisions by scanning electrochemical microscopy. J Am Chem Soc. 2012 Apr 27;134(16):7102-8.

150. Zhou YG, Rees NV, Compton RG. The electrochemical detection of tagged nanoparticles via particle-electrode collisions: nanoelectroanalysis beyond immobilisation. Chem Commun. 2012 Jan 16;48(19):2510-2.

151. Kwon SJ, Fan FR, Bard AJ. Observing iridium oxide (IrO x) single nanoparticle collisions at ultramicroelectrodes. J Am Chem Soc. 2010 Sep 1;132(38):13165-7.

152. Kwon SJ, Zhou H, Fan FR, Vorobyev V, Zhang B, Bard AJ. Stochastic electrochemistry with electrocatalytic nanoparticles at inert ultramicroelectrodes—theory and experiments. Phys Chem Chem Phys. 2011 Feb 28;13(12):5394-402.

153. Zhou YG, Rees NV, Compton RG. Electrochemistry of nickel nanoparticles is controlled by surface oxide layers. Phys Chem Chem Phys. 2013 Nov 16;15(3):761-3.

154. Stuart EJ, Rees NV, Compton RG. Particle-impact voltammetry: The reduction of hydrogen peroxide at silver nanoparticles impacting a carbon electrode. Chem Phys Lett. 2012 Apr 2;531:94-7.

155. Rees NV, Zhou YG, Compton RG. Making contact: charge transfer during particle-electrode collisions. Rsc Adv. 2012;2(2):379-84.

156. Zhou YG, Rees NV, Compton RG. The electrochemical detection and characterization of silver nanoparticles in aqueous solution. Angew Chem Int Ed. 2011 Apr 7;18(50):4219-21.

157. Cheng W, Zhou XF, Compton RG. Electrochemical sizing of organic nanoparticles. Angew Chem Int Ed. 2013 Oct 16;52(49):12980-2.

158. Stuart EJE, Tschulik K, Batchelor-McAuley C, Compton RG. Electrochemical Observation of Single Collision Events: Fullerene Nanoparticles. ACS Nano. 2014 Jun 23;8(8):7648-54.

159. Xiao X, Bard AJ. Observing single nanoparticle collisions at an ultramicroelectrode by electrocatalytic amplification. J Am Chem Soc. 2007 Aug 8;129(31):9610-2.

160. Guo Z, Percival SJ, Zhang B. Chemically Resolved Transient Collision Events of Single Electrocatalytic Nanoparticles. J Am Chem Soc. 2014 Jun 7;136(25):8879-82.

161. Zhou YG, Rees NV, Compton RG. Nanoparticle-electrode collision processes: the underpotential deposition of thallium on silver nanoparticles in aqueous solution. ChemPhysChem. 2011 Jun 7;12(11):2085-7.

162. Keal ME, Courtney JM, Rees NV. Redox Electrochemistry of Mn(II) via Carbon Black Nanoparticle Impacts. J. Phys. Chem. C. 2023 Jun 28;127(27):13380-8.

163. Zampardi G, Compton RG. Fast electrodeposition of zinc onto single zinc nanoparticles. J Solid State Electrochem. 2020 Mar 14;24:2695-702.

164. Ma H, Chen JF, Wang HF, Hu PJ, Ma W, Long YT. Exploring dynamic interactions of single nanoparticles at interfaces for surface-confined electrochemical behavior and size measurement. Nat Commun. 2020 May 8;11(1):2307.

165. Dasari R, Robinson DA, Stevenson KJ. Ultrasensitive Electroanalytical Tool for Detecting, Sizing, and Evaluating the Catalytic Activity of Platinum Nanoparticles. J Am Chem Soc. 2013 Dec 27;135(2):570-3.

166. Zhou YG, Rees NV, Compton RG. Electrode-nanoparticle collisions: The measurement of the sticking coefficient of silver nanoparticles on a glassy carbon electrode. Chem Phys Lett. 2011 Oct 6;514(4-6):291-3.

167. Tuncuk A, Stazi V, Akcil A, Yazici EY, Deveci H. Aqueous metal recovery techniques from e-scrap: Hydrometallurgy in recycling. Miner Eng. 2012 Jan;25(1):28-37.

168. Botelho JAB, Vicente AdA, Espinosa DCR, Tenório JAS. Recovery of metals by ion exchange process using chelating resin and sodium dithionite. J Mater Res Technol. 2019 Sept;8(5):4464-9.

169. Pohl A. Removal of Heavy Metal Ions from Water and Wastewaters by Sulfur-Containing Precipitation Agents. Water Air Soil Pollut. 2020 Sept 28;231(10):503.

170. Jha MK, Lee JC, Kim MS, Jeong J, Kim BS, Kumar V. Hydrometallurgical recovery/recycling of platinum by the leaching of spent catalysts: A review. Hydrometallurgy. 2013 Feb;133:23-32.

171. Song D, Zhou YG. From ensemble electrochemistry to nanoparticle-impact electrochemistry: Altered reaction process and possible applications. Curr Opin Electrochem. 2022 Aug;34:101011.

172. Kumar AKS, Zhang Y, Li D, Compton RG. A mini-review: How reliable is the drop casting technique? Electrochem Commun. 2020 Dec;121:106867.

173. Nguyen NT. Chapter 4 - Fabrication technologies. In: Nguyen NT, editor. Micromixers (Second Edition). William Andrew Publishing;2012. p. 113-61.

174. Jerkiewicz G. Standard and reversible hydrogen electrodes: theory, design, operation, and applications. ACS Catalysis. 2020;10(15):8409-17.

175. Celante VG, Freitas MBJG. Electrodeposition of copper from spent Li-ion batteries by electrochemical quartz crystal microbalance and impedance spectroscopy techniques. J Appl Electrochem. 2010;40(2):233-9.

176. Granados-Fernández R, Montiel MA, Díaz-Abad S, Rodrigo MA, Lobato J. Platinum Recovery Techniques for a Circular Economy. Catalysts. 2021 Jul 31;11(8):937.

177. Montegrossi G, Giaccherini A, Berretti E, Di Benedetto F, Innocenti M, d'Acapito F, Lavacchi A. Computational Speciation Models: A Tool for the Interpretation of Spectroelectrochemistry for Catalytic Layers under Operative Conditions. J Electrochem Soc. 2017 Aug 11;164(11):E3690.

178. Batchelor-McAuley C, Ellison J, Tschulik K, Hurst PL, Boldt R, Compton RG. In situ nanoparticle sizing with zeptomole sensitivity. Analyst. 2015;140(15):5048-54.

179. Jiao X, Batchelor-McAuley C, Lin C, Kätelhön E, Tanner EE, Young NP, Compton RG. Role of nanomorphology and interfacial structure of platinum nanoparticles in catalyzing the hydrogen oxidation reaction. Acs Catalysis. 2018 May 25;8(7):6192-202.

180. Kanokkanchana K, Saw EN, Tschulik K. Nano impact electrochemistry: effects of electronic filtering on peak height, duration and area. ChemElectroChem. 2018 Oct 12;5(20):3000-5.

181. Bilo F, Cirelli P, Borgese L. Elemental analysis of particulate matter by X-ray fluorescence methods: A green approach to air quality monitoring. Trends Anal Chem. 2024 Jan;170:117427.

182. Singh MK, Singh A. Scanning electron microscope. In: Singh MK, Singh A, editors. Characterization of Polymers and Fibres. Woodhead Publishing;2022. p. 387-419.

183. Stachowiak GW, Batchelor AW, Stachowiak GB. Surface Micrography and Analysis. In: Stachowiak GW, Batchelor AW, Stachowiak GB, editors. Tribology Series. Elsevier;2004. p. 165-220.

184. Wilschefski SC, Baxter MR. Inductively Coupled Plasma Mass Spectrometry: Introduction to Analytical Aspects. Clin Biochem Rev. 2019 Aug;40(3):115-33.

185. Huang H, Qiao Y, Yuan Y, Zhang J. Surface functionalization for heterogeneous catalysis. In: Yin Y, Lu Y, Xia Y, editors. Encyclopedia of Nanomaterials. Elsevier;2023. p. 407-19.

186. Lee HJ, Cho MK, Jo YY, Lee KS, Kim HJ, Cho EA, Kim SK, Henkensmeier D, Lim TH, Jang JH. Application of TGA techniques to analyze the compositional and structural degradation of PEMFC MEAs. Polym Degrad Stab. 2012;97(6):1010-6.

187. Rees NV. Electrochemical insight from nanoparticle collisions with electrodes: a mini review. Electrochem Commun. 2014 Jun 1;43:83-6.

188. Markham J, Young NP, Batchelor-McAuley C, Compton RG. Bipolar nanoimpact transients: controlling the redox potential of nanoparticles in solution. The Journal of Physical Chemistry C. 2020 May 29;124(25):14043-53.

189. Zhang JH, Zhou YG. Nano-impact electrochemistry: Analysis of single bioentities. Trends Anal Chem. 2020 Feb;123:115768.

190. Nose K, Okabe TH. Platinum Group Metals Production. In: Seetharaman S, editor. Treatise on Process Metallurgy. Elsevier;2014. p. 1071-97.

191. Hagelüken C. Recycling of (critical) metals. In: Gunn G, editor. Critical Metals Handbook. Wiley;2013. p. 41.

192. Sheoran AS, Sheoran V. Heavy metal removal mechanism of acid mine drainage in wetlands: A critical review. Minerals Engineering. 2006;19(2):105-16.

193. Barakat MA. New trends in removing heavy metals from industrial wastewater. Arabian Journal of Chemistry. 2011;4(4):361-77.

194. Lu H, Wang Y, Wang J. Recovery of Ni2+ and pure water from electroplating rinse wastewater by an integrated two-stage electrodeionization process. J Clean Prod. 2015;92:257-66.

195. Kurniawan TA, Chan GYS, Lo WH, Babel S. Physico-chemical treatment techniques for wastewater laden with heavy metals. Chem Eng J. 2006;118(1-2):83-98.

196. Jin W, Zhang Y. Sustainable Electrochemical Extraction of Metal Resources from Waste Streams: From Removal to Recovery. ACS Sustain Chem Eng. 2020;8(12):4693-707.

197. Meunier N, Drogui P, Montané C, Hausler R, Mercier G, Blais JF. Comparison between electrocoagulation and chemical precipitation for metals removal from acidic soil leachate. J Hazard Mater. 2006;137(1):581-90.

198. Zhang C, Jiang Y, Li Y, Hu Z, Zhou L, Zhou M. Three-dimensional electrochemical process for wastewater treatment: A general review. Chem Eng J. 2013;228:455-67.

199. Tran TK, Leu HJ, Chiu KF, Lin CY. Electrochemical Treatment of Heavy Metal-containing Wastewater with the Removal of COD and Heavy Metal Ions. J Chin Chem Soc. 2017;64:493-502.

200. Scott K, Paton EM. An analysis of metal recovery by electrodeposition from mixed metal ion solutions—part II. Electrodeposition of cadmium from process solutions. Electrochim Acta. 1993;38(15):2191-7.

201. Diaz LA, Lister TE, Parkman JA, Clark GG. Comprehensive process for the recovery of value and critical materials from electronic waste. J Clean Prod. 2016;125:236-44.

202. Tanong K, Tran LH, Mercier G, Blais JF. Recovery of Zn (II), Mn (II), Cd (II) and Ni (II) from the unsorted spent batteries using solvent extraction, electrodeposition and precipitation methods. J Clean Prod. 2017;148:233-44.

203. Zhang L, Song Q, Liu Y, Xu Z. An integrated capture of copper scrap and electrodeposition process to enrich and prepare pure palladium for recycling of spent catalyst from automobile. Waste Manag. 2020;108:172-82.

204. Masavetas I, Moutsatsou A, Nikolaou E, Spanou S, Zoikis-Karathansis A, Pavlatou EA, Spyrellis N. Production of copper powder from printed circuit boards by electrodeposition. Glob. Nest J. 2009;11:241.

205. Vassilev SV, Vassileva CG. Methods for Characterization of Composition of Fly Ashes from Coal-Fired Power Stations: A Critical Overview. Energy & Fuels. 2005;19(3):1084-98.

206. Ranjbar N, Kuenzel C. Cenospheres: A review. Fuel. 2017 Nov 1;207:1-12.

207. Shukla S, Seal S, Akesson J, Oder R, Carter R, Rahman Z. Study of mechanism of electroless copper coating of fly-ash cenosphere particles. Appl Surf Sci. 2001;181(1-2):35-50.

208. Yu X, Xu Z, Shen Z. Metal copper films deposited on cenosphere particles by magnetron sputtering method. J Phys D Appl Phys. 2007;40:2894.

209. Yu YT. Preparation of nanocrystalline TiO2-coated coal fly ash and effect of iron oxides in coal fly ash on photocatalytic activity. Powder Technology. 2004;146(1-2):154-59.

210. Żukowski W, Migas P, Bradło D, Dulian P. Synthesis and Performance of TiO2/Fly Ash Cenospheres as a Catalytic Film in a Novel Type of Periodic Air-Sparged Photocatalytic Reactor. Materials. 2020;13(7):1691.

211. Blissett RS, Rowson NA. A review of the multi-component utilisation of coal fly ash. Fuel. 2012;97:1-23.

212. Scott K, Chen X, Atkinson JW, Todd M, Armstrong RD. Electrochemical recycling of tin, lead and copper from stripping solution in the manufacture of circuit boards. Resour Conserv Recycl. 1997 Jun 1;20(1):43-55.

213. Dietterle M, Will T, Kolb DM. The initial stages of copper deposition on Ag (111): an STM study. Surf Sci. 1995 Nov 20;342(1-3):29-37.

214. Shi Z, Wu S, Lipkowski J. Coadsorption of metal atoms and anions: Cu upd in the presence of SO42−, Cl− and Br−. Electrochim Acta. 1995 Jan 1;40(1):9-15.

215. Omar IH, Pauling HJ, Jüttner K. Underpotential Deposition of Copper on Au (III) Single-Crystal Surfaces: A Voltammetric and Rotating Ring Disk Electrode Study. J Electrochem Soc. 1993 Aug 1;140(8):2187.

216. Schneeweiss MA, Kolb DM. The inPetrus chemically modified gold electrodes. phys status solidi A. 1999 May;173(1):51-71.

217. Herrero E, Buller LJ, Abruña HD. Underpotential deposition at single crystal surfaces of Au, Pt, Ag and other materials. Chem Rev. 2001 Jul 11;101(7):1897-930.

218. Szabó S. Underpotential deposition of metals on foreign metal substrates. Int Rev Phys Chem. 1991 Aug 11;10(2):207-48.

219. Cappadonia M, Linke U, Robinson KM, Schmidberger J, Stimming U. Anion effects on the cyclic voltammetry of copper underpotential deposition on Au(100). J Electroanal Chem. 1996;405(1-2):227-32.

220. Li J, Eheliyagoda D, Geng Y, Yang Z, Zeng X. Examining the influence of copper recycling on prospective resource supply and carbon emission reduction. Fundam Res. 2022 Oct 15.

221. Wang T, Berrill P, Zimmerman JB, Hertwich EG. Copper Recycling Flow Model for the United States Economy: Impact of Scrap Quality on Potential Energy Benefit. Environmental Science & Technology. 2021 Apr 20;55(8):5485-95.

222. Young KE, Evans CA, Hodges KV, Bleacher JE, Graff TG. A review of the handheld X-ray fluorescence spectrometer as a tool for field geologic investigations on Earth and in planetary surface exploration. Applied Geochemistry. 2016 Sept;72:77-87.

223. Voiry D, Chhowalla M, Gogotsi Y, Kotov NA, Li Y, Penner RM, et al. Best Practices for Reporting Electrocatalytic Performance of Nanomaterials. ACS Nano. 2018 Oct 23;12(10):9635-8.

224. Sanchis-Gual R, Seijas-Da Silva A, Coronado-Puchau M, Otero TF, Abellán G, Coronado E. Improving the onset potential and Tafel slope determination of earth-abundant water oxidation electrocatalysts. Electrochim Acta. 2021 Aug 20;388:138613.

225. Andersen JET, Bech-Nielsen G, Møller P, Reeve JC. Bulk copper electrodeposition on gold imaged by in situ STM: morphology and influence of tip potential. J Appl Electrochem. 1996;26(2):161-70.

226. Tschulik K, Batchelor-McAuley C, Toh HS, Stuart EJ, Compton RG. Electrochemical studies of silver nanoparticles: a guide for experimentalists and a perspective. Phys. Chem. Chem. Phys. 2014;16(2):616-23.

227. Hachiya T, Honbo H, Itaya K. Detailed underpotential deposition of copper on gold(III) in aqueous solutions. J Electroanal Chem Interfac Electrochem. 1991 Oct 10;315(1-2):275-91.

228. Randler RJ, Kolb DM, Ocko BM, Robinson IK. Electrochemical copper deposition on Au(100): a combined in situ STM and in situ surface X-ray diffraction study. Surf Sci. 2000 Feb 20;447(1-3):187-200.

229. Liu J, Liang Y, Lui T, Li D, Yang X. Anti-EGFR-Conjugated Hollow Gold Nanospheres Enhance Radiocytotoxic Targeting of Cervical Cancer at Megavoltage Radiation Energies. Nanoscale Res Lett. 2015 May 15;10:218.

230. Thiel K-O, Hintze M, Vollmer A, Donner C. A new approach on the Cu UPD on Ag surfaces. J Electroanal Chem. 2008 Sept 1;621(1):7-12.

231. Bolz RE. CRC Handbook of Tables for Applied Engineering Science. 2nd ed. CRC Press;1973.

232. Bartlett TR, Sokolov SV, Compton RG. Electrochemical Nanoparticle Sizing Via Nano-Impacts: How Large a Nanoparticle Can be Measured?. ChemistryOpen. 2015 Oct;4(5):600-5.

233. Russel WB. Brownian motion of small particles suspended in liquids. Annu Rev Fluid Mech. 1981;13(1):425-55.

234. Ma W, Ma H, Chen J-F, Peng YY, Yang Z-Y, Wang HF, et al. Tracking motion trajectories of individual nanoparticles using time-resolved current traces. Chem Sci. 2017 Dec 12;8(3):1854-61.

235. Brainina KZ, Galperin LG, Vikulova EV. Electrochemistry of metal nanoparticles: the effect of substrate. J Solid State Electrochem. 2012;16(7):2357-63.

236. Danilov AI, Molodkina EB, Polukarov YM. Initial stages of copper electrocrystallization on a glassy-carbon ring-disk electrode from sulfate electrolytes of various acidity: a cyclic voltammetry study. Russ J Electrochem. 2002;38(7):732-42.

237. Crousier J, Bimaghra I. Electrodeposition of copper from sulphate and chloride solutions. Electrochim Acta. 1989;34(8):1205-11.

238. Vannoy KJ, Ryabykh A, Chapoval AI, Dick JE. Single enzyme electroanalysis. Analyst. 2021;146(11):3413-21.

239. Jamali MR, Assadi Y, Kozani RR. Determination of Trace Amounts of Palladium in Water Samples by Graphite Furnace Atomic Absorption Spectrometry after Dispersive Liquid-Liquid Microextraction. J Chem. 2012;2013:671743.

240. Antolini E. Palladium in Fuel Cell Catalysis. Energy Environ Sci. 2009;2:915-31.

241. Kumar SS, Ramakrishna SUB, Devi BR, Himabindu V. Phosphorus-doped carbon nanoparticles supported palladium electrocatalyst for the hydrogen evolution reaction (HER) in PEM water electrolysis. Ionics. 2018;24:3113-21.

242. Huang Y-X, Liu X-W, Sun X-F, Sheng G-P, Zhang Y-Y, Yan G-M, et al. A new cathodic electrode deposit with palladium nanoparticles for cost-effective hydrogen production in a microbial electrolysis cell. Int J Hydrogen Energy. 2011;36:2773-6.

243. Alexeyeva N, Sarapuu A, Tammeveski K, Vidal-Iglesias FJ, Solla-Gullón J, Feliu JM. Electroreduction of Oxygen on Vulcan Carbon Supported Pd Nanoparticles and Pd-M Nanoalloys in Acid and Alkaline Solutions. Electrochim Acta. 2011;56:6702-8.

244. Seo MH, Choi SM, Lee DU, Kim WB, Chen Z. Correlation Between Theoretical Descriptor and Catalytic Oxygen Reduction Activity of Graphene Supported Palladium and Palladium Alloy Electrocatalysts. J Power Sources. 2015;300:1-9.

245. Safavi A, Kazemi SH, Kazemi H. Electrocatalytic Behaviors of Silver−Palladium Nanoalloys Modified Carbon Ionic Liquid Electrode Towards Hydrogen Evolution Reaction. Fuel. 2014;118:156-62.

246. Shao M. Palladium-based Electrocatalysts for Hydrogen Oxidation and Oxygen Reduction Reactions. J Power Sources. 2011;196:2433-44.

247. Limpattayanate S, Hunsom M. Electrocatalytic Activity of Pt−Pd Electrocatalysts for The Oxygen Reduction Reaction in Proton Exchange Membrane Fuel Cells: Effect of Supports. Renewable Energy. 2014;63:205-11.

248. Sarkar S, Peter SC. An Overview on Pd-Based Electrocatalysts for The Hydrogen Evolution Reaction. Inorg Chem Front. 2018;5:2060-80.

249. Katara P. Review Paper on Catalytic Converter for Automobile Exhaust Emission. Int J Sci Res. 2016;5:30-3.

250. Roy K, Jain R, Ghosalya MK, Reddy KP, Gopinath CS. Three-Way Catalytic Converter Reactions Aspects at Near-Ambient Temperatures on Modified Pd-Surfaces. C R Chim. 2016;19:1363-9.

251. Wolfe JP, Singer RA, Yang BH, Buchwald SL. Highly Active Palladium Catalysts for Suzuki Coupling Reactions. J Am Chem Soc. 1999;121:9550-61.

252. Li Z, Bucbaum C, Heaner WL IV, Fisk J, Jaganathan A, Holden B, et al. Palladium-Catalyzed Suzuki Reactions in Water with No Added Ligand: Effects of Reaction Scale, Temperature, pH of Aqueous Phase, and Substrate Structure. Org Process Res Dev. 2016;20:1489-99.

253. Miyaura N, Suzuki A. Palladium-Catalyzed Cross-Coupling Reactions of Organoboron Compounds. Chem Rev. 1995;95:2457-83.

254. Suzuki A. Recent Advances in The Cross-Coupling Reactions of Organoboron Derivatives with Organic Electrophiles. J Organomet Chem. 1999;576:147-68.

255. Bellina F, Carpita A, Rossi R. Palladium Catalysts for the Suzuki Cross-Coupling Reaction: An Overview of Recent Advances. Synthesis. 2004;2004:2419-40.

256. Magano J, Dunetz JR. Large-Scale Applications of Transition Metal-Catalyzed Couplings for the Synthesis of Pharmaceuticals. Chem Rev. 2011;111:2177-250.

257. Nasrollahzadeh M, Sajadi SM, Maham M. Green Synthesis of Palladium Nanoparticles Using Hippophae Rhamnoides Linn Leaf Extract and Their Catalytic Activity for The Suzuki−Miyaura Coupling in Water. J Mol Catal A: Chem. 2015;396:297-303.

258. Siddiqi KS, Husen A. Green Synthesis, Characterization and Uses of Palladium/Platinum Nanoparticles. Nanoscale Res Lett. 2016;11:482.

259. Mandali PK, Chand DK. Palladium Nanoparticles Catalyzed Suzuki Cross-Coupling Reactions in Ambient Conditions. Catal Commun. 2013;31:16-20.

260. Oosthuizen RS, Nyamori VO. Carbon Nanotubes as Supports for Palladium and Bimetallic Catalysts for Use in Hydrogenation Reactions. Platinum Met Rev. 2011;55:154-69.

261. Fuentes AS, Filippin AF, Aguirre MDC. Pd Nucleation and Growth Mechanism Deposited on Different Substrates. Procedia Mater Sci. 2015;8:541-50.

262. Singh SB, Tandon PK. Catalysis: A Brief Review on Nano-Catalyst. J Energy Chem. 2014;2:106-15.

263. Mahesh KN, Balaji R, Dhathathreyan KS. Palladium Nanoparticles as Hydrogen Evolution Reaction (HER) Electrocatalyst in Electrochemical Methanol Reformer. Int J Hydrogen Energy. 2016;41:46-51.

264. Wang XX, Tan ZH, Zeng M, Wang JN. Carbon Nanocages: A New Support Material for Pt Catalyst with Remarkably High Durability. Sci Rep. 2014;4:4437.

265. Su DS, Centi GA. Perspective on Carbon Materials for Future Energy Application. J Energy Chem. 2013;22:151-73.

266. Pushkarev AS, Pushkareva IV, Grigoriev SA, Kalinichenko VN, Presniakov MY, Fateev VN. Electrocatalytic Layers Modified by Reduced Graphene Oxide for PEM Fuel Cells. Int J Hydrogen Energy. 2015;40:14492-7.

267. Ramakrishna SUB, Reddy DS, Kumar SS, Himabindu V. Nitrogen Doped CNTs Supported Palladium Electrocatalyst for Hydrogen Evolution Reaction in PEM Water Electrolyser. Int J Hydrogen Energy. 2016;41:20447-54.

268. Serp P, Corrias M, Kalck P. Carbon Nanotubes and Nanofibers in Catalysis. Appl Catal A. 2003;253:337-58.

269. Mondal KC, Cele LM, Witcomb MJ, Coville NJ. Carbon Microsphere Supported Pd Catalysts for Hydrogenation of Ethylene. Catal Commun. 2008;9:494-8.

270. Rao CRK, Trivedi DC. Chemical and Electrochemical Depositions of Platinum Group Metals and Their Applications. Coord Chem Rev. 2005;249:613-31.

271. Thiagarajan S, Yang R, Chen S. Palladium Nanoparticles Modified Electrode for The Selective Detection of Catecholamine Neurotransmitters in Presence of Ascorbic Acid. Bioelectrochemistry. 2009;75:163-9.

272. Liu S, Li H, Shi M, Jiang H, Hu X, Li W, Fu L, Chen H. Pd/C as a Clean and Effective Heterogeneous Catalyst for C−C Couplings toward Highly Pure Semiconducting Polymers. Macromolecules. 2012;45:9004-9.

273. Miyake H, Okada T, Samjeskéb G, Osawa M. Formic Acid Electrooxidation on Pd in Acidic Solutions Studied by Surface-Enhanced Infrared Absorption Spectroscopy. Phys Chem Chem Phys. 2008;10:3662-9.

274. Pavese AG, Solis VM, Giordano MC. Oxidation of Formic Acid on Palladium Anodes in Acidic Medium. Effect of Pd(II) Ions. Electrochim Acta. 1987;32:1213-6.

275. Zhu Y, Khan Z, Masel RI. The Behavior of Palladium Catalysts in Direct Formic Acid Fuel Cells. J Power Sources. 2005;139:15-20.

276. Erikson H, Sarapuu A, Tammeveski K, Solla-Gullón J, Feliu JM. Enhanced Electrocatalytic Activity of Cubic Pd Nanoparticles Towards the Oxygen Reduction Reaction in Acid Media. Electrochem Commun. 2011;13:734-7.

277. Wang X, Li Z, Qu Y, Yuan T, Wang W, Wu Y, Li Y. Review of Metal Catalysts for Oxygen Reduction Reaction: From Nanoscale Engineering to Atomic Design. Chem. 2019;5:1486-511.

278. Chen A, Ostrom C. Palladium-Based Nanomaterials: Synthesis and Electrochemical Applications. Chem Rev. 2015;115:11999-2044.

279. Aarzoo, Nidhi, Samim M. Palladium Nanoparticles as Emerging Pollutants from Motor Vehicles: An In-Depth Review on Distribution, Uptake, and Toxicological Effects in Occupational and Living Environment. Sci Total Environ. 2022;823:153787.

280. Leśniewska BA, Godlewska-Żyłkiewicz B, Bocca B, Caimi S, Caroli S, Hulanicki A. Platinum, Palladium and Rhodium Content in Road Dust, Tunnel Dust and Common Grass in Biaystok Area (Poland): A Pilot Study. Sci Total Environ. 2004;321(1-3):93-104.

281. Gómez B, Palacios MA, Gómez M, Sanchez JL, Morrison G, Rauch S, et al. Levels and Risk Assessment for Humans and Ecosystems Of Platinum-Group Elements In The Airborne Particles And Road Dust Of Some European Cities. Sci Total Environ. 2002;299(1-3):1-19.

282. Helmers E, Schwarzer M, Schuster M. Comparison of Palladium and Platinum in Environmental Matrices: Palladium Pollution by Automobile Emissions? Environ Sci Pollut Res. 1998;5:44-50.

283. Boch K, Schuster M, Risse G, Schwarzer M. Microwave-Assisted Digestion Procedure for The Determination of Palladium in Road Dust. Anal Chim Acta. 2002;459(2):257-65.

284. Lottermoser BG. Noble Metals in Municipal Sewage Sludges of Southeastern Australia. Ambio. 1995;24:354-7.

285. Mansor N, Mohamed N, Suah FBM. Electrochemical Recovery of Low Concentration of Palladium from Palladium(II) Chloride of Electroplating Wastewater. J Chem Technol Biotechnol. 2021;96(11):3216-23.

286. Melber C, Keller D, Mangelsdorf I. International Programme on Chemical Safety. Palladium. Environmental Health Criteria Series. 2002.

287. Moore JW, Hall L, Campbell K, Stara J. Preliminary Studies on The Toxicity and Metabolism of Palladium and Platinum. Environ Health Perspect. 1975;10:63-71.

288. Hassanien MM, Mortada WI, Kenawy IM. Selective Separation of Palladium from Synthetic Highly Active Liquid Waste By Cloud Point Extraction Using Benzil Mono-(2-Pyridyl) Hydrazone And Triton X-114. J Radioanal Nucl Chem. 2014;303:261-9.

289. Rosso JP. Maximize Precious Metal Recovery from Spent Catalysts. Chem Eng Prog. 1992;88:66-72.

290. Lassner JA, Lasher LB, Koppel RL, Hamilton JN. Reclaim Spent Catalysts Properly. Chem Eng Prog. 1994;90:95.

291. Le MN, Lee MS. A Review on Hydrometallurgical Processes for The Recovery of Valuable Metals From Spent Catalysts And Life Cycle Analysis Perspective. Miner Process Extr Metall Rev. 2020;42(5):335-54.

292. Sethurajan M, Hullebusch EDV, Fontana D, Akcil A, Deveci H, Batinic B,et al. Recent Advances on Hydrometallurgical Recovery of Critical and Precious Elements from End of Life Electronic Wastes - A Review. Crit Rev Environ Sci Technol. 2019;49(3):212-75.

293. Hoffmann JE. Recovery of Platinum-Group Metals from Gabbroic Rocks Metals from Auto Catalysts. JOM. 1988;40(6):40-4.

294. Bourgeois D, Lacanau V, Mastretta R, Contino-Pépin C, Meyer D. A Simple Process for The Recovery of Palladium from Wastes of Printed Circuit Boards. Hydrometallurgy. 2020;191:105241.

295. Zhang Z, Zhang S. Selective Recovery of Palladium from Waste Printed Circuit Boards by A Novel Non-Acid Process. J Hazard Mater. 2014;279:46-51.

296. Yazici EY, Deveci H. Extraction of Metals from Waste Printed Circuit Boards (WPCBs) in H2SO4−CuSO4−NaCl Solutions. Hydrometallurgy. 2013;139:30-8.

297. Prabaharan G, Barik SP, Kumar B. A Hydrometallurgical Process for Recovering Total Metal Values from Waste Monolithic Ceramic Capacitors. Waste Manage. 2016;52:302-8.

298. Fontana D, Pietrantonio M, Pucciarmati S, Torelli GN, Bonomi C, Masi F. Palladium Recovery from Monolithic Ceramic Capacitors by Leaching, Solvent Extraction and Reduction. J Mater Cycles Waste Manag. 2018;20:1199-206.

299. Behnamfard A, Salarirad M, Veglio F. Process Development for Recovery of Copper and Precious Metals from Waste Printed Circuit Boards with Emphasize on Palladium and Gold Leaching and Precipitation. Waste Manage. 2013;33:2354-63.

300. Ponou J, Wang LP, Dodbiba G, Fujita T. Separation of Palladium and Silver from Semiconductor Solid Waste by Means of Liquid-Liquid-Powder Extraction Using Dodecyl Amine Acetate as A Surfactant Collector. Sep Purif Technol. 2018;191:86-93.

301. Liu K, Zhang Z, Zhang F. Direct Extraction of Palladium and Silver from Waste Printed Circuit Boards Powder by Supercritical Fluids Oxidation-Extraction Process. Hazard Mater. 2016;318:216-23.

302. Xiu F, Qi Y, Zhang F. Leaching of Au, Ag, And Pd from Waste Printed Circuit Boards of Mobile Phone by Iodide Lixiviant After Supercritical Water Pre-Treatment. Waste Manage. 2015;41:134-41.

303. Singh L, Mahapatra DA, Thakur S. Bioelectrochemical Systems for removal and recovery of heavy metals. In Bioremediation, nutrients, and other valuable product recovery. Elsevier, 2020.p. 185−203.

304. Fu F, Wang Q. Removal of Heavy Metal Ions from Wastewaters: A Review. J Environ Manage. 2011;92(3):407-18.

305. Khan M, Albalawi GH, Shaik MR, Khan M, Adil SF, Kuniyil M, et al. Miswak Mediated Green Synthesized Palladium Nanoparticles as Effective Catalysts for The Suzuki Coupling Reactions in Aqueous Media. J Saudi Chem Soc. 2017;21(4):450-7.

306. Thakkar KN, Mhatre SS, Parikh RY. Biological Synthesis of Metallic Nanoparticles. Nanomedicine. 2010;6(2):257-62.

307. Virkutyte J, Varma RS. Green Synthesis of Metal Nanoparticles: Biodegradable polymers and enzymes in stabilization and surface functionalization. Chem Sci. 2011;2:837-46.

308. Alemu T, Assresahegn BD, Soreta TR. Tuning the Initial Electronucleation Mechanism of Palladium on Glassy Carbon Electrode. Port Electrochim Acta. 2014;32(1):21-33.

309. Benea L. Surface modifications of materials by electrochemical methods to improve the properties for industrial and medical applications. IOP Conf. Ser.: Mater. Sci. Eng. 2018;374:012014.

310. Jing M, Wu T, Zou G, Hou H, Ji X. Nanomaterials for Electrochemical Energy Storage. Front Nanosci. 2021;18:421-84.

311. Chang JH, Ellis AV, Yan CT, Tung CH. The electrochemical phenomena and kinetics of EDTA−copper wastewater reclamation by electrodeposition and ultrasound. Sep Purif Technol. 2009;68:(2)216-21.

312. Colantonio N, Kim Y. Cadmium(II) removal mechanisms in microbial electrolysis cells. J Hazard Mater. 2016;311:134-41.

313. Farooq R, Wang Y, Lin F, Shaukat SF, Donaldson J, Chouhdary AJ. Effect of ultrasound on the removal of copper from the model solutions for copper electrolysis process. Water Res. 2002;36(12):3165-9.

314. Shao M, Li S, Jin C, Chen M, Huang Z. Recovery of Pd(II) From Hydrochloric Acid Medium by Solvent Extraction−Direct Electrodeposition Using Hydrophilic/Hydrophobic Ils. ACS Omega. 2020;5(42):27188-96.

315. Terrazas-Rodríguez JE, Gutiérrez-Granados S, Alatorre-Ordaz MA, Ponce de León C, Walsh FC. A comparison of the electrochemical recovery of palladium using a parallel flat plate flow-by reactor and a rotating cylinder electrode reactor. Electrochim Acta. 2011;56(25):9357-63.

316. Marshall RJ, Walsh FC. Review of Some Recent Electrolytic Cell Designs. Surf Technol. 1985;24(1):45-77.

317. Oladeji AV, Courtney JM, Rees NV. Copper Deposition on Metallic and Non-Metallic Single Particles Via Impact Electrochemistry. Electrochim Acta. 2022;405:139838.

318. Wang T, Chutia A, Brett DJL, Shearing PR, He G, Chai G, et al. Palladium Alloys Used as Electrocatalysts for The Oxygen Reduction Reaction. Energy Environ Sci. 2021;14:2639-69.

319. Bell MF, Harrison JA. The deposition of palladium. J Electroanal Chem Interfacial Electrochem. 1973;41:15-25.

320. Maniam KK, Muthukumar V, Chetty R. Electrodeposition of Dendritic Palladium Nanostructures on Carbon Support for Direct Formic Acid Fuel Cells. J Hydrogen Energy. 2016;41(41):18602-9.

321. Heydari H, Abdolmaleki A, Gholivand MB. Electro-deposition and characterization of palladium nanostructures on stainless steel and application as hydrogen sensor. Ciência E Natura. 2015;37:23-33.

322. Smirnov MY, Klembovskii IO, Kalinkin AV, Bukhtiyarov VI. An XPS Study of the Interaction of a Palladium Foil with NO2. Kinet Catal. 2018;59:786-91.

323. Militello MC, Simko SJ. Elemental Palladium By XPS. Surf Sci Spectra. 1994;3:387-94.

324. Briggs D, Seah MP. Practical Surface Analysis, Auger and X-ray Photoelectron Spectroscopy;2nd edition. John Wiley & Sons.1990.

325. Kim KS, Gossmann AF, Winograd N. X-ray photoelectron spectroscopic studies of palladium oxides and the palladium-oxygen electrode. Anal Chem. 1974;46(2):197-200.

326. Militello MC, Simko SJ. Palladium Oxide (PdO) By XPS. Surf Sci Spectra. 1994;3(4):395-401.

327. Militello MC, Simko SJ. Palladium Chloride (PdCl2) By XPS. Surf Sci Spectra. 1994;3(4):402-9.

328. Meng H, Wang C, Shen P. K, Wu G. Palladium thorn clusters as catalysts for electrooxidation of formic acid. Energy Environ Sci. 2011;4(4):1522-6.

329. Olivares JA, Houk RS. Suppression of Analyte Signal by Various Concomitant Salts in Inductively Coupled Plasma Mass Spectrometry. Anal Chem. 1986;58(1):20-5.

330. Ogden JM. Hydrogen: The Fuel of the Future? Phys Today. 2002;55(4):69-75.

331. Wang Y, Pang Y, Xu H, Martinez A, Chen KS. PEM Fuel cell and electrolysis cell technologies and hydrogen infrastructure development - a review. Energy Environ. Sci. 2022;15(6):2288-328.

332. Peighambardoust SJ, Rowshanzamir S, Amjadi M. Review of the proton exchange membranes for fuel cell applications. Int J Hydrogen Energy. 2010;35(17):9349-84.

333. Li Y, Zhu X, Chen Y, Zhang S, Li J, Liu J. Rapid synthesis of highly active Pt/C catalysts with various metal loadings from single batch platinum colloid. J Energy Chem. 2020;47:138-45.

334. Zhang Y, Peng Y, Wan Q, Ye D, Wang A, Zhang L, Jiang W, Liu Y, Li J, Zhuang X, Zhang J, Ke C. Fuel cell power source based on decaborane with high energy density and low crossover. Mater Today Energy. 2023;32:101244.

335. Yang H, Liu J, Wang J, Poh CK, Zhou W, Lin J, Shen Z. Electrocatalytically Active Graphene supported MMo Carbides (MNi, Co) for Oxygen Reduction Reaction. Electrochim Acta. 2016;216:246-52.

336. Wang J, Yin G, Shao Y, Zhang S, Wang Z, Gao Y. Effect of carbon black support corrosion on the durability of Pt/C catalyst. Journal of Power Sources. 2007;171(2):331-9.

337. Zhang W, Sherrell P, Minett AI, Razal JM, Chen J. Carbon nanotube architectures as catalyst supports for proton exchange membrane fuel cells. Energy Environ Sci. 2010;3(9):1286-93.

338. Gupta C, Maheshwari PH, Dhakate SR. Development of multiwalled carbon nanotubes platinum nanocomposite as efficient PEM fuel cell catalyst. Mater Renew Sustain Energy. 2016;5(2):1-11.

339. Ghosh A, Srinath A, Verma A. Synthesis and Evaluation of Graphene for PEMFC Catalyst Support. Int J Innov Res Dev. 2012;1:7-12.

340. Chandran P, Ghosh A, Ramaprabhu S. High-performance Platinum-free oxygen reduction reaction and hydrogen oxidation reaction catalyst in polymer electrolyte membrane fuel cell. Sci Rep. 2018;8(1):3591.

341. Paoletti C, Cemmi A, Giorgi L, Giorgi R, Pilloni L, Serra E, Pasquali M. Electro-deposition on carbon black and carbon nanotubes of Pt nanostructured catalysts for methanol oxidation. J Power Sources. 2008;183(1):84-91.

342. Prabhuram J, Zhao TS, Wong CW, Guo JW. Synthesis and physical/electrochemical characterization of Pt/C nanocatalyst for polymer electrolyte fuel cells. J Power Sources. 2004;134(1):1-6.

343. Alekseenko AA, Guterman VE, Volochaev VA, Belenov SV. Effect of wet synthesis conditions on the microstructure and active surface area of Pt/C catalysts. Inorg Mater. 2015;51(12):1258-63.

344. Ma HC, Xue XZ, Liao JH, Liu CP, Xing W. Effect of borohydride as reducing agent on the structures and electrochemical properties of Pt/C catalyst. Appl Surf Sci. 2006;252(24):8593-7.

345. Nores-Pondal FJ, Vilella IMJ, Troiani H, Granada M, de Miguel SR, Scelza OA, Corti HR. Catalytic activity vs. size correlation in platinum catalysts of PEM fuel cells prepared on carbon black by different methods. Int J Hydrog Energy. 2009;34(19):8193-203.

346. Novomlinskiy IN, Tabachkova NY, Safronenko OI, Guterman VE. A novel electrochemical method for the preparation of Pt/C nanostructured materials. Monatsh Chem. 2019;150(4):631-7.

347. Newton JE, Preece JA, Rees NV, Horswell SL. Nanoparticle catalysts for proton exchange membrane fuel cells: Can surfactant effects be beneficial for electrocatalysis? Phys Chem Chem Phys. 2014 Jun 21;16(23):11435-46.

348. Barakat MA, Mahmoud MHH. Recovery of platinum from spent catalyst. Hydrometallurgy. 2004 Mar;72(3-4):179-84.

349. Li H, Zhang X, Sun Z, Ma W. Rapid Screening of Bimetallic Electrocatalysts Using Single Nanoparticle Collision Electrochemistry. J Am Chem Soc. 2022 Sep 14;144(36):16480-9.

350. Oladeji AV, Courtney JM, Fernandez-Villamarin M, Rees NV. Electrochemical Metal Recycling: Recovery of Palladium from Solution and In Situ Fabrication of Palladium-Carbon Catalysts via Impact Electrochemistry. J Am Chem Soc. 2022;144(40):18562-74.

351. Dickinson EJF, Limon-Petersen JG, Rees NV, Compton RG. How Much Supporting Electrolyte Is Required to Make a Cyclic Voltammetry Experiment Quantitatively “Diffusional”? A Theoretical and Experimental Investigation. J. Phys. Chem. C. 2009;113(25):11157-71.

352. Shinozaki K, Zack JW, Richards RM, Pivovar BS, Kocha SS. Oxygen Reduction Reaction Measurements on Platinum Electrocatalysts Utilizing Rotating Disk Electrode Technique: I. Impact of Impurities, Measurement Protocols and Applied Corrections. J Electrochem Soc. 2015;162(10):F1144.

353. Garsany Y, Singer IL, Swider-Lyons KE. Impact of film drying procedures on RDE characterization of Pt/VC electrocatalysts. J Electroanal Chem. 2011;662(2):396-406.

354. Campos-Roldán CA, González-Huerta RG, Alonso-Vante N. Experimental Protocol for HOR and ORR in Alkaline Electrochemical Measurements. J Electrochem Soc. 2018;165(15):J3001.

355. Kriek RJ, Mogwase BMS, Vorster SW. Relation of the electrochemical interplay between H2PtCl6 and H2O/H3O+/H2+ and the hydrogen-evolution reaction. Electrochem Sci Adv. 2022;2(2):e2100041.

356. Lu G, Zangari G. Electrodeposition of Platinum on Highly Oriented Pyrolytic Graphite. Part I: Electrochemical Characterization. J Phys Chem B. 2005;109(16):7998-8007.

357. Hagihara T, Yaori K, Iwakura K, Fukumuro N, Yae S. Electrochemical quartz crystal microbalance study of the electrodeposition of platinum. Electrochim. Acta. 2015;176:65-9.

358. Feltham AM, Spiro M. Platinized platinum electrodes. Chem. Rev. 1971;71(2):177-93.

359. Itaya K, Takahashi H, Uchida I. Electrodeposition of Pt ultramicroparticles in Nafion films on glassy carbon electrodes. J. Electroanal. Chem. Interfac. Electrochem. 1986;208(2):373-82.

360. Mazzotta E, Di Giulio T, Mastronardi V, Pompa PP, Moglianetti M, Malitesta C. Bare Platinum Nanoparticles Deposited on Glassy Carbon Electrodes for Electrocatalytic Detection of Hydrogen Peroxide. ACS Appl. Nano Mater. 2021;4(8):7650-62.

361. Zhao D, Xie S, Wang Y, Zhu H, Chen L, Sun Q, Zhang DW. Synthesis of large-scale few-layer PtS2 films by chemical vapor deposition. AIP Advances. 2019 Feb 27;9(2):025225.

362. Gama-Lara SA, Natividad R, Vilchis-Nestor AR, López-Castañares R, García-Orozco I, Gonzalez-Pedroza MG, Morales-Luckie RA. Ultra-Small Platinum Nanoparticles with High Catalytic Selectivity Synthesized by an Eco-friendly Method Supported on Natural Hydroxyapatite. Catalysis Letters. 2019 Dec 1;149(12):3447-53.

363. Choi HC, Shim M, Bangsaruntip S, Dai H. Spontaneous Reduction of Metal Ions on the Sidewalls of Carbon Nanotubes. Journal of the American Chemical Society. 2002 Aug 1;124(31):9058-9.

364. Wei ZD, Yan C, Tan Y, Li L, Sun CX, Shao ZG, Shen PK, Dong HW. Spontaneous Reduction of Pt(IV) onto the Sidewalls of Functionalized Multiwalled Carbon Nanotubes as Catalysts for Oxygen Reduction Reaction in PEMFCs. J Phys Chem C. 2008;112(7):2671-7.

365. Liu J, Zhang H, Shi L, Liu X, Wang T, Zhang L, et al. Metal-free efficient photocatalyst for stable visible water splitting via a two-electron pathway. Science. 2015;347(6225):970-4.

366. Qu Y, Shao M, Shao Y, Yang M, Xu J, Kwok CT, Shi X, Lu Z, Pan H. Ultra-high electrocatalytic activity of VS2 nanoflowers for efficient hydrogen evolution reaction. J Mater Chem A. 2017;5(29):15080-6.

367. Han Y, Yue X, Jin Y, Huang X, Shen PK. Hydrogen evolution reaction in acidic media on single-crystalline titanium nitride nanowires as an efficient non-noble metal electrocatalyst. J Mater Chem A. 2016;4(10):3673-7.

368. Duan J, Chen S, Jaroniec M, Qiao SZ. Porous C3N4 Nanolayers@N-Graphene Films as Catalyst Electrodes for Highly Efficient Hydrogen Evolution. ACS Nano. 2015;9(1):931-40.

369. Łukaszewski M, Soszko M, Czerwiński A. Electrochemical Methods of Real Surface Area Determination of Noble Metal Electrodes - an Overview. Int J Electrochem Sci. 2016 Jun 1;11(6):4442-69.

370. Wang Q, Cha CS, Lu J, Zhuang L. The electrochemistry of “solid/water” interfaces involved in PEM-H2O reactors Part I. The “Pt/water” interfaces. Phys. Chem. Chem. Phys. 2009;11(4):679-87.

371. Do CL, Pham TS, Nguyen NP, Tran VQ. Properties of Pt/C nanoparticle catalysts synthesized by electroless deposition for proton exchange membrane fuel cell. Adv Nat Sci Nanosci Nanotechnol. 2013 Jun 25;4(3):035011.

372. Pozio A, De Francesco M, Cemmi A, Cardellini F, Giorgi L. Comparison of high surface Pt/C catalysts by cyclic voltammetry. J Power Sources. 2002 Mar 5;105(1):13-9.

373. Holewinski A, Linic S. Elementary Mechanisms in Electrocatalysis: Revisiting the ORR Tafel Slope. J Electrochem Soc. 2012 Sep 5;159(11):H864.

374. Chen W, Xiang Q, Peng T, Song C, Shang W, Deng T, Wu J. Reconsidering the Benchmarking Evaluation of Catalytic Activity in Oxygen Reduction Reaction. iScience. 2020 Oct 23;23(10):101532.

375. Kumar Y, Jaiswal P, Panda D, Nigam KDP, Biswas KG. A critical review on nanoparticle-assisted mass transfer and kinetic study of biphasic systems in millimeter-sized conduits. Chemical Engineering and Processing - Process Intensification. 2022 Jan 1;170:108675.

376. Freitas JM, Oliveira TC, Munoz RA, Richter EM. Boron Doped Diamond Electrodes in Flow-Based Systems. Front Chem. 2019;7:190.

377. Ribeiro MC, Silva LG da, Sumodjo PTA. The influence of electrochemical pre-treatment of B-doped diamond films on the electrodeposition of Pt. J Braz Chem Soc. 2006;17.

378. Gu S, Wang X, Wei Y, et al. Mechanism for nucleation and growth of electrochemical deposition of palladium(II) on a platinum electrode in hydrochloric acid solution. Sci China Chem. 2014;57(5):755-62.

8. Appendix

APPENDIX A: Calculate the equilibrium concentrations of Pd-chloro complexes in the reaction solution

The stability constant (β) is an equilibrium constant for the formation of a complex in solution and measures the strength of the interaction between reagents forming the complex. This has been used to calculate the equilibrium concentrations of Pd-chloro complexes in the reaction solution as shown in Table 8.

For example:

Equation 105

$$[Pd(H_2O)_6]^{2+} + Cl^- \rightarrow [Pd(H_2O)_5Cl]^+ + H_2O$$

Where $Log_{10}\beta_1 = 4.47$[378]

Equilibrium constant $\beta_1 = 10^{4.47} \approx 2.95\times10^4$

Initial concentration $[Pd(H_2O)_6]^{2+}$= 0.0005 M

Initial concentration of Cl^-= 0.02M

β_1 is given by:

Equation 106

$$\beta_1 = \frac{[Pd(H_2O)_5Cl]^+}{[Pd(H_2O)_6]^{2+}[Cl^-]}$$

Equation 107

$$2.95 \times 10^4 = \frac{x}{(0.0005 - x)(0.02 - x)}$$

Where x is the equilibrium concentration of $[Pd(H_2O)_6]^{2+}$, and can be solved by rearranging for x and solving the resulting quadratic equation:

Equation 108

$$2.95 \times 10^4\, x^2 - 591.590x + 0.295 = 0$$

Where a=2.95×10^4, b= 591.590 and c=0.295

$$x = 1.57 \times 10^{-6}\ M$$

APPENDIX B: Calibration curve for palladium and platinum ICP studies.

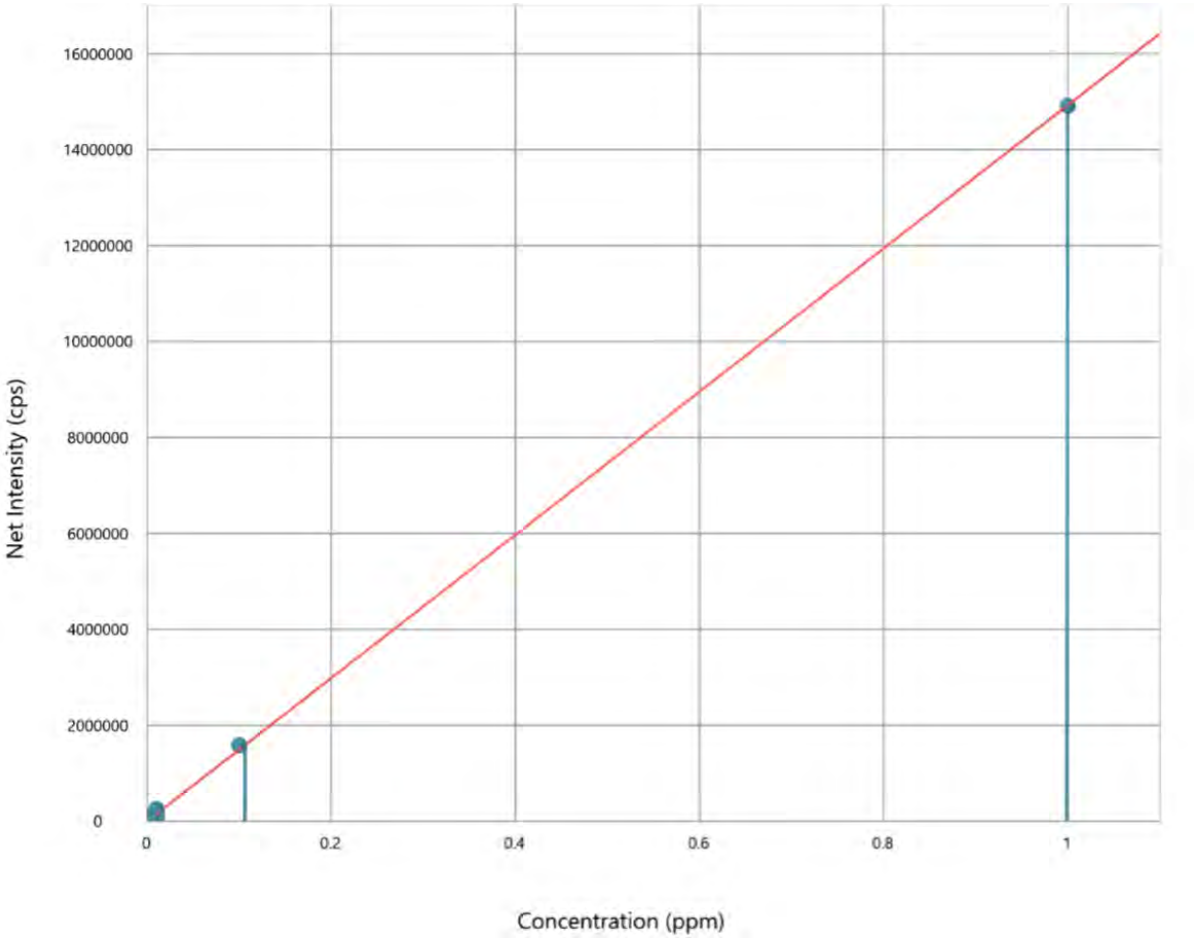

Figure 65 shows a calibration curve generated with a 10 ppm multielement calibration standard for ICP (Agilent), in ultrapure water at concentrations of 5–0.01 ppm, R^2=0.9999

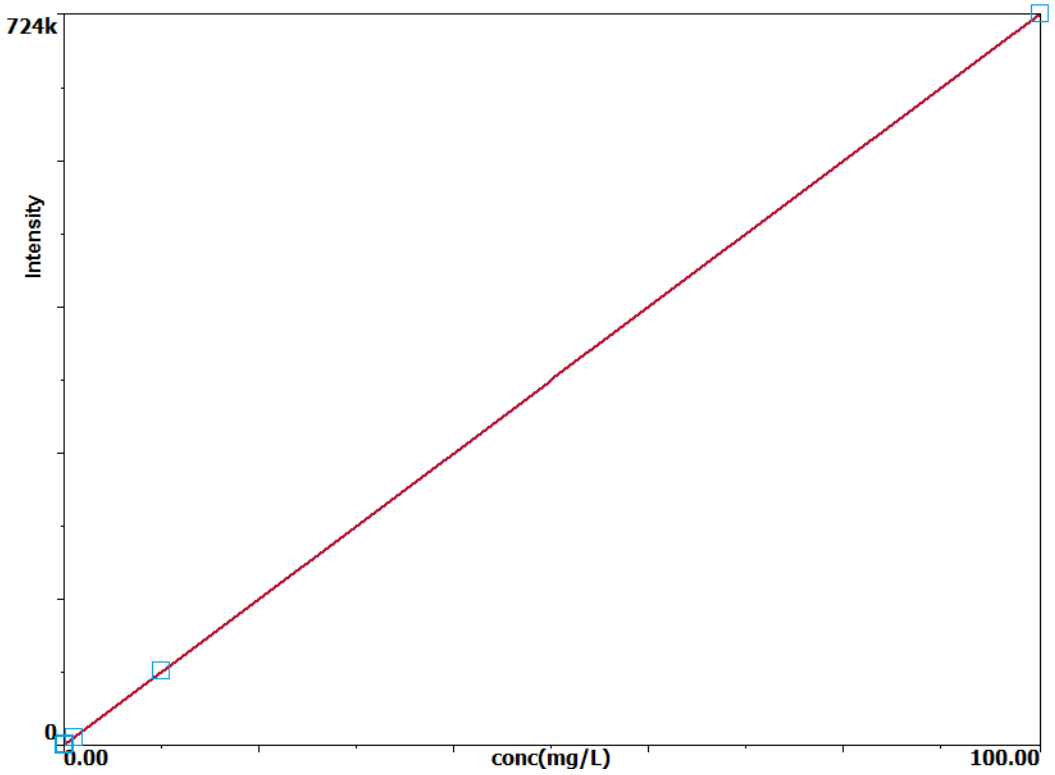

Figure 66 shows a calibration curve ranging from 0.01 ppm to 100 ppm was produced using a Pt standard solution (VWR ARISTAR),R^2=0.9999.